Theoretische Physik

SUSY-QCD Corrections to the (Co)Annihilation of Neutralino Dark Matter within the MSSM

Inaugural-Dissertation
zur Erlangung des Doktorgrades
der Naturwissenschaften im Fachbereich Physik
der Mathematisch-Naturwissenschaftlichen Fakultät
der Westfälischen Wilhelms-Universität Münster

vorgelegt von
Moritz Meinecke
aus Osnabrück
–2015–

Dekan:	Prof. Dr. Christian Weinheimer
Erster Gutachter:	Prof. Dr. Michael Klasen
Zweiter Gutachter:	Prof. Dr. Gernot Münster
Tag der mündlichen Prüfung:	15.6.2015
Tag der Promotion:	

Zusammenfassung

Basierend auf der Grundlage verschiedener experimenteller Beobachtungen wird heutzutage mehrheitlich davon ausgegangen, dass ein Großteil der im Universum auftretenden Materie aus sogenannter kalter dunkler Materie besteht. Mittels der Vermessung der Temperaturfluktuation des kosmischen Mikowellenstrahlungshintergrunds ist es möglich, die Dichte der im Universum vorliegenden dunklen Materie fast bis auf das Prozent genau (1σ-Unsicherheit) zu bestimmen. Mit dem leichtesten Neutralino $\tilde{\chi}_1^0$, einem Teilchen, welches zu der aus phänomenologischer Sicht interessanten Klasse der schwach wechselwirkenden, massiven Teilchen gehört, existiert nun für eine Vielzahl supersymmetrischer (SUSY) Modelle ein hervorragender Kandidat für dunkle Materie, dessen Restdichte $\Omega_{\tilde{\chi}_1^0}$ auf natürliche Weise innerhalb der experimentell favorisierten Größenordnung liegt. Diese hohe Genauigkeit der Messdaten kann dazu genutzt werden, die kosmologisch bevorzugten Bereiche des SUSY-Parmeterraumes zu bestimmen und so phänomenologisch interessante Szenarien zu identifizieren. Dazu gilt es jedoch, auch auf Seiten der Theorie mögliche Unsicherheiten zu lokalisieren und zu minimieren. Eine wichtige Größe, die maßgeblich die Neutralino-Restdichte bestimmt, ist die thermisch gemittelte Summe über verschiedene Annihilations- und Koannihilationswirkungsquerschnitte zwischen dem leichtesten Neutralino und weiteren supersymmetrischen Teilchen. Diese Größe kann erheblichen Schleifenkorrekturen unterliegen, wie sie im Rahmen der störungstheoretischen Behandlung von Quantenfeldtheorien auftreten. Doch obwohl vermutet wird und teilweise auch nachgewiesen werden konnte, dass die theoretische Unsicherheit der Neutralino Restdichte $\Omega_{\tilde{\chi}_1^0}$ auf Grund dieser Korrekturen höherer Ordnung die experimentelle Unsicherheit übertreffen kann, sind diese Schleifenkorrekturen bisher nur unvollständig berechnet worden. *In der vorliegenden Dissertation berechnen wir nun im Rahmen einer minimalen supersymmetrischen Erweiterung des Standardmodells (MSSM) mit erhaltener R-Parität bis dato unbekannte Korrekturen höherer Ordnung zu verschiedenen Annihilations- und Koannihilationswirkungsquerschnitten des leichtesten Neutralinos $\tilde{\chi}_1^0$ und untersuchen die zugehörige Restdichte $\Omega_{\tilde{\chi}_1^0}$ auf deren Einfluss hin.* Genauer bestimmen wir in dieser Arbeit Korrekturen der Ordnung $\mathcal{O}(\alpha_s)$ zur (Ko)Annihilation von Neutralinos und Charginos in Quarks sowie zur (Ko)Annihilation von Squarks in elektroschwache Endzustände im Rahmen der supersymmetrischen Quantenchromodynamik. Des Weiteren beschreiben wir im Kontext der Behandlung ultravioletter Divergenzen detailliert das von uns verwendete $\overline{DR}$/on-shell Renormierungsschema sowie die Verfahren des ,,phase-space slicings" und der ,,dipole subtraction", welche wir zur numerischen Evaluation der im Rahmen von Korrekturen höherer Ordnung auftretenden infrarot und kollinear divergenter Wirkungsquerschnitte benötigen. Zusätzlich schließen wir auch nicht-perturbative sogenante Coulomb-Korrekturen, welche im Fall der Squark-Annihilation die Wirkungsquerschnitte maßgeblich beeinflussen können, mit in die Berechnungen ein.
Die oben genannten Korrekturen sind in ein Softwarepaket namens `DM@NLO` implementiert worden, welches in der Lage ist, eine Vielzahl relevanter (Ko)Annihilations Wirkungsquerschnitte auf Einschleifen-Niveau in α_s zu bestimmen. `DM@NLO` stellt damit eine Erweiterung öffentlich zugänglicher Software dar, die zumeist nur eine Berechnung auf Ebene des effektiven Born-Levels ermöglichen. Zur numerischen Auswertung untersuchen wir innerhalb der zwei oben genannten Prozessklassen für jeweils drei repräsentative Szenarien den

Einfluss dieser Korrekturen auf die Neutralino-Restdichte $\Omega_{\tilde{\chi}_1^0}$. Innerhalb beider Prozessklassen, d.h. sowohl für die (Ko)Annihilation von Neutralinos und Charginos, als auch für die (Ko)Annihilation von Squarks, zeigt sich, dass unsere Korrekturen die experimentelle 1σ-Unsicherheit weit übertreffen können. Diese Arbeit bestätigt somit die Relevanz von Korrekturen höherer Ordnung und gewährt darüber hinaus einen tieferen Einblick in das Zusammenspiel verschiedenster, teils exotischer (Ko)Annihilations-Kanäle innerhalb der Berechnung von $\Omega_{\tilde{\chi}_1^0}$.

Abstract

Based on experimental observations, it is nowadays assumed that a large component of the matter content in the universe is comprised of so-called cold dark matter. Furthermore, latest measurements of the temperature fluctuations of the cosmic microwave background provided an estimation of the dark matter relic density at a measurement error of one percent (concerning the experimental 1σ-error). The lightest neutralino $\tilde{\chi}_1^0$, a particle which subsumes under the phenomenologically interesting category of weakly interacting massive particles, is a viable dark matter candidate for many supersymmetric (SUSY) models whose relic density $\Omega_{\tilde{\chi}_1^0}$ happens to lie quite naturally within the experimentally favored ballpark of dark matter. The high experimental precision can be used to constrain the SUSY parameter space to its cosmologically favored regions and to pin down phenomenologically interesting scenarios. However, to actually benefit from this progress on the experimental side it is also mandatory to minimize the theoretical uncertainties. An important quantity within the calculation of the neutralino relic density is the thermally averaged sum over different annihilation and coannihilation cross sections of the neutralino and further supersymmetric particles. It is now assumed and also partly proven that these cross sections can be subject to large loop corrections which can even shift the associated $\Omega_{\tilde{\chi}_1^0}$ by a factor larger than the current experimental error. However, most of these corrections are yet unknown. *In this thesis, we calculate higher-order corrections for some of the most important (co)annihilation channels both within the framework of the R-parity conserving Minimal Supersymmetric Standard Model (MSSM) and investigate their impact on the final neutralino relic density* $\Omega_{\tilde{\chi}_1^0}$. More precisely, this work provides the full $\mathcal{O}(\alpha_s)$ corrections of supersymmetric quantum chromodynamics (SUSY-QCD) to the (co)annihilation channels of neutralinos and charginos into quarks as well as of squark (co)annihilation into electro weak final states. Therefore, we give a detailed description of the $\overline{DR}$/on-shell renormalization scheme used in the context of associated UV-divergences. On top of that, we introduce the methods of "phase-space slicing" and "dipole subtraction", which are needed to evaluate infrared and collinear singular cross sections numerically. Furthermore, we describe additional non-perturbative effects, so-called Coulomb corrections, which turn out to alter the cross sections connected to the (co)annihilation of squarks sizeably.

We have implemented all of the corrections aforementioned into a software package called `DM@NLO`, which provides the full $\mathcal{O}(\alpha_s)$ corrections for a broad variety of relevant (co)annihilation channels. `DM@NLO` therefore presents a significant extension of currently available public tools, which so far only allow for a calculation of (co)annihilation channels at the effective Born level.

Concerning the numerical analysis of our results, for each of the above two (co)annihilation classes, we choose three different scenarios to present the impact of our higher-order corrections on the final neutralino relic density $\Omega_{\tilde{\chi}_1^0}$. We find that both classes of cross sections, namely for the (co)annihilation of neutralinos and charginos as well as for the squark (co)annihilation, yield sizeable corrections to the final $\Omega_{\tilde{\chi}_1^0}$, which can be much larger than the current experimental uncertainty. Hence, this work confirms the relevance of higher-order corrections for a high precision estimation of the neutralino relic density

and, moreover, allows for a distinct insight into the interplay of the different, partly exotic, (co)annihilation channels in the calculation of the final $\Omega_{\tilde{\chi}_1^0}$.

Danksagung

Mein erster Dank an dieser Stelle gilt Prof. Michael Klasen für die Möglichkeit, innerhalb dieses spannenden und aktiven Forschungsgebiets meine Doktorarbeit verfassen zu können. Danke auch für die für Fragen jederzeit offene Tür sowie die Unterstützung und Freiheit, mit der ich an meinem Projekt arbeiten durfte. Danken möchte ich auch Prof. Münster und Prof. Weinheimer für ihre Zeit, die sie in diese Arbeit investieren. Als nächstes Danken möchte ich dem ganzen DM@NLO-Team, sowohl den derzeitigen als auch den ehemaligen Mitgliedern, allen voran Karol Kovařík, Björn Herrmann, Julia Harz, Quentin le Boulc'h und Patrick Steppeler. Danke für die zahlreichen Diskussionen und die Unterstützung, die ihr mir mit großer Geduld gewährt habt. Besonders aber auch vielen Dank für die schöne Zeit abseits der Arbeit während unserer vielen Treffen in Münster, Karlsruhe und Annecy. Nochmal Danken möchte ich an dieser Stelle Karol Kovařík, ohne dessen geduldige Hilfe diese Arbeit sicherlich so nicht möglich gewesen wäre. Danke auch für die ausdauernde Einsatzfreude, mit der du mich bei zahlreichen Käsefondues in Annecy so tatkräftig unterstützt hast. Dank gilt auch den Arbeitsgruppen von Michael Klasen und Anna Kulesza, allen voran meinen Bürogenossen Sonja und Patrick, die es mir immens erleichtert haben, obwohl von Müdigkeit schwer geplagt, mit angemessen guter Laune immer wieder den Weg ins Büro zu finden. Insbesondere danken möchte ich euch für die herzliche Aufnahme auch abseits der Arbeit. Die vergangene Zeit wäre auch nicht halb so schön gewesen ohne eure sowie die vielen weiteren Freundschaften und Bekanntschaften, die ich über euch habe machen dürfen. Dank gilt auch meinen zahlreichen Korrekturlesern: Julia Harz und Björn Herrmann für ein teilweises Korrekturlesen, insbesondere jedoch Patrick Steppeler und Jana Scharfen, die offensichtlich getrieben von einer ordentlichen Portion Willensstärke mein komplettes opus magnum einmal vollständig durchgestanden haben. Danke dafür! Dank gilt auch nochmal all den vielen weiteren Menschen die die letzten Jahre zu einer so schönen Zeit haben werden lassen. Auch wenn ich in erster Linie der Arbeit wegen nach Münster kam ist doch gerade der Wert eurer Gesellschaft und Unterstützung kaum hoch genug einzuschätzen. Besonders danken möchte ich hier Jana Scharfen. Auch wenn du erst auf der Zielgeraden dazugekommen bist, hoffe ich doch, dass wir auch weiterhin noch Vieles gemeinsam erleben und erreichen werden. Mein größter Dank soll an dieser Stelle jedoch meinen Eltern Lutz und Susanne sowie meiner Schwester Charlotte gelten. Euer Rückhalt und eure Unterstützung auch weit über die eigentliche Arbeit hinaus waren und sind stets von größter Bedeutung für mich. Vielen Dank dafür!

Contents

1. Introduction

The questions of the existence and nature of *dark matter* (DM) are nowadays some of the most compelling mysteries of modern physics and led to a deep and fruitful intertwining between the fields of cosmology and theoretical particle physics. After the first observational hints towards its existence in 1933 by Zwicky, many experiments started to look for this new, speculative mass component, dubbed dark matter, which seemed to provide a very natural explanation for the observed discrepancies between theory and experiment. Maybe one of the most noticeable observations in the subsequent series of experiments concerning the clarification of the nature of DM was the measurement of the anisotropies of the cosmic microwave background (CMB) by the COBE satellite in 1992 together with its follow-up experiments WMAP and Planck which provided an insight into its number density and composition, e.g.. However, all of these observations turned out to be rather indirect such that DM still lacks its final concrete experimental proof. Hence, while the very extensive and elaborate searches for DM are still ongoing, theorists try to come up with ideas which can explain the observations obtained and make further testable predictions. During this search for DM-models consistent with experiments, theory has been led to step even beyond the Standard Model of particle physics (SM), the milestone in our understanding of particle physics. This insight has amplified the interest in the nature of DM as it is one of the few experimentally unambiguously underpinned calls for physics beyond the SM (BSM). It turned out that certain so-called R-parity conserving supersymmetric extensions of the SM naturally provide such a viable DM candidate; this is the lightest neutralino $\tilde{\chi}_1^0$. Moreover, since low scale supersymmetric models provide solutions not only for DM but also for many other potential shortcomings of the SM, supersymmetric DM candidates quickly became subject to very detailed analyses. Due to the lack of observational evidence it is clear that low scale supersymmetry (SUSY) as realized, e.g., in the Minimal Supersymmetric Standard Model (MSSM), cannot be an exact symmetry of nature. This insight led physicists to the introduction of a broad variety of different soft SUSY breaking terms which account for the necessary mass splitting between SM particles and their supersymmetric partners as required by experiment while respecting the renormalizability of the underlying quantum field theory. These terms come along with a vast amount of additional SUSY-breaking parameters (in the MSSM more than one hundred), which can be freely adjusted and, hence, undermine the predictive power of the corresponding theory. This is the point where the work of this thesis enters the scene. Turning around the original line of argumentation to find viable DM models which explain the DM observations and to test their predictions in experiments, we use the latest experimental data from the Planck experiment on the DM relic density to cut the large MSSM parameter space down to the small cosmologically favored regions. Moreover, since experimental data already reached a precision in the percent region[1], it becomes mandatory to improve the actual precision of relic density calculations to fully benefit from the experimental accuracy. *For this purpose, we calculate the next-to-leading order (NLO) SUSY-QCD corrections to some of the most important (co)annihilation processes of the lightest neutralino within the MSSM.* More precisely, we provide the full $\mathcal{O}(\alpha_s)$ corrections

[1] The experimental error at 1σ on the DM relic density amounts to 2% of the measured value.

for the (co)annihilation of neutralinos $\tilde{\chi}_i^0$ ($i \in \{1,2,3,4\}$) and charginos $\tilde{\chi}_i^\pm$ ($i \in \{1,2\}$) into quarks as well as for squark (co)annihilation into electroweak (EW) final states. We also consider the so-called Coulomb enhancement of squark annihilation, a non-perturbative effect, which can be ascribed to the exchange of potential gluons between the incoming squark-antisquark pair at low relative velocity and which needs to be resummed to all orders in perturbation theory to yield a reliable result.
This thesis is organized as follows.
In *Chapter 2*, we introduce the basics of supersymmetry providing its motivations and theoretical framework. We introduce the MSSM as well as a constrained version of it, the phenomenological MSSM (pMSSM), which is the setup for our analysis on the actual impact of the $\mathcal{O}(\alpha_s)$ corrections on the DM relic density.
Chapter 3 is devoted to the introduction of dark matter. We give a short summary of the experimental evidences of its existence and discuss the resulting insights about its nature. This is followed by a compact overview over potential DM candidates. Afterwards, we address the very active field of recent searches for particle DM, giving a concise overview of current progress. We further provide the standard calculation of the DM relic density as common to the thermal production of a relic particle. This chapter is completed by a summary of the different uncertainties which enter the estimate of the DM relic density and which one should keep in mind to obtain a complete theoretical picture.
Chapter 4 deals with the presentation of the actual numerical routine, named dark matter at next-to-leading order (`DM@NLO`), in whose context this work takes place. Moreover, we discuss its integration into publically available codes. Thereafter, in *Chapter 5*, we turn to the two sub-projects of `DM@NLO` relevant to this work, namely `ChiChi2qq` (gaugino (co)annihilation into quarks) and `QQ2xx` (squark (co)annihilation into EW final states), and discuss their tree-level contributions as well as the associated phenomenology. Thereby, we introduce the representative scenarios which are used to investigate the relevance of our higher-order corrections. This is followed by the discussion of the higher-order corrections. More precisely, we give an introduction to NLO calculations on quite general grounds, providing the necessary tools to handle the different types of ultraviolet, infrared and collinear divergences, which we encounter throughout our NLO calculations. Furthermore, we present the theoretical framework of the above mentioned Coulomb corrections as well as additional subtleties which arise in the context of `QQ2xx`. In *Chapter 6 and 7*, we present the actual numerical impact of the higher-order corrections on the different (co)annihilation channels introduced in Chapter 3, first on the cross section level and subsequently on the level of the neutralino relic density. A final summary and outlook is given in *Chapter 8*.

The main results of this thesis have already been published in the publications Ref. [1] and Ref. [2]. Whereas Ref. [2] has been subject to this thesis completely, I have contributed a distinct part to Ref. [1], namely the real corrections and associated methods (see below). I further performed certain checks on the tree-level and virtual corrections, but did not calculate them as a whole.

2. Supersymmetry: Motivation, Theory and Model Building

Supersymmetry is nowadays seen as one of the theoretically best motivated extensions of the Standard Model. Guided by the theoretically well established and experimentally affirmed principle of symmetries, SUSY is able to improve on many of the phenomenological and aesthetical shortcomings of the Standard Model. In the following, we present some of the motivations of supersymmetry, provide an introduction to its mathematical formulation and discuss a possible realization in terms of a phenomenologically viable extension of the Standard Model, the MSSM. Before we start with the motivation of $\mathcal{N} = 1$ supersymmetry, we give a short introduction to the representations of the Lorentz group and thereby clarify some definitions and notations which we need in the subsequent paragraphs.

2.1. The Poincaré Group, Definitions and Notations

The Poincaré group is the starting point of the discussion. This is the group of all Minkowski-space-time isometries Λ [3], which obey

$$g_{\mu\nu} \;=\; \Lambda^{\lambda}_{\mu}\Lambda^{\kappa}_{\nu}g_{\lambda\kappa}. \tag{2.1}$$

The algebra of the Poincaré group takes the form

$$[P^{\mu}, P^{\nu}] \;=\; 0, \tag{2.2a}$$
$$[P^{\rho}, M^{\mu\nu}] \;=\; i(g^{\rho\mu}P^{\nu} - g^{\rho\nu}P^{\mu}), \tag{2.2b}$$
$$[M^{\rho\sigma}, M^{\mu\nu}] \;=\; -i(g^{\rho\mu}M^{\sigma\nu} + g^{\sigma\nu}M^{\rho\mu} - g^{\rho\nu}M^{\sigma\mu} - g^{\sigma\mu}M^{\rho\nu}), \tag{2.2c}$$

where the hermitian generators $M^{\mu\nu}$ and P^{μ} are the generators of rotations, boosts and space-time translations. The Lorentz group $O(1,3)$ is a subgroup of the Poincaré group generated by the $M^{\mu\nu}$ of Eq. (2.2c)[1]. It is divided into four non-connected subsets according to the properties of their elements

$$\det\Lambda \;=\; \pm 1, \tag{2.3a}$$
$$\Lambda_{00} \geq 1 \;\text{ or }\; \Lambda_{00} \leq 1, \tag{2.3b}$$

as required by Eq. (2.1). The only subset of the Lorentz group, which is for itself a subgroup as it contains the neutral element $\mathbb{1}$, is the set of proper and ortochronous Lorentz transformations $SO^{+}(1,3) \;=\; \{\Lambda \in O(1,3) : \det\Lambda \;=\; 1, \Lambda_{00} \geq 0\}$, whose elements preserve orientations in space-time. The $SO^{+}(1,3)$ is often referred to as the restricted Lorentz group. Due to the appearance of boosts, the restricted Lorentz group

[1] The Lorentz group is the isotropy subgroup (stabilizer subgroup of the origin) of the isometries of Minkowsi space-time, also called homogenous Lorentz group, whereas the Poincaré group, the group of all isometries of Minkowski space-time, is the Lorentz group extended by space-time translations, also called inhomogenous Lorentz group.

is non-compact. Hence, all of its faithful[2] and finite-dimensional representations are non-unitary.
To get a deeper insight into its representations, one can rewrite the $M^{\mu\nu}$ as

$$J_p = \frac{1}{2}\epsilon_{prs}M_{rs}, \tag{2.4a}$$

$$K_p = -M_{0p}. \tag{2.4b}$$

One can then define the new generators

$$\mathcal{J}_p^{\pm} = \frac{1}{2}(J_p \pm iK_p), \tag{2.5}$$

which fulfill

$$[\mathcal{J}_p^+, \mathcal{J}_q^+] = i\epsilon_{pqr}\mathcal{J}_r^+, \tag{2.6a}$$

$$[\mathcal{J}_p^-, \mathcal{J}_q^-] = i\epsilon_{pqr}\mathcal{J}_r^-, \tag{2.6b}$$

$$[\mathcal{J}_p^+, \mathcal{J}_q^-] = 0. \tag{2.6c}$$

As apparent from Eq. (2.6c) $\mathcal{J}_p^+$ and $\mathcal{J}_p^-$ decouple. Moreover, Eq. (2.6a) and Eq. (2.6b) show the homomorphic relation between $SO^+(1,3)$ and $SU(2)_+ \otimes SU(2)_-$ such that locally $SO^+(1,3) \backsimeq SU(2)_+ \otimes SU(2)_-$ [3]. Hence, the task of finding the finite-dimensional, irreducible representations of the Lorentz group can be reduced to the construction of the corresponding representations for $SU(2)_+ \otimes SU(2)_-$. As known from, e.g., the coupling of different spin-$\frac{1}{2}$ states, one can label the different representations of $SU(2)_+ \otimes SU(2)_-$ by pairs (j^+, j^-) where $j^{\pm}$ can take integer or half integer values. For instance, $(\frac{1}{2}, 0)$ and its complex conjugated representation $(0, \frac{1}{2})$ specify the left and right chiral representation, i.e., the fundamental and anti-fundamental representation of $SL(2,\mathbb{C})$. $(\frac{1}{2}, 0) \oplus (0, \frac{1}{2})$ refers to the representation of massive Dirac spinors. Finally, four vectors correspond to the fundamental representation of the Lorentz group denoted as $(\frac{1}{2}, \frac{1}{2})$.
The Weyl spinors ξ_A and $\bar{\xi}_{\dot{A}}$ with $A, \dot{A} \in \{1, 2\}$, which transform under the lowest-dimensional spinor-representations of $SO^+(1,3)$, labeled $(\frac{1}{2}, 0)$ (big Latin index, e.g., A) and $(0, \frac{1}{2})$ (dotted big Latin index, e.g., $\dot{A}$), turn out to be central objects in the discussion of SUSY. Within this spinor space one can introduce the two-dimensional Levi-Civita symbol

$$\epsilon^{AB} = \epsilon^{\dot{A}\dot{B}} = \begin{pmatrix} 0 & 1 \\ -1 & 0 \end{pmatrix}, \quad \epsilon_{AB} = \epsilon_{\dot{A}\dot{B}} = \begin{pmatrix} 0 & -1 \\ 1 & 0 \end{pmatrix} \tag{2.7}$$

as a metric. It can be used to raise and lower dotted as well as undotted spinor indices, drawing the connection to the corresponding linear forms and *vice versa*. Furthermore, we have

$$\xi = (\bar{\xi})^{\dagger}, \tag{2.8}$$

which can be written in component form as

$$\xi_A = (\bar{\xi}_{\dot{A}})^{\dagger}, \quad \xi^A = (\bar{\xi}^{\dot{A}})^{\dagger}. \tag{2.9}$$

We also make use of the definition

$$\sigma^{\mu\nu} = \frac{i}{4}(\sigma^{\mu}\bar{\sigma}^{\nu} - \sigma^{\nu}\bar{\sigma}^{\mu}), \tag{2.10}$$

[2] Here, the trivial representation is excluded.
[3] To be more precise, in contrast to the elements of $\mathfrak{su}(2)$, $\mathcal{J}_p^{\pm}$ are not hermitian (see the non-unitary statement above). Hence, $\mathcal{J}_p^{\pm}$ are the generators of $SL(2,\mathbb{C})$, the universal covering group of $SO^+(1,3)$, which is, however, locally isomorphic to $SU(2)_+ \otimes SU(2)_-$.

where we have introduced

$$\sigma^{\mu}_{A\dot{B}} \;=\; (\mathbb{1}, \sigma^1, \sigma^2, \sigma^3)_{A\dot{B}} \;=\; (\mathbb{1}, \overrightarrow{\sigma})_{A\dot{B}}, \tag{2.11a}$$

$$\bar{\sigma}^{\mu \dot{A}B} \;=\; (\mathbb{1}, -\sigma^1, -\sigma^2, -\sigma^3)^{\dot{A}B} \;=\; (\mathbb{1}, -\overrightarrow{\sigma})^{\dot{A}B}. \tag{2.11b}$$

Here, σ^i ($i \in \{1,2,3\}$) represents the well known Pauli matrices.
The Weyl or chiral representation of massive Dirac spinors ψ_a, in the following labeled by small Latin indices, e.g., $a \in \{1,2,3,4\}$, is characterized by

$$\gamma_\mu \;=\; \begin{pmatrix} 0 & \sigma_\mu \\ \bar{\sigma}_\mu & 0 \end{pmatrix}. \tag{2.12}$$

We can further define a matrix γ_5

$$\gamma_5 \;=\; i\gamma_0\gamma_1\gamma_2\gamma_3. \tag{2.13}$$

Making use of Eq. (2.12), γ_5 is then brought to diagonal form

$$\gamma_5 \;=\; \begin{pmatrix} -\mathbb{1} & 0 \\ 0 & \mathbb{1} \end{pmatrix}. \tag{2.14}$$

In this representation, one can decompose a Dirac-spinor ψ_a into a direct sum of left and right chiral Weyl spinors ξ_A and $\bar{\chi}^{\dot{A}}$

$$\psi_a \;=\; \begin{pmatrix} \xi_A \\ \bar{\chi}^{\dot{A}} \end{pmatrix}. \tag{2.15}$$

Another quantity, which is needed to form Lorentz-invariant scalar products between two Dirac spinors, is the barred Dirac-spinor $\bar{\psi}$[4]. It is defined as

$$\bar{\psi} \;=\; (\gamma_0\psi)^\dagger. \tag{2.16}$$

Finally, the so-called left and right chiral projectors are defined as

$$P_{\mathrm{L}} \;=\; \frac{1}{2}(\mathbb{1} - \gamma_5), \quad P_{\mathrm{R}} \;=\; \frac{1}{2}(\mathbb{1} + \gamma_5). \tag{2.17}$$

These are composed in a way that they project onto the left and right chiral eigenstates of γ_5 with eigenvalue ± 1.

2.2. Motivations of Supersymmetry

2.2.1. The Hierarchy Problem

One of the most prominent problems of the SM is the hierarchy problem. It is connected to the general assumption that *some effective theory, valid at an energy scale* Λ_{low}*, should arise from the properties of its underlying theory, valid at* Λ_{high}*, without making it necessary to finetune the parameters of the high energy theory with a precision of the order* $\mathcal{O}(\Lambda_{\mathrm{low}}/\Lambda_{\mathrm{high}})$. In such an effective theory, parameters are still allowed to be small, i.e., of the order $\mathcal{O}(\Lambda_{\mathrm{low}}/\Lambda_{\mathrm{high}})$, if they are somehow insensitive against the high scale physics

[4] The obvious guess $\psi^\dagger\psi$ does not work here as the spinor representation of the Lorentz group is non-unitary (see statements above).

(this means not altered by corrections of $\mathcal{O}(\Lambda_{\text{high}}/\Lambda_{\text{low}})$). Guided by this assumption Gerardus 't Hooft was led to the following insight: *A parameter of the effective theory $\lambda_{\text{low}}(\Lambda)$ at a scale Λ is allowed to be very small if taking the limit $\lambda_{\text{low}} \to 0$ increases the symmetry of the theory.* [4]
The SM is nowadays understood as a low energy approximation of some more fundamental theory valid at a much higher scale $\Lambda_{\text{high}} \approx \mathcal{O}(10^{16} - 10^{18})$ GeV[5]. It suffers from the problem that its only fundamental scalar particle, the Higgs boson, which has been discovered recently at the Large Hadron Collider (LHC) at CERN, Geneva, possesses a measured mass of [5, 6]

$$m_{h^0,\text{phys}} \simeq 125.36^{+0.37}_{-0.37}\ (\text{stat.})^{+0.18}_{-0.18}\ (\text{syst.})\ \text{GeV} \quad (\text{ATLAS}), \tag{2.18a}$$

$$m_{h^0,\text{phys}} \simeq 125.03^{+0.26}_{-0.27}\ (\text{stat.})^{+0.13}_{-0.15}\ (\text{syst.})\ \text{GeV} \quad (\text{CMS}). \tag{2.18b}$$

This value, which is connected to the electro-weak (EW) breaking scale $\Lambda_{\text{low}} \approx 100$ GeV ($\approx O(M_Z)$), happens to be much smaller than the assumed Λ_{high}, a finding that somehow contradicts 't Hooft's statement, as the limit $m_{h^0} \to 0$ does not increase any symmetry of the SM. Hence, following the above assumption, one would expect the Higgs mass to tend against the high scale Λ_{high} rather than being somewhere of the order $\mathcal{O}(\Lambda_{\text{low}})$. To be more explicit, one can write down the higher-order corrections $\delta_{m^2_{h^0},\Lambda_{\text{high}}}$ to the bare Higgs mass squared $m^2_{h^0,\text{bare}}$

$$m^2_{h^0,\text{phys}} \;=\; m^2_{h^0,\text{bare}} + \delta_{m^2_{h^0},\Lambda_{\text{high}}}, \tag{2.19}$$

introduced by the top-quark which contributes to $m_{h^0,\text{phys}}$ via the self-energy diagram shown in the first graph of Fig. 2.1[6]. These terms depending on Λ_{high} take the form

$$\delta^{\text{t}}_{m^2_{h^0},\Lambda_{\text{high}}} \;=\; \frac{|\lambda_t|^2}{16\pi^2}\left[-2\Lambda^2_{\text{high}} + 6m_t^2\ln(\frac{\Lambda_{\text{high}}}{m_t})\right]. \tag{2.20}$$

The fact that the measured Higgs mass Eq. (2.18) is nevertheless of the order of the EW scale, even though $\delta^{\text{t}}_{m^2_{h^0},\Lambda_{\text{high}}}$ depends quadratically on Λ_{high}, is then said to be unnatural as it would require an extreme fine-tuning, e.g., for $\Lambda_{\text{high}} = \Lambda_{\text{Planck}}$ of one part in 10^{36} between the two basically independent parameters $m^2_{h^0,\text{bare}}$ and $\delta_{m^2_{h^0},\Lambda_{\text{high}}}$ (see Eq. (2.19)). Hence, Eqs. (2.19) and (2.20) elucidate the high sensitivity of the SM Higgs mass to the high scale physics at Λ_{high}, which is in conflict with the introductory statement. This intertwining of physics at Λ_{high} and Λ_{high} spoils the hierarchy of scales $\Lambda^{\text{EW}} \approx \mathcal{O}(M_Z)$ and $\Lambda^{\text{Gravity}} \approx \mathcal{O}(M_{\text{Pl}})$.We call this the *hierarchy problem* of the SM[7]. Note that although solving the hierarchy problem is one of the strongest theoretical motivations for the introduction of SUSY, this is merely an aesthetical than a real physical or mathematical problem. Furthermore, there may also arise some new physics at an intermediate scale far below Λ_{GUT}, which can result in a significant softening of the hierarchy problem. Due to

[5] Λ_{high} is often considered as the GUT-scale, typically $\Lambda_{\text{GUT}} \simeq \mathcal{O}(10^{16}$ GeV), or the Planck scale Λ_{Planck} quantified by, e.g., the reduced Planck mass $M_{\text{Pl}} = 1/\sqrt{8\pi G_{\text{Newton}}} \simeq 2.4 \cdot 10^{18}$ GeV, the highest known energy scale in physics, where the unification of gravity with strong and electroweak forces is expected to take place.

[6] Due to its large mass, which enters the top-Higgs-coupling, the top quark corrections are expected to be the dominant corrections to the Higgs mass.

[7] All massterms in $\mathcal{L}_{\text{SM}}$ are connected to the characteristic EW-breaking scale, the vacuum expectation value (vev) v of the Higgs-field, which is proportional to the Higgs mass m_{h^0}. Therefore, the question concerning the stability of the Higgs mass against Λ_{high} also translates into the question of the radiative stability for all SM masses.

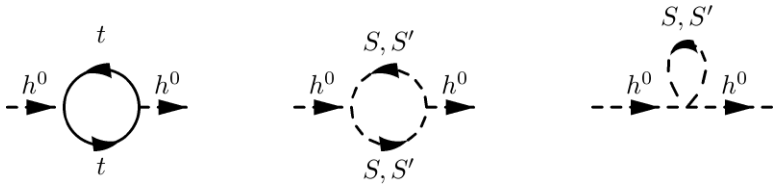

Figure 2.1.: Self-energy diagrams contributing to the Higgs mass for the top quark (left) and the two scalars S, S' (right).

its high sensitivity to the high scale physics, the SM Higgs-boson is however considered as a very interesting object concerning searches for physics beyond the SM (BSM) [8].
An example of how the hierarchy problem might be attacked is now given by the electron. The electron gets large corrections of order $\mathcal{O}(\Lambda_{\text{high}})$ to its mass via the emission and subsequent absorption of photons. However, these corrections cancel against contributions stemming from the positron, a new particle, which happens to be a mandatory ingredient of any relativistic quantum field theory that includes the electron (e.g., Quantum Electrodynamics (QED))[9]. Intertwining electrons and positrons, the symmetry of chiral rotations, which is softly broken in QED via the electron mass-term, becomes an exact symmetry in the limit $m_e \to 0$ and, hence, renders the smallness of the electron mass natural in 't Hooft's sense. It can be shown that new contributions, which arise through the production and annihilation of electron-positron pairs, cancel the $\mathcal{O}(\Lambda_{\text{high}})$ corrections to the electron mass and soften the dependence of the electron mass on Λ_{high} to only a mild logarithmic dependence [3, 7].
SUSY attacks the naturalness problem of the Higgs mass following quite similar lines as chiral symmetry did for the electron[10]. Supersymmetry links the Higgs mass to the mass of its chiral spin-$\frac{1}{2}$ superpartner. The latter is protected against corrections linear and quadratic in Λ_{high} via chiral symmetry, as explained above for the electron, which results in an at most logarithmic dependence of $\delta_{m^2_{h^0},\Lambda_{\text{high}}}$ on Λ_{high}. The mechanism, which leads to this cancellation of terms quadratic in Λ_{high} in Eq. (2.20), relies on the introduction of two new complex scalars S and S'. If these additional scalars couple to the Higgs boson via interaction terms of the form $-\lambda_{\tilde{t}_S}|h^0|^2|S|^2$, $-\lambda_{\tilde{t}_{S'}}|h^0|^2|S'|^2$, the resulting diagram on the outer right of Fig. 2.1 adds a contribution

$$\delta^{\text{S,S}'}_{m_{h^0},\Lambda_{\text{high}}} = \frac{\lambda_S + \lambda_{S'}}{16\pi^2}\Lambda^2_{\text{high}} \tag{2.21}$$

to the Higgs self energy. Requiring $\lambda_S = \lambda_{S'} = |\lambda_{\tilde{t}_t}|^2$ ($m_t = m_S = m_{S'}$) would then lead to a cancellation of quadratic divergences in the sum of Eq. (2.20) and Eq. (2.21). It seems natural to connect the equality of couplings to some symmetry. Hence, assuming $\{S, S'\} = \{\tilde{t}_L, \tilde{t}_R\}$ where $\{\tilde{t}_L, \tilde{t}_R\}$ are the scalar superpartners of the top-quark, one sees that SUSY yields exactly this cancellation of $\mathcal{O}(\Lambda^2_{\text{high}})$ contributions to $\delta^2_{m^2_{h^0},\Lambda_{\text{high}}}$. Therefore, SUSY provides a solution to the hierarchy problem. Making further use of the *non-renormalization theorem*, which is valid in supersymmetric theories, it can be shown that at least in exact SUSY the corrections quadratic in Λ_{high} cancel in perturbation the-

[8] The SM-Higgs is also often said to be a "window" towards BSM-physics.
[9] The positron has been newly introduced when going from non-relativistic to relativistic quantum mechanics.
[10] There are of course other ways out of the hierarchy problem, e.g., via assuming that the scalar Higgs is not a fundamental but rather a composite state (see technicolor theories [8]) or the pseudo-Goldstone boson of some broken symmetry [9].

ory to all orders and are not reintroduced by some higher-order corrections [11].
But since no sparticle has been observed so far, low-energy SUSY, if existent, has to be broken somehow. SUSY-breaking reintroduces corrections of the order $\mathcal{O}(\Lambda^2_{SUSY})$. However, the need of fine-tuning can at least be decreased to an acceptable amount if one expects SUSY-breaking to take place at around $\Lambda_{\mathrm{SUSY}} \approx \mathcal{O}(1\ \mathrm{TeV})$. Then, the radiative corrections to the Higgs mass and in turn to all SM masses would be tied to this new scale Λ_{SUSY}. Finally note that one runs again into the hierarchy problem if experiments turn out to disfavor light SUSY particles making it necessary to push the SUSY breaking scale Λ_{SUSY} to much higher values. But when exactly one says that a model is unnatural is a matter of taste as the naturalness bound, if imposed anyway, can of course not be translated into a strict upper bound.

2.2.2. SUSY in the Context of Grand Unified Theories

Offering a solution to the hierachy problem is not the only appealing feature of SUSY. In the history of physics it turned out that theories which originally described distinct physical phenomena could be understood as different manifestations of the same physical cause, e.g., the theories of electricity and magnetism, which have been successfully unified into the theory of electromagnetism followed by the conflation of the weak theory and electromagnetism into the EW theory. Pursuing the above road it seems to be quite natural to consider the unification of EW and strong forces via the embedding of the corresponding SM-gauge group $U(1)_{\mathrm{Y}} \times SU(2)_{\mathrm{L}} \times SU(3)_c$ into a larger simple group such as $SU(5)$ or $SO(10)$ or, going even further to (heterotic) superstring theories, into the group $SO(32)$ or the exceptional group $E(8) \times E(8)$. Unification of forces would then mean that the EW and strong gauge couplings taken at Λ_{EW} are just the low energy manifestations of a single gauge coupling of some simple unification group which appears in its unbroken form above some high scale Λ_{GUT}. This picture gets further support from the observation that, described via their renormalization group running, the SM-gauge couplings tend to meet each other in a region around $\Lambda_{GUT} \simeq \mathcal{O}(10^{16}\ \mathrm{GeV})$ as shown in Fig. 2.2. However, this intersection of the different SM-gauge couplings is actually not exact. Note that Fig. 2.2 assumes that no new physics arises between the EW and the GUT scale, an assumption which of course does not have to pertain. Via the introduction of additional particles into the renormalization group equations (RGE) of the three gauge couplings at the TeV-scale, SUSY turns out to change the corresponding energy-dependent running in such a way that unification of the different SM gauge couplings into a single gauge coupling at the GUT-scale is improved a lot (see Fig. 2.2). Considering the particle content of the MSSM as a minimal extension of the SM, it now turns out that the changes induced into the RGEs are already sufficient to obtain the unification of gauge couplings at $\Lambda_{GUT} \simeq \mathcal{O}(10^{16}\ \mathrm{GeV})$, whereas the introduction of further gauge non-singlets such as, e.g., a third and fourth Higgs doublet, would already spoil unification. In addition, the renormalization group analysis turns out to be rather robust against changes of Λ_{SUSY} showing only a mild logarithmic dependence on the choice the breaking scale. Hence, a

[11] The non-renormalization theorem states that in exact SUSY any perturbative correction can be rewritten as a single integral $\int \mathrm{d}^4\Theta := \int \mathrm{d}^2\Theta \mathrm{d}^2\bar{\Theta}$ (see Sec.2.3.2 for more details about the Grassmann variables Θ_A, $\bar{\Theta}^{\dot{A}}$). Hence, due to $\int \mathrm{d}\Theta^A = \int \mathrm{d}\bar{\Theta}_{\dot{A}} = 0$, no counterterm in the Lagrangian can have the structure of a holomorphic superpotential term (see Sec. 2.3.3 for more details about the superpotential $\mathcal{W}(\Phi)$). Therefore, the renormalization of couplings and masses must completely balance the wave function renormalization of chiral superfields. Since the latter has to be dimensionless it can be deduced that the former can at most depend logarithmically on Λ_{high}, true to all orders in perturbation theory [3].

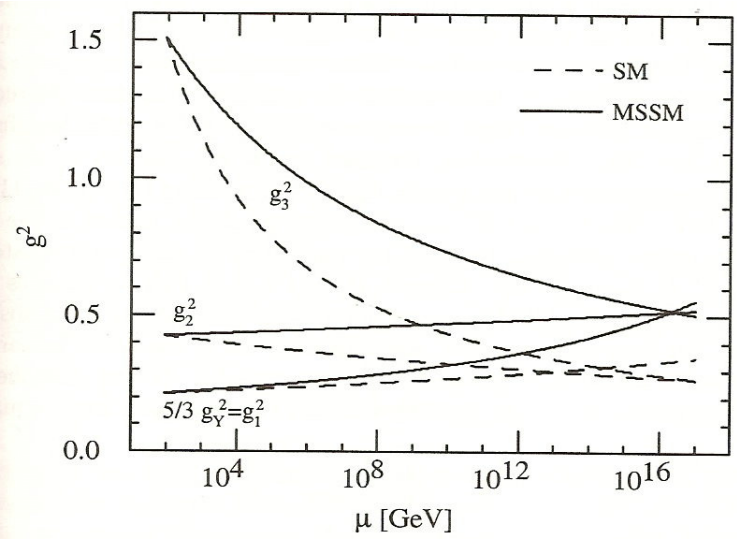

Figure 2.2.: Energy-dependent running of the three SM gauge couplings in the SM and in the MSSM. Figure taken from [3].

Λ_{SUSY} somewhere between Λ_{EW} up to $\mathcal{O}(10$ TeV) turns out to be in accordance with unification [7]. Since going from global to local SUSY (the so-called supergravity models) automatically leads to the incorporation of gravity due to the appearance of a spin-2 boson typically identified with the graviton, SUSY finally seems to be an important cornerstone of the unification of known forces.

2.2.3. The Haag-Łopuszański-Sohnius Theorem

Another important motivation for SUSY arose in the context of the famous no-go-theorem of Coleman and Mandula [10]. It states that starting under the physically reasonable assumptions that, i.a.,

- all particle types correspond to positive energy representations of the Poincaré group,
- for any mass M, there is only a finite number of particle types with mass less than M,
- the amplitude for elastic two-body scattering is analytic in the Mandelstam variables s and t except at normal thresholds,
- any two-particle state $|pp'\rangle$ undergoes some scattering ($T|pp'\rangle \neq 0$[12]) at almost all energies,

the full symmetry group of the S-Matrix has to be a direct product of the Poincaré group and internal symmetry groups

$$[P^\rho, T^a] \;=\; [M^{\mu\nu}, T^a] \;=\; 0, \tag{2.22}$$

inhibiting any non-trivial mixing.
SUSY now circumvents this constraint by going beyond Lie algebras. As SUSY turns

[12] T is defined as a part of the S-matrix $S \;=\; \mathbb{1} - i(2\pi)^4\delta^{(4)}(P - P')T$ with total ingoing/ outgoing momentum P/P'.

bosons into fermions and *vice versa*,

$$Q_a|\text{fermion}\rangle \;=\; |\text{boson}\rangle, \quad Q_a|\text{boson}\rangle \;=\; |\text{fermion}\rangle, \tag{2.23}$$

its generators have to be anticommuting quantities to obtain the correct (anti)commutation relation as required by the spin-statistics theorem. Extending the symmetry algebra of the S-matrix, comprised of purely bosonic (even) generators as covered by the Mandula-Coleman theorem, by fermionic (odd) generators of the SUSY-algebra

$$[\text{even}, \text{even}] \;=\; \text{even}, \tag{2.24a}$$
$$[\text{even}, \text{odd}] \;=\; \text{odd}, \tag{2.24b}$$
$$\{\text{odd}, \text{odd}\} \;=\; \text{even}, \tag{2.24c}$$

to a so-called $\mathbb{Z}_2$-graded Lie algebra[13], one can circumvent the tight constraints on a non-trivial mixing with the external symmetry group (Poincaré group) of the S-matrix Eq. (2.22).
The Haag-Łopuszański-Sohnius theorem [11] exactly covers this case of graded Lie algebras. It states that the most general continuous symmetry group of the S-matrix consistent with the assumptions of the Coleman-Mandula theorem is generated by elements of a $\mathbb{Z}_2$-graded algebra, whose odd generators belong to the $(\frac{1}{2}, 0)$ or $(0, \frac{1}{2})$ representation of the Lorentz group and whose even generators are a direct sum of the Poincaré and other generators. Hence, supersymmetry turns out to be the most general extension of the Poincaré group. This deep insight raised further interest in supersymmetric theories.

2.2.4. SUSY in the Context of Dark Matter

As it is shown later, for many realizations of SUSY such as the MSSM the lightest supersymmetric particle is stabilized by a residual $\mathbb{Z}_2$-symmetry, the so-called R-parity. Within the MSSM, the lightest supersymmetric particle (LSP) often happens to be the lightest neutralino $\tilde{\chi}_1^0$, a state comprised of the superpartners of the B and W^0 gauge bosons as well as of the uncharged Higgs fields. The resulting particle is hence only weakly interacting. Together with the observation that for most of the realizations of the MSSM the lightest neutralino acquires a mass of $\mathcal{O}(100\text{ GeV})$, the neutralino falls under the category of weakly interacting massive particle (WIMP). Since WIMPs yield quite automatically a dark matter relic density within the right ball park as favored by experiments (see the so-called *WIMP-miracle*), WIMPs turn out to be very prominent candidates to explain the amount of cold dark matter (CDM) observed in today's universe. In contrary to the SM the MSSM hence provides with the lightest neutralino $\tilde{\chi}_1^0$ a viable DM candidate. However, this is explained in greater detail further below.

This ends the discussion of the different motivations for the introduction of low-scale SUSY, which were both of purely theoretical and phenomenological kind. However, note that although SUSY provides interesting solutions to these problems, there is yet no experimental evidence that SUSY is realized in nature.

[13] A general graded Lie Algebra takes the form $t_a t_b - (-1)^{\eta_a \eta_b} t_b t_a \;=\; i\mathcal{C}_{ab}^c T_c$ (no summation over a,b on the left hand side), where generators t_a with $\eta_a \;=\; 0$ are called even (bosonic) and generators t_a with $\eta_a \;=\; 1$ are called odd (fermionic).

2.3. The Theory behind Supersymmetry

In this section, we provide an overview of the mathematical framework of SUSY. For this purpose, we start with the presentation of the enlarged Super-Poincaré algebra and discuss its phenomenological implications. We then turn to the construction of a supersymmetric Lagrangian providing its basic building blocks within the superfield formalism. Afterwards, we discuss the phenomenologically required SUSY breaking as well as the topics R-symmetry and R-parity, which are of particular interest in the context of supersymmetric dark matter.

2.3.1. Algebraic Aspects of Supersymmetry

In the context of the Haag-Łopuszański-Sohnius theorem stated in Ref. [11] the authors derived the exact form of the super Poincaré algebra. They showed that the extension of the Poincaré algebra Eq. (2.2a)-(2.2c) associated to the new left and right chiral Weyl supercharges[14] takes the following form in two-component notation:

$$\{Q_A, \bar{Q}_{\dot{B}}\} = 2\sigma^{\mu}_{A\dot{B}} P_\mu, \quad \{\bar{Q}^{\dot{A}}, Q^B\} = 2\bar{\sigma}^{\mu\dot{A}B} P_\mu, \tag{2.25a}$$

$$[Q_A, P_\mu] = [\bar{Q}^{\dot{A}}, P_\mu] = 0, \tag{2.25b}$$

$$[M_{\mu\nu}, Q_A] = -(\sigma_{\mu\nu})^B_A Q_B, \tag{2.25c}$$

$$[M_{\mu\nu}, \bar{Q}^{\dot{A}}] = -(\bar{\sigma}_{\mu\nu})^{\dot{A}}_{\dot{B}} \bar{Q}_{\dot{B}}, \tag{2.25d}$$

$$\{Q_A, Q_B\} = \{\bar{Q}^{\dot{A}}, \bar{Q}^{\dot{B}}\} = 0. \tag{2.25e}$$

This extension of the Poincaré algebra has far reaching consequences for the arising physics of the corresponding supersymmetric theory. First of all, Eq. (2.25a)-(2.25c) imply the equality of bosonic and fermionic degrees of freedom (d.o.f.)

$$n_b = n_f \tag{2.26}$$

within each irreducible representation of the Super-Poincaré algebra, a so-called supermultiplet[15]. Furthermore, due to Eq. (2.25b), the SUSY generators Q_a commute with P^2 such that all particles within a supermultiplet have to possess the same mass. However, a selectron with the same mass as its SM counterpart, the electron, would have already been discovered if existent. Hence, one is directly led to the need of SUSY-breaking, an insight of great theoretical as well as phenomenological importance, which is discussed in greater detail in Sec. 2.3.4.
One can further introduce a chiral rotation on the supercharges

$$e^{i\phi R} Q_A e^{-i\phi R} = \exp(i\phi \mathbb{1})_{AB} Q_B, \tag{2.27}$$

$$e^{i\phi R} \bar{Q}^{\dot{A}} e^{-i\phi R} = Q^{\dot{B}} \exp(-i\phi \mathbb{1})^{\dot{B}\dot{A}}, \tag{2.28}$$

[14] A four component Majorana like supercharge can then be written as

$$Q_a = \begin{pmatrix} Q_A \\ (\bar{Q}^{\dot{A}})^T \end{pmatrix}.$$

[15] $n_B - n_F$ is the so-called Witten-Index of the particle spectrum. It can be shown that a ground state $|\Omega\rangle$, which breaks SUSY spontaneously, needs to have vanishing Witten index [3].

with a real phase ϕ, basically a separate $U(1)$ phase transformation on the left and right chiral Weyl spinors Q_A and $\bar{Q}_{\dot{A}}$, which leaves the algebra Eqs. (2.25a)-(2.25e) unchanged. The generator R of the symmetry fulfills

$$[Q_A, R] \;=\; Q_A, \quad [\bar{Q}^{\dot{A}}, R] \;=\; -\bar{Q}^{\dot{A}}. \tag{2.29}$$

Due to Eq. (2.29) R is a bosonic operator. Hence, its relation to the Poincaré group is constrained by the Coleman-Mandula theorem

$$[R, P_\mu] \;=\; [R, M_{\mu\nu}] \;=\; 0. \tag{2.30}$$

However, this $U(1)_R$-symmetry may or may not be a good symmetry of nature. We see later that if R-symmetry is imposed on some low scale SUSY model, it is typically broken down to a residual $\mathbb{Z}_2$ symmetry, which turns out to be of great phenomenological importance, e.g., in the context of dark matter.

2.3.2. The Superspace-Formalism

We now introduce the superspace-formalism, a convenient form for constructing the above-mentioned supermultiplets, which are the main building blocks of a superymmetric Lagrangian.
The superspace is spanned by the coordinates $(x^\mu, \Theta_A, \bar{\Theta}^{\dot{A}})$. The new spinorial coordinates Θ_A and $\bar{\Theta}^{\dot{A}}$ $(A, \dot{A} \in \{1, 2\})$, whose number agrees with the number of space-time coordinates, transform under the $(\frac{1}{2}, 0)$ and $(0, \frac{1}{2})$ representation of the Lorentz group. These so-called Grassmann variables obey the relations

$$\{\Theta^A, \Theta^B\} \;=\; \{\bar{\Theta}^{\dot{A}}, \bar{\Theta}^{\dot{B}}\} \;=\; \{\Theta^A, \bar{\Theta}^{\dot{B}}\} \;=\; 0. \tag{2.31}$$

One can formally introduce derivatives and integrations with respect to Grassmannian coordinates. The corresponding definitions can be found in Ref. [3]. Furthermore, dimensional consistency requires to attribute the mass dimension $-\frac{1}{2}$ to Θ_A and $\bar{\Theta}^{\dot{A}}$.
A global SUSY-transformation in superspace takes the form

$$(x^\mu, \Theta, \bar{\Theta}) \to (x^\mu - i\Theta\sigma^\mu\bar{\epsilon} + i\epsilon\sigma^\mu\bar{\Theta}, \Theta + \epsilon, \bar{\Theta} + \bar{\epsilon}), \tag{2.32}$$

with ϵ, $\bar{\epsilon}$ being anticommuting spinorial constants. The above transformation is chosen such that x^μ remains real. Hence, a global SUSY-transformation corresponds to just a coordinate transformation in superspace. For some linear realization of SUSY-transformation generated by Q_A and $\bar{Q}^{\dot{A}}$, e.g., of the form

$$x^\mu \to i(\epsilon Q + \bar{\epsilon}\bar{Q})x^\mu, \tag{2.33}$$

the superspace representations of Q_A and $\bar{Q}^{\dot{A}}$ can be written as

$$Q_A \;=\; -i(\partial_A + i\sigma^\mu_{A\dot{B}}\bar{\Theta}^{\dot{B}}\partial_\mu), \tag{2.34a}$$

$$\bar{Q}^{\dot{A}} \;=\; -i(\bar{\partial}^{\dot{A}} + i\bar{\sigma}^{\mu\dot{A}B}\Theta_B\partial_\mu). \tag{2.34b}$$

In Eq. (2.34a) and (2.34b) we have introduced the Grassmannian derivatives

$$\partial_A \;=\; \partial/\partial\Theta^A, \tag{2.35a}$$

$$\bar{\partial}^{\dot{A}} \;=\; \partial/\partial\bar{\Theta}_{\dot{A}} \tag{2.35b}$$

which are for themselves anticommuting quantities.
A superfield is now understood as a function in superspace which depends on the coordinate-set $z = \{x, \Theta, \bar{\Theta}\}$. A general, even superfield $\mathcal{F}$, which transforms as a singlet under the Lorentz group, can then be grasped in its most general form as

$$\begin{aligned}\mathcal{F}(z) &= f(x) + \sqrt{2}\Theta\xi(x) + \sqrt{2}\bar{\Theta}\bar{\chi}(x) + \Theta\Theta M(x) + \bar{\Theta}\bar{\Theta}N(x) \\ &\quad + \Theta\sigma^{\mu}\bar{\Theta}A_{\mu}(x) + \Theta\Theta\ \bar{\Theta}\bar{\lambda}(x) + \bar{\Theta}\bar{\Theta}\ \Theta\zeta(x) + \frac{1}{2}\Theta\Theta\ \bar{\Theta}\bar{\Theta}D(x). \end{aligned} \tag{2.36}$$

Due to Eq. (2.31), the expansion of $\mathcal{F}(z)$ in the Grassmanian coordinates stops with the so-called D-Term $\propto \Theta\Theta\ \bar{\Theta}\bar{\Theta}$ (summation over the spinorial indices of is implicitly assumed). Since $\mathcal{F}(z)$ is required to transform as a scalar under the Lorentz group, the component functions of $\mathcal{F}(z)$ inherit the transformation behavior from their prefactors. This means that $f(x)$ transforms as $(0,0)$, whereas $\xi(x)$ transforms in the $(\frac{1}{2}, 0)$ representation of the Lorentz group etc.. The transformation behavior of the component fields of $\mathcal{F}$ with respect to a global SUSY transformation Eq. (2.32) can then be worked out from the requirement that the variation $\delta\mathcal{F}$ is again of the form of a superfield Eq. (2.36) with all components replaced by their variations. The resulting transformations can also be found in Ref. [3].
To identify the proper supermultiplets we have to make sure that the superfield $\mathcal{F}$ of Eq. (2.36) transforms irreducibly under $i(\epsilon Q + \bar{\epsilon}\bar{Q})$ as given by Eq. (2.33). It actually turns out that $\mathcal{F}$ is highly reducible. To end up with an irreducible supermultiplet, one imposes additional constraints on $\mathcal{F}$. For this purpose, we introduce the new so-called left and right chiral covariant derivatives

$$\mathcal{D}_A = \partial_A - i\sigma^{\mu}_{A\dot{B}}\bar{\Theta}^{\dot{B}}\partial_{\mu}, \tag{2.37a}$$

$$\bar{\mathcal{D}}_{\dot{A}} = -\bar{\partial}_{\dot{A}} + i\Theta^{B}\sigma^{\mu}_{B\dot{A}}\partial_{\mu}, \tag{2.37b}$$

which transform covariantly under global SUSY transformations Eq. (2.32), satisfying

$$\{\mathcal{D}_A, Q_B\} = \{\mathcal{D}_A, \bar{Q}^{\dot{B}}\} = \{\bar{\mathcal{D}}_{\dot{A}}, \bar{Q}^{\dot{B}}\} = \{\bar{\mathcal{D}}_{\dot{A}}, Q_B\} = 0. \tag{2.38}$$

This can be explicitly checked using Eq. (2.37a) and (2.37b) together with Eq. (2.34a) and (2.34b).
Possible constraints on $\mathcal{F}$, which result in irreducible superfields with respect to the transformation Eq. (2.32), are

$$\bar{\mathcal{D}}_{\dot{A}}\mathcal{F} = 0, \tag{2.39a}$$

$$\mathcal{D}_A\mathcal{F}^{\dagger} = 0, \tag{2.39b}$$

$$\mathcal{F} = \mathcal{F}^{\dagger}. \tag{2.39c}$$

The different types of superfields arising from the constraints Eq. (2.39a), Eq. (2.39b) and Eq. (2.39c) are discussed in more detail in the next two sections.

Chiral Superfields

The superfields fulfilling Eq. (2.39a) or (2.39b) are called *left and right chiral superfields*, in the following denoted as Φ and $\Phi^\dagger$. The chiral superfields take the general form

$$\begin{aligned}\Phi(z) &= \phi(x) - i\Theta\sigma^\mu\bar{\Theta}\partial_\mu\phi(x) - \frac{1}{4}\Theta\Theta\,\bar{\Theta}\bar{\Theta}\partial^\mu\partial_\mu\phi(x) \\ &\quad + \sqrt{2}\Theta\xi(x) + \frac{i}{\sqrt{2}}\Theta\Theta\partial_\mu\xi\sigma^\mu\bar{\Theta} + \Theta\Theta F(x), \qquad (2.40a)\\ \Phi^\dagger(z) &= \phi^*(x) + i\Theta\sigma^\mu\bar{\Theta}\partial_\mu\phi^*(x) - \frac{1}{4}\Theta\Theta\,\bar{\Theta}\bar{\Theta}\partial^\mu\partial_\mu\phi^*(x) \\ &\quad + \sqrt{2}\Theta\bar{\xi}(x) - \frac{i}{\sqrt{2}}\bar{\Theta}\bar{\Theta}\,\Theta\sigma^\mu\partial_\mu\bar{\xi} + \bar{\Theta}\bar{\Theta}F^*(x). \qquad (2.40b)\end{aligned}$$

Their field content is comprised of a complex scalar $\phi(x)$, a two-component complex spinor $\xi(x)$ and another complex scalar $F(x)$, a so-called auxiliary field. It vanishes when the equation of motions (e.o.m.) are imposed upon $\Phi(z)$. Hence, $F(x)$ is actually not a dynamical field. However, $F(x)$ turns out to be mandatory for the SUSY-transformation to close over Φ, if it is taken off the mass shell[16]. Furthermore, the scalar $\phi(x)$ determines the mass dimension of the $\Phi(z)$ to be equal to one. Note that within such a superfield n_f equals n_B as required by SUSY Sec. 2.3.2. Following the Eqs. (2.32) to (2.34b) the transformations of the different components take the form

$$\begin{aligned}\delta\phi &= \sqrt{2}\epsilon\xi, \qquad (2.41a)\\ \delta\xi_A &= \sqrt{2}\epsilon_A F - \sqrt{2}i(\sigma^\mu\bar{\epsilon})_A\partial_\mu\phi, \qquad (2.41b)\\ \delta F &= i\partial_\mu(\sqrt{2}\xi\sigma^\mu\bar{\epsilon}). \qquad (2.41c)\end{aligned}$$

The transformations Eqs. (2.41a) to (2.41c) transform fermionic components of Φ irreducibly into bosonic components and *vice versa*. Note that the component proportional to $F(x)$ in Eq. (2.40a), the so-called F-term, transforms into $F(x)$ plus a space-time derivative as given by Eq. (2.41c). Hence, a Lagrangian $\mathcal{L}$ build out of the F-Term of some left or right chiral superfield $[\Phi]_F = \mathcal{D}_A\mathcal{D}^A\Phi(x,\Theta,\bar{\Theta})|_{\bar{\Theta}=0}$, $[\Phi^\dagger]_F = \bar{\mathcal{D}}_{\dot{A}}\bar{\mathcal{D}}^{\dot{A}}\Phi^\dagger(x,\Theta,\bar{\Theta})|_{\Theta=0}$ is SUSY-invariant up to some total derivative, which typically vanishes in the associated action.

Vector Superfields

Superfields which satisfy the reality-condition Eq. (2.39c) are called *vector superfields*, in the following denoted as V. Imposing Eq. (2.39c) upon Eq. (2.36) one is left with

$$\begin{aligned}V(z) &= C(x) + \sqrt{2}\Theta\xi(x) + \sqrt{2}\bar{\Theta}\bar{\xi}(x) + \Theta\Theta M(x) + \bar{\Theta}\bar{\Theta}M^*(x) \\ &\quad + \Theta\sigma^\mu\bar{\Theta}A_\mu(x) + \Theta\Theta\,\bar{\Theta}\bar{\lambda}(x) + \bar{\Theta}\bar{\Theta}\,\Theta\lambda(x) + \frac{1}{2}\Theta\Theta\,\bar{\Theta}\bar{\Theta}D(x). \qquad (2.42)\end{aligned}$$

$C(x)$ is a real scalar, $M(x)$ is complex scalar field, $A_\mu(x)$ is a real vector and $\lambda(x)$ as well as $\xi(x)$ are complex, two-component spinors. Finally, $D(x)$ is a real scalar which vanishes if the e.o.m. are imposed upon $V(x,\Theta,\bar{\Theta})$. Counting fermionic and bosonic degrees of freedom, one ends up with $n_B = n_F$, as expected. It is known that a real vector $A_\mu(x)$ possesses the mass dimension one, a fact, which directly translates into the mass dimension

[16] The fact that the theory maintains its SUSY invariance even off the mass shell is however an important property for a supersymmetric quantum-field theory.

of the full vector superfield being zero (see Sec. 2.3.2).
A SUSY transformation Eq. (2.32) acts on the component fields of $V(x,\Theta,\bar{\Theta})$ via the following variations of its component fields:

$$\delta C(x) \;=\; \sqrt{2}\epsilon\xi + \sqrt{2}\bar{\epsilon}\bar{\xi}, \tag{2.43a}$$

$$\delta(\sqrt{2}\xi_A) \;=\; 2\epsilon_A M + (\sigma^\mu\bar{\epsilon})_A(-i\partial_\mu C + A_\mu), \tag{2.43b}$$

$$\delta M \;=\; \bar{\epsilon}\bar{\lambda} + \frac{i}{\sqrt{2}}\partial_\mu\xi\sigma^\mu\bar{\epsilon}, \tag{2.43c}$$

$$\delta A_\mu \;=\; \epsilon\sigma_\mu\bar{\lambda} + \lambda\sigma_\mu\bar{\epsilon} - \frac{i}{\sqrt{2}}(\epsilon\partial_\mu\xi - \partial_\mu\bar{\xi}\bar{\epsilon}) + i\sqrt{2}(\epsilon\sigma_{\mu\nu}\partial^\nu\xi - \bar{\epsilon}\bar{\sigma}_{\mu\nu}\partial^\nu\bar{\xi}), \tag{2.43d}$$

$$\delta\lambda_A \;=\; \epsilon_A D + \frac{i}{2}\epsilon_A\partial^\mu A_\mu - i(\sigma^\mu\bar{\epsilon})_A\partial_\mu M^* - (\sigma^{\mu\nu}\epsilon)_A\partial_\mu A_\nu, \tag{2.43e}$$

$$\delta D \;=\; i\partial_\mu(\lambda\sigma^\mu\bar{\epsilon} + \bar{\lambda}\bar{\sigma}^\mu\epsilon). \tag{2.43f}$$

As can be deduced from Eq. (2.43a) - (2.43f), a vector field transforms irreducibly under Eq. (2.32). One can now define a vector superfield by postulating an invariance under a linear transformation in the space of all vector superfields of the form

$$V \to V + i(\Lambda - \Lambda^\dagger). \tag{2.44}$$

In Eq. (2.44), Λ is a left chiral superfield. Then, $i(\Lambda - \Lambda^\dagger)$ forms a vector superfield, which fulfills Eq. (2.39c). The transformation Eq. (2.44) can be understood as a supersymmetrized version of an Abelian gauge transformation. A specific supergauge choice is the *Wess-Zumino gauge* which brings the general vector superfield Eq. (2.42) to the form

$$V_{WZ}(z) \;=\; \Theta\sigma^\mu\bar{\Theta}A_\mu(x) + \Theta\Theta\;\bar{\Theta}\bar{\lambda}(x) + \bar{\Theta}\bar{\Theta}\;\Theta\lambda(x) + \frac{1}{2}\Theta\Theta\;\bar{\Theta}\bar{\Theta}D(x). \tag{2.45}$$

Hence, using a certain supergauge one can reduce the component fields of an arbitrary vector field to just one real vectorfield $A_\mu(x)$, its fermionic spin-$\frac{1}{2}$ superpartner $\lambda(x)$ and an auxiliary scalar $D(x)$. Note that the Wess-Zumino gauge includes the transformation

$$A^\mu(x) \to A^\mu(x) - 2\partial^\mu\Im\{\phi(x)\} \tag{2.46}$$

on the real vector field $A^\mu(x)$. However, bringing a general vector superfield to the form of Eq. (2.45) does not impose any constraints upon $\Im\{\phi(x)\}$. Hence, this freedom is not used up yet. This is an important observation since the A^μ are identified with the SM gauge fields and the transformation Eq. (2.46) is considered as the corresponding $U(1)$-gauge transformation. Moreover, it is apparent from Eq. (2.43d) - (2.43f) that V_{WZ} does not maintain its form under a SUSY-transformation. However, its form can always be restored by an appropriate subsequent supergauge transformation.
Finally, note that the highest component in the expansion of $V(x,\Theta,\bar{\Theta})$ in Θ and $\bar{\Theta}$ transforms into a full space-time derivative Eq. (2.43f). In addition, this so-called D-term is supergauge invariant such that adding a term $[V]_D \;=\; \int \mathrm{d}^2\Theta\mathrm{d}^2\bar{\Theta}\; V(x,\Theta,\bar{\Theta})$ [17] to the Lagrangian results in an action which is invariant under SUSY as well as under supergauge transformations.

2.3.3. Supersymmetric Lagrangian

To build a supersymmetric Lagrangian, the SUSY-invariant and renormalizable building blocks comprised of chiral and vector superfields need to be identified. Note that products

[17] As e.g. $\int d^2\Theta \;=\; \int d^2\bar{\Theta} \;=\; 0$ integration of this form project the D-term out of some vector superfield.

of only left or only right chiral superfields are again left or right chiral superfields and the number of factors is only limited by the demand for the renormalizabilty of the model requiring a mass dimension of at most four for each term in the Lagrangian $\mathcal{L}$. Hence, as a chiral superfield acquires a mass dimension of one, only the F-terms of products fulfilling

$$\#[\Theta_i\Theta_j...\Theta_l] \leq 3, \tag{2.47}$$

$$\#[\Theta_i^\dagger\Theta_j^\dagger...\Theta_l^\dagger] \leq 3 \tag{2.48}$$

are allowed to appear in $\mathcal{L}$. Here, i, j,... stand for the different types of chiral superfields. In addition $\Phi_i\Phi_j^\dagger$ apparently fulfills the reality condition Eq. (2.39c). Hence, it can be brought to the form of a vector superfield. Its D-term provides the kinetic energy term for a complex scalar field as well as for its superpartner, a Weyl fermion, as shown below. A first SUSY-invariant Lagrangian $\mathcal{L}$ describing a set of left and right chiral interacting superfields Φ and $\Phi^\dagger$ can be written as

$$\mathcal{L}_{\text{chiral}} \;=\; \left[\Phi_i^\dagger\Phi_i\right]_D + [\mathcal{W}(\Phi) + \text{h.c.}]_F, \tag{2.49}$$

where

$$\mathcal{W}(\Phi_i) \;=\; h_i\Phi_i + \frac{1}{2}m_{ij}\Phi_i\Phi_j + \frac{1}{3!}f_{ijk}\Phi_i\Phi_j\Phi_k \tag{2.50}$$

is the so-called *superpotential*. Since only the F-term of a chiral supermultiplet transforms into itself plus a space-time derivative (see Eq. 2.41c), SUSY invariance requires $\mathcal{W}$ ($\mathcal{W}^\dagger$) to depend only on Φ ($\Phi^\dagger$), a property known as holomorphy. Let us define

$$\mathcal{W}_i(\phi) \;=\; \frac{\partial\mathcal{W}}{\partial\Phi_i}|_{\Theta\,=\,\bar\Theta\,=\,0}, \tag{2.51a}$$

$$\overline{\mathcal{W}}_i(\bar\phi) \;=\; \frac{\partial\overline{\mathcal{W}}}{\partial\Phi_i^\dagger}|_{\Theta\,=\,\bar\Theta\,=\,0}, \tag{2.51b}$$

$$\mathcal{W}_{ij}(\phi) \;=\; \frac{\partial\mathcal{W}}{\partial\Phi_i\Phi_j}|_{\Theta\,=\,\bar\Theta\,=\,0}, \tag{2.51c}$$

$$\overline{\mathcal{W}}_{ij}(\bar\phi) \;=\; \frac{\partial\overline{\mathcal{W}}}{\partial\Phi_i^\dagger\Phi_j^\dagger}|_{\Theta\,=\,\bar\Theta\,=\,0}. \tag{2.51d}$$

Written in component fields $\mathcal{L}_{\text{chiral}}$ takes the form

$$\mathcal{L}_{\text{chiral}} \;=\; \frac{i}{2}((\partial_\mu\xi_i)\sigma^\mu\bar\xi_i - \xi_i\sigma^\mu\partial_\mu\bar\xi_i + \partial^\mu\phi_i^*\partial_\mu\phi_i - (\xi_i\xi_j\mathcal{W}_{ij}(\phi) + \text{h.c.}) - \mathcal{W}_i\overline{\mathcal{W}}^i(\bar\phi), \tag{2.52}$$

where we omit terms which are just a space-time derivative. Moreover, the e.o.m.

$$\partial\mathcal{L}/\partial F_i - \partial^\mu(\partial\mathcal{L}/\partial(\partial F_i^\mu)) \;=\; \partial\mathcal{L}/\partial F_i \;=\; 0, \tag{2.53a}$$

$$\partial\mathcal{L}/\partial F_i^* - \partial^\mu(\partial\mathcal{L}/\partial(\partial F_i^{*\mu})) \;=\; \partial\mathcal{L}/\partial F_i^* \;=\; 0 \tag{2.53b}$$

which lead to

$$F_i \;=\; -\overline{\mathcal{W}}^i(\bar\phi) \;=\; -h_i^* - m_{ij}\bar\phi^j - \frac{1}{2}f_{ijk}^*\bar\phi^i\bar\phi^k, \tag{2.54a}$$

$$F_i^* \;=\; -\mathcal{W}_i(\phi) \;=\; -h_i - m_{ij}\phi_j - \frac{1}{2}f_{ijk}\phi_i\phi_k, \tag{2.54b}$$

are already imposed upon the auxiliary fields F_i (F_i^*).
Looking at the first three terms of Eq. (2.52) one recovers the Lagrangians associated with

the Weyl equation for a left and right chiral massless spinor as well as the Klein Gordon equation for massless complex scalar. In addition, Eq. (2.52) contains the associated Yukawa-interactions via $(\xi_i\xi_j\mathcal{W}_{ij}(\phi) + \text{h.c.})$ as well as the scalar potential term

$$V(\phi_i, \phi_j^*) \;=\; \mathcal{W}_i\overline{\mathcal{W}}^i(\bar{\phi}) \;=\; F_i^* F_i. \tag{2.55}$$

The next step is the incorporation of gauge interactions. For this purpose we have to include some real vector field in Eq. (2.49) or Eq. (2.52) which plays the role of the gauge field. Real vector fields reside in the vector superfield V. We start directly with the non-Abelian case as it simplifies in the well known way to the Abelian case by simply assuming the generators T_a of the gauge group to commutate with each other. A gauge transformation acting on chiral superfields can be written as

$$\Phi_I' \;=\; \exp(-2ig\Lambda^a(z)T_a)_{IJ}\Phi_J, \tag{2.56}$$

$$\Phi_I^{\dagger'} \;=\; \Phi_J \exp(-2ig\Lambda^{a\dagger}(z)T_a)_{JI}. \tag{2.57}$$

I and J are gauge group-indices and the $\Lambda^a(z)$ are complex left and right chiral functions specified by the gauge transformation. They have to obey

$$\bar{\mathcal{D}}^{\dot{A}}\Lambda^a T^a \;=\; 0, \tag{2.58a}$$

$$\mathcal{D}_A\Lambda^{a\dagger}T^a \;=\; 0 \tag{2.58b}$$

to maintain the chiral nature of Φ_I and $\Phi_I^\dagger$ under the transformations Eq. (2.56) and (2.57). A vector superfield V transforms according to

$$e^{V'} \;=\; e^{-i\Lambda^\dagger}e^V e^{i\Lambda}, \tag{2.59a}$$

$$e^{-V'} \;=\; e^{-i\Lambda}e^V e^{i\Lambda^\dagger}. \tag{2.59b}$$

Defining $V_{IJ} \;=\; (2gV^aT^a)_{IJ}$ and $\Lambda_{IJ} \;=\; 2g\Lambda^a T^a_{IJ}$ one can set up the gauge invariant trace

$$\text{Tr}[\Phi^\dagger e^V \Phi] \;=\; \sum_I (\Phi^\dagger e^V \Phi)_{II}, \tag{2.60}$$

which, i.a., constitutes the supersymmetric analogue of the interaction terms between gauge and matter fields[18]. Note that exponentiating the vector superfield V does not destroy renormalizabilty. This can be seen by going to the Wess-Zumino gauge Eq. (2.45), where due to Eq. (2.31) products of the form $(V_{WZ})^n$ vanish for $n \geq 3$. Hence, the D-term of the form $[\Phi^\dagger e^V_{WZ}\Phi]|_D$ does not exceed mass dimension four and therefore does not introduce any non-renormalizable terms in $\mathcal{L}$. To describe the dynamics of gauge fields it is further necessary to build the corresponding supersymmetric version of the field strength tensor $F^a_{\mu\nu}$. This can be done via

$$W_A \;=\; -\frac{1}{4}\bar{\mathcal{D}}\bar{\mathcal{D}}e^{-V}D_A e^V, \tag{2.61a}$$

$$\overline{W}^{\dot{A}} \;=\; -\frac{1}{4}\mathcal{D}\mathcal{D}e^V\bar{D}^{\dot{A}}e^{-V}. \tag{2.61b}$$

Moreover, $W_A W^A$ and $\overline{W}_{\dot{A}}\overline{W}^{\dot{A}}$ are left and right chiral superfields. With this at hand one can write down the supersymmetric analogue of a gauge theory

$$\mathcal{L} \;=\; \frac{1}{16g^2k}\text{Tr}\left[W^A W_A + \overline{W}_{\dot{A}}\overline{W}^{\dot{A}}\right]_F + \left[\Phi_i^\dagger(e^V)_{ij}\Phi_j\right]_D + [\mathcal{W}(\Phi_i) + \text{h.c.}]_F \tag{2.62}$$

[18] Note that a general vector superfield Eq. 2.42 possesses mass dimension zero and can therefore be exponentiated.

including $k = T(\mathcal{R})$, defined via $\mathrm{Tr}[T^a T^b] = T(\mathcal{R})\delta^{ab}$, and the superpotential $\mathcal{W}(\Phi_i)$ already discussed in the context of Eq. (2.52). The index i now covers the particle type as well as the gauge group index I. Having eliminated all auxiliary fields F_i and D_i via their e.o.m., a supersymmetric version of a non-Abelian gauge theory Lagrangian Eq. (2.62) can be written in terms of component fields as

$$\begin{aligned}\mathcal{L} &= i\xi_j\sigma_\mu D^{\dagger\mu}_{ij}\bar{\xi}_i + (D^\mu_{ij}\phi_i)^\dagger(\Delta_{\mu ik}\phi_k) - \frac{1}{4}F^a_{\mu\nu}F^{a\mu\nu} + i\lambda^a\sigma^\mu D_\mu\bar{\lambda}^a \\ &\quad - \sqrt{2}g(\bar{\lambda}^a\bar{\xi}_i T_{ij}\phi_j + \text{h.c.}) - V(\phi_i,\phi_j^*) - \left[\frac{1}{2}\xi_i\xi_j\mathcal{W}_{ij}(\phi) + \text{h.c.}\right]. \end{aligned} \tag{2.63}$$

Here, we made use of

$$D^\mu_{ij} = \delta_{ij}\partial^\mu + igA^{\mu a}T^a_{ij} \tag{2.64}$$

as well as of the generalization of the scalar potential Eq. (2.55)

$$V(\phi_i,\phi_j^*) = F_iF_i^* + \frac{1}{2}D^aD^a \tag{2.65}$$

with

$$F_i = -\frac{\partial\mathcal{W}^\dagger}{\partial\Phi^\dagger}|_{\Theta=0,\bar{\Theta}=0}, \quad D^a = -g\phi_i^\dagger T^a_{ij}\phi_j. \tag{2.66}$$

So far, the Lagrangian Eq. (2.62) also includes the description of unphysical degrees of freedom connected to the gauge freedom of the corresponding gauge theory. Following a suggestion proposed by Faddeev and Popov [12], one can restrict Eq. (2.62) to only the physical degrees of freedom, via the introduction of so-called gauge-fixing terms. The inclusion of these terms into $\mathcal{L}$ corresponds to fixing a certain gauge for the gauge fields. A typical choice, which corresponds to the generalized Lorentz gauge

$$\partial^\mu A_\mu(x) - w(x) = 0, \tag{2.67}$$

($w(x)$ can be any scalar function) takes in its non-Abelian formulation the form [3]

$$\mathcal{L}_{\text{gf}} = -\frac{1}{8\xi g^2 k}\mathrm{Tr}\left(\partial^\mu A_\mu\partial^\nu A_\nu\right). \tag{2.68}$$

ξ is a gauge parameter, which can be any finite constant. It leads to the so-called R_ξ gauges [12]. The supersymmetric generalization of Eq. 2.68 can than be written as

$$\mathcal{L}^{\text{SUSY}}_{\text{gf}} = -\frac{1}{128\xi g^2 k}\mathrm{Tr}\left(V\{\bar{\mathcal{D}}\bar{\mathcal{D}},\mathcal{D}\mathcal{D}\}V\right). \tag{2.69}$$

The latter leads to the introduction of additional scalar fields with Fermi-Dirac statistics, the so-called ghost fields c, for each component of the gauge fields, which follow from a path-integral formulation of the gauge fixing terms [12]. These ghost fields can be understood as negative degrees of freedom, which compensate for the above mentioned miscounting. Due to the definition of the supersymmetric gauge transformation Eqs. (2.59a) in terms of the two chiral superfields Λ and $\Lambda^\dagger$, we are lead to the introduction of two gauge fixing functions and, hence, to the inclusion of two sets of ghost fields, which we embed into the ghost superfields C and C' comprehensively. Up to quadratic order in the gauge superfields V and with $\xi = 1$ (the case relevant to us), the ghost terms finally take the form

$$\begin{aligned}\mathcal{L}^{(2)}_{\text{ghost}} &= \frac{1}{4g^2k}\mathrm{Tr}\Big(C^{\dagger\prime}C + C^\dagger C' + \frac{1}{2}(C' + C^{\dagger\prime})[V, C - C^\dagger] \\ &\quad + \frac{1}{12}(C' + C^{\dagger\prime})[V,[V,C + C^\dagger]]\Big). \end{aligned} \tag{2.70}$$

Note, that due to the appearance of commutators, the ghost superfields C and C' decouple from the actual physical fields if one goes to the Abelian case. These are basically all building blocks needed for the construction of a supersymmetrized version of a non-Abelian gauge theory. Its actual formulation in terms of a phenomenologically interesting theory, the MSSM, is given further below in Sec. 2.4.

2.3.4. The Breaking of Supersymmetry

Since no supersymmetric partner of any SM particle has been observed so far, one is led to the insight that SUSY, at least in its low-energy realization, can not be an exact symmetry of nature. A way to break a symmetry from which we already know that it is used by nature is the spontaneous symmetry breakdown. Phrased in terms of SUSY, this means that the ground state $|\Omega\rangle$ can not be invariant under the supersymmetry transformations Eq. (2.33), or equivalently, that at least one SUSY-generator does not annihilate the ground state

$$Q_A|\Omega\rangle \neq 0 \text{ and/or } \bar{Q}^{\dot{A}}|\Omega\rangle \neq 0. \tag{2.71}$$

Moreover, following Eq. (2.25a) the Hamilton-operator H can be expressed through the supercharges

$$H \;=\; P^0 \;=\; \frac{1}{4}\left(\{Q_1, \bar{Q}_{\dot{1}}\} + \{Q_2, \bar{Q}_{\dot{2}}\}\right). \tag{2.72}$$

This translates directly into a ground state energy

$$\langle\Omega|H|\Omega\rangle \;=\; \frac{1}{4}\left(||Q_1\rangle||^2 + ||\bar{Q}_{\dot{1}}\rangle||^2 + |||Q_2\rangle||^2 + ||\bar{Q}_{\dot{2}}\rangle||^2\right) > 0, \tag{2.73}$$

provided that Eq. (2.71) holds true. As the non-vanishing ground state energy is connected to a non vanishing minimum of the scalar potential Eq. (2.65)

$$\langle\Omega|V(\phi_i, \phi_j^*)|\Omega\rangle \neq 0, \tag{2.74}$$

it follows that the scalar potential has to feature a non-zero minimum. One can hence deduce from Eq. (2.65) that

$$\langle\Omega|F|\Omega\rangle \;=\; \Lambda_s^2 \neq 0 \text{ and/or } \langle\Omega|D|\Omega\rangle \;=\; \tilde{\Lambda}_s^2 \neq 0 \tag{2.75}$$

for the auxiliary fields F and D of Eq. (2.40a) and Eq. (2.42), where the scales Λ_s and $\tilde{\Lambda}_s$ can be identified as the mass scales of the SUSY-breaking. The former case is the so-called F-term breaking (O'Raifeartaigh mechanism [13]) while the latter case is known as D-and term breaking (Fayet-Iliopoulos mechanism [14]) of supersymmetry. Since within the MSSM a purely spontaneous breakdown of SUSY turns out to be in tension with the non-observance of sparticles, it becomes necessary to step beyond the MSSM [3]. This can be done via adding a so-called *hidden sector*, a singlet with respect to the SM gauge group, to the MSSM where supersymmetry is spontaneously broken together with a *messenger sector*, which propagates the SUSY breaking from the hidden sector to the visible sector. Consistent examples for the mediation of SUSY breaking are known, for example, *gauge mediated* or *gravity mediated* SUSY-breaking, which are both extensively discussed in Ref. [3].

To stay on more general grounds, one can violate SUSY through the *Heisenberg-Wigner mode*, namely by adding all theoretically allowed SUSY-breaking terms to $\mathcal{L}_{\text{MSSM}}$ without stating their actual theoretical origin. This is an approach, which in a way just parametrizes our lack of knowledge about the actual mechanism behind the breakdown of

supersymmetry. These new terms are chosen such that they respect the well established principles of gauge-invariance and renormalizability[19] leading to the so-called soft breaking of supersymmetry, most generally grasped in the form

$$\mathcal{L}_{\text{soft}} \;=\; -\phi_i^*(m^2)_{ij}\phi_j + (\frac{1}{3!}\mathcal{A}_{ijk}\phi_i\phi_j\phi_k - \frac{1}{2}\mathcal{B}_{ij}\phi_i\phi_j + \mathcal{C}_i\phi_i - \frac{1}{2}M^a\lambda^a\lambda^a + h.c.). \quad (2.76)$$

In Eq. (2.76), ϕ_i is the scalar component of some chiral superfield Φ_i with a mass term proportional to the hermitian matrix $(m^2)_{ij}$. Eq. (2.76) further contains terms linear, bilinear and trilinear in the scalar fields proportional to the tensors $\mathcal{C}_i$, $\mathcal{B}_{ij}$ (symmetric in i,j) and $\mathcal{A}_{ijk}$ (symmetric in i,j,k), as well as a gaugino mass term proportional to M^a. For not to break gauge-invariance, the gaugino-mass has to be the same for all gauginos within some simple Lie-group. Hence, we have one bino- $(U(1)_{\text{Y}})$, one wino- $(SU(2)_{\text{L}})$ and one gluino-mass parameter $(SU(3)_{\text{C}})$. But as already mentioned in Sec. 2.3.5, such a Majorana mass term violates the R-symmetry introduced in Sec. 2.3.1 as can be easily seen from Eq. (2.27). Hence, only a residual $\mathbb{Z}_2$-symmetry, named R-parity, can be maintained. The values of the soft-breaking parameters $(m^2)_{ij}$, $\mathcal{A}_{ijk}$, $\mathcal{C}$ and M^a can then be obtained or at least constrained via fitting the theoretical predictions to experiments. For a low energy realization of supersymmetry, $\mathcal{L}_{\text{soft}}$ can now be understood as a part of some effective Lagrangian valid at a scale Λ_{low}. As the mass scale of the messenger sector, which propagates the SUSY-breaking from some hidden sector to the supersymmetric part of the model, has to be much larger then Λ_{low} to be phenomenologically acceptable, the terms of Eq. (2.76) may then be recovered from some more comprehensive theory by integrating out the heavier d.o.f. down to Λ_{low}.

2.3.5. R-Symmetry

As already introduced in Eq. (2.27) and Eq. (2.29), one can extend the super-Poincaré algebra by chiral rotations, the so-called R-symmetry. The transformation behavior Eq. (2.27) leads to the R-charges -1 and 1 for the two-component supercharges Q_A and $\bar{Q}^A$. Furthermore, due to their representation in superspace Eqs. (2.34a) and (2.34b) the Grassmann coordinates Θ and $\bar{\Theta}$ attain the R-charges 1 and -1 such that

$$\Theta \to e^{i\phi}\Theta \quad (2.77a)$$

$$\bar{\Theta} \to e^{-i\phi}\bar{\Theta}. \quad (2.77b)$$

If one defines an R-transformation on the superfields as

$$\Phi'(x, e^{i\phi}\Theta, e^{-i\phi}\bar{\Theta}) \;=\; e^{i\phi R_\Phi}\Phi(x,\Theta,\bar{\Theta}), \quad (2.78a)$$

$$\Phi'^{\dagger}(x, e^{i\phi}\Theta, e^{-i\phi}\bar{\Theta}) \;=\; e^{-i\phi R_\Phi}\Phi^{\dagger}(x,\Theta,\bar{\Theta}), \quad (2.78b)$$

$$V'(x, e^{i\phi}\Theta, e^{-i\phi}\bar{\Theta}) \;=\; e^{i\phi R_V}V(x,\Theta,\bar{\Theta}), \quad (2.78c)$$

this indicates the following assignment of R-charges for the various component fields (see Eqs. (2.40a), (2.40b)):

$$R(\phi) \;=\; R_\Phi, \quad (2.79)$$

$$R(\xi) \;=\; -R(\bar{\xi}) \;=\; R_\Phi - 1, \quad (2.80)$$

$$R(F) \;=\; R_\Phi - 2. \quad (2.81)$$

[19] This means that at least every field operator in $\mathcal{L}_{SUSY}$ has to have a mass dimension not more than four.

Note that due to the reality condition Eq. (2.39c) $R(V)$ equals zero such that (see Eq. (2.42))

$$R(A_\mu) = 0, \tag{2.82}$$
$$R(\lambda) = -R(\bar{\lambda}) = 1, \tag{2.83}$$
$$R(D) = 0, \tag{2.84}$$
$$R(C) = 0, \tag{2.85}$$
$$R(\xi) = -R(\bar{\xi}) = 1, \tag{2.86}$$
$$R(M) = -R(M^*) = -2. \tag{2.87}$$

Further, note that the kinetic energy term of chiral superfields Eq. (2.49) (the D-term) as well as the the supersymmetric version of the gauge interactions Eq. (2.60) turn out to be invariant under the transformations Eqs. (2.78a)-(2.78c). But as already stated before, R-symmetry cannot be a symmetry of the full theory because conservation of the corresponding Noether current would be violated within a supergauge theory by quantum anomalies. In addition, R-symmetry is explicitly broken by the gaugino mass terms of Eq. (2.76). These terms can not be avoided as the existence of massless EW or strongly interacting gauginos are excluded by nullresults of corresponding searches at LEP and TEVATRON. Furthermore, extending global supersymmetry to a local symmetry leads to models of supergravity and, hence, to the inclusion of the gravitino, the superpartner of the graviton, whose mass term violates R-symmetry, too. However, in all these cases, a residual $\mathbb{Z}_2$-symmetry, the so-called matter-parity (R_m in terms of superfields) or R-parity (R_p in terms of component fields), can still be preserved. Being symmetric with respect to R_m or R_p states then corresponds to the invariance of the theory under multiplication of super- or component- fields with the factor $e^{i\pi R} = (-1)^R$. One can implement R-parity by defining the R_Φ in Eqs. (2.79)-(2.81) for the different left and right chiral superfields in such a way that the SM-particles obtain positive R_p (by convention $R_\Phi = \{0, \pm 1\}$ throughout while their superpartners possess a R_p less than zero. It turns out that, following these definitions, R_m and R_p can be identified with

$$R_m = (-1)^{3(B-L)}, \tag{2.88a}$$
$$R_p = (-1)^{3(B-L)+2S}, \tag{2.88b}$$

where B and L are the baryon and lepton number and S is the spin of the particle described by the particular component field. As the total baryon and lepton number are separately conserved within the SM, the assumption of R_p-symmetry, which can be understood as the supersymmetric generalization of baryon and lepton number conservation, may not seem to be too arbitrary. The reason which raises particular interest in R-symmetry in terms of model building is the observation that imposing R-parity conservation upon a model rejects terms which would otherwise lead to an unacceptable low lifetime of the proton and, hence, to a phenomenologically unacceptable theory. E.g., the requirement of renormalizability and gauge invariance would in general allow for the terms

$$[(D_i N_j - U_i E_j)\bar{D}_k]_F, \tag{2.89a}$$
$$[(E_i N_j - N_i E_j)\bar{E}_k]_F, \tag{2.89b}$$
$$[\bar{D}_i \bar{D}_j \bar{U}_k]_F \tag{2.89c}$$

in $\mathcal{L}$. These interactions introduce processes of the form

$$u_L d_R u_R \to \bar{e_R}, \tag{2.90}$$

which would manifest themselves as a proton decay

$$p \to \pi^0 e^+ \tag{2.91}$$

at a way too high rate. However, beside the prevention of rapid proton decay the introduction of R-parity conservation possesses very important additional phenomenological implications:

- All sparticles decay at some point into the lightest supersymmetric particle, the LSP.
- Sparticles can only be produced in pairs.
- The LSP becomes stable. This is a necessary, though not sufficient requirement for a viable dark matter candidate.
- The collider signatures for sparticle searches with an EW LSP typically include searches for missing energy as the LSP may escape the detector unhinderedly (e.g., in case of a neutralino-LSP).

Since we are interested in supersymmetric models which feature a viable dark matter candidate, we assume R-parity conservation throughout the following[20].

2.4. The Minimal Supersymmetric Standard Model

The MSSM is the minimal[21], R-parity conserving, $\mathcal{N} = 1$ supersymmetric version of the SM. To construct such a minimal extension, every particle field of the SM has to be embedded into a chiral or a vector superfield and is hence accompanied by its associated superpartners. The full particle content of the MSSM is given in Tab. (2.1) and Tab. (2.2) where superpartners of SM-particles are furnished with a tilde. Since there is no relativistic

Table 2.1.: The chiral supermultiplets (see Sec. 2.3.2) of the MSSM.

chiral superfields: particle content		spin 0	spin 1/2	$SU(3)_C$, $SU(2)_\mathrm{L}$, $U(1)_\mathrm{Y}$
squarks, quarks	Q	$(\tilde{u}_\mathrm{L}\, \tilde{d}_\mathrm{L})$	$(u_\mathrm{L}\, d_\mathrm{L})$	$(\mathbf{3},\, \mathbf{2},\, \frac{1}{3})$
($\times$3 generations)	$\bar{u}$	$\tilde{u}^*_\mathrm{R}$	$u^\dagger_\mathrm{R}$	$(\bar{\mathbf{3}},\, \mathbf{1},\, -\frac{4}{3})$
	$\bar{d}$	$\tilde{d}^*_\mathrm{R}$	$d^\dagger_\mathrm{R}$	$(\bar{\mathbf{3}},\, \mathbf{1},\, \frac{2}{3})$
sleptons, leptons	L	$(\tilde{\nu}\, \tilde{e}_\mathrm{L})$	$(\nu\, e_\mathrm{L})$	$(\mathbf{1},\, \mathbf{2},\, -1)$
($\times$3 generations)	$\bar{e}$	$\tilde{e}^*_\mathrm{R}$	$e^\dagger_\mathrm{R}$	$(\mathbf{1},\, \mathbf{1},\, 2)$
Higgs, higgsinos	H_1	$(h^0_1\, h^-_1)$	$(\tilde{h}^0_1\, \tilde{h}^-_1)$	$(\mathbf{1},\, \mathbf{2},\, -1)$
	H_2	$(h^+_2\, h^0_2)$	$(\tilde{h}^+_2\, \tilde{h}^0_2)$	$(\mathbf{1},\, \mathbf{2},\, 1)$

QFT known, which includes spin-1 matter fields, the spin-$\frac{1}{2}$ SM fermions decomposed with respect to chirality are embedded into left and right chiral superfields Φ_i, $\Phi^\dagger_i$. Due to the Eqs. (2.40a) and (2.40b), each chirality part is accompanied by a complex scalar, its spin zero superpartner. They are given in the first two rows of Tab. 2.1 and must be

[20] Note that models which violate B *or* L separately can still be in accordance with the non-observance of the proton-decay and, hence, be phenomenologically allowed. Therefore, many investigations also deal with R-parity violating theories [15].

[21] in terms of field-content

Table 2.2.: The vector supermultiplets (see Sec. 2.3.2) of the MSSM.

vector superfields: particle content	spin 1/2	spin 1	$SU(3)_C$, $SU(2)_\mathrm{L}$, $U(1)_\mathrm{Y}$
gluino, gluon	$\tilde{g}$	g	$(\mathbf{8}, \mathbf{1}, 0)$
winos, W bosons	$\tilde{W}^\pm \tilde{W}^0$	$W^\pm W^0$	$(\mathbf{1}, \mathbf{3}, 0)$
bino, B boson	$\tilde{B}^0$	B^0	$(\mathbf{1}, \mathbf{1}, 0)$

reproduced three times, once for each family of the SM[22]. The name of the corresponding superfield is written in the second column of Tab. 2.1. The last row of Tab. 2.1 contains the chiral supermultiplets which include the Higgs fields of the MSSM. In the SM one Higgs doublet is already sufficient to build up the $U(1)_\mathrm{Y}$ invariant Yukawa-terms for the quarks. However, due to the holomorphy condition of the superpotential Eq. (2.50), this is not possible within the MSSM. Here two Higgs doublets

$$h_1 \;=\; \begin{pmatrix} h_1^0 \\ h_1^- \end{pmatrix}, \;\; h_2 \;=\; \begin{pmatrix} h_2^+ \\ h_2^0 \end{pmatrix} \tag{2.92}$$

with the assigned $U(1)_\mathrm{Y}$ quantum numbers $Y_{h_1} = -1$ (down-type), $Y_{h_2} = 1$ (up-type) are necessary to achieve the gauge invariant supersymmetric versions of the Yukawa-interactions (see Tab. 2.1)

$$-\, f_{ij}^d H_1 \cdot Q_i \bar{d}_j - f_{ij}^u Q_i \cdot H_2 \bar{u}_j + \text{h.c.} \tag{2.93}$$

for the quarks[23].
Their vacuum expectation values are

$$\langle h_1 \rangle \;=\; \frac{1}{\sqrt{2}} \begin{pmatrix} v_1 \\ 0 \end{pmatrix}, \;\; \langle h_2 \rangle \;=\; \frac{1}{\sqrt{2}} \begin{pmatrix} 0 \\ v_2 \end{pmatrix}, \tag{2.94}$$

which can always chosen to be real, and the vevs have to fulfill

$$\sqrt{v_1^2 + v_2^2} \;=\; 1/(\sqrt{2} G_F)^{\frac{1}{2}} \simeq 246 \text{ GeV}. \tag{2.95}$$

In Eq. (2.95), G_F is the Fermi constant. Since Eq. (2.95) only fixes one vev, the other one is left free. This degree of freedom is typically parametrized via

$$\tan\beta \;=\; \frac{v_2}{v_1}. \tag{2.96}$$

Of course only the uncharged Higgs fields are allowed to evolve a non-zero vev (Eq. (2.94)). Finally, the spin-$\frac{1}{2}$ superpartners of the two Higgs-doublets h_1 and h_2 are the so-called higgsinos

$$\tilde{h}_1 \;=\; \begin{pmatrix} \tilde{h}_1^0 \\ \tilde{h}_1^- \end{pmatrix}, \;\; \tilde{h}_2 \;=\; \begin{pmatrix} \tilde{h}_2^+ \\ \tilde{h}_2^0 \end{pmatrix}. \tag{2.97}$$

For a selfconsistent supersymmetric version of the SM, the SM-gauge bosons B^0, W^i ($i = 0, 1, 2$, a $SU(2)_\mathrm{L}$-index), g^a ($a = 1, ..8$, a $SU(3)_\mathrm{C}$-index) have to be included into vector superfields. Their superpartners, the bino ($\tilde{B}^0$), the winos ($\tilde{W}^i$ ($i = 0, 1, 2$)) and

[22] Note, that chirality is not defined for scalar fields. Hence, in terms of scalars the subscripts L and R, which refer to left and right chiral states, are just names to distinguish between different particles.
[23] Note, that in Eq. 2.93 the SU(2)-scalar product is defined as $A \cdot B = \epsilon_{ED} A^D B^E$.

the gluinos ($\tilde{g}^a$ ($a = 1,..,8$)) are listed in Tab. 2.2. Since the SUSY-transformations commute with the generators of internal symmetries, all particles within a supermultiplet possess the same quantum numbers (see right column in Tab. (2.1) and (2.2)) and transform under the same representation of the gauge group.
With all necessary ingredients at hand, one can construct the MSSM Lagrangian $\mathcal{L}_{\text{MSSM}}$. One just has to set up the kinetic and interaction terms as given in Eq. (2.62) for the field content of Tab. (2.1) and (2.2). One further has to specify the vector superfield V in $\Phi_i^\dagger (e^V)_{ij} \Phi_j$ according to the quantum numbers of the respective left and right chiral superfields Φ_j and $\Phi_i^\dagger$. The only part left to further specification is the superpotential $\mathcal{W}$. In addition to the assumptions which entered the superpotential Eq. (2.50), the conservation of R-parity by $\mathcal{W}_{\text{MSSM}}$ is now explicitly assumed. $\mathcal{W}_{\text{MSSM}}$ then takes the form

$$\mathcal{W}_{\text{MSSM}} = \mu H_1 \cdot H_2 - f_{ij}^{e*} H_1 \cdot L_i \bar{E}_j - f_{ij}^{d*} H_1 \cdot Q_i \bar{D}_j - f_{ij}^{u*} Q_i \cdot H_2 \bar{U}_j. \tag{2.98}$$

The first term of Eq. (2.98) can be understood as a supersymmetric generalization of an higgsino massterm since, due to dimensional analysis, its prefactor μ turns out to possess the mass dimension one[24]. The last three terms are supersymmetric versions of the SM-Yukawa mass terms. Moreover, the full gauge fixing Lagrangian of the MSSM for the Feynman-gauge including the corresponding ghost terms can be found in Ref. [17]. There, it is given in the 't Hooft-Feynman gauge ($\xi = 1$), which is the gauge used throughout this work.
As already discussed in Sec. 2.3.4, low energy supersymmetry can not be an exact symmetry of nature. Within the MSSM, an explicit breaking of supersymmetry via soft breaking terms of the form Eq. (2.76) is assumed. Written out in component fields $\mathcal{L}_{\text{soft}}^{\text{MSSM}}$ takes the form

$$\begin{aligned} -\mathcal{L}_{\text{soft}}^{\text{MSSM}} &= \tilde{q}_{iL}^* (\mathcal{M}_{\tilde{q}}^2)_{ij} \tilde{q}_{iL} + \tilde{u}_{iR}^* (\mathcal{M}_{\tilde{u}}^2)_{ij} \tilde{u}_{jR} + \tilde{d}_{iR}^* (\mathcal{M}_{\tilde{d}}^2)_{ij} \tilde{d}_{jR} + \tilde{\ell}_{iL}^* (\mathcal{M}_{\tilde{\ell}}^2)_{ij} \ell_{jL} \\ &\quad + \tilde{e}_{iR}^* (\mathcal{M}_{\tilde{e}}^2)_{ij} \tilde{e}_{jR} + [h_1 \cdot \tilde{\ell}_{iL} (f^{e*} A_{\tilde{e}})_{ij} \tilde{e}_{jR}^* + h_1 \cdot \tilde{q}_{iL} (f^{d*} A_{\tilde{d}})_{ij} \tilde{d}_{jR}^* \\ &\quad + \tilde{q}_{iL} \cdot h_2 (f^{u*} A_{\tilde{u}})_{ij} \tilde{u}_{jR}^* + \text{h.c.}] + m_1^2 |h_1|^2 + m_2^2 |h_2|^2 + (B\mu \, h_1 \cdot h_2 + \text{h.c.}) \\ &\quad + \frac{1}{2} (M_1 \tilde{B}\tilde{B} + M_2 \tilde{W}^i W^i + M_3 \tilde{g}^a \tilde{g}^a + \text{h.c.}). \end{aligned} \tag{2.99}$$

Note the absence of any $\mathcal{C}$-type terms of Eq. (2.76) in Eq. (2.99) which is due to the fact that the MSSM, which is required to preserve gauge invariance, does not contain any singlets under the SM-gauge group. Let us now quickly go through the different terms of Eq. (2.99). $\mathcal{M}_{\tilde{f}}^2$ with $\tilde{f} = \{\tilde{q}, \tilde{l}\}$ are the left handed soft breaking mass matrices for sleptons and squarks. They are hermitian 3×3 matrices in generation space. They further have to be the same for up- and down-type sfermions to leave the $SU(2)_{\text{L}}$-symmetry intact. $\mathcal{M}_{\tilde{u},\tilde{d},\ell}^2$ represent the analogues for the right-chiral sector. They can in general differ from each other as they are not connected by any gauge symmetry. The terms proportional to the $A_{\tilde{f}}$ ($\tilde{f} = \tilde{e}, \tilde{u}, \tilde{d}$) for sfermion type $\tilde{f}$ are the trilinear scalar coupling terms. The $A_{\tilde{f}}$ are complex 3×3 matrices in generation space. The last three terms are the gaugino mass terms already mentioned in Eq. (2.76). Note, that we set $\nu_R, \tilde{\nu}_R$ in Eq. (2.99) to zero for all three generations. The full set of Feynman rules which result from the full MSSM-Lagrangian can again be found in Ref. [17]. This is also the main reference for all

[24] Within the MSSM the radiative breakdown of EW symmetry requires μ to be around the EW scale. Like in the discussion of the hierarchy problem in the context of the Higgs-mass Sec. 2.2.1 this raises the question, why μ should stick to the EW-breaking scale and not rather tend against some high scale. This is the so-called μ-problem, which can be solved, e.g., in extensions of the MSSM such as in gravity mediated SUSY-breaking models (see Ref. [16] and references therein).

the calculations of Feynman diagrams connected to this work.
Having included $\mathcal{L}_{\text{soft}}^{\text{MSSM}}$, the full MSSM Lagrangian contains 124 parameters in total. 105 of these 124 new parameters stem from the soft breaking terms Eq. (2.99), e.g., from intergenerational mixings or complex phases. In order to not become completely undetermined or unpredictive due to this vast amount of degrees of freedom, one can go to more constrained versions of the MSSM parameter space. In addition, there are severe constraints on the MSSM-parameters due to measurements on CP-violation and flavor changing neutral currents (FCNC) which constrain the set of soft breaking parameters. The phenomenological MSSM (pMSSM) is one example of a constrained version of the MSSM which tries to minimize dangerous sources of CP violation or FCNCs. Since the pMSSM is the relevant model for the analysis connected to this work, it is shortly addressed in the following section.

2.5. The Phenomenological MSSM

Depending on the choice of its parameters, $\mathcal{L}_{\text{soft}}^{\text{MSSM}}$ can have a sizable impact on precision observables of the SM via higher-order corrections. This requires to constrain the MSSM soft-breaking parameters to avoid tensions with experiments. The pMSSM, which is a 19-parameter version of the MSSM, takes these phenomenological constraints *ab initio* into account. It is built on the following assumptions [18]:

- **No new sources of CP-violation:**
  To minimize potential sources of CP-violation, already tightly constrained by experimental limits on the electron and neutron electric dipole moment, all soft breaking parameters are taken to be real.

- **No Flavor Changing Neutral Currents:**
  Non diagonal terms in the sfermion mass matrices and trilinear couplings can induce new, already tightly constrained sources of FCNC. To circumvent these large contributions, mass matrices and trilinear couplings are taken to be diagonal in generation-space.

- **First and Second Generation Universality:**
  Since the trilinear couplings of a particular fermion always appears accompanied by the associated fermion-mass, the trilinear couplings for the first two generations are only of minor importance and can hence be set to zero. Furthermore, the splitting between first and second generation sfermions is severely limited by experimental data, e.g., from $K^0 - \bar{K}^0$-mixing, unless they are much heavier than one TeV. Hence, one may assume universality of the soft breaking sfermion-masses between the first two generations.

The 105 additional MSSM parameters are then reduced to the following set of only 19 free parameters:

- $\tan\beta$: the ratio of the Higgs vevs Eq. (2.96)
- m_{A^0}: the pseudoscalar Higgs mass
- μ: the higgsino mass parameter Eq. (2.98)
- M_1, M_2, M_3: the gaugino masses Eq. (2.99)

- $m_{\tilde{q}_{1,2}}$, $m_{\tilde{u}_{1,2}}$, $m_{\tilde{d}_{1,2}}$, $m_{\tilde{l}_{1,2}}$, $m_{\tilde{e}_{1,2}}$: first/second generation left/right soft breaking sfermion masses Eq. (2.99)
- $m_{\tilde{q}_3}$, $m_{\tilde{u}_3}$, $m_{\tilde{d}_3}$, $m_{\tilde{l}_3}$, $m_{\tilde{e}_3}$: third generation left/right soft-breaking sfermion masses Eq. (2.99)
- A_t, A_b, A_τ: third generation trilinear couplings Eq. (2.99)

Since we study the impact of perturbative as well as non-perturbative corrections on gaugino and stop annihilation into SM particles, the slepton sector as well as the bottom-squark are of minor relevance. Hence we further impose the constraints

- $m_{\tilde{l}_{1,2}} = m_{\tilde{e}_{1,2}} = m_{\tilde{l}_3} = m_{\tilde{e}_3}$: a common soft breaking mass $m_{\tilde{\ell}}$ in the slepton sector
- $m_{\tilde{q}_3} = m_{\tilde{d}_3}$: a common third generation left and bottom-right soft breaking mass $m_{\tilde{q}_3}$
- $m_{\tilde{q}_{1,2}} = m_{\tilde{u}_{1,2}} = m_{\tilde{d}_{1,2}}$: a common left/right soft breaking mass $m_{\tilde{q}_{1,2}}$ for first and second generation squarks
- $A_b = A_\tau = 0$: negligible trilinear coupling for the bottom-squark and all sleptons.

Moreover, in the following we state our results using the parameter T_t instead of A_t. These are related via

$$T_t = Y_t A_t, \tag{2.100}$$

with the top-Yukawa coupling Y_t. This leaves us with an 11-parameter version of the pMSSM, spanned by the free parameters

$$\left\{\tan\beta, m_{A^0}, \mu, M_1, M_2, M_3, m_{\tilde{\ell}}, m_{\tilde{q}_3}, m_{\tilde{q}_{1,2}}, T_t, m_{\tilde{u}_3}\right\}. \tag{2.101}$$

This model is used throughout the analysis presented in the following chapters.

2.6. Going from Interaction to Mass Eigenstates

So far we have defined the MSSM Lagrangian in terms of interaction eigenstates. But as already known from, e.g., the EW sector of the SM, one has to distinguish between interaction and mass eigenstates, of which the latter are the states that correspond to freely propagating particles at fixed mass. The mass eigenstates are now defined as the basis in which the mass terms of $\mathcal{L}_{\text{MSSM}}$ take diagonal form. They are a linear combination of the different interaction eigenstates and, hence, their phenomenology is connected to the properties they inherit through the corresponding admixture. Therefore, we go through those sectors of the MSSM that turn out to be of special importance for the subsequent analysis and present the arising mass eigenstates as well as their connection to the particular interaction eigenstates.

2.6.1. The Higgs Sector

The $SU(2)_{\text{L}}$ doublets h_1 and h_2 of Eq. (2.92), which are comprised of four complex scalars, give rise to in total eight degrees of freedom. As seen in Sec. 2.4, these two $SU(2)_{\text{L}}$ doublets allow for the construction of $U(1)_{\text{Y}}$-invariant Yukawa-terms Eq. (2.93) while still being compatible with the requirement of a holomorphic superpotential $\mathcal{W}_{\text{MSSM}}$. The

contributions to the complete scalar potential written in terms of h_1 and h_2 are derived from Eq. (2.65) together with Eq. (2.98) and Eq. (2.99). At tree level, these take the form

$$\begin{aligned} V_H &= \frac{1}{8}(g_{\mathrm{Y}}^2+g_2^2)(|h_1|^2-|h_2|^2)^2+\frac{g_2^2}{2}|h_1^\dagger h_2|^2+(m_1^2+|\mu|^2)|h_1|^2+(m_2^2+|\mu|^2)|h_2|^2 \\ &\quad +(B\mu\; h_1\cdot h_2+\text{h.c.}), \end{aligned} \tag{2.102}$$

where the $SU(2)_{\mathrm{L}}$-scalar product is defined as in Sec. 2.4. Eq. (2.102) implies a non-trivial mixing between the two Higgs doublets. This results in mass eigenstates, which generally do not coincide with the components of h_1 and h_2 as given in Eq. (2.92). Expanding the fields h_1^0 and h_2^0 near their vevs Eq. (2.102) gives rise to the following mixing pattern:

- The imaginary parts of the complex scalars h_1^0 and h_2^0 combine to

$$A^0 = \sqrt{2}\left(\Im\left\{h_1^0\right\}\sin\beta+\Im\left\{h_2^0\right\}\cos\beta\right), \tag{2.103a}$$
$$G^0 = \sqrt{2}\left(-\Im\left\{h_1^0\right\}\cos\beta+\Im\left\{h_2^0\right\}\sin\beta\right), \tag{2.103b}$$

  with masses

$$m_{A^0}^2 = \frac{v_1^2+v_2^2}{v_1v_2}B\mu = \frac{2B\mu}{\sin 2\beta}, \tag{2.104}$$
$$m_{G^0}^2 = 0. \tag{2.105}$$

- The remaining two degrees of freedom stemming from the real parts of h_1^0 and h_2^0 mix to

$$h^0 = \sqrt{2}\left(-(\Re\left\{h_1^0\right\}-\frac{v_1}{\sqrt{2}})\sin\alpha+(\Re\left\{h_2^0\right\}-\frac{v_2}{\sqrt{2}})\cos\alpha\right), \tag{2.106a}$$
$$H^0 = \sqrt{2}\left((\Re\left\{h_1^0\right\}-\frac{v_1}{\sqrt{2}})\cos\alpha+(\Re\left\{h_2^0\right\}-\frac{v_2}{\sqrt{2}})\sin\alpha\right), \tag{2.106b}$$
$$\tag{2.106c}$$

  the SM-like lighter Higgs h^0 and the heavier scalar Higgs H^0 with squared tree-level masses

$$m_{h^0,H^0}^2 = \frac{1}{2}\left[m_{A^0}^2+M_{Z^0}^2\mp\left\{(m_{A^0}^2+M_{Z^0}^2)^2-4M_{Z^0}^2m_{A^0}^2\cos^2 2\beta\right\}^{1/2}\right]. \tag{2.107}$$

- The charged Higgs $h_1^\pm$ and $h_2^\pm$ form the states

$$H^\pm = \sin\beta h_1^\pm+\cos\beta h_2^\pm, \tag{2.108a}$$
$$G^\pm = -\cos\beta h_1^\pm+\sin\beta h_2^\pm. \tag{2.108b}$$

  Here, the $H^\pm$ and $G^\pm$ acquire the squared tree-level masses

$$m_{H^\pm}^2 = \left(\frac{B\mu}{v_1v_2}+\frac{1}{4}g_2^2\right)(v_1^2+v_2^2) = m_{A^0}^2+m_{W^\pm}^2, \tag{2.109}$$
$$m_{G^\pm}^2 = 0. \tag{2.110}$$

The Higgs masses given here are only tree-level masses as derived from the tree-level potential Eq. (2.102). Hence, they can still be subject to large higher-order corrections (see Sec. 2.2.1). Moreover, note that the neutral and charged Goldstone bosons, one for each generator of the spontaneously broken symmetry (here three, $SU(2)_\mathrm{L} \times U(1)_\mathrm{Y} \to U(1)_\mathrm{em}$), remain massless as required by the Goldstone theorem [12].
So far, we did not include the contributions of the gauge fixing terms Eq. (2.69) in the estimation of the tree-level masses. The masses of the Goldstone bosons G^0 and $G^\pm$, which are associated with the longitudinal polarization states of the Z^0 and $W^\pm$ boson, are dependent on the specific gauge choice and, hence, modified by terms from $\mathcal{L}_\mathrm{gf}^\mathrm{SUSY}$. In the general R_ξ-gauge, the contributions to the Goldstone bosons (the supersymmetric partners are the so-called Goldstinos) take the form [17]

$$m_{G^0} \;=\; \sqrt{\xi} m_Z, \quad m_{G^\pm} \;=\; \sqrt{\xi} m_{W^\pm}, \tag{2.111}$$

which in the 't Hooft-Feynman gauge ($\xi \;=\; 1$) leads to the masses

$$m_{G^0} \;=\; m_Z, \quad m_{G^\pm} \;=\; m_{W^\pm}. \tag{2.112}$$

The corresponding Fadeev-Popov ghosts of Eq. (2.70) obtain the same masses as the Goldstone bosons [12]. The propagators of massive vector bosons, which results from Eq. (2.68) can then be written as

$$\frac{-i(g_{\mu\nu} - (1-\xi)\frac{p_\mu p_\nu}{p^2})}{p^2 - m_V^2} \to \frac{-i g_{\mu\nu}}{p^2 - m_V^2}. \tag{2.113}$$

This simplifies the form of propagators of massive vector bosons. In contrary to, e.g., the unitary gauge, the Goldstone bosons are not automatically included as the longitudinal polarizations of the massive vector bosons but need to be taken into account separately.
Let us close this section with two additional comments on the scalar potential V_H as given in Eq. (2.102). It follows from Eq. (2.102) that for the uncharged field content of V_H the requirement of a non-zero vev and a potential that is bounded from below can be grasped into the two inequalities

$$m_1^2 + m_2^2 + 2|\mu|^2 > 2|B\mu|, \tag{2.114a}$$
$$|B\mu|^2 > (m_1^2 + |\mu|^2)(m_2^2 + |\mu|^2). \tag{2.114b}$$

It turns out that in the limit $m_1 \;=\; m_2$ these two inequalities become mutually incompatible (SUSY-invariance corresponds to the limit $m_1 \;=\; m_2 \;=\; 0$). This observation leads to the intriguing insight that, at least within the MSSM, SUSY breaking is deeply connected to the spontaneous breakdown of EW symmetry $SU(2)_\mathrm{L} \times U(1)_\mathrm{Y} \to U(1)_\mathrm{em}$. However, it is a nice feature of the MSSM that even if one starts with the same soft breaking masses $m_1 \;=\; m_2$ (see Eq. (2.99)) at some high scale the required inequality $m_1 \neq m_2$ can be dynamically obtained via the corresponding renormalization group running. More precisely, since only the beta function of the squared soft breaking mass m_2^2 depends on the relatively large top-Yukawa coupling the RGE running of the soft breaking scalar masses m_1 and m_2 can induce the required splitting at the EW scale. Whereas in the SM the prefactor $\mu^2 < 0$ has to be adjusted by hand to achieve EW symmetry breaking, the MSSM hence provides a mechanism to drive the prefactors of the scalar potential to the required values.

2.6.2. The Neutralino and Chargino Sector

With a look at $\mathcal{L}_{\text{MSSM}}$ one sees that after EW symmetry breaking $U(1)_{\text{Y}} \times SU(2)_{\text{L}} \to U(1)_{\text{em}}$ the higgsinos and gauginos mix with each other. However, gauge invariance forbids the mixing between different interaction eigenstates if they do not possess the same gauge quantum numbers.
Starting with the electrically neutral gaugino-higgsino sector, the full contributions in $\mathcal{L}_{\text{MSSM}}$ to the mass mixing given in the basis $(\psi^0)^T = (\tilde{B}, \tilde{W}^0, \tilde{h}_0^1, \tilde{h}_0^2)$ can be grasped in the form

$$\mathcal{L}_{\text{MSSM}}|_{\text{neutralino-mass}} = -\frac{1}{2}(\psi^0)^T M_{\chi^0} \psi^0, \tag{2.115}$$

where

$$M_{\chi^0} = \begin{pmatrix} M_1 & 0 & -M_{Z^0}\cos\beta\sin\Theta_W & M_{Z^0}\sin\beta\sin\Theta_W \\ 0 & M_2 & M_{Z^0}\cos\beta\cos\Theta_W & -M_{Z^0}\sin\beta\cos\Theta_W \\ -M_{Z^0}\cos\beta\sin\Theta_W & M_{Z^0}\cos\beta\cos\Theta_W & 0 & -\mu \\ M_{Z^0}\sin\beta\sin\Theta_W & -M_{Z^0}\sin\beta\cos\Theta_W & -\mu & 0 \end{pmatrix}. \tag{2.116}$$

The mass matrix M_{χ^0} can then be brought to diagonal form via

$$M_{\chi^0}^D = \mathbf{Z}^* M_{\chi^0} \mathbf{Z}^{-1} = \text{diag}(m_{\chi_1^0}, m_{\chi_2^0}, m_{\chi_3^0} m_{\chi_4^0}). \tag{2.117}$$

Here, we choose $0 \leq |m_{\chi_1^0}| < |m_{\chi_2^0}| < |m_{\chi_3^0}| < |m_{\chi_4^0}|$ by convention and $\mathbf{Z}$ is a unitary 4×4-matrix. Eq. (2.117) induces a change of basis

$$\chi_i^0 = \mathbf{Z}_i^n \psi_n^0, \tag{2.118}$$

which corresponds to going from interaction to mass eigenstates. The χ_i^0 $(i = 1, 2, 3, 4)$ are the so-called neutralinos. Depending on whether they possess a large admixture of gauginos or higgsinos, they are called gaugino or higgsino like. Due to the unitarity of $\mathbf{Z}$, $M_{\chi^0}^D$ can be computed from

$$(M_{\chi^0}^D)^2 = \mathbf{Z} M_{\chi^0}^\dagger M_{\chi^0} \mathbf{Z}^{-1}. \tag{2.119}$$

Note that if all potential phases in M_{χ^0} are ignored[25] $\mathbf{Z}$ can be assumed to be orthogonal and real. The price to pay is that there may arise negative mass squares on the diagonal of $(M_{\chi^0}^D)^2$. One can then use chiral rotations $\chi_i^0 \to \chi_i^{0'}$ to obtain the physical fields with $m_{\tilde{\chi}_i^0} := m_{\chi_i^{0'}} > 0$.
The four component Majorana spinors can be comprised of the two-component $\chi_i^{0'}$ via

$$\tilde{\chi}_i^0 = \begin{pmatrix} \chi_i^{0'} \\ (\bar{\chi}_i^{0'})^T \end{pmatrix} \tag{2.120}$$

such that Eq. (2.115) can be finally written as

$$\mathcal{L}_{\text{MSSM}}|_{\text{neutralino-mass}} = -\frac{1}{2} \sum_{l=1}^{4} m_{\tilde{\chi}_l^0} \overline{\tilde{\chi}_l^0} \tilde{\chi}_l^0. \tag{2.121}$$

Let us now turn to the charged part of the gaugino-higgsino sector. Defining $\tilde{W}^\pm = \frac{1}{\sqrt{2}}(\tilde{W}_1 \pm i\tilde{W}_2)$, the contributions in $\mathcal{L}_{\text{MSSM}}$ to the mass mixing in the charged sector takes the form

$$\mathcal{L}_{\text{MSSM}}|_{\text{chargino-mass}} = -(\psi^-)^T M_{\chi^\pm} \psi^- + \text{h.c.}. \tag{2.122}$$

[25] This is one of the building assumptions of the pMSSM (see Sec. 2.5).

Here, the definitions $(\psi^+)^T = (\tilde{W}^+, \tilde{h}_2^+)$ and $(\psi^-)^T = (\tilde{W}^-, \tilde{h}_1^-)$ are used. $M_{\chi^\pm}$ is a 2×2-mass matrix which in the $\psi^\pm$-basis given above can be written as

$$M_{\chi^\pm} = \begin{pmatrix} M_2 & \sqrt{2} m_W \sin\beta \\ \sqrt{2} m_W \cos\beta & \mu \end{pmatrix}. \tag{2.123}$$

Eq. (2.123) can then be brought to diagonal form via

$$M_{\chi^\pm}^D = \mathbf{U}^* M_{\chi^\pm} \mathbf{V}^{-1} = \mathrm{diag}(m_{\chi_1^\pm}, m_{\chi_2^\pm}) \tag{2.124}$$

with $0 \leq m_{\chi_1^+} = m_{\chi_1^-} < m_{\chi_2^+} = m_{\chi_2^-}$ and $\mathbf{U}$ as well as $\mathbf{V}$ are some unitary matrices. Due to the definition of $\mathbf{U}$ and $\mathbf{V}$ in Eqs. (2.122) together with (2.124), the corresponding mass eigenstates can then be obtained via

$$\chi_k^+ = \mathbf{V}_k^n \psi_n^+, \tag{2.125a}$$
$$\chi_k^- = \mathbf{U}_k^n \psi_n^-. \tag{2.125b}$$

Going from the two-component spinors to Dirac spinors the charginos take the form

$$\tilde{\chi}_1^+ = \begin{pmatrix} \chi_1^+ \\ \overline{\chi_1^-}^T \end{pmatrix}, \tag{2.126a}$$
$$\tilde{\chi}_2^+ = \begin{pmatrix} \chi_2^+ \\ \overline{\chi_2^-}^T \end{pmatrix}. \tag{2.126b}$$

In terms of these Dirac spinors $\mathcal{L}_{\mathrm{MSSM}}|_{\mathrm{chargino-mass}}$ can be rewritten as

$$\mathcal{L}_{\mathrm{MSSM}}|_{\mathrm{chargino-mass}} = -\sum_{i=1}^{2} m_{\tilde{\chi}_i^+} \overline{\tilde{\chi}_i^+} \tilde{\chi}_i^+, \tag{2.127}$$

where we have redefined $m_{\tilde{\chi}i} := m_{\chi_i}$ $(i \in \{1, 2\})$ for convenience. Further note, that the gluinos do not contribute to the above mixing as they are strongly charged. Therefore, they cannot mix with the gauginos and higgsinos of the EW sector. Since all gluinos have to encounter the same mass terms as required by $SU(3)_\mathrm{C}$ symmetry, their mixing pattern is such that there is no difference between interaction and mass eigenstates.

2.6.3. The Sfermion Sector

The sfermion sector encounters some important mixing, too. Since only the squark sector turns out to be of greater importance for this work we solely concentrate on this part. The mixing of sleptons, which follows the same line, can be found in Ref. [3]. We further neglect all flavor-mixing and, hence, neglect the off-diagonal elements of the CKM-matrix. We finally require all soft-breaking parameters to be diagonal in generation space[26] such that only the mixing between left and right chiral scalars of a specific squark-type are taken into account. In this case the mass matrices simplify significantly. Written in the basis

$$\tilde{\mathbf{q}} = \begin{pmatrix} \tilde{q}_L \\ \tilde{q}_R \end{pmatrix} \tag{2.128}$$

[26] A valid assumption in the context of the pMSSM as discussed in Sec. 2.5.

the sfermion-mass terms in $\mathcal{L}_{\text{MSSM}}$ can be grasped in the compact form

$$\mathcal{L}_{\text{MSSM}}|_{\text{sfermion-mass}} \;=\; \sum_{\tilde{q}} \tilde{\mathbf{q}}^{\dagger} \mathcal{M}^2_{\tilde{\mathbf{q}}} \tilde{\mathbf{q}}, \tag{2.129}$$

where

$$\mathcal{M}^2_{\tilde{\mathbf{q}}} \;=\; \begin{pmatrix} \mathcal{M}^2_{\tilde{f}_{\text{LL}}} & \mathcal{M}^2_{\tilde{f}_{\text{LR}}} \\ \mathcal{M}^2_{\tilde{\mathbf{f}}_{\text{RL}}} & \mathcal{M}^2_{\tilde{f}_{\text{RR}}} \end{pmatrix} \tag{2.130}$$

is a 2×2-matrices in chirality space. Since we neglect all flavor mixing, these matrices need do be reproduced only thrice, once for every generation, while $\tilde{q}$ runs through $\tilde{q} \;=\; \{\tilde{u}, \tilde{d}\}$. For up- and down-type squarks $\mathcal{M}^2_{\tilde{\mathbf{q}}}$ possesses the following entries

$$M^2_{\tilde{q}_i} \;=\; \begin{pmatrix} \mathcal{M}^2_{\tilde{q}_i} + M^2_{Z^0}(T^{\tilde{q}}_{3L} - Q_q \sin^2\Theta_W)\cos 2\beta + \boldsymbol{m}^2_{q_i} & \boldsymbol{m}_{q_i}(-A_{\tilde{q}_i} - \mu(\tan\beta)^{-2T^{\tilde{q}}_{3L}}) \\ (-A_{\tilde{q}_i} - \mu(\tan\beta)^{-2T^{\tilde{q}}_{3L}})\boldsymbol{m}_{q_i} & \mathcal{M}^2_{\tilde{u}_i,\tilde{d}_i} + Q_q M^2_{Z^0}\cos 2\beta \sin^2\Theta_W + \boldsymbol{m}^2_{q_i} \end{pmatrix}. \tag{2.131}$$

Here, $i \;=\; \{1,2,3\}$ is a generation index and $\tilde{q}$ can be either up- or down-type. $T^{\tilde{q}}_{3L}$ is the third component of the weak isospin and Q_q are the quark-electric charges in units of e. Finally, the $\boldsymbol{m}_{q_i}$ are the i^{th} diagonal entry of

$$(\mathbf{m}_u)_{ij} \;=\; \frac{1}{\sqrt{2}} f^u_{ij} v_2 \tag{2.132}$$

for the up-type and of

$$(\mathbf{m}_d)_{ij} \;=\; \frac{1}{\sqrt{2}} f^d_{ij} v_1 \tag{2.133}$$

for the down type (see Eq. (2.93)) ($f^u_{ij} \;=\; f^d_{ij} \;=\; 0$ for $i \neq j$ as stated above). The remaining parameters $\mathcal{M}^2_{\tilde{q}_i}$, $\mathcal{M}^2_{\tilde{u}_i,\tilde{d}_i}$ and $A_{\tilde{q}_i}$ are the i^{th} diagonal entries of the soft-breaking matrices $\mathcal{M}^2_{\tilde{q}}$, $\mathcal{M}^2_{\tilde{u},\tilde{d}}$ and $A_{\tilde{q}}$ as discussed below Eq. (2.99). Further note that all soft breaking and EW parameters in Eq. (2.131) are taken to be real as it is common in terms of the pMSSM (see Sec. 2.5). The mass matrices $M^2_{\tilde{q}}$ can now be brought to diagonal form via the real rotations

$$\mathbf{M}^{2(D)}_{\tilde{q}_i} \;=\; (\mathbf{U}^{\tilde{q}_i})\mathcal{M}^2_{\tilde{q}_i}(\mathbf{U}^{\tilde{q}_i})^{\dagger} \;=\; \text{diag}(m^2_{\tilde{q}_{i,1}}, m^2_{\tilde{q}_{i,2}}), \tag{2.134}$$

where we coose the convention $m^2_{\tilde{q}_1} < m^2_{\tilde{q}_2}$. The sfermion mass eigenstates can then be obtained from

$$\begin{pmatrix} \tilde{q}_{i,1} \\ \tilde{q}_{i,2} \end{pmatrix} \;=\; (\mathbf{U}^{\tilde{q}_i}) \begin{pmatrix} \tilde{q}_{i,L} \\ \tilde{q}_{i,R} \end{pmatrix} \;=\; \begin{pmatrix} \cos(\Theta_{\tilde{q}_i}) & -\sin(\Theta_{\tilde{q}_i}) \\ \sin(\Theta_{\tilde{q}_i}) & \cos(\Theta_{\tilde{q}_i}) \end{pmatrix} \begin{pmatrix} \tilde{q}_{i,L} \\ \tilde{q}_{i,R} \end{pmatrix}. \tag{2.135}$$

Due to the proportionality of the off diagonal elements in Eq. (2.131) to the quark mass, only the third generation chiral squark eigenstates are expected to mix significantly, which can result in a sizable mass splitting between the corresponding mass eigenstates. Since the quark masses on the off diagonal of Eq. (2.131) are further multiplied by the trilinear couplings $A_{\tilde{q}_i}$, a large $A_{\tilde{q}_i}$ is expected to enlarge the splitting and to drive the lighter squark mass eigenstate to even lower values.

Let us close this section with a short look beyond the pure tree level as discussed above by providing the renormalization group equations, which describe the renormalization scale

dependent running of the squark soft breaking-masses. For third generation squarks, the scale dependence takes the form[27]

$$\frac{\mathrm{d}\mathcal{M}^2_{\tilde{q}_3}}{\mathrm{d}t} = \frac{1}{8\pi^2}\left(f_t^2 S_t + f_b^2 S_b - \frac{16}{3}g_3^2|M_3^2| - 3g_2^2|M_2^2| - \frac{1}{9}g_\mathrm{Y}^2|M_1^2| + \frac{1}{6}g_\mathrm{Y}^2 S_\mathrm{Y}\right), \quad (2.136)$$

$$\frac{\mathrm{d}\mathcal{M}^2_{\tilde{u}_3}}{\mathrm{d}t} = \frac{1}{8\pi^2}\left(2f_t^2 S_t - \frac{16}{3}g_3^2|M_3^2| - \frac{16}{9}g_\mathrm{Y}^2|M_1^2| - \frac{2}{3}g_\mathrm{Y}^2 S_\mathrm{Y}\right), \quad (2.137)$$

$$\frac{\mathrm{d}\mathcal{M}^2_{\tilde{d}_3}}{\mathrm{d}t} = \frac{1}{8\pi^2}\left(2f_b^2 S_b - \frac{16}{3}g_3^2|M_3^2| - \frac{4}{9}g_\mathrm{Y}^2|M_1^2| + \frac{1}{3}g_\mathrm{Y}^2 S_\mathrm{Y}\right), \quad (2.138)$$

where $f_t = f^u_{33}$ and $f_b = (f^d)_{33}$ are the third generation Yukawa couplings. Moreover, in the pMSSM we have $|M_i^2| = M_i^2$ ($i \in \{1,2,3\}$. We further made use of the definitions

$$S_t = m_2^2 + \mathcal{M}^2_{\tilde{q}_3} + \mathcal{M}^2_{\tilde{u}_3} + |A_t|^2, \quad (2.139)$$

$$S_b = m_1^2 + \mathcal{M}^2_{\tilde{q}_3} + \mathcal{M}^2_{\tilde{d}_3} + |A_b|^2 \quad (2.140)$$

as well as

$$S_\mathrm{Y} = \frac{1}{2}\sum_i Y_i m_i^2 \quad (2.141)$$

with hypercharges Y_i. Here, i runs over all MSSM scalars, i.e., over all Higgs bosons, squarks and sleptons. In the Eqs. (2.136)-(2.137) the large third generation Yukawa coupling f_t multiplies a positive term. This may be even more enhanced by a large trilinear coupling A_t such that third generation squark masses are expected to rise particularly strong with growing energy (or quickly decrease their masses towards low energies), driving the stop $\tilde{t}_1$ to be rather light at low energies. Since the right handed stop breaking parameter $\mathcal{M}^2_{\tilde{u}_3}$ comes with a factor of two in front of the terms $\propto f_t$ and with no wino-mass term $\propto |M_2^2|$ subtracted, $\mathcal{M}^2_{\tilde{u}_3}$ is expected to vary even stronger with energy than the left breaking mass. This may lead to a $\tilde{t}_1$, which features a potentially larger admixture of $\tilde{t}_R$, $|\sin\Theta_{\tilde{u}_3}|^2 > |\cos\Theta_{\tilde{u}_3}|^2$[28].

[27] t is defined as $t := \ln(\mu/\mu_0)$ with some arbitrary constant μ_0 and the renormalization scale μ which can be set to the "external" energy scale of the corresponding process.

[28] This is of course strongly dependent on the initial parameter choice.

3. Dark Matter: Evidence, Candidates and Calculations

3.1. Experimental Evidence for Dark Matter

Nowadays, there exists is a lot of evidences for the existence of a sizable, yet unknown matter component in the universe. Experiments suggest that this new type of matter does not emit any detectable amount of light, such that hints toward the existence of this so-called dark matter are only obtained via its gravitational interactions down to the present days.

3.1.1. The First Hints

One of the first observations which hinted toward the existence of DM were made by J. H. Oort and F. Zwicky in the early 1930's [19]. Making use of well defined mass-to-luminosity relations van Oort was able to give a rough estimate of the luminous mass within the milky way. When he further measured the velocities of stars near the galactic center via redshift analyses, he ascertained that the velocities of stars exceeded the escape velocity of the galaxy. He was thus led to the conclusion that an additional non-luminous mass component should be added to the luminous mass to strengthen its gravitational pull [20][1].
At the same time, Zwicky studied the Coma cluster, a cluster comprised out of about a thousand galaxies roughly 400 million lightyears away from our solar system [21]. As a starting point of his consideration Zwicky assumed that the Coma cluster has reached mechanical equilibrium. Footing on this assumption, he applied the virial theorem

$$\overline{U} = \frac{k}{2}\overline{V}, \tag{3.1}$$

which relates the averaged total kinetic energy

$$\overline{U} = \frac{1}{2}M\overline{v^2} \tag{3.2}$$

with total mass M and mass averaged velocity v, to the time averaged potential energy $\overline{V}$. Assuming an equal distribution of masses over a sphere, which interacts only gravitationally ($k = -1$), the averaged potential $\overline{V}$ at distance R follows from the third Keplerian law as

$$\overline{V} = -\frac{3G_{\text{Newton}}M^2}{5R} \tag{3.3}$$

with the gravitational constant G_{Newton}. By further assuming that no direction of velocity, apart from the overall velocity component caused by the movement of the Coma cluster

[1] It should be mentioned that Oort also considered further possibilities that he thought may account for this discrepancy. However, this was one of the first evidences which may be interpreted as a hint toward the existence of DM.

relative to us, is distinguished from another, i.e.,

$$\overline{v^2} = 3\overline{v_p^2}, \tag{3.4}$$

Zwicky was able to estimate a peculiar velocity

$$\overline{v_p} = \sqrt{\frac{G_{\text{Newton}}M}{5R}} \tag{3.5}$$

for this configuration. He took $R \approx 10^6\,\text{ly}$ as the radius of the cluster. As Zwicky was further able to give a rough estimate of the luminous mass $M_L = 1.6 \times 10^{45}\text{g}$ via known mass-to-luminosity relations for galaxies, he compared the $\overline{|v_p|}$ of Eq. (3.5) and the observed velocities along the line of sight obtained via redshift analyses. He found that the mass of the Coma cluster has to be about two to three orders of magnitude larger than M_L. Phrased differently, the luminous mass makes up only 2% of the total mass of the Coma cluster [19], which can be understood as another early hint toward the existence of DM.

3.1.2. Rotation Curves

Roughly four decades after Zwicky's discovery Rubin, Ford, Thonnard and others started to measure the rotation curves of many isolated galaxies [22]. These were preferably oriented in such a way that material on one side of the galactic nucleus approached our galaxy while material on the other side receded. They found that the rotation velocities v_{rot} of visible matter around their galactic center were way too large to be caused by the visible amount of matter only. Footing on Newtonian mechanics, one would expect a mass dependence of v_{rot} according to

$$v_{\text{rot}}(r) = \sqrt{\frac{G_{\text{Newton}}M(r)}{r}} \tag{3.6}$$

with the mass up to radius r given by

$$M(r) = 4\pi \int_0^r \mathrm{d}R R^2 \rho(R). \tag{3.7}$$

In Eq. (3.7), $M(r)$ is determined by the mass density $\rho(r)$, which is assumed to be radially symmetric. Hence, v_{rot} should decrease if one goes to the far exterior of the visible disk where $M(r)$ is expected to raise more slowly than r. However, via measuring the redshift of stars and H1-gas clouds via spectral spectroscopy and the measurement of the 21-cm line, investigations led to the insight that this is actually not the case for many galaxies. Examples of measured rotation curves are now given in Fig. 3.1. There, the dependence of v_{rot} on the distance r to the galactic center is shown for many different galaxies.The possible solutions to this dissent between theory and experiment are mainly two-fold. On the one hand, there is the so-called theory of modified Newtonian dynamics [23], where a change of the $1/\sqrt{r}$-dependence in Eq. (3.6) is assumed for large r such that $v_{\text{rot}}(r)$ tends toward a constant value. On the other hand, there is the idea of an additional mass component which changes $M(r)$ in such a way that its profile is able to account for the measured $v_{\text{rot}}(r)$. Following Eq. (3.6) and Eq. (3.7), it turns out that a $M(r) \propto r$ for radii way larger than the visible disk is needed. This new mass component should therefore be located in an approximately spherical halo around the galaxy (see the plot on the left hand side of Fig. 3.1) and, due to its non-observance, should be non-luminous. Hence,

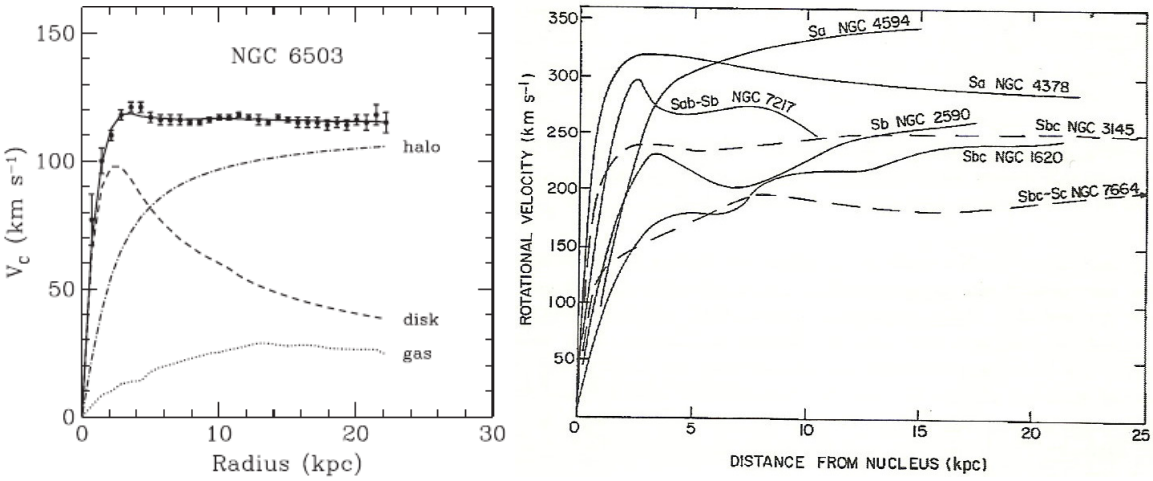

Figure 3.1.: On the left, the rotation curve of the spiral galaxy NGC 6503 is shown. Contributions of different mass components in dependence of the distance R to the galactic center are given. A hypothetical DM halo, necessary to account for the observed velocities, is added. On the right hand side rotation curves for further spiral galaxies are shown. Graphics taken from [24] and [25].

its interaction with photons have to be at least highly suppressed. These rotation curves are of course only measured for visible objects such that it is yet unknown how far the dark matter halo outreaches the disc of visible matter[2]. Furthermore, a similar behavior has been measured for the rotation of galaxies and gas clouds around other galaxies. The results suggest that for most of the cases at least 90% of the matter of their centers of rotation should be compounded out of DM.

3.1.3. The Bullet Cluster

There is further evidence for DM on the scale of galaxy clusters. Its origin is the observation of the bullet cluster by the Chandra telescope, which has already been claimed as the first direct observation of dark matter [26].
The bullet cluster 1E0657-558 consists of the two merging galaxy clusters. Due to collisions, their matter distributions were brought out of dynamic equilibrium. This allows for new insights into their mass compositions contrary to, e.g., the already relaxed spiral galaxies, which are the typical targets to measurements of rotation curves. In 2006, the Chandra telescope was able to observe the bullet cluster as shown in Fig. 3.2. The X-ray emissions of the hot gas and the intergalactic plasma are given in red and blue which are typically the largest components of the visible mass. The green contours show the gravitational potential in the bullet cluster obtained via weak gravitational lensing. The main outcome of the investigations on the bullet cluster is a clear 8-σ spatial deviation between the gravitational centers and the centers of the baryonic components. Moreover, whereas the gas clouds show a typical shockfront, the gravitational centers seemed to have passed through each other without any collisions, leaving the gas clouds behind somehow. This observation finds a quite natural explanation in terms of DM whereas MOND theories struggle to give a coherent explanation.

[2]Here the test objects are gas clouds which typically outreach the stellar disc.

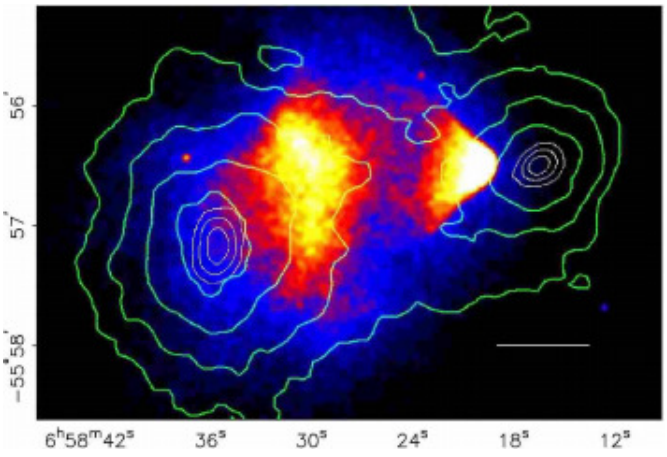

Figure 3.2.: The merging cluster 1E0657-558 as seen from the Chandra telescope. The green contours represent the mass distributions as reconstructed from weak gravitational lensing. The blue regions represent the intergalactic plasma clouds as obtained from X-ray emission. The red to white shaded regions show the shock cones of the colliding hot gas clouds. Image taken from [26].

3.1.4. N-Body Simulations

By means of today's computing power, it is possible to study the formation of cosmic structures via N-body simulation with quite high resolution.
Starting from seed inhomogenities, the evolution of structures through time are then most commonly approximated via non-linear gravitational clustering from the dark matter particles with specific initial conditions and further refined via the inclusion of astrophysical processes such as gas dynamics, chemistry etc. [24].
Within these simulations, the inclusion of a sizable *cold DM* (CDM) component was found to yield good agreements between the simulated and the actually observed structures in the universe. Here, CDM refers to matter, e.g., neutralinos or axions, which was non-relativistic at the beginning of structure formation in the universe. This happened roughly at redshift $z \sim 10^6$ ($t \sim 1yr$), when mass of the order of DM halos of galaxies such as our Milky Way ($\sim 10^{12} M_\odot$) has been encompassed by the cosmic event horizon. Due to the slow motion of CDM their *free streaming length*, i.e., the distance, which a particle can in average cover until it is gravitationally trapped, tends to be rather low. CDM could thus have been quickly captured within gravitational wells. Hence, CDM yields an hierarchical clustering, which starts at small scales and grows larger and larger [28]. Moreover, N-body simulations yielded a universal CDM halo density profile of the form

$$\rho(r) = \frac{\rho_0}{(r/R)^\gamma (1 + (r/R)^\alpha)^{\frac{\beta-\gamma}{\alpha}}}, \tag{3.8}$$

which supports the halo shape as predicted by the measurement of rotation curves (see Ch. 3.1.2) [3]. However, the cuspy behavior in the innermost region $r \to 0$ of Eq. (3.8) is still under debate as it turned out to be in tension with observations. But in this region, the impact of baryons, which contribute with increasing importance to the overall matter distribution for $r \to 0$, is not yet well understood such that the precise theoretical description of the innermost region is still speculative.

[3] One example is the famous Nawarro-Frenkel-White profile $\alpha = 1$, $\beta = 3$, $\gamma = 1$, $R = 20$ kpc [27].

Note that in the context of N-body simulations with a sizable CDM component, further tension arose with observations due to the non-observance of small scale structures like dwarf galaxies and subhalos as predicted by the hierarchical clustering favored by CDM models [29,30]. Their predicted number exceeds the number of observed satellite galaxies, e.g., of the Milky Way, which has become famous as the "missing satellites problem" of CDM [31]. The non-observance of predicted small scale structures raised interest in other DM species, mainly in *hot* (HDM) and *warm DM* (WDM) models, whose distinct behaviors at the beginning of structure formation have been expected to soften the satellite problem. HDM is typically composed of very light particles, for example neutrinos with masses up to a few electron volts, which move with highly relativistic velocities and hence possess a large free streaming length. HDM therefore smeared out the initial density perturbations eliminating fluctuations on scales below a characteristic wave number. This cutoff on the matter power spectrum yields an inverted hierarchy of clustering, which starts with high scales structures. This can be a supercluster with a mass $m_{\text{super}} \gtrsim 10^{15} M_{\odot}$, which subsequently fragmented into the observed small scale structures such as galaxies etc.. However, simulations yielded a collapse of superclusters at a redshift $z < 2$. This is in contradiction to experiments, in which the observation of superclusters or stellar populations indicate galaxy-formations way earlier,i.e., before $z \simeq 3$ [28]. WDM, particles with masses typically in the keV range such as a sterile neutrino [32] or axino [33], is yet another type of DM which raises large interest. WDM has been brought up as a model which may maintain the strengths of HDM and CDM and at the same time avoids their shortcomings. WDM is heavier than HDM and has not been highly relativistic at the beginning of structure formation. Therefore, the WDM free streaming length turns out to be smaller than the one of HDM, leading to first mass fluctuations in the range of $\gtrsim 10^{11} M_{\odot}$, which could have formed earlier than the superclusters encountered in HDM models. These structures may have subsequently fragmented into the smaller structures observed today, while suppressing the overproduction of small scale structures on the Megaparsec (Mpc) scale and below. Furthermore, structure formation driven by WDM results in DM halos with a shallower inner profile, avoiding the problem of a too cuspy CDM profile in the inner most halo region as stated above. On the other hand, WDM models permit the production of small DM halos at large redshift. It is expected that the first stellar populations were formed inside such small halos which led to the uniform production of metal in the early universe as indicated by observations of the Lyman α forest[4] [28]. Furthermore, doubts have recently been raised if WDM with masses constraint by studies of the Lyman α forest [34] is really capable to alleviate the problem of the CDM small scale structures [35]. Finally, the Sloan Digital Sky Survey has reported the discovery of many additional ultra faint dwarf galaxies, which may help to alleviate the missing satellite problem, lending credence to the hypothesis that many of these missing satellites may have remained undiscovered as they have formed little to no stars [23, 36]. Hence, the investigations of structure formation through N-body simulations revealed important insights into the nature of DM and motivated the distinction between cold, warm and hot DM[5]. Though, a conclusive answer about the true nature of DM has yet not been given.

[4] The Lyman α forest is a collection of sharp absorption lines in the spectra of quasars, which were caused by the light passing through intergalactic clouds of hydrogen.

[5] DM can of course also be a mixture of different components.

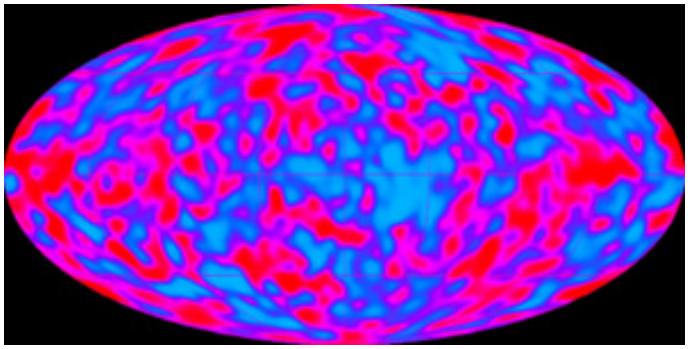

Figure 3.3.: CMB anisotropies as seen by the COBE satellite. Figure taken from [39].

3.1.5. The Cosmic Microwave Background

From the list of hints toward the existence of DM, the cosmic microwave background (CMB) is quite exceptional as it allows to give a very precise estimation of the DM density in today's universe. Originated during the time of recombination at a redshift of $z \approx 1100$ ($t \sim 3.7 \times 10^5$yrs after the big bang), when the universe has cooled down far enough to allow an efficient formation of neutral atoms without subsequent ionization, the CMB photons traveled mainly unaffected from the surface of last scattering all the way to us. Thus, through intrinsic temperature fluctuations in combination with gravitational redshifts (non-integrated Sachs-Wolfe effect) [37], the CMB represents an exceptional imprint of seed inhomogenities of the very early universe, allowing for a view far back in time.
Though already predicted by Georg Gamow and Robert Dicke in 1946, the first observation of the CMB actually happened accidentally, when Arno Penzias and Robert W. Wilson noticed an unexpected background noise, while experimenting with a Holmdel Horn Antenna at the Bell Labs back in 1964. In 1978, the Nobel Prize for Physics was awarded to Penzias and Wilson for their joint discovery. In 1992, the COBE satellite confirmed the existence of the CMB [38]. The collaboration measured a nearly perfect black body spectrum, implying that the universe was in thermal equilibrium during the time of last scattering, with a temperature $T \approx 2.725$ K isotropic down to a scale of 10^{-5} ($\simeq 30\mu$K). These very small temperature fluctuations ΔT shown in Fig. 3.3, the so-called CMB anisotropies, which have been measured for the first time by the COBE experiment, have been extensively studied since then as they turned out to provide very rich cosmological information. The COBE results have been refined by the WMAP and most recently by the Planck experiment, which yielded the measurements of the CMB anisotropies shown in Fig. 3.4. Furthermore, the exceptional isotropy of the CMB spectrum well beyond the cosmological horizon, i.e., over regions in the sky which could not have been in causal contact during the time of decoupling, has raised the so-called horizon problem. This leads to the assumption of a time of exponential growth of the universe, the so-called inflationary epoch [40], most presumably between $10^{-35} - 10^{-11}$ seconds after the Big Bang, where initial inhomogenities have been smeared out, leaving us with this extremely isotropic universe which we observe in the CMB[6]. Moreover, the CMB-photons can suffer from several effects on their way from the surface of last scattering to us. One important effect is the integrated Sachs-Wolfe effect, which describes the change of the

[6]Inflation also helps to solve the flatness problem, the question, why the universe seems to be so close to being perfectly flat.

spectrum of CMB photons on their way to us caused by the transition of time dependent potential wells. These can change the energy of CMB photons, e.g., when the energy gained by falling into the potential is not completely compensated on the way out of the potential due to a flattened potential caused by the spatial expansion of the universe. To correctly recover the original CMB spectrum at the time of decoupling, one has to account for these modifications. More details on this can be found in Ref. [41].
Starting with [43, 44]

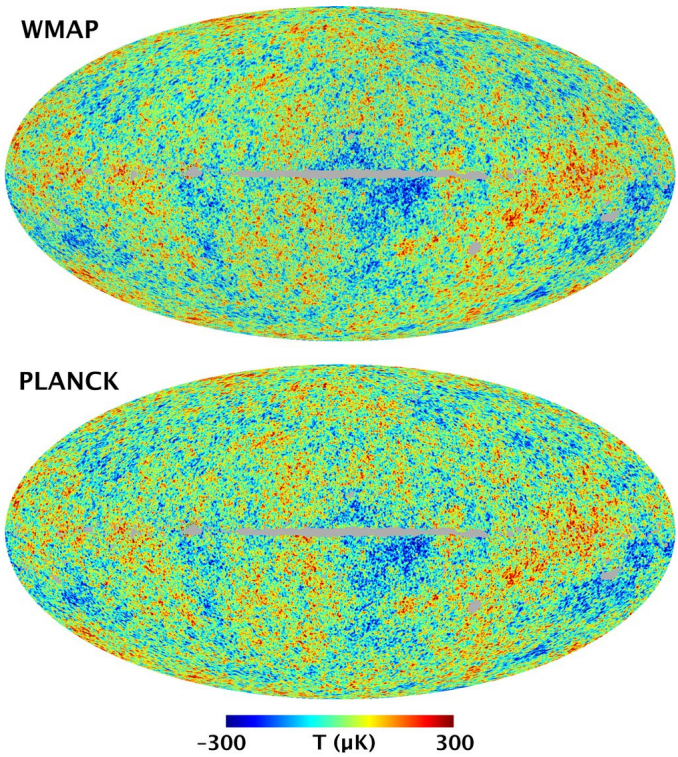

Figure 3.4.: CMB anisotropies as seen by WMAP (upper) and Planck (lower) figure. Figure taken from [42].

$$\Theta(\hat{n}) = \frac{\Delta T}{T} \tag{3.9}$$

for some direction $\hat{n}$, one can expand $\Theta(\hat{n})$ in the orthonormal basis of spherical harmonics

$$\Theta(\hat{n}) = \sum_{l=2}^{\infty} \sum_{m=-l}^{l} a_{lm} Y_{lm}(\hat{n}). \tag{3.10}$$

Projecting the coefficients of this expansion onto a certain Y_{lm}, the so-called multipole moments a_{lm} are obtained via

$$a_{lm} = \int \mathrm{d}\hat{n} Y^*_{lm}(\hat{n}) \Theta(\hat{n}). \tag{3.11}$$

Averaging over the different angular orientations of the fluctuation modes $m = \{-l, -l+1, ..., l\}$, one finally ends up with the variance of the a_{lm}

$$C_l = \sum_{m=-l}^{l} \frac{1}{2l+1} a^*_{lm} a_{lm}, \tag{3.12}$$

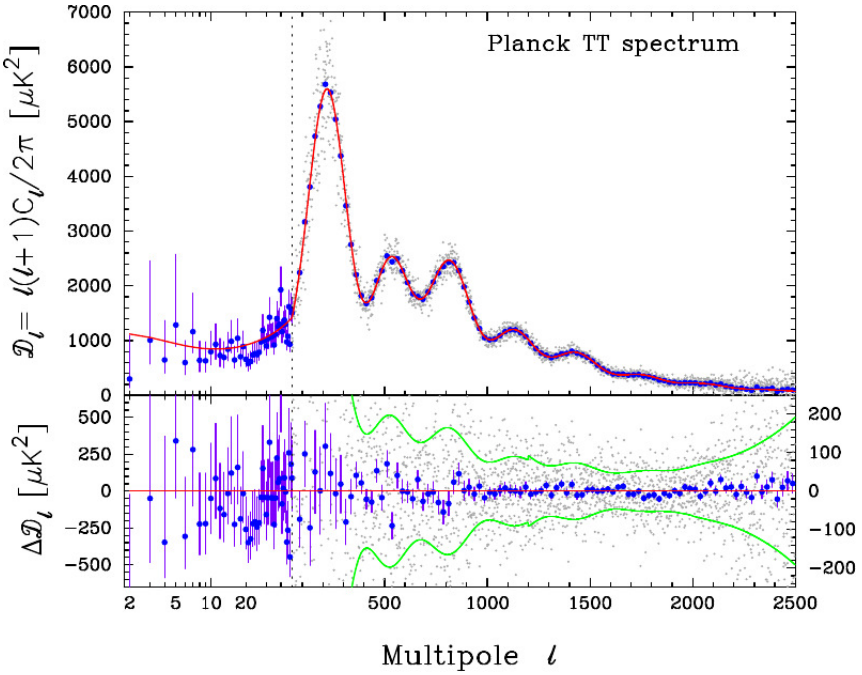

Figure 3.5.: The upper panel shows the power spectrum of the CMB temperature anisotropies as seen by the Planck-satellite, together with the best fit of ΛCDM cosmology, shown in red. The lower plot shows the residuals of the power spectrum together with the best ΛCDM fit. Figure taken from [45].

which is usually plotted as $l(l+1)C_l/2\pi$ against the corresponding l (see Fig. 3.5). The multipole moment l corresponds to the characteristic angular size of the temperature fluctuation following roughly $\Theta \approx \frac{60}{l}$ (Θ in degrees). The power spectrum can then be interpreted in certain cosmological models, whose parameters are fixed via fitting theory to the data. Finally note that there is a limit on the precision of the C_l, the so-called cosmic variance[7]

$$\Delta C_l = \sqrt{\frac{2}{2l+1}}\, C_l. \tag{3.13}$$

This is due to the fact that we are bound to only $(2l+1)$ "probes" to detect a particular multipole l. For example, the cosmic variance on the monopole moment is basically undetermined as we have only one CMB which we can measure. A fit of a certain cosmological model, the *ΛCDM*, to the CMB anisotropies is presented in Fig. 3.5 in red. The theoretical error including the cosmic variance is given by the error bars in the lower panel of Fig. 3.5 that show the residuals of the power spectrum. The name ΛCDM refers to a 6-parameter model dominated by components of dark energy (Λ), whose origin is even less understood than DM, and cold dark matter [45]. The different parameters of ΛCDM are introduced in greater detail in Ch. 3.5. As apparent from Fig. 3.5, the ΛCDM turns out to be very successful in reproducing the observed power spectrum of the CMB. As stated above, one is able to deduce the total relic density of CDM in the universe from this, which is usually given in terms of the critical density ρ_c[8] times the reduced Hubble constant h squared. The most recent measurements of the CMB carried out by the Planck collaboration [45]

[7] There are of course further sources of uncertainties which enter the C_l such as instrumental noise, finite beam resolution, subtraction of foreground sources such as the Milky Way etc..

[8] ρ_c corresponds to the mass density of a flat universe.

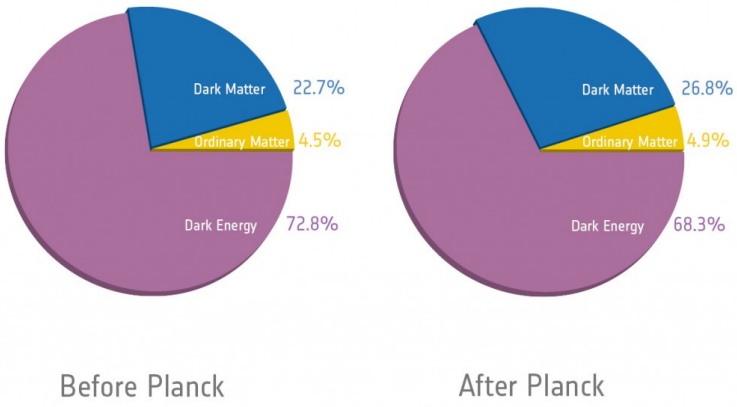

Figure 3.6.: These diagrams present the decomposition to the energy content of our universe as estimated from a best fit of ΛCDM to the CMB-anisotropies before (left) and after (right) the Planck experiment. Figure taken from [46].

in combination with WMAP data have led to a precise determination of the dark matter relic density

$$\Omega_{\text{CDM}} h^2 = 0.1199 \pm 0.0027, \tag{3.14}$$

with h in units of 100 km s^{-1} Mpc^{-1}, given at the 1σ confidence level.
Another interesting result is the amount of baryonic matter, which can also be deduced from Fig. 3.5. As a best fit to the Planck measurements, one obtains the value

$$\Omega_{\text{b}} h^2 = 0.02207 \pm 0.00033. \tag{3.15}$$

Hence, only around one sixth of the total amount of matter in the universe turns out to be baryonic. The full energy composition of the universe is concisely shown in Fig. 3.6. It is apparent that dark energy is actually the dominant energy component in the universe. Hence, the CMB provides us with rich information about fundamental cosmological parameters and can be used for their determination with exceptionally high precision.

This list of evidence for the existence of DM is actually far from being complete. E.g., we did not mention the results of gravitational lensing at galaxy cluster, another way to estimate the total amount of mass independent from the actual amount of luminous mass [47]. However, the above list already presents evidence for DM stemming from a large variety of experiments which follow very different ideas. Hence, it seems fair to say that DM is a very good guess to solve the different discrepancies between experiment and theory.
As a final remark, note that in 2014 the BICEP2 collaboration announced the discovery of imprints of primordial gravitational waves in the B-mode polarization (the curl component in CMB polarizations) pattern of CMB anisotropies, which are a generic prediction of inflationary models [48]. However, in a joint analysis of the BICEP2 and the Planck collaboration, it turned out that the analysis was incorrect as the foreground effect of interstellar dust-polarization has not been taken into account properly, such that the supposed discovery had to be withdrawn [49].

3.2. Requirements and Candidates for Dark Matter

In the last chapters we have encountered many hints for the existence of a sizable DM component in the universe, ranging from cosmological scales, e.g. the formation of large scale structures in N-body simulations over galaxy cluster as the bullet or Coma cluster down to the scale of galaxies via the analyses of rotation curves. From this perspective, the introduction of new models that provide a viable DM candidate became a field of central interest. But as there is no direct evidence for DM so far, this prompted the proliferation of many ideas about its nature. However, based on the insights on the nature of DM from the previous chapter, one can draw a number of requirements from observations that need to be fulfilled by a potential DM candidate in order to pertain as viable. These is stated in the following.

- **The candidate should be dark**:
  As already apparent from its name, dark matter has to be non-luminous in order to be in accordance with the current non-observance, e.g., of the assumed DM halo around our galaxies, whose existence and rough form are suggested by the measurements of rotation curves (Sec. 3.1.2) and by N-body simulations (Sec. 3.1.4). Therefore, the DM coupling to photons has to be at least highly suppressed, taking place, e.g., through higher orders in perturbation theory (as it is the case for the neutralino). Moreover, null results in searches for exotic isotopes, i.e., boundstates of DM with ordinary nuclei, suggest that DM is not only electrically neutral but also transforms as a singlet under the $\mathrm{SU}(3)_{\mathrm{C}}$ [51, 52].

- **The candidate should be stable on cosmological time scales**:
  Since experiments suggest that DM is all around us even today, the formation of long-lived structures such as galactic halos suggest that a viable DM candidate has to be stable on cosmological time scales. Hence, the lifetime of the DM particle should be of the same size as (or larger than) the lifetime of the universe $\tau \gtrsim 4.3 \times 10^{17}$ as provided by the Hubble Space Telescope Key Project [50]. This long lifetime is typically achieved via the introduction of a symmetry that prevents the particle from decaying. From this perspective, one of the most prominent examples is the lightest neutralino in SUSY models with R-parity conservation.

- **The candidate should be non-baryonic**:
  This is suggested by the fitting of the ΛCDM model to the CMB. As already discussed in Sec. 3.1.5, this led to a very low fraction of baryons compared to the total amount of matter in the universe (see Fig. 3.6). Hence, DM can not be solely baryonic to be in no tension with the CMB. This excludes the so-called MACHOS, Massive Astrophysical Compact Halo Objects, such as planets or brown dwarfs, which are purely baryonic[9] as viable DM candidates. Though, they would have been a first good guess as they would not make it necessary to introduce some entirely new physics.

- **The candidate should be cold**:
  The arguments which speak in favor of cold DM in contrast to hot and warm dark matter, a distinction that was discussed in the context of N-body simulations, have been given in Sec. 3.1.4. Although we found that this question still waits for its

[9] Furthermore, searches for MACHOs via weak gravitational lensing toward the galactic center yielded a too low density for MACHOs to account for the DM.

final clarification, the CMB as fitted by ΛCDM favors the existence of a sizable cold DM component in the universe (see Eq. 3.14), too. Hence, we expect a viable DM candidate to be cold. This excludes the SM-neutrinos as the dominant component of DM which subsume under the HDM[10].

These are only a few of the requirements a viable DM candidate has to meet to be in accordance with the current theoretical and experimental knowledge. However, already at this stage, we see ourselves forced to consider extensions of the SM in order to find an appropriate DM candidate. Now, the authors of Ref. [53] refined the catalogue of requirements of a viable DM candidate, proposing a catalogue of ten questions, which a potential DM candidate has to affirm to be in accordance with the up to date experimental and theoretical wisdom. Assuming that the candidate accounts for the whole DM, these questions can be phrased as follows:

1. *Does it match the appropriate relic density?*
2. *Is it cold?*
3. *Is it neutral?*
4. *Is it consistent with Big Bang Nucleosynthesis (BBN)?*
5. *Does it leave stellar evolution unchanged?*
6. *Is it compatible with constraints on selfinteractions?*
7. *Is it consistent with DM searches?*
8. *Is it compatible with gamma ray constraints?*
9. *Is it consistent with other astrophysical bounds?*
10. *Can it be probed experimentally?*

For more details see Ref. [53]. The authors checked some of the most prominent DM candidates against this catalogue of questions. Their result is comprehensively shown in Fig. 3.7. It turns out that many different models provide a good DM candidate yielding a rich zoo of potential candidates. A good overview over these different types of DM can be found in Ref. [54]. As it can be seen in the table of Fig. 3.7, the neutralino turns out to be in agreement with all of the theoretical as well as the experimental requirements, phrased by the ten-point catalogue written above. The neutralino, as introduced in Ch. 2.6.2, is a weakly interacting particle with a typical mass of $\mathcal{O}(100\text{ GeV})$. It therefore subsumes under the category of WIMPs, a category, which is one of the best studied ones in the context of particle DM. Maybe one of the most driving motivations in favor of WIMP-DM is the so-called *WIMP miracle*. The relic density Ω_{WIMP} of WIMP-DM can for many WIMP-models be approximated as

$$\Omega_{\text{WIMP}} h^2 \approx \frac{3 \times 10^{-27} \text{cm}^3 \text{s}^{-1}}{\langle \sigma_{\text{eff}} v \rangle}. \tag{3.16}$$

[10] Furthermore, the SM-neutrinos can not be abundant enough to account for the (whole) DM in the universe, since $\Omega_\nu = \sum_{i=1}^{3} \frac{m_i}{93\text{ eV}} \rightarrow \Omega_\nu h^2 \lesssim 0.07$ for neutrino masses $m_i < 2.05$ ($i \in \{1,2,3\}$) eV as suggested by experiments [24].

DM candidate	**I.** Ωh^2	**II.** Cold	**III.** Neutral	**IV.** BBN	**V.** Stars	**VI.** Self	**VII.** Direct	**VIII.** γ-rays	**IX.** Astro	**X.** Probed	**Result**
SM Neutrinos	×	×	✓	✓	✓	✓	✓	–	–	✓	×
Sterile Neutrinos	∼	∼	✓	✓	✓	✓	✓	✓	✓!	✓	∼
Neutralino	✓	✓	✓	✓	✓	✓	✓!	✓!	✓!	✓	✓
Gravitino	✓	✓	✓	∼	✓	✓	✓	✓	✓	✓	∼
Gravitino (broken R-parity)	✓	✓	✓	✓	✓	✓	✓	✓	✓	✓	✓
Sneutrino $\tilde{\nu}_L$	∼	✓	✓	✓	✓	✓	×	✓!	✓!	✓	×
Sneutrino $\tilde{\nu}_R$	✓	✓	✓	✓	✓	✓	✓!	✓!	✓!	✓	✓
Axino	✓	✓	✓	✓	✓	✓	✓	✓	✓	✓	✓
SUSY Q-balls	✓	✓	✓	✓	∼	–	✓!	✓	✓	✓	∼
B^1 **UED**	✓	✓	✓	✓	✓	✓	✓!	✓!	✓!	✓	✓
First level graviton UED	✓	✓	✓	✓	✓	✓	✓	×	×	✓	×[a]
Axion	✓	✓	✓	✓	✓	✓	✓!	✓	✓	✓	✓
Heavy photon (Little Higgs)	✓	✓	✓	✓	✓	✓	✓	✓!	✓!	✓	✓
Inert Higgs model	✓	✓	✓	✓	✓	✓	✓	✓!	–	✓	✓
Champs	✓	✓	×	✓	×	–	–	–	–	✓	×
Wimpzillas	✓	✓	✓	✓	✓	✓	✓	✓	✓	∼	∼

Figure 3.7.: Check on the ten point test for selected DM candidates. A "✓" symbols that the requirement is satisfied by the DM candidate and a "×" is used when this is not the case. The "!" appears, when present or upcoming experiments are able to probe a significant portion of the candidate's parameter space. The "∼" is used if the requirement is not generically or only in tension with other observations fulfilled by the considered DM candidate. Since the requirements phrased by the ten point test are *necessary* conditions, which must be fulfilled in order for a particle type to be viable DM candidate, a single "×" is already sufficient to exclude a certain particle species. Table taken from [53].

Eq. (3.16) shows an inverse proportionality of Ω_{WIMP} to the thermally averaged annihilation cross section of the WIMPs into SM particles $\langle \sigma_{\mathrm{eff}} v \rangle$, meaning that efficient annihilation yields a low relic density, whereas a low annihilation cross section may lead to a potential overproduction of DM compared to the experimental bounds as stated in Eq. (3.14). For particles with only weak-scale interactions such as WIMPs, Ω_{WIMP} happens to be in the right ballpark quite naturally as favored by experiments. This is a circumstance that is often referred to as the *WIMP miracle* mentioned above.

This chapter has highlighted that DM is most presumably composed out of a new particle species, e.g., out of neutralinos. There are many experiments, completed or ongoing, which look for this new speculative particle and put additional very stringent constraints upon a viable DM candidate. These are shortly presented in the following sections.

3.3. DM Detection Experiments

Though there seem to be many hints toward the existence of DM as discussed in the previous section, DM still lacks any concrete evidence that does not base on gravitational interactions. Assuming the existence of a DM particle χ, Fig. 3.8 shows schematically

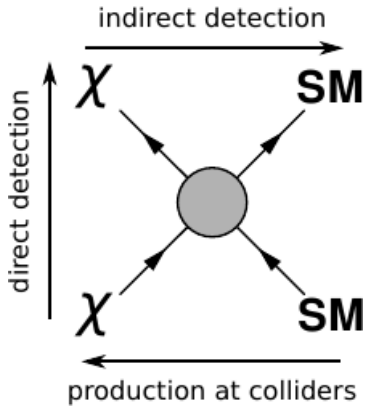

Figure 3.8.: Sketch of different detection modes connected to the interaction of DM particles χ with SM particles. Figure taken from [55].

the conceivable detection modes via DM interactions with SM particles. There are many different experiments planned, ongoing or already completed which rest upon the different search strategies of Fig. 3.8. These are typically divided into the three categories

- *direct detection*: χ SM $\rightarrow \chi$ SM,
- *indirect detection*: $\chi\chi \rightarrow$ SM SM,
- *production at colliders*: SM SM $\rightarrow \chi\chi$.

The actual type of detection, its realization in experiment as well as current results and future prospects are discussed in greater detail in the following subsections.

3.3.1. Direct Detection

If the DM halo of our milky way is composed of WIMPs, an expected WIMP flux of the order $10^5 \times \frac{100\,\mathrm{GeV}/c^2}{m_\chi} \mathrm{s}^{-1}\mathrm{cm}^{-2}$ should hit the earth [23]. Even for weakly interacting

particles this flux is sufficiently large such that a potentially detectable fraction of WIMPs should scatter elastically off terrestrial nuclei [56]. Hence, many different experiments aim at the measurement of these nuclear recoils caused by elastic WIMP scattering, where the scattering rate as well as the recoil energy (sometimes the direction of scattering) serve as the most important identification criteria. However, the radioactive background from the surrounding material, which is expected to be more than a million times larger then the WIMP-nucleus interaction rate, as well as the production of neutrons by incident cosmic muons, which could fake a dark matter signal [11], make this a very challenging task. Such experiments with all DM reactions taking place inside some terrestrial apparatus are called *direct-detection* experiments.
Following Fermi's golden rule, the differential WIMP-nucleus recoil spectrum at recoil energy Q can be written as [57, 58]

$$\frac{\mathrm{d}R}{\mathrm{d}Q} = \frac{\sigma_{0,WN}\rho_0}{\sqrt{\pi}v_0 m_\chi \mu_r^2} F^2(Q) T(Q), \tag{3.17}$$

where $\sigma_{0,WN}$ is the Q-independent WIMP-nucleon cross section for elastic scattering and $F(Q)$ is the nuclear form factor, which accounts for the structure effects of the nucleus. Furthermore, ρ_0 is the local WIMP density ($\rho_0 \approx 0.3\ \mathrm{GeV/cm^3 c^2}$), $T(Q)$ is a dimensionless integral over the local WIMP velocity distribution and $\mu_r = \frac{m_\chi m_N}{m_\chi + m_N}$ is the reduced mass of the WIMP-nucleus system. In experiments the recoil energy Q takes values between

$$Q_{\min} = Q_{\mathrm{thresh}}, \quad Q_{\max} = \frac{2m_N}{(1+\frac{m_N}{m_\chi})^2} v_{\mathrm{esc}}^2. \tag{3.18}$$

In Eq. (3.18), v_{esc} is the escape velocity $v_{\mathrm{esc}} \approx 544$ km/s (≈ 0.002 c), the velocity, above which WIMPs are no longer trapped within the gravitational potential of our galaxy. For typical WIMP and nucleus masses ($m_\chi, m_N \approx \mathcal{O}(100\,\mathrm{GeV}/c^2)$), this corresponds to a maximal energy $Q_{\max} \approx \mathcal{O}(100\,\mathrm{keV})$, which sets the range of nuclear recoil energies relevant for direct-detection experiments. Direct-detection experiments further possess a threshold energy Q_{thresh}, which corresponds to the lowest amount of energy that has to be deposited within the detector during a single WIMP-event to yield a signal. In current experiments, Q_{thresh} reaches down to typically $\approx$5 keV. Eq. (3.18) shows that, due to the decrease of $Q_{\max}$ with decreasing m_χ, direct-detection measurements turn out to be insensitive to the WIMP-nucleus scattering if the WIMP-mass m_χ drops below a certain value.
Since WIMPs are expected to move non-relativistically in the earth's rest frame, it seems reasonable to decompose $\sigma_{0,WN}$ into a spin-independent and a spin-dependent part [59]

$$\sigma_{0,WN} = \frac{4\mu_r^2}{\pi}[Z f_p + (A-Z) f_n]^2 + \frac{32 G_F^2 \mu_r^2}{\pi} \frac{J+1}{J} (a_p \langle S_p \rangle + a_n \langle S_n \rangle)^2. \tag{3.19}$$

Here, f_p and f_n (a_p and a_n) stand for the effective spin-independent (spin-dependent) couplings for WIMP-proton and WIMP-neutron interactions, respectively, Z is the atomic number, N is the number of neutrons inside the nucleus and $A = Z + N$ is the mass number. J corresponds to the total spin of the nucleus and $\langle S_{p,n} \rangle = \langle N | S_{p,n} | N \rangle$ is the spin expectation value of the proton or neutron within the nucleus ($\langle S_{p,n} \rangle = 0.5$ for a free proton or neutron).

[11] To be well shielded from cosmic rays, direct-detection experiments are typically installed deep under ground.

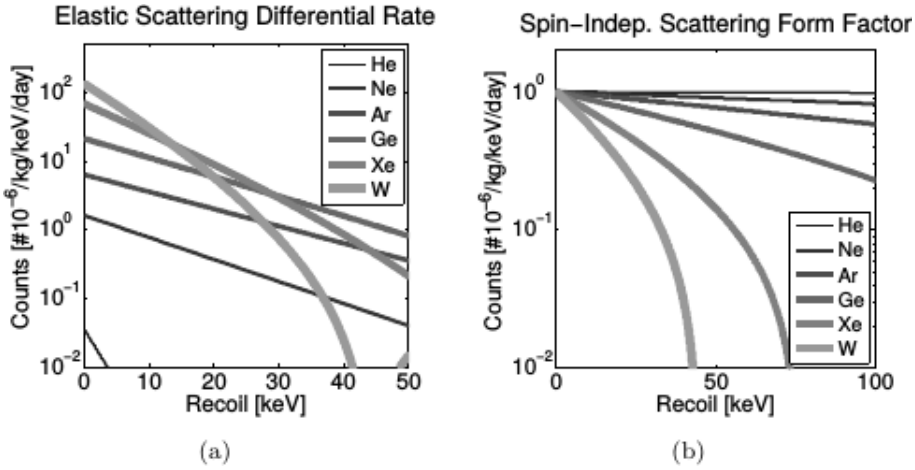

Figure 3.9.: Elastic scattering differential rate and spin-independent scattering form factor plotted against the transferred energy for various nuclei [57].

Since for many WIMP models there is no difference between f_p and f_n, the spin-independent part of Eq. 3.19 can be approximated as

$$\sigma_{0,WN,SI} \approx \frac{4\mu_r^2}{\pi} f_n^2 A^2. \tag{3.20}$$

Eq. (3.20) now reveals a dependence $\sigma_{0,WN,SI} \propto \mu_r^2 A^2$, which indicates the advantage of using rather heavy nuclei to measure the spin-independent WIMP recoil spectrum. On the other hand, in both spin-independent as well as spin-dependent WIMP-nucleus scattering, coherence on a nucleus as a whole gets lost when the de Broglie wave length $\lambda = \hbar/\mathbf{q}$ of the incoming WIMP with momentum $\mathbf{q}$ drops below the radius of the nucleus. This leads to a lowering of the form factor $F(Q)$ of Eq. (3.17) at high Q, which can be translated into an upper bound on the recoil energy

$$Q_{\text{coh}} < \frac{2 \times 10^4}{A^{\frac{5}{3}}} \text{ keV} \tag{3.21}$$

below which coherent scattering takes place. Hence, for high recoil energies, there is only a modest gain in sensitivity for spin-independent scattering if one goes to higher mass numbers A. This is presented in greater detail for the spin-independent case in Fig. 3.9 for a WIMP with mass $m_\chi = 100$ GeV/c^2 and $\sigma_{0,WN} = 10^{-45}$ cm^2. It is apparent that the use of heavy nuclei such as Xenon or Wolfram leads to a sensitivity that is enhanced at low recoil energy but turns out to be diminished for larger values of Q due to a decreasing form factor $F(Q)$. Whereas the spin-independent interactions depend on the total number of nucleons within the nucleus, the spin-dependent part is mainly sensitive to the total angular momentum J of the nucleus, resulting in a pre-factor $(J+1)/J$ (see Eq. (3.19)). One further distinguishes between the spin-dependent scattering off neutrons and protons. The total event rate can finally be calculated as the integral over the differential event rate Eq. (3.17), starting from $Q_{\min}$ up to $Q_{\max}$.

In direct-detection experiments, the main search strategies rest upon the techniques of *ionization*, *scintillation* and the detection of *phonons* [58, 60]. This is comprisingly shown in Fig. 3.10 together with the used detection material, energy sensitivity and efficiency for various direct-detection experiments. Current experiments often combine different detection techniques to be sensitive to a wide range of recoil energies on the one hand and to

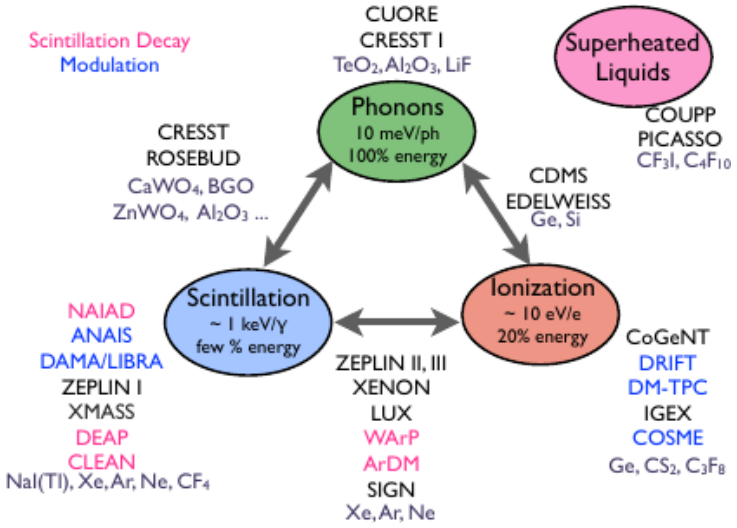

Figure 3.10.: Forms of energy dissipation from particle recoil for various direct-detection experiments [57].

be able to better discriminate between background (electron recoils on orbital electrons, caused by, e.g., γ and β backgrounds, which results in sparse ionization density and high ionization efficiency) and signal (WIMP recoil on nuclei, results in high ionization density and low ionization efficiency) on the other hand. A calibration plot of the Cryogenic Dark Matter Search (CDMS) [61] for discrimination between nucleus and electron recoil via the measurement of both phonon and ionization energy for every single event, is shown in Fig. 3.11. Here, the electron events (blue), where nearly all energy of an event given by the associated phonon energy is transferred into ionization energy, are shown in combination with the energy dissipation of nuclear recoils (green), where the ionization efficiency turns out to be rather low.

Current results on the spin-dependent cross sections are shown in Fig. 3.12. The tightest constraints on spin-dependent WIMP scattering off neutrons are set by the XENON100 experiment [62], which uses the Xenon isotopes ^{129}Xe and ^{131}Xe. These isotopes possess an even number of protons but an odd number of neutrons in order that the latter combine to a larger net-spin leading to a high sensitivity for the spin-dependent neutron-WIMP coupling [58]. This can be seen in Fig. 3.12, where the tightest constraints on spin-dependent WIMP scattering off protons are actually due to the SIMPLE II [63] and the COUPP [64] experiment whose DM detection does not rely on the use of Xenon. The SIMPLE II experiment further released new results in 2014, which are given in Ref. [65]. These new bounds are still not competitive against XENON100 for spin-dependent WIMP scattering off neutrons but show a slight decrease in their upper bound shown in Fig. 3.12 for the case of protons roughly by a factor of 3/4.

The most stringent results on spin-independent WIMP-nucleon elastic scattering for WIMP masses $m_\chi > 6$ GeV are provided by the Large Underground Xenon experiment (LUX) located in the Stanford Underground Research Facility Lead in South Dakota [66]. It uses liquified Xenon as detection material which features a high sensitivity at the recoil energies of interest besides a very high self shielding against external electromagnetic backgrounds due to a large atomic number and a high density. The experiment takes further advantage of the excellent scintillator and ionizer properties of liquid Xenon to discriminate between nuclear and electron recoils. Moreover, Xenon possesses no long-lived isotopes whose de-

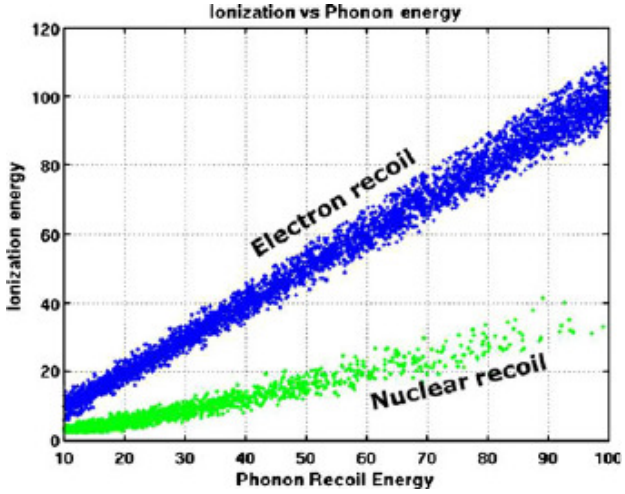

Figure 3.11.: Calibration plot for photon (blue dots) and neutron (green dots) sources showing the high ionization efficiency of electron recoils vs the low ionization efficiency of nuclear recoils [60].

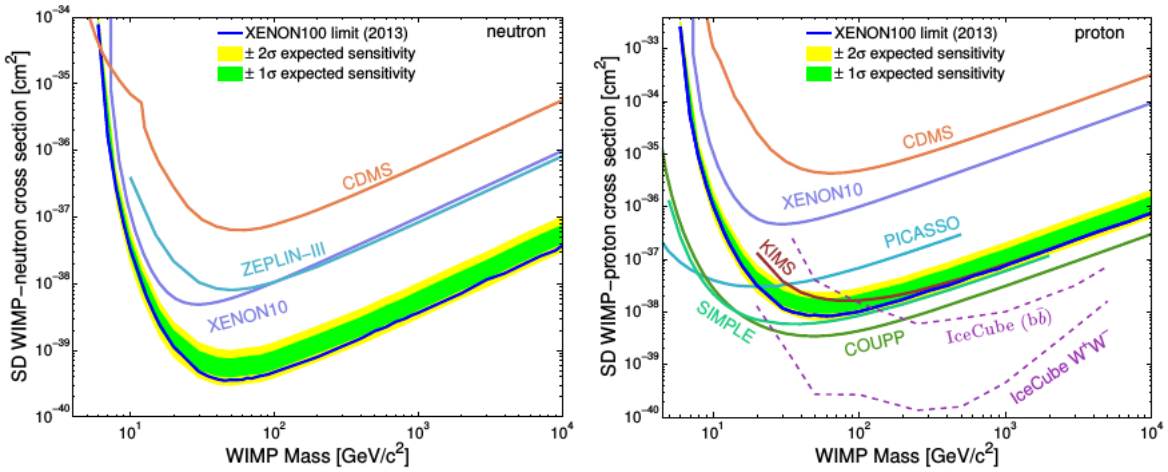

Figure 3.12.: Upper limits on spin-dependent WIMP scattering off neutrons (left) and off protons (right) at 90% C.L. taken from [62].

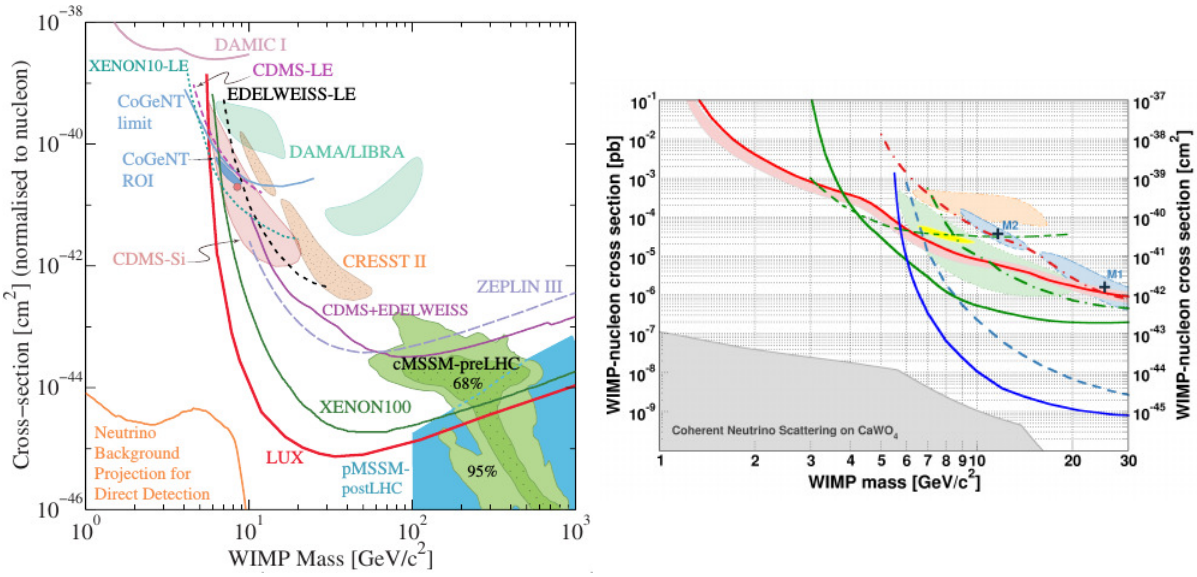

Figure 3.13.: The left and right plot show upper bounds on the spin-independent WIMP-nucleon cross section. The left plot, taken from [68], includes the latest LUX result at 90% confidence level (blue line) in comparison with further experiments named within the plot. It further shows favored regions of certain supersymmetric models (green and blue regions) as well as preferred regions from annual modulation experiments also named within the plot. The right plot, taken from [69], shows CoGeNT (99% C.L.-region, yellow), DAMA (3σ C.L.-region, light orange), CRESST (2σ C.L-region, light blue) and CDMS-Si (90% C.L.-region, light green) favored regions from annual modulation measurements together with upper bounds on the spin-independent cross section stemming from CRESST-II (solid red and red shaded), SuperCDMS (solid green), CDMSlite (dashed green), EDELWEISS (dashed-dotted green), XENON100 (dashed blue) and LUX (solid blue).

cays would increase the background. Finally, Xenon features a good scalability toward larger masses (currently $< 800\$/\text{kg}$).

LUX firstly took WIMP search datasets during the period of April to August 2013. The results from 85.3 live-days for the upper bound on the spin-independent WIMP-nucleon cross section σ_{SI} at a 90% confidence level are shown in blue in the left plot of Fig. 3.13. There, the recent LUX result is compared with other experiments such as, e.g., the XENON100 result [67] after 225 live days in red, showing the improvement of the exclusion limits, e.g., in the minimum around $m_\chi = 55\ \text{GeV}/c^2$ from $\sigma_{\text{SI}} \approx 2 \cdot 10^{-45}\ \text{cm}^2$ (Xenon100) down to $\sigma_{\text{SI}} \approx 8 \cdot 10^{-46}\ \text{cm}^2$ (LUX). With this reach in sensitivity, direct-detection experiments are already able to probe (and exclude) certain interesting SUSY models as shown in Fig. 3.13.

Moreover, CRESST-II started a run in 2013 probing the low mass region of WIMPs below $m_\chi \approx 3\ \text{GeV}/c^2$, which has not been tested before in direct-detection experiments [69]. This comparatively high sensitivity to the low-mass region can be ascribed to the specific detection material used by the CRESST-II experiment, $CaWO_4$, which contains the heavy Wolfram nuclei besides the relatively light nuclei Calcium and Oxygen. The new upper limits on the spin-independent WIMP-nucleon scattering are shown in red in the plot on the right side of Fig. 3.13. The kink in the red solid line is the point where WIMP scat-

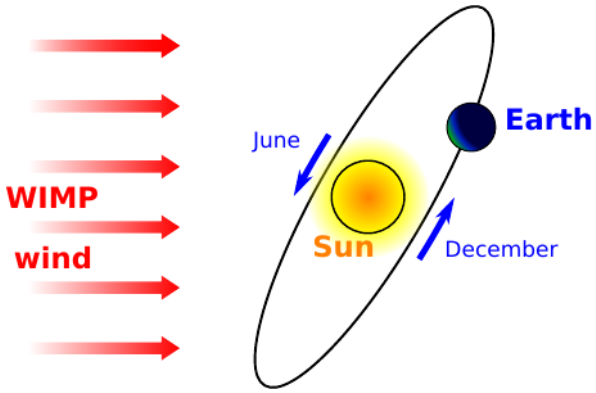

Figure 3.14.: Simplified view on the source of the WIMP winds annual modulation on earth [71].

tering off Oxygen and Calcium takes over, whereas for larger masses $\sigma_{0,WN}$ is dominated by WIMPs scattering off Wolfram.
There are further direct-detection experiments that try to detect the WIMP wind on earth through its annual modulation [71]. This WIMP wind, which is caused by the movement of our solar system around the center of the milky way leading through the essentially non-rotating DM halo, is expected to be modulated by the earth orbital motion around the sun. This modulation depends on whether the direction of rotation of the earth around the sun points toward the direction or opposite of the direction of the WIMP wind (see Fig. 3.14). The solar system moves at a speed of roughly $v_0 \approx 220\frac{\text{km}}{s}$ around the center of our galaxy, which is expected to correspond to the mean value of the WIMP velocity on earth. Since potential backgrounds should lack any form of similar modulations, these annual modulations are expected to facilitate the signal-to-background discrimination.
Since several years, the DAMA/NaI (DAMA/Libra) experiment claims the observation of annual modulations at now more than 9 σ confidence level, favoring a $\sim$10 GeV/c^2 or $\sim$80 GeV/c^2 WIMP [72]. Whereas the high mass window opened by DAMA has already been excluded by the non-observance of modulation by subsequent experiments in both spin-dependent as well as spin-independent measurements, the CoGENT experiment reported a 2.8σ evidence for annual modulation [73] in the favored low mass region. A third experiment, CRESST-II, also reported 67 events [74] in the region of potential low mass nucleus-WIMP recoils. A likelihood analysis revealed with high statistical significance that these events are not explainable by usual background sources alone. However, these results have been corrected by the latest CRESST-II run excluding parts of the previously favored low mass region (see Fig. 3.13). To sum up, all three experiments seem to favor the low mass region $m_\chi \sim 10$ GeV/c^2 with $\sigma_{0,WN} = 10^{-41} - 10^{-40}$ cm^2 although their consistency is still under debate.
Reporting null results in this preferred region until 2012 [75], CDMS II updated their analysis of data acquired during their final four runs from July 2007 to September 2008 in October 2013, revealing three WIMP-candidate events with a highest likelihood at mass $m_\chi = 8.6$ GeV/c^2 and $\sigma_{0,WN} = 1.9 \times 10^{-41}$ cm^2, potentially consistent with CO-GENT data [76]. To clarify the annual modulation results, a complementary experiment to DAMA/LIBRA and DAMA/NaI, the DM-Ice17 experiment, has been built from 2010 to 2011 deep in the south pole glacial ice. First results of a two year run from July 2011 to June 2013 were published in 2014, but no WIMP signal has been observed so far [77]. Finally, all regions favored by annual-modulation experiments have already been fully ex-

cluded by, e.g., XENON10, XENON100 and the LUX experiment as shown in Fig. 3.13. In the future, LUX plans to perform a second run with 300 live-days in 2014/15. These new datasets are expected to improve their sensitivity on the spin-independent cross section of Fig. 3.13 by another factor of 5. Additional direct-detection experiments are still ongoing or planned such as Xenon1T [79], DarkSideG2 [80] and LZ (a merger between the LUX and the ZEPLIN experiment [81]). These experiments are expected to gain a sensitivity of $\sigma_{\mathrm{SI}} \approx 10^{-47}$cm and better, in order that even coherent scattering of astrophysical neutrinos on nuclei is expected to become a non-negligible source of background.

To summarize, there is currently much tension between different direct-detection experiments, which still waits for clarification. However, potential loopholes are, for example, a more involved structure of the DM halo, which enters Eq. (3.17) or a more complicated WIMP coupling to nucleons, which may differentiate between neutrons and protons (see Eq. (3.20)) [59, 78].

3.3.2. Indirect Detection

Indirect-detection experiments search for secondary particles such as γ-rays, neutrinos, positrons, antideuterons or charged leptons, emanating from the annihilation of DM particles at a distant location [82, 83]. Typical targets of such observations are the center of the earth or the sun and the galactic center, where an enhancement of the DM density due to gravitational accumulation is expected. Further subjects to many investigations are galaxy clusters and supernova remnants such as the Crab nebula in 6300 ly distance. But since the annihilation rate depends quadratically on the DM density, the robustness of obtained constraints or signals from certain objects hinges sensitively on the knowledge of the associated DM density. Hence, also the halo of our galaxy as well as nearby dwarf galaxies, where the density profiles are presumably better understood than, e.g., at the core of our galaxy (see Ch. 3.1.4), are subject to indirect-detection experiments[12].
To identify a DM signal, it is important to possess a distinct knowledge of potential background sources as well as of potential signal distortions that the DM signal may encounter during the propagation from its origin to the earth. In this perspective, γ-rays as well as neutrinos are considered good signals since they only suffer from absorption and, in the case of neutrinos, from flavor oscillation, whereas charged cosmic rays are further sensitive to magnetic turbulences which they may pass on their way to us. Therefore, their spectral shape is much more likely to be deformed during their travel and reconstruction of the original signal turns out to be far from trivial. From the observation of the annihilation products one can draw conclusions about the properties of DM particles. In this regard, spectral features within the energy spectra of the observed particles, in the best case unique energy lines, turn out to be of main use.
Starting with **γ-ray searches**, these can be produced via DM annihilation into quark-anti-quark pairs and gauge bosons followed by subsequent hadronization and pion decay yielding a continuous spectrum. Furthermore, γ-rays can also be produced directly, eventually revealing spectral features, which are difficult to attribute to astrophysical processes. These are signals such as a monochromatic γ-ray line, a smoking gun signal in terms of DM-indirect detection, or sharply peaked lines from photons radiated off virtual particles,

[12] Hierarchical clustering, growing from small to large structures as favored by CDM models, led to a much richer substructure of the DM halo in many N-body simulations. This substructure is, however, expected to be coverable by just an enhancement or boost factor applied to the whole primary spectrum.

the so-called internal bremsstrahlung [84][13]. A key experiment, which has measured the sky's γ-ray spectrum from below $\sim$ 20 MeV to more than 300 GeV, is the Fermi Large Area Telescope (Fermi LAT) launched in 2008 by the NASA [85]. The datasets collected are publicly available on their homepage. Moreover, energies above 100 GeV are better probed by Imaging Air Cherenkov Telescopes (IACT), such as HESS [86], Magic [87] and VERITAS [88].
In 2012, evidence for a spectral line at 130 GeV stemming from the region close to the galactic center was reported in Ref. [89,90] based on the first 43 month Fermi LAT dataset. This line feature was confirmed in Fermi LAT observations of nearby galaxy clusters, even revealing a double line feature at 110 GeV and 130 GeV [91]. Using an Einasto or NFW DM density profile (see Sec. 3.1.4), the 130 GeV line can be interpreted as a photon signal of WIMP-DM annihilation with a WIMP mass $m_\chi = 129.8 \pm 2.4^{+7}_{-13}$ GeV and an annihilation cross section into photons of $\sigma v|_{\chi\chi\to\gamma\gamma} = (1.27 \pm 0.32^{+0.18}_{-0.28}) \times 10^{-27}$ cm$^3 s^{-1}$ at 3.2 σ significance. Another possibility is the interpretation of the 130 GeV γ-line as caused by internal bremsstrahlung. Interpreted within a model specified in Ref. [90], this would suggest a WIMP-DM mass $m_\chi = 149 \pm 4^{+8}_{-15}$ GeV with a cross section including photon bremsstrahlung $\sigma v|_{\chi\chi\to f\bar{f}\gamma} = (6.2 \pm 1.5^{+0.19}_{-1.4}) \times 10^{-27}$ cm$^3 s^{-1}$ at 3.1 σ significance. However, an improved analysis of the Fermi LAT data presented in Ref. [92] decreased the significance of this line feature and, while rejecting that the line could be caused by known systematic effects alone, raised doubts in its interpretation as a DM signal. Clarification of this situation is expected by the ongoing or upcoming HESS-II experiment, Cherenkov Telescope array (CTA) and GAMMA-400 which are expected to allow for a final conclusion within the next years [94].
The discovery of a peak in the Fermi LAT γ-ray spectrum between 1-3 GeV from the inner volume of the galactic center has also raised further attention. It can be well fitted by, e.g., leptophilic DM (here, dominantly annihilating into $\tau\bar{\tau}$-pairs) of mass between $m_\chi = 7 - 10$ GeV [95] and $\langle\sigma v\rangle = 4.6 \cdot 10^{-27} - 5.3 \cdot 10^{-26}$ cm^{3}s^{-1} as well as by DM particles with mass $m_\chi = 49^{+0.13}_{-0.10}$ GeV and $\langle\sigma v\rangle = 1.76^{+0.28}_{-0.27} \cdot 10^{-26}$ cm^{3}s^{-1} annihilating into $b\bar{b}$-pairs [96]. However, due to large uncertainties in the interpretation of Fermi LAT data for the inner most region of our galaxy, the ascription of this excess to DM annihilation is still under debate [97, 98].

Neutrino searches are performed by neutrino telescopes such as IceCube [99], situated at the south-pole, ANTARES [100], located in the Mediterranean sea close to France, or Super-Kamiokande in Japan [101], which target basically the same objects as γ-ray searches. However, one of the most interesting objects in terms of neutrino signal searches is the sun, where gravitational capturing followed by subsequent annihilation of the DM particles such as WIMPs is expected to appear. Since neutrinos can pass dense masses quite unhinderedly, the WIMP induced neutrino flux from the sun is expected to be measurable on earth. Due to the hydrogen dominance of the sun, which possesses a low mass number, neutrino searches for solar neutrinos turn out to be very sensitive to the spin-dependent WIMP-nucleon cross section (see Eq. (3.19)). Hence, the currently world-leading constraints on the spin-dependent WIMP-proton cross section are set by the IceCube experiment, which turn out to be even better than the best constraints from direct-detection experiments such as COUPP (see right plot of Fig. 3.12). However, in contrast to γ-ray searches, no potential hint for DM annihilation has been found in neu-

[13] The latter can even dominate the total photon spectrum in the case of annihilation of Majorana-fermions (e.g. neutralinos), since radiation of an additional vector boson can lift the helicity suppression of the typically important s-wave amplitude for annihilation into fermions.

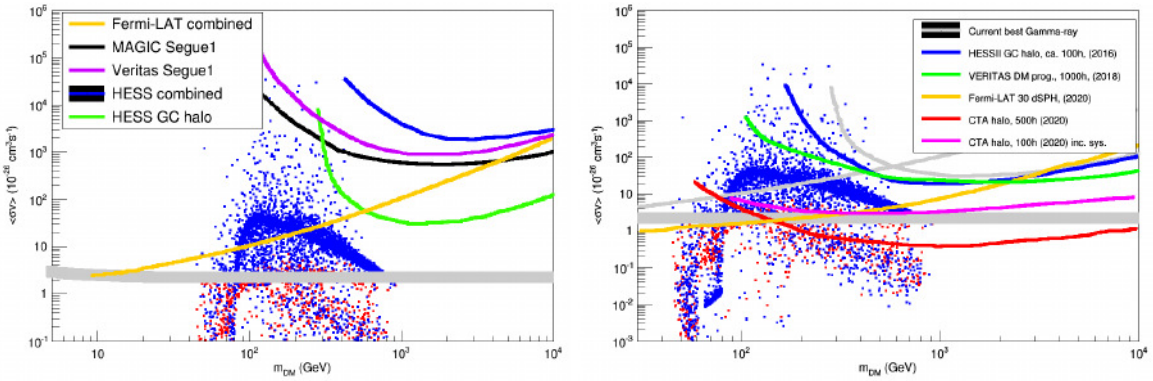

Figure 3.15.: The left plot shows current γ-ray bounds for DM annihilation via b-quark channels against the DM mass for several experiments. The right plot shows expected limits of existing and upcoming experiments, already starting to probe cosmologically favored regions of the MSSM-7 (specified in [93]) parameter space: red points consistent with DM relic density, blue points have lower relic density. Plots taken from [82].

trino spectra so far. The present status of limits on annihilation cross sections together with constraints from γ-ray searches are comprehensively shown in Fig. 3.16.

In **charged cosmic ray searches** experiments mainly concentrate on signals in antimatter spectra such as antiprotons or positrons. Since these turn out to be only a very rare component of the cosmic radiation background, even a small rise caused by DM annihilation is expected to result in a detectable signal. The antimatter-spectra are conveniently presented as positron to electron or antiproton to proton ratio to cancel acceptance systematics from which particles as well as antiparticles should both suffer equally.
An anomaly connected to a potential DM signal in the energy spectrum of cosmic positrons has been reported by the PAMELA experiment [102] in 2008, which measured a deviation in the positron spectrum from predictions of standard secondary particle production models[14] for energies above 10 GeV. The observed deviation has been confirmed by the AMS experiment in 2013, which has been installed in 2011 on the International Space Station (ISS) [103]. AMS also encountered an unexpected rise of the positron fraction with energies starting at $\sim$ 10 Gev up to $\sim$ 200 GeV (see plot on the left of Fig. 3.17), suggesting modifications in acceleration and propagation models for cosmic rays or the existence of a primary source of high energy positrons. Described in terms of DM, the datasets may be interpreted in favor of DM with a mass $m_\chi \sim 1$ TeV and a somehow enhanced annihilation cross section (e.g. via Sommerfeld enhancement, see Ch. 5.3 below) $\langle \sigma v \rangle \sim 10^{-24}$ cm^{3}s^{-1} to be in accordance with PAMELA measurements [82, 104]. On the other hand, these DM models are already subject to significant constraints due to γ-ray or antiproton results, where in the latter case no clear evidence for a deviation from background expectations has been found so far (see right plot of Fig. 3.17) [105]. In addition, there are also well motivated conventional sources, e.g., pulsars (rapidly spinning neutron stars) or super nova remnants (SNR), which may give rise to the observed positron flux such that an ascription of the observed excess to DM annihilation alone is in fact quite speculative [106].

[14] Secondary particles are particles typically produced in collisions of cosmic ray protons with interstellar matter.

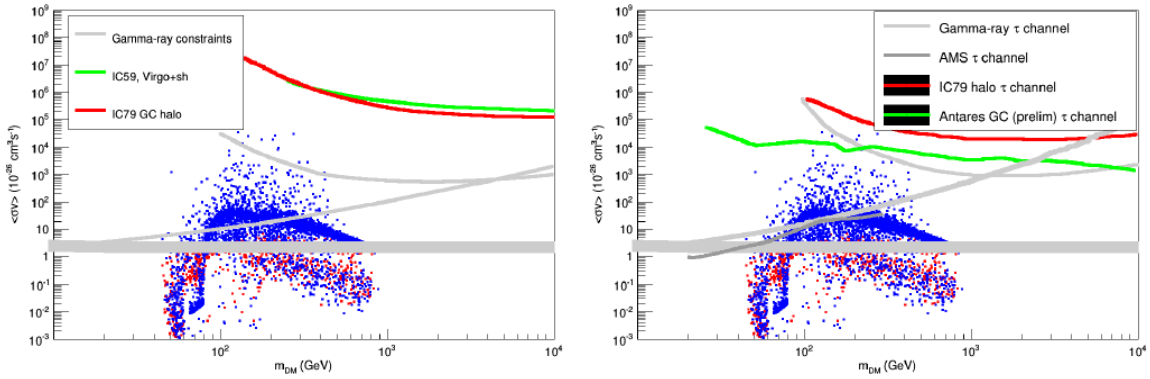

Figure 3.16.: Both plots show current bounds from neutrino telescopes on the DM annihilation cross section for several experiments. The plot on the left shows IceCube59 and IceCube79 results for different targets. The plot on the right contains current limits from ANTARES, IceCube79, and AMS. For comparison, bounds from γ-ray searches are shown in gray. Plots are taken from [82].

Future experiments also concentrate on the detection of antideuteron, since in this case DM signals are expected to exceed the background even by orders of magnitude. Current measurements of the antideuteron flux are performed by the AMS experiment though main improvements in this direction are expected from the upcoming General AntiParticle Spectrometer (GAPS) [107].

To conclude, there are several hints in the energy spectra of cosmic rays which may be interpreted as due to DM annihilation. However, large uncertainties arise in the estimation of, e.g., the background, particle propagation or the theoretical modeling of the DM density, which complicate any final conclusion. Hence, the situation still waits for its clarification.

3.3.3. Production at Colliders

DM searches at colliders provide a third way of DM experiments discussed here. Since DM, which is detectable in direct-detection experiments, couples to nucleons, it should in principle be possible to produce this kind of DM also at, e.g., proton-(anti)proton colliders such as the TEVATRON [108] or the LHC [109]. It turns out that the main advantage of DM production at colliders is the independence from astrophysical uncertainties as well as the sensitivity to very low DM masses which complements direct and indirect DM searches. To keep things as model independent as possible, one usually makes use of the framework of effective field theories [110], the low energy limit of a more comprehensive theory valid up to higher energies, where the low energy limit can be obtained from the corresponding high energy theory by integrating out the heavy degrees of freedom. The latter typically appear in DM models to connect the DM sector to the SM and are often expected to be too heavy to be produced directly at the provided energies (for example at the LHC $M_* \gtrsim$ a few TeV). After integrating over these heavy degrees of freedom, one is left with a set of higher dimensional operators, so-called effective or contact operators, which describe the coupling of the DM sector to the SM sector without the heavy mediators but suppressed by their characteristic mass scale M_*. Turning this approach around, via writing down all relevant effective operators up to a certain power in $1/M_*$ the resulting set of higher dimensional operators can be fitted to the experimental results, which can provide addi-

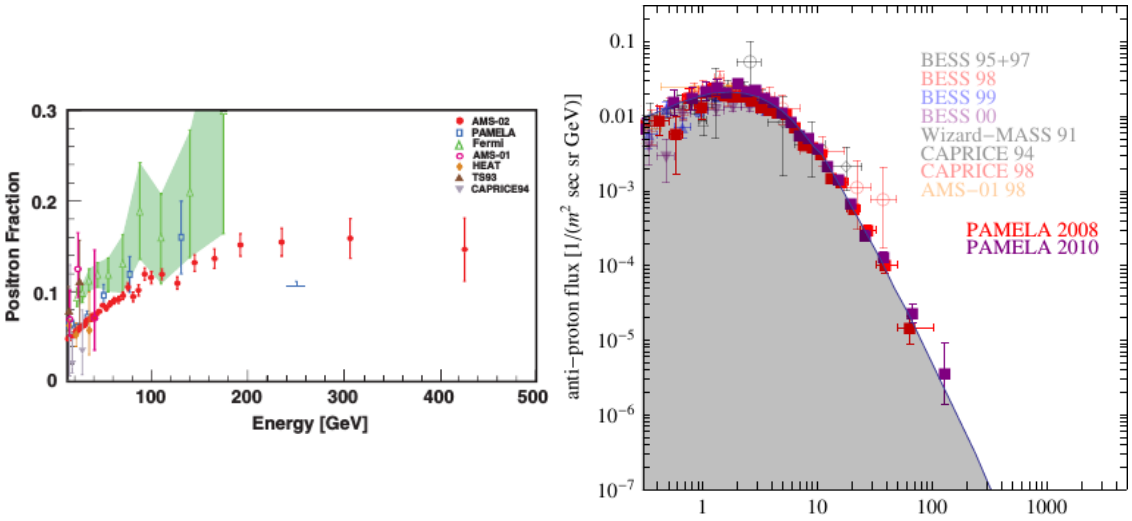

Figure 3.17.: The plot on the left shows the positron fraction $e^+/(e^+ + e^-)$ as a compilation of FERMI, PAMELA and recent AMS-02 data [103]. The plot on the right shows the antiproton flux as a compilation of older and more recent data from experiments named within in the plot. The astrophysical background is depicted in gray [83].

tional information about the nature of the DM particle. As known from direct-detection experiments, spin-dependent and spin-independent scattering cross sections off nucleons are common quantities to characterize the DM particle. Since some of the contact operators contribute to these cross sections, one can finally estimate associated limits of the DM-nucleon cross section *drawing a connection between results from direct, indirect and collider searches.*

For DM production in proton-antiproton (Tevatron) or proton-proton (LHC) collisions the initial state consists of (anti)quarks and gluons only. A collection of corresponding contact vertices for different kinds of dark matter (fermionic, real scalar and complex scalar) together with the associated suppression of these higher dimensional operators by the heavy mass M_* is given in Fig. 3.18. For example, the DM-nucleon cross section for fermionic DM depends on the effective vertices D1, D5 and D11 (D stands for Dirac fermion) as given in Fig. 3.18.

Especially at low DM masses, current colliders turn out to give the most stringent bounds on DM-nucleon scattering. On the other hand, since DM is expected to be stable on timescales such as the lifetime of the universe, DM is efficiently produced at colliders only in pairs such that their production rate drops very quickly with raising m_χ. Hence, collider experiments can complement direct and indirect DM searches, which are rather insensitive to the DM low mass region but give good results at higher masses (see Ch. 3.3.1).

Since DM has to be stable, it does not decay inside the detector and as it is further expected to be electrically neutral and colorless (e.g. WIMPs), it escapes the detection volume basically unhinderedly. Hence, the presence of DM particles in a single event is typically inferred from an imbalance in the total momentum in the plane transverse to the beam axis[15]. The magnitude of this imbalance is the so-called missing transverse energy

[15]The transversality to the beam axis is at least important for hadron colliders, where the longitudinal momenta of the colliding particles are basically unknown.

Name	Operator	Coefficient
D1	$\bar{\chi}\chi\bar{q}q$	m_q/M_*^3
D2	$\bar{\chi}\gamma^5\chi\bar{q}q$	im_q/M_*^3
D3	$\bar{\chi}\chi\bar{q}\gamma^5 q$	im_q/M_*^3
D4	$\bar{\chi}\gamma^5\chi\bar{q}\gamma^5 q$	m_q/M_*^3
D5	$\bar{\chi}\gamma^\mu\chi\bar{q}\gamma_\mu q$	$1/M_*^2$
D6	$\bar{\chi}\gamma^\mu\gamma^5\chi\bar{q}\gamma_\mu q$	$1/M_*^2$
D7	$\bar{\chi}\gamma^\mu\chi\bar{q}\gamma_\mu\gamma^5 q$	$1/M_*^2$
D8	$\bar{\chi}\gamma^\mu\gamma^5\chi\bar{q}\gamma_\mu\gamma^5 q$	$1/M_*^2$
D9	$\bar{\chi}\sigma^{\mu\nu}\chi\bar{q}\sigma_{\mu\nu}q$	$1/M_*^2$
D10	$\bar{\chi}\sigma_{\mu\nu}\gamma^5\chi\bar{q}\sigma_{\alpha\beta}q$	i/M_*^2
D11	$\bar{\chi}\chi G_{\mu\nu}G^{\mu\nu}$	$\alpha_s/4M_*^3$
D12	$\bar{\chi}\gamma^5\chi G_{\mu\nu}G^{\mu\nu}$	$i\alpha_s/4M_*^3$
D13	$\bar{\chi}\chi G_{\mu\nu}\tilde{G}^{\mu\nu}$	$i\alpha_s/4M_*^3$
D14	$\bar{\chi}\gamma^5\chi G_{\mu\nu}\tilde{G}^{\mu\nu}$	$\alpha_s/4M_*^3$

Name	Operator	Coefficient
C1	$\chi^\dagger\chi\bar{q}q$	m_q/M_*^2
C2	$\chi^\dagger\chi\bar{q}\gamma^5 q$	im_q/M_*^2
C3	$\chi^\dagger\partial_\mu\chi\bar{q}\gamma^\mu q$	$1/M_*^2$
C4	$\chi^\dagger\partial_\mu\chi\bar{q}\gamma^\mu\gamma^5 q$	$1/M_*^2$
C5	$\chi^\dagger\chi G_{\mu\nu}G^{\mu\nu}$	$\alpha_s/4M_*^2$
C6	$\chi^\dagger\chi G_{\mu\nu}\tilde{G}^{\mu\nu}$	$i\alpha_s/4M_*^2$
R1	$\chi^2\bar{q}q$	$m_q/2M_*^2$
R2	$\chi^2\bar{q}\gamma^5 q$	$im_q/2M_*^2$
R3	$\chi^2 G_{\mu\nu}G^{\mu\nu}$	$\alpha_s/8M_*^2$
R4	$\chi^2 G_{\mu\nu}\tilde{G}^{\mu\nu}$	$i\alpha_s/8M_*^2$

Figure 3.18.: Different effective couplings for DM-quark and DM-gluon contact interactions. D stands for fermionic (Dirac fermion), C for complex scalar and R for real scalar DM [111].

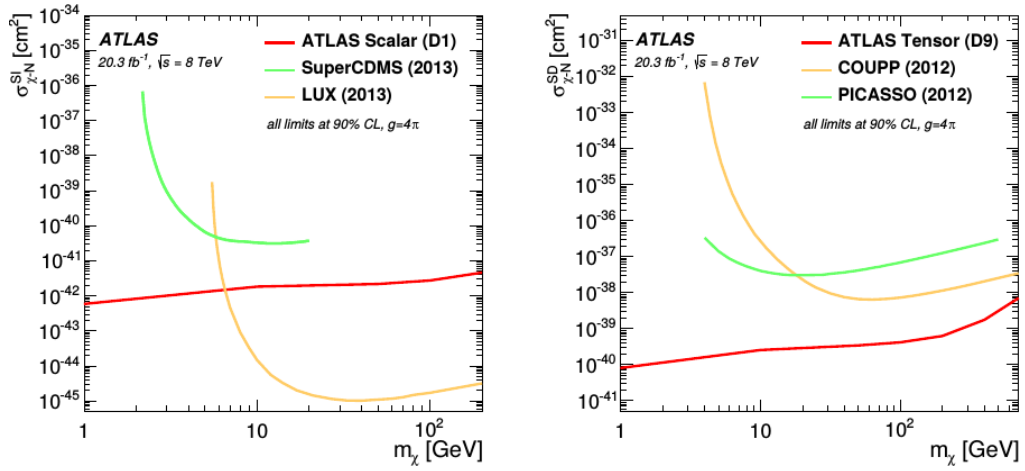

Figure 3.19.: ATLAS bounds on the spin-independent DM-nucleon cross section from the scalar operator D1 (plot on the left, red) and on the spin-dependent DM-nucleon cross section from the tensor operator D9 (plot on the right, red) at 90% C.F. as a function of the DM mass m_χ. In comparison, the currently best bounds from the direct detection experiments (named within the plot) are given in yellow and green [117].

E_T^{miss} (or missing transverse momentum p_T^{miss}).
Colliders, whose results we shortly address in the following, are the electron-positron colliders LEP (Large Electron Positron collider) [112] and the future ILC (Internation Linear collider) [113] as well as the TEVATRON and LHC with its two large general-purpose experiments ATLAS and CMS.
Results on DM production for LEP and TEVATRON datasets are presented in [114,115]. As LEP and TEVATRON provided cms energies of up to $\sqrt{s} = 209$ GeV and $\sqrt{s} = 1.96$ TeV, they were mainly able to constrain rather light DM models which fall within their kinematic reach ($m_\chi \lesssim 100$ GeV at LEP, $m_\chi \lesssim$ a few 100 GeV at TEVATRON) . The limits obtained turn out to be complementary to or competitive with direct and indirect searches. However, no excess over the SM background which could be assigned to the production of DM has been found in the data.
LHC searches mainly rely on events that are tagged by monojets or single photons from initial- or final-state radiation (ISR/FSR). These are needed to balance the total momentum of the DM particles such that they are not produced back-to-back, which would result in a negligible p_T^{miss} [116]. ATLAS results for searches on DM production in association with b-tagged jets for 20.3 fb^{-1} at $\sqrt{s} = 8$ TeV have currently been published in [117] (also see Ref. [118] for earlier results). The data are found to be consistent with SM expectations. Upper bounds of the spin-independent and spin-dependent DM-nucleon cross section from the scalar and tensor operators D1 and D9 (see Fig. 3.18) are shown in Fig. 3.19. One can see that the LHC has been able to improve on both spin-dependent as well as on spin-independent DM-nucleon cross section compared to the latest direct-detection results, especially imposing the upper bounds $\sigma_{\text{SI}} \approx 6 \cdot 10^{-42}$ cm^2 and $\sigma_{\text{SD}} \approx 8 \cdot 10^{-40}$ cm^2 on the D1 and D9 contact operators in the low masses region $m_\chi < 10$ GeV. A current CMS analysis for the $\sqrt{s} = 8$ TeV run at 19.7 fb^{-1} integrated luminosity also fitted the expected SM background. Upper bounds of spin-dependent and spin-independent cross sections are shown in Fig. 3.20 for the vector and axial vector operators D5 and D8, which couple DM to quarks, as well as for the scalar operator D11, which describes the coupling

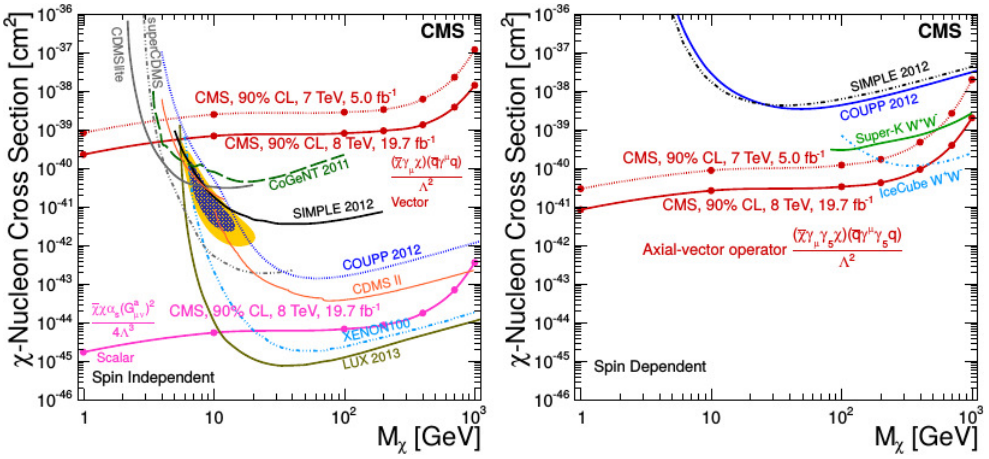

Figure 3.20.: CMS bounds on the spin-independent DM-nucleon cross section from vector coupling to quarks and scalar coupling to gluons D5 and D11 (left plot, red and purple) and on the spin-dependent DM-nucleon cross section from the axial vector operator D8 (right plot, red) at 90% C.F. as function of the DM mass m_χ ($\Lambda = M_*$). In comparison, the plots show the currently best bounds from direct and indirect-detection experiments (named within the plot) [119].

of DM to gluons. It is evident that, similar to the ATLAS results, these new constraints are competitive with current direct and indirect-detection bounds with sensitivities of $\sigma_{\mathrm{SI}} \approx 2 \cdot 10^{-45}$ cm^2 and $\sigma_{\mathrm{SD}} \approx 8 \cdot 10^{-41}$ cm^2 for the scalar DM-gluon and the axial vector DM-quark contact operators.

There are also theories, in which the mediators between the DM and the SM sector are light enough to be accessible at the provided energy in order that it would be a bad approximation to collaps the DM-SM mediation into contact interactions. In these cases, limits on the spin-dependent as well as on spin-independent DM-nucleon cross section set by mono-jet searches turn out to be weakened[16] and can become less constraining than limits from direct-detection experiments. This is shown in more detail in Fig. 3.21 for an analysis of TEVATRON datasets in terms of fermionic (Dirac) DM for vector and axial vector mediators.

Finally, there are also theories such as SUSY, in which the model is fully specified maybe up to some UV completion and in whose terms the DM candidate, e.g., the lightest neutralino, transforms non-trivially under the SM-gauge group. In these cases, a more detailed investigation of DM signatures is possible. Searches for SUSY at colliders typically look for events with large E_T^{miss}, accompanied by a high final-state multiplicity, which arises when the (heavy) SUSY particles produced turn into the LSP via cascade decays. A recent review on SUSY searches for the LHC run at $\sqrt{s} = 8$ TeV is given in Ref. [120]. However, no hint for the existence of SUSY has been found so far.

A future collider experiment is the International Linear Collider (ILC), an electron-positron collider such as LEP, which is designed to work at cms energies of $\sqrt{s} = 500$ GeV with a potential upgrade to $\sqrt{s} = 1$ TeV. Its discovery potential has been investigated in Ref. [121, 122]. Furthermore, lepton-antilepton colliders such as the ILC may be of special interest in terms of DM production, as the tension between DAMA as well as

[16] A slight enhancement is however possible when the mediator can be produced on shell (see Fig. 3.21 for $M = M_* = 100$ GeV and $m_\chi < 50$ GeV).

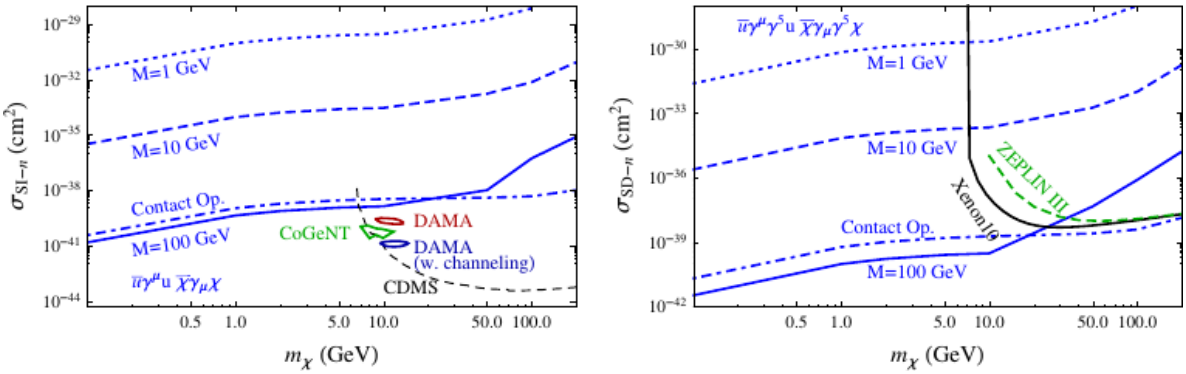

Figure 3.21.: TEVATRON bounds on the spin-independent (left) and spin-dependent (right) DM-neutron cross section for small mediator masses $M = M_*$ and fermionic (Dirac) DM [115].

CoGENT annual modulation data and bounds of WIMP-nucleon cross sections from, e.g., LUX, may be reconciled by the existence of leptophilic (i.e.., possessing tree-level couplings only to leptons) DM, which can only be produced through higher-order loops at hadron colliders. But these theories are under debate and partly disfavored by other analyses [123].

To summarize, there is no evidence for the production of DM particles at colliders so far. Stringent bounds on the spin-dependent and spin-independent DM-nucleon cross section, especially at low DM mass, have been obtained, which complement results from direct and indirect searches nicely. Further improvements in this direction are on their way such as the LHC upgrade to a cms energy of approximately $\sqrt{s} = 13$ TeV or the future ILC, which are expected to reveal more details about the nature of DM.

3.4. Standard Calculations in the Context of Neutralino Dark Matter

3.4.1. Prelude

In the following, we show how to calculate the relic density $\Omega_{\tilde{\chi}_1^0}$ of the neutralino LSP in case of a supersymmetric model with R-parity conservation. Therefore, we expect the space-time to be well described by the Friedmann-Robertson-Walker-metric (FRW-metric) $g_{\mu\nu}^{\mathrm{FRW}}$, an exact solution to the Einsteins field equation [3]

$$\mathcal{R}_{\mu\nu} - \frac{1}{2} g_{\mu\nu}\mathcal{R} = 8\pi G_{\mathrm{Newton}} T_{\mu\nu}. \tag{3.22}$$

Here, $\mathcal{R}_{\mu\nu}$, $\mathcal{R}$ and $T_{\mu\nu}$ are the Ricci-tensor, the curvature scalar and the energy momentum tensor. $g_{\mu\nu}^{\mathrm{FRW}}$ can be derived from the assumptions of isotropy and homogenity of our universe which base on the observed isotropy of the CMB as well as on the conjecture that our place in the universe is not somehow distinguished from others. Its concrete form can be inferred from the line element

$$\mathrm{d}s^2 = \mathrm{d}t^2 - R^2(t)\left[\frac{\mathrm{d}r^2}{1-\kappa r^2} + r^2 \mathrm{d}\Omega^2\right]. \tag{3.23}$$

In Eq. (3.23), $\kappa = -1, 0, +1$ corresponds to an open/flat/closed universe. $R(t)$ is the scale factor. It is related to the Hubble parameter H via $H = \dot{R}(t)/R(t)$, which quantifies the

expansion rate of the universe. Its today's value is measured to be

$$H_0 = \frac{100\text{km}}{\text{s}\cdot\text{Mpc}}\cdot h = 67.4 \pm 1.4 \frac{\text{km}}{\text{s}\cdot\text{Mpc}}. \tag{3.24}$$

Making use of the FRW-metric in Eq. (3.22), for the 00-component this leads to the equation

$$H^2 + \frac{\kappa^2}{R^2} = \frac{\rho}{3M_{\text{Pl}}^2}. \tag{3.25}$$

By further combining the 00-component of Eq. (3.22) with its ii-components ($i \in \{1,2,3\}$), one is left with

$$\dot{H} + H^2 = \frac{1}{6M_{\text{Pl}}^2}(\rho + 3p). \tag{3.26}$$

Eqs. (3.25) and (3.26) are the famous Friedman equations. They describe the expansion of the universe and its acceleration in dependence on the curvature κ and its total averaged energy content ρ and pressure p. Moreover, one can introduce the so-called critical density ρ_c, which follows from Eq. (3.25) in the case of vanishing curvature $\kappa = 0$. In the following, all energy densities of some component i are given in terms of this critical density via $\Omega_i = \rho_i/\rho_c$.

3.4.2. The Boltzmann Equation

In this section, we present the formalism used to calculate today's neutralino relic density $\Omega_{\tilde{\chi}_1^0}$. We further cover coannihilation effects such that all calculations directly include the presence of N species of unstable sparticles χ_i ($i \in \{1,...,N\}$) heavier than the neutralino-LSP $\tilde{\chi}_1^0 = \chi_0$. The time evolution of their number densities n_i is then well described by a system of coupled Boltzmann equations [124, 125]

$$\begin{aligned}\frac{\mathrm{d}n_i}{\mathrm{d}t} =& -3Hn_i - \sum_{j=0}^{N} \langle\sigma_{ij}v_{ij}\rangle \left(n_i n_j - n_i^{\text{eq}} n_j^{\text{eq}}\right) \\ &- \sum_{j\neq i}^{N} \Big[\left\langle\sigma'_{Xij}v_{ij}\right\rangle \left(n_i n_X - n_i^{\text{eq}} n_X^{\text{eq}}\right) - \left\langle\sigma'_{Xji}v_{ij}\right\rangle \left(n_j n_X - n_j^{\text{eq}} n_X^{\text{eq}}\right)\Big] \\ &- \sum_{j\neq i} \Big[\Gamma_{ij}(n_i - n_i^{\text{eq}}) - \Gamma_{ji}(n_j - n_j^{\text{eq}})\Big]\end{aligned} \tag{3.27}$$

with $i,j = 0,1,\ldots,N$. In Eq. (3.27), n_i^{eq} is the particle number density of the species χ_i in thermal equilibrium (chemical potential $\mu_\chi = 0$)

$$n_i^{\text{eq}}(T) = g_i \int \frac{\mathrm{d}^3\mathbf{p}_i}{(2\pi)^3} f_i^{\text{eq}}(\mathbf{p}_i, T). \tag{3.28}$$

For usual freeze-out temperatures $T \ll m_{\tilde{\chi}_1^0}$, the occurring equilibrium phase space density f_i^{eq} can be well approximated by a Maxwell-Botzmann-distribution

$$f_i^{\text{eq}} \approx e^{-E_i/T}. \tag{3.29}$$

Then, the n_i^{eq} take the form

$$n_i^{\text{eq}}(T) = g_i \int \frac{\mathrm{d}^3\mathbf{p}_i}{(2\pi)^3} f_i^{\text{eq}}(E_i, T) = \frac{g_i m_i^2 T}{2\pi^2} K_2\left(\frac{m_i}{T}\right). \tag{3.30}$$

In Eq. (3.30), g_i is the number of internal degrees of freedom of the particular species i and $K_i\left(\frac{m_i}{T}\right)$ is the modified Bessel of the second kind of order i, which in the non-relativistic limit $T \ll m_i$ $K_i\left(\frac{m_i}{T}\right)$ turns into the Boltzmann suppression factor

$$K_i(x) \sim \sqrt{\frac{\pi}{2x}} e^{-x} \text{ for } x \gg 1. \tag{3.31}$$

Finally, $\langle \sigma v_{ij} \rangle$ is the thermal average of the respective cross section σ times the relative velocity v_{ij}

$$v_{ij} = \frac{\sqrt{(p_i \cdot p_j)^2 - m_i m_j}}{E_i E_j}. \tag{3.32}$$

$\langle \sigma v_{ij} \rangle$ is discussed in greater detail in the subsequent section.
Now, the first term on the right-hand side of Eq. (3.27), proportional to the Hubble parameter H, stands for the dilution of the particle number density due to the expansion of the universe. The second term describes the creation and (co)annihilation of the species χ_i and χ_j via processes of the form

$$\chi_i \chi_j \longleftrightarrow X \Rightarrow \sigma_{ij} = \sum_X \sigma(\chi_i \chi_j \to X). \tag{3.33}$$

Finally, the third and fourth term of Eq. (3.27) account for the conversion of sparticles via scattering on the thermal background

$$\chi_{i,j} X \longleftrightarrow \chi_{j,i} X' \Rightarrow \sigma_{ij} = \sum_{X,X'} \sigma(\chi_{i,j} X \to \chi_{j,i} X') \tag{3.34}$$

as well as via decays of the form

$$\chi_{j,i} \longleftrightarrow \chi_{i,j} X \Rightarrow \sigma_{ij} = \sum_X \sigma(\chi_{i,j} \to \chi_{j,i} X) \tag{3.35}$$

addded up over all possible sets of SM particles X and X', which are allowed by R-parity. All other processes that cannot be resolved into the above processes turn out to be forbidden by the symmetry imposed.
At some point, all sparticles heavier than $\tilde{\chi}_1^0$ decay into the lightest neutralino. Hence, the quantity relevant for the estimation $\Omega_\chi h^2$ is the total number density of sparticles $n_\chi = \sum_{i=0}^{N} n_i$. Since only processes of the type Eq. (3.33) can change n_χ, the second and third line of Eq. (3.27) cancel in the sum. The time dependence of n_χ can then be brought to the concise form

$$\frac{\mathrm{d}n_\chi}{\mathrm{d}t} = -3Hn_\chi - \langle \sigma_{\text{eff}} v \rangle \left[n_\chi^2 - \left(n_\chi^{\text{eq}}\right)^2 \right] \tag{3.36}$$

with the thermally averaged effective cross section

$$\langle \sigma_{\text{eff}} v \rangle = \sum_{ij} \langle \sigma_{ij} v_{ij} \rangle \frac{n_i^{\text{eq}}}{n_\chi^{\text{eq}}} \frac{n_j^{\text{eq}}}{n_\chi^{\text{eq}}}. \tag{3.37}$$

For the case under consideration, the cross sections of Eqs. (3.33) - (3.35) are of similar size. Since processes of type Eq. (3.33) are Boltzmann suppressed relative to the processes in Eq. (3.34) and Eq. (3.35), the latter take place at a much higher rate keeping the ratios n_i/n_χ via decays or scattering on the thermal SM-background within thermal equilibrium. Hence, it seems valid to assume that $n_i/n_\chi \approx n_i^{\text{eq}}/n_\chi^{\text{eq}}$, which has been used in Eq. (3.36). Let us conclude this section with a short qualitative discussion of the solution of Eq. (3.36).

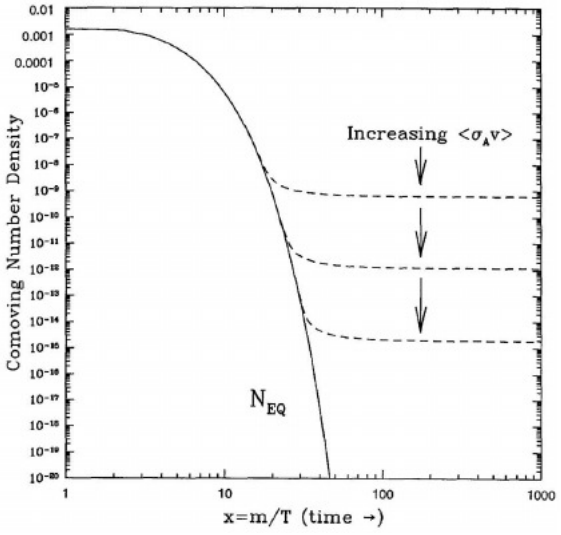

Figure 3.22.: The comoving number density in dependence of x. The comoving equilibrium number density is shown as solid line. Depending on the size of $\langle\sigma_{eff}v\rangle$ the freeze-out occur at different x_F. Then, the comoving number density remains constant following one of the dashed lines. Graphic originally published in Ref. [126].

The Boltzmann equation (3.36) now nicely resembles the Boltzmann equation in the case of a single sparticle species without any coannihilation. Dominated by the term $\propto \langle\sigma_{\text{eff}}v\rangle$ at high temperatures ($T \gg m_i$), the sparticles species χ_i stay in thermal equilibrium with their environment comprised of SM particles and other sparticles. As the temperature T decreases further and further ($T \lesssim m_i$), the production of the χ_i's becomes kinematically more and more suppressed, basically following $n_{\chi_i} \propto e^{-m_i/T}$, since only SM particles in the tail of the Boltzmann distribution have enough kinetic energy to produce the heavy sparticles. At some point, the expansion term starts to sizably alter the time evolution of the total number density n_χ. When the mean free path for sparticle-producing collisions grow larger than the Hubble radius, the n_i are solely dominated by the expansion term of the universe such that their number density per comoving volume remains constant (see Fig. 3.22). This fall out of thermal equilibrium is called *freeze-out* of a particle species from the thermal bath, which is typically characterized by the associated freeze-out temperature $T_F^{(\mathrm{i})}$ or $x_F^{(\mathrm{i})} = m_{\mathrm{i}}/T_{\mathrm{F}}^{(\mathrm{i})}$. The exact point of freeze out and, hence, the final relic density Ω_χ hinges on the relative size between the expansion term $\propto H$ and the creation and (co)annihilation term $\propto \langle\sigma_{\text{eff}}v\rangle$. It is therefore highly sensitive to $\langle\sigma_{\text{eff}}v\rangle$. This makes it *crucial to precisely determine* σ_{eff}. To improve on this is the main subject of this work.

3.4.3. The Thermal Average

Since the particle velocities can not be assumed to take a certain value but should rather follow a distribution, one is led to the introduction of a so-called thermal average in the following denoted by $\langle ... \rangle$ (see Eqs. (3.27) and (3.36)). Following Ref. [124], $\langle\sigma_{\text{eff}}v\rangle$ is now

defined as

$$\begin{aligned}\langle\sigma_{\text{eff}}v\rangle &= \sum_{ij}\langle\sigma_{ij}v_{ij}\rangle\frac{n_i^{\text{eq}}}{n_\chi^{\text{eq}}}\frac{n_j^{\text{eq}}}{n_\chi^{\text{eq}}} \\ &= \sum_{ij}\frac{g_ig_j}{(2\pi)^6}\int \mathrm{d}^3\mathbf{p}_i\mathrm{d}^3\mathbf{p}_j f_i f_j \sigma_{ij}v_{ij}. \end{aligned} \tag{3.38}$$

Using again the Maxwell-Boltzmann approximation but now for f_i and f_j, which seems to be reasonable at least for $T \ll m_i$, the final result suitable for numerical evaluations can be written in the form

$$\langle\sigma_{\text{eff}}v\rangle = \frac{\int_0^\infty \mathrm{d}p_{\text{eff}}\; p_{\text{eff}}^2 W_{\text{eff}} K_1(\sqrt{s}/T)}{m_0^4 T\left[\sum_i \frac{g_i}{g_0}\frac{m_i^2}{m_0^2}K_2(m_i/T)\right]^2}. \tag{3.39}$$

In Eq. (3.39), W_{eff} is defined as

$$W_{\text{eff}} = \sum_{ij}\frac{p_{ij}}{p_{\text{eff}}}\frac{g_ig_j}{g_0^2}W_{ij}. \tag{3.40}$$

p_{ij} is the absolute value of the three-momentum of χ_i (or χ_j) in the center-of-mass frame of the (χ_i–χ_j) pair

$$p_{ij} = \frac{[s-(m_i+m_j)^2]^{\frac{1}{2}}[s-(m_i-m_j)^2]^{\frac{1}{2}}}{2\sqrt{s}}, \tag{3.41}$$

($p_{\text{eff}} = p_{00}$) and

$$W_{ij} = \frac{1}{g_ig_jS_f}\sum_{\text{internal d.o.f.}}\int |\mathcal{M}|^2(2\pi)^4\delta^4(p_i+p_j-\sum_f p_f)\prod_f\frac{\mathrm{d}^3\mathbf{p}_f}{(2\pi)^3 2E_f} \tag{3.42}$$

for a general n-body final state with momenta p_f. Finally, in Eq. (3.42), S_f is a symmetry factor which accounts for identical particles in the final state. More details on the derivation of Eq. (3.39) can be found in Ref. [124].

3.4.4. Solving the Boltzmann Equation

Now, the remaining step is to obtain the final relic density from Eq. (3.36). Following Ref. [124], one can start with the introduction of the yield

$$Y := \frac{n_\chi}{s} \tag{3.43}$$

with the entropy density

$$s = \frac{2\pi^2}{45}h_{\text{eff}}(T)T^3 \tag{3.44}$$

and photon temperature T. Assumed that the effective number of relativistic degrees of freedom $h_{\text{eff}}(T)$ is constant[17] $\dot{h}_{\text{eff}} = 0$ as well as a mainly adiabatic evolution of the

[17] Here, T has to be away from the QCD-phase-transition at $T_{\text{QCD}} \approx 200$ MeV, since due to the formation of hadrons out of free quarks and gluons (due to asymptotic freedom, quarks and gluons move nearly freely at temperatures $T \gg T_{\text{QCD}}$), $h_{\text{eff}}(T)$ changes quickly at $T \approx T_{\text{QCD}}$. However, for our typical scenarios the freeze-out of sparticles occurs at temperatures $T_F \approx m_i/20$ with typical WIMP masses of $\mathcal{O}(100\,\text{GeV})$ such that $T_F \gg T_{\text{QCD}}$ is expected be a viable assumption (see Sec. 3.5 for a more detailed discussion).

universe, $s \propto R^{-3}(t) \rightarrow s \cdot R^3(t) = \text{const.}$ ($T \propto R^{-1}(t)$), s can be related to the Hubble parameter H via

$$\dot{s} = -3Hs. \tag{3.45}$$

Thus, it follows that

$$\frac{1}{T} = \frac{1}{\dot{s}}\frac{\mathrm{d}s}{\mathrm{d}T} = -\frac{1}{3Hs}\frac{\mathrm{d}s}{\mathrm{d}T}. \tag{3.46}$$

Taking the time derivative of Eq. (3.43), this yields

$$\dot{Y} = \frac{\dot{n}_\chi}{s} + 3H\frac{n_\chi}{s}. \tag{3.47}$$

Hence, Eq. (3.36) can be rewritten as

$$\dot{Y} = -s\langle\sigma_{\text{eff}}v\rangle(Y^2 - Y_{\text{eq}}^2). \tag{3.48}$$

Since the time dependence of Eq. (3.48) can be completely expressed through the temperature T, it is common to replace the time derivative by a derivative with respect to $x := m_{\tilde{\chi}_1^0}/T$. So, using Eq. (3.46), one is left with

$$\frac{\mathrm{d}Y}{\mathrm{d}x} = \frac{1}{3H}\frac{\mathrm{d}s}{\mathrm{d}x}\langle\sigma_{\text{eff}}v\rangle(Y^2 - Y_{\text{eq}}^2). \tag{3.49}$$

By making further use of the Friedmann equation Eq. (3.25)

$$H^2 = \frac{\rho}{3M_{\text{Pl}}^2} \tag{3.50}$$

for a flat universe ($\kappa = 0$) as well as of the energy density

$$\rho = \frac{\pi^2}{30}g_{\text{eff}}(T)T^4 \tag{3.51}$$

for a radiation dominated universe with effective degrees of freedom $g_{\text{eff}}(T)$, one can finally rewrite Eq. (3.49) as

$$\frac{\mathrm{d}Y}{\mathrm{d}x} = -\frac{4\pi}{\sqrt{90}}M_{\text{Pl}}m_0\frac{\sqrt{g_*}}{x^2}\langle\sigma_{\text{eff}}v\rangle(Y^2 - Y_{\text{eq}}^2). \tag{3.52}$$

In Eq. (3.52) g_* is defined as

$$\sqrt{g}_* = \frac{h_{\text{eff}}}{\sqrt{g_{\text{eff}}}}\left(1 + \frac{1}{3}\frac{T}{h_{\text{eff}}}\frac{\mathrm{d}h_{\text{eff}}}{\mathrm{d}T}\right) \tag{3.53}$$

and Y^{eq} can be expressed through

$$Y^{\text{eq}} = \frac{n^{\text{eq}}}{s} = \frac{45x^2}{4\pi^4 h_{\text{eff}}(T)}\sum_i g_i\left(\frac{m_i}{m_0}\right)^2 K_2\left(x\frac{m_i}{m_0}\right), \tag{3.54}$$

where Eqs. (3.30) and (3.44) have been used. Integrating Eq. (3.52) from $x = 0$ up to $x_0 = m_{\tilde{\chi}_1^0}/T_0$ with $T_0 = T_0^\gamma$, the current temperature of CMB-photons, today's relic density can be expressed through today's yield Y_0 as

$$\Omega_\chi = \frac{\rho_\chi^0}{\rho_{\text{c}}} = \frac{m_0 s_0 Y_0}{\rho_{\text{c}}}. \tag{3.55}$$

Here, the definition Eq. (3.43) has been used. Moreover, ρ_χ^0 and s_0 are today's energy density for $\tilde{\chi}_1^0$ and entropy density, respectively. Using $T_0 = T_0^\gamma = 2.726$ K this finally yields [124]

$$\Omega_\chi h^2 = 2.755 \times 10^8 \frac{m_0}{\text{GeV}} Y_0, \tag{3.56}$$

which due to Eq. (3.52) results in the qualitative behavior

$$\Omega_\chi h^2 \propto \frac{1}{\langle \sigma_{\text{eff}} v \rangle} \tag{3.57}$$

as already discussed in the context of Fig. 3.22.
Since in the following analyses we investigate on the impact of coannihilation on the neutralino relic density $\Omega_{\tilde{\chi}_1^0} = \Omega_\chi$, let us end this section with a more detailed view on the Boltzmann suppression factors from Eq. (3.37). Recall that using Eq. (3.30) in the non-relativistic limit $T \ll m_i$ ($x \gg 1$, see Eq. (3.31)), the ratios $n_i^{\text{eq}}/n_\chi^{\text{eq}} n_j^{\text{eq}}/n_\chi^{\text{eq}}$ turn into the factors [127]

$$\frac{n_i^{\text{eq}}}{n_\chi^{\text{eq}}} \frac{n_j^{\text{eq}}}{n_\chi^{\text{eq}}} \approx \frac{g_i g_j \left(\frac{m_i}{m_0}\right)^{\frac{3}{2}} \left(\frac{m_j}{m_0}\right)^{\frac{3}{2}} e^{-x_F \frac{m_i + m_j}{m_0}}}{\left[\sum_i g_i \left(\frac{m_i}{m_0}\right)^{\frac{3}{2}} e^{-x_F \frac{m_i}{m_0}}\right]^2}. \tag{3.58}$$

In the case of $m_0 \approx m_1 \ll m_2$ mostly relevant to this work and neglecting all contributions for $i > 1$ in the sum Eq. (3.58), this yields

$$\frac{n_0^{\text{eq}}}{n_\chi^{\text{eq}}} \frac{n_0^{\text{eq}}}{n_\chi^{\text{eq}}} \approx 1, \tag{3.59a}$$

$$\frac{n_0^{\text{eq}}}{n_\chi^{\text{eq}}} \frac{n_1^{\text{eq}}}{n_\chi^{\text{eq}}} \approx \frac{g_1}{g_0} \left(\frac{m_1}{m_0}\right)^{\frac{3}{2}} e^{-x_F \frac{m_1 - m_0}{m_0}}, \tag{3.59b}$$

$$\frac{n_1^{\text{eq}}}{n_\chi^{\text{eq}}} \frac{n_1^{\text{eq}}}{n_\chi^{\text{eq}}} \approx \left(\frac{g_1}{g_0}\right)^2 \left(\frac{m_1}{m_0}\right)^3 e^{-2x_F \frac{m_i - m_0}{m_0}}. \tag{3.59c}$$

Thus, for $x_F \approx 20$ only particles with a mass close to m_0 can give sizable contributions to $\langle \sigma_{\text{eff}} v \rangle$ and, hence, are able to sizably alter the time dependence of n_χ. This means that coannihilation for a next-to-lightest supersymmetric particle (NLSP) χ_i may significantly alter Ω_χ only if $m_0 \approx m_i$. To be a bit more quantitative, let us assume the mass hierarchy $m_1 = 1.5 \cdot m_0$. Then, the exponential in Eq. (3.59a) turns into a suppression factor of $\mathcal{O}(10^{-5})$ and Eq. (3.59b) would be even more suppressed by a factor $\mathcal{O}(10^{-10})$. Thus, an approximate mass degeneracy $m_0 \approx m_1$ is a mandatory prerequisite for a sizable coannihilation contribution, though these supressions may still be compensated by large cross sections σ_{01}, $\sigma_{11} \gg \sigma_{00}$.
Finally note that there is no general solution to the Eqs. (3.49) and (3.55). However, it is possible to expand Eq. (3.55) in $\mathcal{O}(1/x_F = T_F/m_0)$. In this case an analytic or semianlaytic solution turns out to be possible (see Ref. [128, 129]). For neutralino dark matter, x_F is roughly of the size $x_F \simeq 20$ and, hence, should lead to a quickly converging power series. But since Ω_χ is in general no analytic function of x_F, this way is also far from trivial and potentially affected by large errors[18] [127]. Due to the growing computative power, Eq. (3.55) can today be solved completely numerically with quite high accuracy

[18] More precisely, expanding Ω_χ in x_F typically includes the expansion of $\langle \sigma_{ij} v_{ij} \rangle$ in orders of v_{ij}. This is expected to yield a quickly convergent power series since sparticles freeze out at non-relativistic velocities. But since σ_{ij} is in general no analytic function of v_{ij}, e.g., at normal thresholds or propagator poles, this can spoil the actual convergence of this series.

at low time cost. Public codes, which are able to solve Eq. (3.55), e.g., within the MSSM including a comprehensive set of different (co)annihilation channels, are `DarkSUSY` [130], `SuperIso Relic` [131], `IsaRED` (as subroutine of the `IsaJET 7.84` package [132]) and `micrOMEGAs` [133]. For this analyses we make use of the latter.

3.5. Uncertainties in the Estimation of the Relic Density

The oldest data about the history of the universe stem from the abundances of light elements such as Deuterium, Helium etc., whose formation is described by the big bang nucleosynthesis, which took place roughly 200 seconds after the big bang (at $T \approx 0.8\,\mathrm{MeV}$). Since the freeze-out of WIMP particles is expected to occur at much higher temperatures $T_F \approx m_0/20$ and, hence, at much earlier times, the DM relic density relies on the properties of the universe during the pre-BBN era from which we do not have any direct experimental information. Therefore, one has to rely on several assumptions about the universe during the pre-BBN era, which enter the final estimation of Ω_χ in Eq. (3.55) and which do not necessarily have to pertain. Some of them are the following:

1. *WIMPs have once been in thermal equilibrium with the surrounding hot gas of SM particles*: For this to be true, it is necessary to assume that the reheating temperature after inflation T_R has been high enough such that WIMPs were able to reach thermal equilibrium. This means that at least $T_R \gtrsim m/10$ should have been reached whereas we have only direct evidence of the BBN epoch and the subsequent evolution of the universe where a $T_R = 4$ MeV turns out to be already sufficient (note that for WIMPs/sparticles typically $m \gtrsim \mathcal{O}(100\,\mathrm{GeV})$). An alternative model describing DM candidates, which never reached thermal equilibrium, can be found e.g. in [134].

2. *The entropy density per comoving volume was conserved during the pre-BBN epoch* (see Eq. (3.45)): It was already mentioned in Sec. 3.4.4 that, e.g., some time-dependent change in the effective number of entropy-effective degrees of freedom h_{eff} Eq. (3.44) may spoil this assumption.

3. *The freeze-out occurred during the radiation dominated epoch* (see above Eq. (3.52)): This assumption rests upon the success of BBN models, which relied on a radiation dominated universe during the BBN era. But this assumption does not necessarily pertain for the pre-BBN era (see below).

There are many more potential loopholes in the estimation of the relic density not necessarily directly connected to the derivation of the Boltzmann equation. These can arise, e.g., in the estimation of input parameters as well as in the analyses of experimental data. Therefore, this chapter shall serve as a concise overview over some potential sources of uncertainties and subtleties in the calculation of Ω_{CDM}.

The model dependence in the interpretation of CMB data:
Any interpretation of experimental data relies on some theoretical framework. This is the case for the interpretation of the CMB data and thus for the value of Ω_{CDM} obtained through the analysis of these data. The cosmological model which underlies the result given in Eq. (3.14) is the so-called ΛCDM, also referred to as the standard model of big bang cosmology. It is a six parameter model, which bases on the assumption of an expanding, spatially flat universe, whose dynamics are governed by general relativity. At late times, its constituents are dominated by a CDM component and a cosmological constant Λ as

parameter	**value at 1σ**	**description**
$\Omega_\mathrm{b}h^2$	0.02207 ± 0.00033	baryon density
$\Omega_\mathrm{CDM}h^2$	0.1196 ± 0.0031	cold dark matter density
Ω_Λ	0.686 ± 0.020	dark energy density
$\ln[10^{10}A_\mathrm{s}]$	3.103 ± 0.072	log-power of primordial curvature fluctuations ($k_0 = 0.05\,\mathrm{Mpc}^{-1}$)
n_s	0.9616 ± 0.0094	scalar spectrum power law index ($k_0 = 0.05\,\mathrm{Mpc}^{-1}$)
τ	0.097 ± 0.038	Thomson scattering optical depth due to ionization

Table 3.1.: Parameter set of the ΛCDM model with current values given at 1σ confidence level [45]

implied by the acronym ΛCDM. The ΛCDM six parameter set is given in Tab. 3.5 [45]. The values in the second column of Tab. 3.5 are given at 1σ confidence level and are obtained via fitting the CMB power spectrum as measured by the Planck collaboration within ΛCDM (see Ch. 3.1.5). Note that this parameter set is to some extent ambiguous as it is possible to replace one parameter by another if they are somehow dependent. Whereas the first three parameters Ω_b, Ω_CDM and Ω_Λ are more or less self-explanatory, the last three are concisely explained in the following [45].

- *The primordial scalar density fluctuations $\mathcal{P}(k)$ and its connection to A_s and n_s*: The CMB is understood as an imprint of the density fluctuations of the primordial universe. It is believed that these density fluctuations rely on seed inhomogenities caused by quantum fluctuations, which were enlarged by inflation and froze into the observed density fluctuations when inflation stopped. These density fluctuations $\mathcal{P}(k)$ in dependence of the wave number k are commonly grasped in the form

$$\mathcal{P}(k) = A_s \left(\frac{k}{k_0}\right)^{n_\mathrm{s}-1} \tag{3.60}$$

  with the power law index n_s, the size of the inhomogenities parametrized by A_s and the Pivot scale k_0. Hence, n_s measures the deviation from a scale invariant fluctuation spectrum ($n_s = 1, \mathrm{d}n_\mathrm{s}/\mathrm{d}\ln(k) = 0$, Harrison-Zel'dovich spectrum). It turned out that the density fluctuation seen in the CMB deviates only slightly from a scale invariant spectrum (see Tab. 3.5).

- *The Thomson scattering optical depth τ*: The small scale fluctuations of the CMB are damped via Thomson scattering on electrons which propagated freely after reionization. This damping translates into a lowering of the acoustic peaks of the CMB power spectrum for l-values, which correspond to angular distances smaller than the Hubble radius at the time of reionization. This damping is connected to the optical depth for Thomson scattering τ via a factor $e^{-2\tau}$, which multiplies the amplitudes of the acoustic peaks for the particular l-values.

Despite the big success of the ΛCDM, studies pose the questions of how robust the results obtained, such as Ω_CDM, actually are against some changes of the cosmological model. This question has been explored in Ref. [45] for one-parameter extensions of the fiducial ΛCDM model. There, the authors allowed for a deviation of, e.g., a flat universe parametrized as

$$\Omega_\mathrm{k} = 1 - \Omega_\mathrm{b} - \Omega_\mathrm{CDM} - \Omega_\Lambda \tag{3.61}$$

and a k-dependence of the power law index n_s, extending Eq. (3.60)

$$\mathcal{P}(k) = A_s \left(\frac{k}{k_0}\right)^{n_\mathrm{s}-1+\frac{1}{2}(\mathrm{d}n_\mathrm{s}/\mathrm{d}\ln(k))\ln(k/k_0)} . \tag{3.62}$$

Moreover, they allowed for a deviation of the w-parameter from the usual value $w = -1$ for a cosmological constant $\equiv$ vacuum energy in the equation of state

$$p = w\rho \tag{3.63}$$

with pressure p as well as for a variable effective number of relativistic neutrino species N_eff at decoupling $T_\nu \approx 2 - 3$ MeV [135]. The main outcome is presented in Fig. 3.23. It is shown that the quality of these fits to the data for the extended ΛCDM is not much improved. But the error bands, e.g., for Ω_CDM turn out to be broadened in case of strong degeneracy with the additional parameter. Following Occams razor, the ΛCDM seems to be the right choice, although one should keep in mind that an extension of the standard model of cosmology can broaden the ranges allowed for values of observables gained through the analyses of the CMB.
Following this road, Ref. [136] investigated on an up to 5-parameter extension of the ΛCDM. There, it turned out that Ω_CDM is even allowed to vary by a factor of two while still being in accordance with the data.

The Hubble parameter H in the pre-BBN era:
As already mentioned above, it is explicitly assumed within the derivation of Eq. (3.52) that the freeze-out of the relic particle took place during the radiation dominated epoch. This assumption rests upon the success of BBN models, which rely on a radiation dominated universe during the BBN era at $T_\mathrm{BBN} \approx 0.8$ MeV. But since the freeze-out of WIMPs should have taken place long before the BBN $T_F \gg 0.8$ MeV, the extrapolation $T_\mathrm{BBN} \rightarrow T_F$ concerning the energy content of the universe is far from trivial. Hence, following models like quintessence [137], k-essence [138] or dark fluid [139], it seems possible that a dark energy component may have played a sizable role in the evolution of the universe at high $T \gg T_\mathrm{BBN}$.
It is therefore conceivable that, following the Friedmann equation, different assumptions about the energy content of the pre-BBN era may de- or increase the expansion rate of the universe H and may thus have changed the freeze-out temperature T_F of the relic particle (see Eqs. (3.25) and (3.26)). For this purpose, the authors of Ref. [140] have added an additional temperature dependent dark energy density

$$\rho_D(T) = \rho_D(T_0) \left(\frac{T}{T_0}\right)^{n_D} \tag{3.64}$$

to the Friedmann equation of a radiation dominated universe (see Eq. (3.25))

$$H^2 = \frac{\rho_\mathrm{Rad} + \rho_D}{3M22_\mathrm{Pl}}, \tag{3.65}$$

where both $\rho_D(T_0) > 0$, $\rho_D(T_0) < 0$[19] are possible. Depending on the particular choice of $n_D = (3, 4, 6)$ in Eq. (3.64), ρ_D mimics a matter density, radiation density or, e.g., a density of a quintessence field. The authors of Ref. [140] explored the change of the final relic

[19]Note that ρ_D does not have to be a real energy density but can also be understood as some effective term to parametrize the change in the expansion rate.

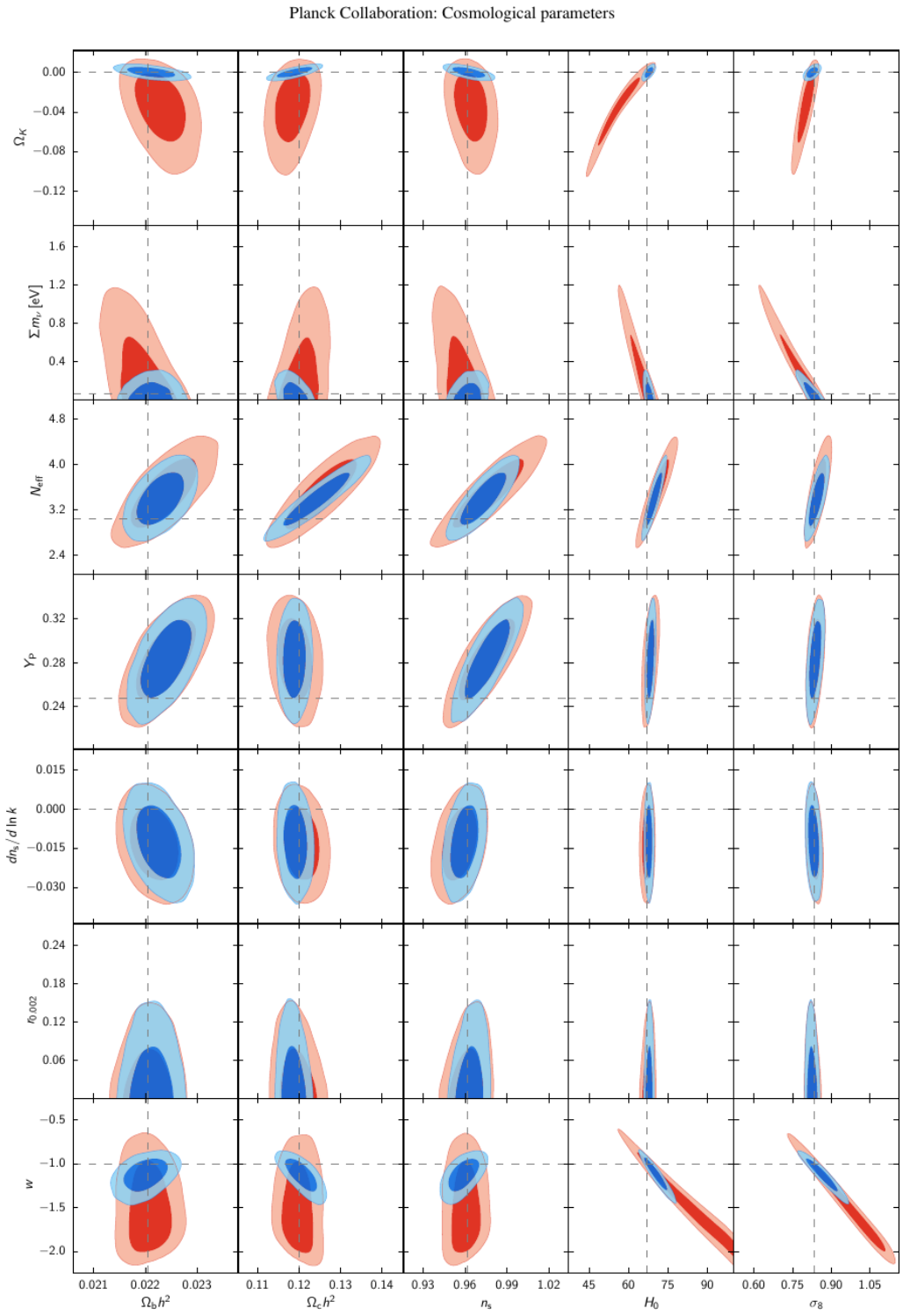

Figure 3.23.: 68% and 95% confidence regions for the one parameter extensions of the ΛCDM based on Planck+WMAP data (red) and Planck+WMAP+Baryonic Acoustic Oscillation data (blue). Horizontal dashed lines belong to the additional parameters estimated in the fixed 6-parameter ΛCDM, vertical dashed lines show the preferred fit values of ΛCDM parameters based on Planck+WMAP data [45].

density Ω_χ for different values n_D and $\rho_D(T_0)$ and for different mSUGRA or NUHM (non universal Higgs mass) scenarios. Their analyses revealed that even a very small increase of H before the BBN, presently undetectable in cosmological observations, can change T_F and is able to shift the final Ω_χ by a factor up to 10^6 toward higher values. On the contrary, they found that Ω_χ is never or only very slightly decreased (for $\rho_D(T_0) < 0$) by an additional component ρ_D. The authors of Ref. [140] concluded that the lower bound of the relic density obtained from, e.g., Planck, should be used with care as parameter points with a too low Ω_χ may always be shifted toward the correct region via altering the expansion rate in the pre-BBN era, while the upper bound on the DM relic density turned out to be rather robust against these changes.

The effective degrees of freedom revisited:
The effective degrees of freedom g_* enter the estimation of the relic density Eq. (3.52). It has already been pointed out that in the derivation of Eq. (3.45), it is necessary to assume a freeze out temperature well above $T_{\mathrm{QCD}} \approx 200$ MeV. For temperatures larger than T_{QCD}, quarks und gluons couple only weakly due to the asymptotic freedom and, hence, may be well described by an ideal gas. As non-perturbative studies and experiments revealed a significant departure of this assumptions in Ref. [141] the equation of states of quarks and gluons have been re-examined in the critical regime around T_{QCD}. The authors improved, e.g., in the deconfined regime on the assumption of an ideal gas by rescaling the pressure of the colored degrees of freedom within the equation of state by a factor deduced from lattice and perturbative calculations. With these results at hand, the authors recalculated the associated effective degrees of freedom of Eqs. (3.51) and (3.53) and in turn the relic density. They discovered a significant change within some of their investigated mSUGRA-benchmark scenarios even for freeze-out temperatures $T_F \gg T_{\mathrm{QCD}}$. After comparison with `DarkSUSY`[20], they found a shift larger than 2% due to their improvements even for temperatures $T_F \gtrsim 20\ T_{\mathrm{QCD}}$. The authors further stated a systematic error of 0.5%-1% due to used approximations in the equation of state near T_{QCD}.

Finite-temperature effects:
In terms of relic density calculations, one usually estimates the (co)annihilation cross section via the vacuum expectation value of some operator $\mathcal{O}$, e.g., S-matrix elements, at zero temperature

$$\langle 0|\mathcal{O}|0\rangle. \tag{3.66}$$

Due to weak scale interactions, the freeze-out of WIMPs occurs roughly at $T_F \approx m_\chi/20$. Therefore, calculations of cross sections should rather take place at non-zero temperature, thus making it necessary to replace Eq. (3.66) by

$$\frac{\sum_n \langle n|\mathcal{O}e^{-\beta H}|n\rangle}{\sum_n \langle n|e^{-\beta H}|n\rangle}. \tag{3.67}$$

The partition function in Eq. (3.67) given in state space spanned by the $|n\rangle$, accounts for the excitations of the vacuum occupied with probability $e^{-\beta E_n}$ ($\beta = 1/(k_{\mathrm{B}}T)$) as a consequence of the finite temperature. These corrections yield a set of modified Feynman rules for the S-matrix as appropriate for perturbation theory at finite temperature [142]. A throughout investigation of finite-temperature effects in the context of NLO calculation

[20] `DarkSUSY` relies on the assumption of quarks and gluons interacting via a linear potential $V(r) = K \cdot r$ ($K = 0.18\,\mathrm{GeV}^2$) for temperatures $T > T_{\mathrm{QCD}}$, an assumption, which almost corresponds to an ideal gas.

has been done in Ref. [143]. There, it is shown that thermal effects leave the Boltzmann equation intact

$$\frac{\mathrm{d}n_\chi}{\mathrm{d}t} + 3Hn_\chi = \langle\sigma_{\mathrm{eff}}^{\mathrm{NLO}} v_{\mathrm{rel}}\rangle|_{T\neq 0}(n_\chi^{\mathrm{eq}} n_{\bar{\chi}}^{\mathrm{eq}} - n_\chi n_{\bar{\chi}}) \tag{3.68}$$

and only alter the velocity averaged annihilation cross section, which has to be calculated at non-zero temperature. Furthermore, the cancellation of infrared and collinear divergences for sufficiently inclusive observables is checked at finite temperature, a prerequisite for $\sigma_{\mathrm{eff}}^{\mathrm{NLO}}$ to be well defined at $T \neq 0$. Guaranteed by the Bloch-Nordsieck and the Kinoshita-Lee-Nauenberg theorem for zero-temperature QFT, the authors showed that these cancellations also hold at non-zero temperature.
Finally, it was found in Ref. [143] that finite-temperature corrections enter the calculation of $\sigma_{\mathrm{eff}}^{\mathrm{NLO}}$ suppressed by a factor $\alpha \times (T_F/m_0)^2$ ($T_F \ll m_0$) and, thus, are expected to be parametrically smaller than the zero-temperature NLO corrections. Finite-temperature effects can hence alter the relic density but are not sizable, compared to the current level of precision, which is a subsequent justification for the zero-temperature approach taken in, e.g., the Refs. [1], [2] and [144]- [148].
The impact of finite-temperature effects in the presence of coannihilation has to some extend been investigated in Ref. [142]. There, the non-zero temperature effects on the LSP-NLSP mass splitting for neutralino DM with a stau LSP within the MSSM have been considered. Since the mass splitting enters the final relic density exponentially, as apparent from Eqs. (3.58) and following, small changes in this splitting may potentially evolve to large shifts in $\Omega_{\tilde{\chi}_1^0}$. However, the authors found that the finite-temperature effects on the neutralino relic density are at most of the relative order 10^{-4}, which is considerably below the detection threshold of any ongoing or planned relic density experiment. They can hence be neglected at the current level of precision.

The impact of higher-order corrections on the (co)annihilation cross section:
As already pointed out at the end of Sec. (3.4.2), a precise estimation of Ω_χ relies sensibly on an accurate calculation of σ_{eff}. It is well known that the (co)annihilation cross sections which add up to σ_{eff} in Eq. (3.38) can be subject to large higher-order corrections. There have been many investigations which study the effect of higher-order corrections. Starting from the Born-level, one of the first improvements were accomplished via the effective coupling approach. Mainly motivated by the lower computational effort, only the leading radiative corrections are typically taken into account within this formalism. In Ref. [149, 150], certain classes of EW corrections[21] to neutralino annihilation were calculated and their impact on Ω_{CDM} was analyzed. Furthermore, complete NLO calculations have been performed including electro weak (EW) corrections to neutralino annihilation [151] or SUSY-QCD corrections to neutralino annihilation and coannihilation with heavier neutralinos and charginos going into quarks [1, 144–146], coannihilation between the neutralino and the lighter stop [147, 148] as well as annihilation of lighter stops into EW final states [2]. The authors concluded that, depending on the exact parameter point of the DM model under consideration, the higher-order corrections can exceed current experimental uncertainties by far. It thus makes sense to improve the calculation of radiative corrections to σ_{eff} to benefit from the precision gained in experiments. However, current state of the art tools like `micrOMEGAs` or `DarkSUSY` calculate the relic density at effective tree level only.
It should further be mentioned that there are additional higher-order corrections to the (co)annihilation of DM particles, which can become non-perturbative in certain kinematic

[21] These classes cover corrections which are less suppressed than the expected NLO suppression α_{EW}/π.

regions. In these cases, it is necessary to sum up the corrections to all orders in perturbation theory in order to gain a reliable result, since the expected suppression with higher orders in the coupling constant is lifted by some large (kinematic) factor. A very prominent example for such non-perturbative corrections are the so-called Coulomb or Sommerfeld corrections as discussed in greater detail in Sec. 5.3. These become most important when the (co)annihilating DM particles move at non-relativistic velocities v as it is, e.g., the case for thermally produced WIMPs after freeze-out. If these particles exchange a massless or relatively light (compared to the masses of the annihilating particles) particle, it turns out that every exchange of an additional particle comes with a factor α/v. Due to $\alpha/v \gtrsim 1$ for sufficiently small v, this can lead to a large enhancement of such higher-order corrections rendering them non-perturbative. The impact of Coulomb or Sommerfeld corrections on DM production has been extensively discussed in the literature [152,153]. For example, the effect of gluon exchanges on stop annihilation in the case of neutralino DM accompanied by a stop NLSP is thematized in Ch. 5.3 below. It is found that these non-perturbative corrections can overcome current experimental uncertainties by far. These non-perturbative corrections should hence also be taken into account.

Additional sources of uncertainties:
Finally note that this list of uncertainties in DM calculations is far from being complete. Further investigations about potential sources of uncertainties can be found in the Refs. [154, 155], where the uncertainties in the estimation of low scale parameters, obtained from the corresponding high scale parameters via their renormalization group running, is considered. In those studies, several public SUSY spectrum calculators like `SPheno` [156], `Suspect` [157], `Isajet` [132] or `SOFTSUSY` [158] are compared with each other and an uncertainty of $\mathcal{O}(1\%)$ in parameters like masses was found. In Ref. [155], these deviations in the generated SUSY spectra turned out to be already sufficient to alter Ω_{CDM} by up to 30%, of course strongly dependent on the particular region of the SUSY-parameter space. It is of particular interest for this work that, in the case of stop coannihilation, Ref. [155] found differences of $\mathcal{O}(10\%)$ in the generated masses for certain regions of parameter space, which translated into an order of magnitude difference for the corresponding Ω_{CDM}. However, note that the latest paper referenced here is from 2005. Since then, the cited SUSY-spectrum calculators have undergone several improvements such that a new cross check of the different routines may be of certain interest.
n-body final states with $n > 2$ are another potential source of uncertainties. So far, they are not fully considered in public tools like `micrOMEAGs`, `SuperIso Relic` or `DarkSUSY` as they are usually of higher order and propagator suppressed. But below production thresholds, when a certain two particle final state is kinematically just not allowed, they can become important as they allow for the production of a massive particle away from its mass shell, followed by its subsequent decay into two lighter, physical particles. In Ref. [159] the author showed that, taking into account annihilation to three-body final states such as $(\tilde{\chi}_1^0\tilde{\chi}_1^0 \to t^*\bar{t} \to W^+b\bar{t})$, can thus lower the neutralino relic density by more than 10% .
Finally note that with `SuperIso Relic`, there is a public code which accounts for some of the uncertainties described above. By means of `SuperIso Relic`, it is possible to change the radiation equation of state and hence the Hubble expansion rate in the pre-BBN era following Ref. [140]. There is also the possibility to improve on the QCD equation of state as described in Ref. [141]. This variety of possible changes in the underlying model turns `SuperIso Relic` into an interesting tool for more non-standard studies in the context of Ω_{CDM} calculations.

This completes the discussion of uncertainties on Ω_χ, though not all of them are discussed, here. However, we have seen that there are many different loopholes through which our experimental as well as theoretical lack of knowledge of the true nature of DM may enter the estimation of the final relic density. Hence, the work presented in the following should be understood as a step on the way to a precise estimation of the amount of DM in our today's universe.

4. The DM@NLO Project

In the previous chapters, we presented many potential sources of uncertainties that arise in the estimation of Ω_{CDM}. In particular, we mentioned that perturbative as well as non-perturbative radiative corrections to annihilation as well as to coannihilation channels of the neutralino LSP alter the final relic density sizeably. But even though these corrections turned out to be much larger than the actual experimental error on Ω_{CDM}, as provided by the Planck collaboration, they are not yet completely covered by current public DM-tools such as `micrOMEGAs` or `DarkSUSY`.
The work presented here is embedded into a larger project called *Dark Matter @ Next to Leading Order* (`DM@NLO`), which is developed to improve exactly on this shortcoming of currently available DM-tools. In the following, we introduce the `DM@NLO` project in more detail and present its usage in combination with public tools for relic density calculations as well as the current status of its sub-projects connected to this work. Afterwards, we address the actual calculation of the corresponding higher-order corrections and survey their impact on the associated (co)annihilation cross sections as well as on the neutralino relic density Ω_{CDM}.

4.1. DM@NLO and its Sub-Projects

`DM@NLO` is a `Fortran` code that provides automatic calculation of NLO-SUSY-QCD corrections for many (co)annihilation cross sections relevant for the estimation of the neutralino relic density within the R-parity conserving MSSM. The usage of the `DM@NLO` software package in combination with current DM-tools such as `micrOMEGAs` is depicted in Fig. 4.1. This usage is shortly discussed in the following.
The starting point of the calculation of Ω_{CDM} within a certain model is the choice of a particular scenario via the specification of a set of input parameters at a given input scale M_{in}, e.g., within the MSSM or pMSSM, as introduced in the Chs. 2.4 and 2.5. These input parameters, which are commonly given in a format specified by the SUSY *Les Houches Accord* (SLHA) [166], are then passed to a spectrum calculator, which provides the full mass spectrum of the SUSY and Higgs sector as well as connected mixings at a required output scale M_{out}. The spectrum calculator has to solve a set of renormalization group equations (RGEs), which describe the scale dependent running of parameters like couplings and masses for the SUSY and Higgs sector, starting at M_{in} down to the output scale[1]. Typical scale choices are $M_{\text{in}} \sim$ GUT scale, or, following the Supersymmetric Parameter Analysis (SPA) convention [167], $M_{\text{in}} = 1$ TeV, whereas the output scale within supersymmetric models is typically set to the SUSY-scale $M_{\text{out}} = \sqrt{m_{\tilde{t}_1} m_{\tilde{t}_2}} \sim \mathcal{O}(1\text{ TeV})$. In our case of the pMSSM with SPA-input, we use $M_{\text{in}} = M_{\text{out}} = 1$ TeV[2]. Moreover, spectrum calculators often provide associated branching ratios and production cross sections as well as further important observables such as the flavor changing neutral current (FCNC) observable $b \to s\gamma$

[1] or in terms of SM-parameters, the running, e.g., from the scale of electroweak symmetry breaking $\sim \mathcal{O}(M_Z)$ up to M_{out}

[2] In contrast to, e.g., mSUGRA RGE-running is of course not of primary interest if one starts with a low scale SUSY-model like the MSSM without any high scale completion such as a GUT theory. In this case, the input parameters are typically understood as being defined at the output scale.

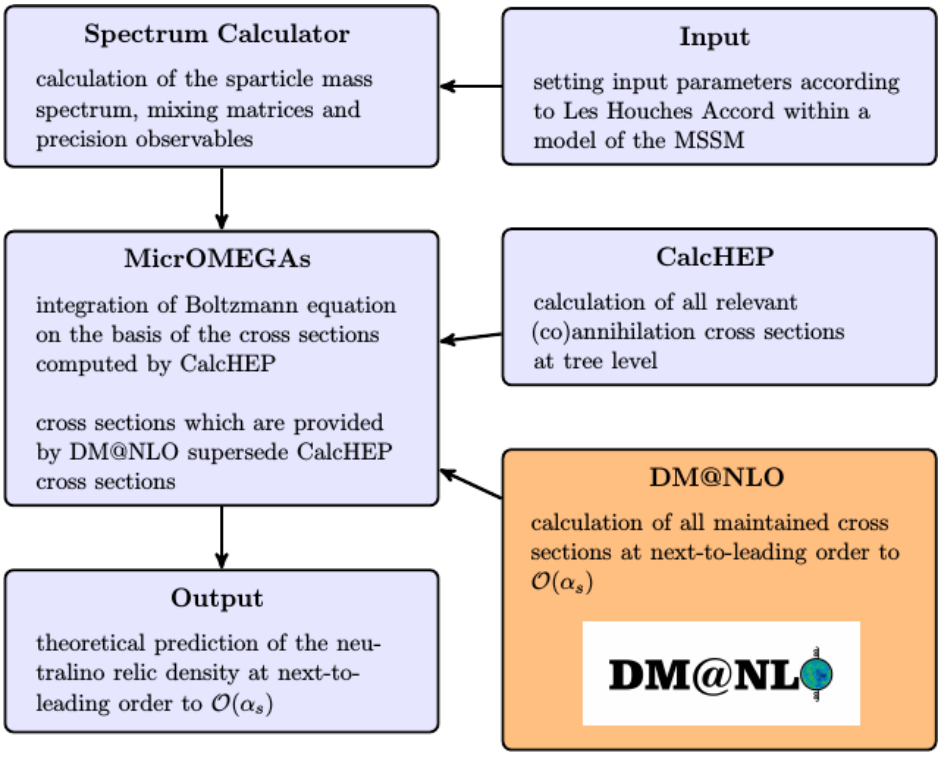

Figure 4.1.: Software chain of the relic density calculation including `DM@NLO`. Flow chart taken from Ref. [55].

and corrections to the muon g-factor g_μ. Throughout this work, we use `SPheno-3.2.3` as the spectrum calculator. `SPheno-3.2.3` provides the RGE running at two-loop precision as well as complete one-loop corrections to all SUSY and Higgs masses supplemented by two-loop corrections to the neutral Higgs bosons and to the μ parameter. Since version 3.0, `SPheno` includes the full flavor as well as CP structure of the MSSM. Moreover, it is possible to include the violation of R-parity into the calculations. Decay widths and cross sections are calculated at tree level though certain higher-order corrections are captured via the use of running couplings [156]. However, note that `DM@NLO` has also been tested with other publically available spectrum calculators such as `Suspect`, `Isajet` and `SOFTSUSY`. In a next step, the low-scale parameters are passed to `micrOMEGAs-2.4.1`, which we use throughout this work. `micrOMEGAs` is able to calculate the relic density of a DM-candidate within many predefined models. Beside the particularly important MSSM, these are additional models such as the next-to MSSM (NMSSM) [160], the CP-violating MSSM (CPVMSSM), the little Higgs model [161], a right handed neutrino model [162] and the inert doublet model [163][3]. The Born level (co)annihilation cross sections, as required by `micrOMEGAs`, are provided by CalcHEP [164] at effective tree level as discussed in Ch. 3.5. Using these cross sections `micrOMEGAs-2.4.1` further improves on the Higgs Yukawa coupling to bottom quarks as provided by `CalcHEP`, which can be affected by large SUSY-QCD corrections Δm_b of the order $\Delta m_b \sim \mathcal{O}((\alpha_s \mu \tan\beta)^n)$. These corrections can become non-perturbative, e.g., for large $\tan\beta$, but can be resumed to all orders [165] (see Sec. 5.1.5 below). With the necessary input at hand, `micrOMEGAs` solves the Boltzmann equation Eq. (3.36) as discussed in Sec. 3.4.2 numerically to obtain the final relic density within the considered model.

[3]Besides these predefined models, it is also possible to use completely user defined models within `micrOMEGAs-2.4.1`

The interface between `micrOMEGAs` and `CalcHEP` is the point where `DM@NLO` enters the stage. For every cross section called from `micrOMEGAs`, it is checked if `DM@NLO` can improve on the cross section via the inclusion of higher-order SUSY-QCD corrections. If this is the case, `DM@NLO` replaces the `CalcHEP` result including the Born level cross section with input parameters consistently passed between `micrOMEGAs-2.4.1` and `DM@NLO`. Otherwise, the default `CalcHEP` cross section is kept.
At the moment, the different SUSY-QCD corrections for (co)annihilation processes included in `DM@NLO` are split into three sub-projects:

- `ChiChi2qq`: Includes all (co)annihilation channels of neutralinos and charginos into quarks;
- `NeuQ2qx`: Includes all neutralino-squark coannihilation channels into a quark plus an additional SM-boson;
- `QQ2xx`: Includes all squark (co)annihilation channels into EW SM-bosons.

The sub-projects connected to this work are `ChiChi2qq` and `QQ2xx`. They are therefore presented in greater detail in the following, whereas the status and results of `NeuQ2qx` can be found in Refs. [147, 148].

4.2. ChiChi2qq: Gaugino (Co)Annihilation into Quarks

The following section and especially all results shown in the context of `ChiChi2qq` rely on the publication [1].
`ChiChi2qq` covers SUSY-QCD corrections to (co)annihilation channels of neutralinos $\tilde{\chi}_i^0$ ($i \in \{1,2,3,4\}$) and charginos $\tilde{\chi}_i^\pm$ ($i \in \{1,2\}$) (in the following collectively called gauginos) into quark-antiquark pairs

$$\tilde{\chi}_i^0 \tilde{\chi}_j^0 \to q\bar{q} \ (i,j \in \{1,2,3,4\}), \tag{4.1}$$
$$\tilde{\chi}_i^\pm \tilde{\chi}_j^0 \to q\bar{q}' \ (i \in \{1,2\}, j \in \{1,2,3,4\}), \tag{4.2}$$
$$\tilde{\chi}_i^+ \tilde{\chi}_j^- \to q\bar{q} \ (i,j \in \{1,2\}), \tag{4.3}$$

with $q, q' \in \{u,d,c,s,t,b\}$ as shown in Fig. 4.2. Gaugino (co)annihilation can hence take place through the s-channel exchange of one of the five Higgs-bosons h^0, H^0, A^0 and $H^\pm$ as well as through the s-channel vector exchange of a Z-, or $W^\pm$ boson or a photon γ depending on the initial-state charges (photon exchange contributes only for incoming $\tilde{\chi}_i^+ \tilde{\chi}_j^-$ ($i,j \in \{1,2\}$)). Additional contributions stem from the $t-$ and $u-$ channel exchange of scalar quarks. Moreover, since neutralinos are Majorana fermions, there is no difference between particle or antiparticle. One can therefore arbitrarily assign a fermion flow to their lines within a Feynman diagram. A particular choice can then be understood as fixing a convention for the corresponding mathematical expressions obtained via the applications of the associated Feynman rules. The assignment of the fermion flow and external momenta used throughout all calculations in the context of `ChiChi2qq` is given in Fig. 4.3. Finally note that all tree-level cross sections have been cross checked with `CalcHEP`, replacing running masses (exemplified in Sec. 5.1.6) and effective couplings (exemplified in Sec. 5.1.6) in `CalcHEP` as well as in `ChiChi2qq` if necessary.
We perform our studies on the relevance of the channels depicted in Fig. 4.2 for the neutralino relic density within the pMSSM-11 as introduced in Sec. 2.5. We further make use of the SPA-convention [167] such that all soft breaking parameters are given at the

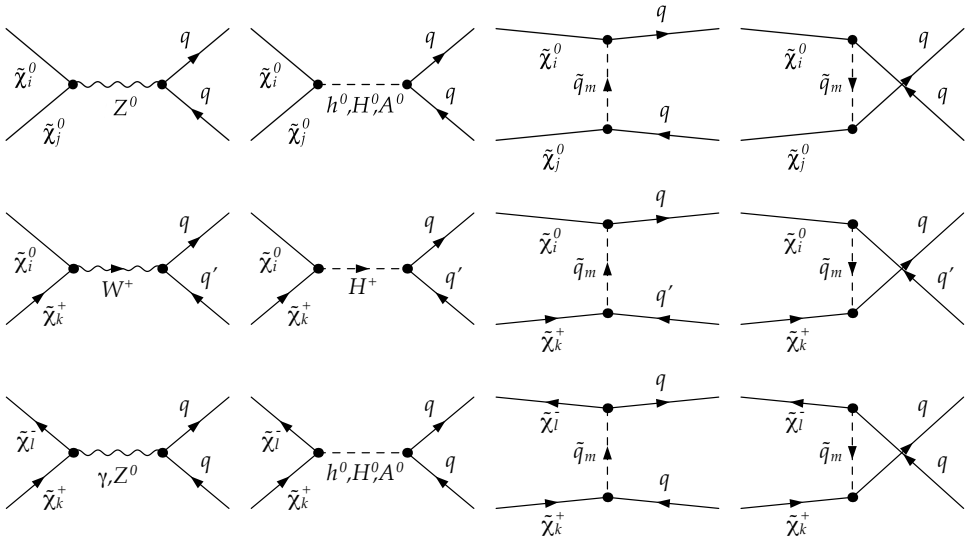

Figure 4.2.: Tree-level diagrams of gaugino (co)annihilation processes included in `ChiChi2qq`. Figures originally taken from Ref. [1].

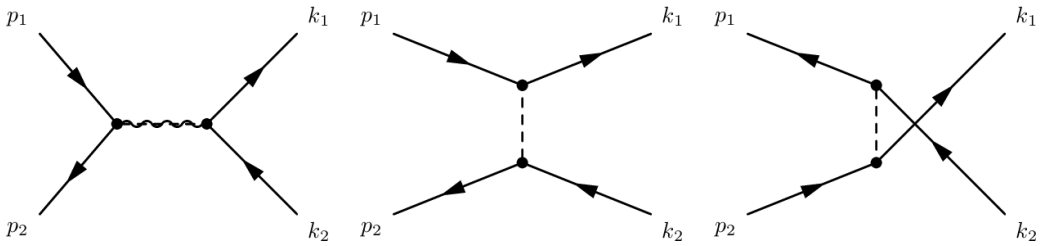

Figure 4.3.: Assigned fermion flow to Majorana lines used in the calculations in the context of `ChiChi2qq`.

input scale $Q = 1$ TeV. Within the pMSSM-11 the typical GUT-induced low energy ordering of the soft-breaking gaugino masses

$$2M_1 : M_2 : M_3/3 \tag{4.4}$$

does not hold anymore. Since the masses M_1 and M_2 in combination with μ determine the decomposition of neutralinos and charginos as discussed in Sec. 2.6.2, this higher degree of freedom consequently allows for a more interesting ordering of gaugino masses and, hence, for a larger variety of gaugino-coannihilation channels relevant to the final relic density $\Omega_{\tilde{\chi}_1^0}$ (see Sec. 3.4.4). In order to find appropriate scenarios to present the impact of our corrections, we perform a random scan over one million points of the pMSSM-11 parameter space within the boundaries

$$\begin{gathered}
2 \leq \tan\beta \leq 50, \\
-3000 \text{ GeV} \leq \mu \leq 3000 \text{ GeV}, \\
100 \text{ GeV} \leq m_{A^0}, M_1, M_2 \leq 2000 \text{ GeV}, \\
1000 \text{ GeV} \leq M_3 \leq 2000 \text{ GeV}, \\
500 \text{ GeV} \leq m_{\tilde{q}_{1,2}}, m_{\tilde{l}} \leq 4000 \text{ GeV}, \\
500 \text{ GeV} \leq m_{\tilde{q}_3}, m_{\tilde{u}_3} \leq 2500 \text{ GeV}, \\
-5000 \text{ GeV} \leq T_t/Y_t = A_t \leq 5000 \text{ GeV}.
\end{gathered}$$

Out of the resulting sample of scenarios, we finally choose three representative scenarios which have to fulfill the following constraints:

$$(1) \quad \Omega_{\text{CDM}} h^2 = 0.1199 \pm 0.0027 \tag{4.5}$$

We require the neutralino relic density $\Omega_{\tilde{\chi}_1^0}$ to fall within the vicinity of the above Planck-result given at 1σ confidence level [45]. Hence, we expect the lightest neutralino to account for the whole CDM relic density in the universe. But since our higher-order corrections shift the final $\Omega_{\tilde{\chi}_1^0}$, we apply this bound rather loosely.

$$(2) \quad 122 \text{ GeV} \leq m_{h^0} \leq 128 \text{ GeV} \tag{4.6}$$

The mass of the lighter, CP-even Higgs h^0 (SM-like) is required to lie within the vicinity of LHC observations. We allow for an additional theoretical uncertainty of $\Delta m_{h^0} = \pm 3$ GeV due to higher-order corrections [169] that are not included in the used spectrum calculator `SPheno-3.2.3`.

$$(3) \quad 2.77 \cdot 10^{-4} \leq \text{BR}(b \to s\gamma) \leq 4.07 \cdot 10^{-4} \tag{4.7}$$

These bounds on the branching ratio $b \to s\gamma$ correspond to the HFAG value published in Ref. [170] at 3σ confidence level. They limit flavor changing neutral current contributions from the SUSY sector.

Finally, the chosen scenarios have to feature sizeable contributions of gaugino (co)annihilation into quarks to allow for a comprehensive analysis of the SUSY-QCD corrections calculated in the context of `ChiChi2qq`.

Table 4.1.: pMSSM input parameters for three selected reference scenarios. All parameters except $\tan\beta$ are given in GeV.

	$\tan\beta$	μ	m_A	M_1	M_2	M_3	$M_{\tilde{q}_{1,2}}$	$M_{\tilde{q}_3}$	$M_{\tilde{u}_3}$	$M_{\tilde{\ell}}$	T_t
I	13.4	1286.3	1592.9	731.0	766.0	1906.3	3252.6	1634.3	1054.4	3589.6	-2792.3
II	6.6	842.3	1566.9	705.4	1928.4	1427.0	1238.5	2352.1	774.1	2933.2	-3174.6
III	10.0	1100.0	1951.4	1848.0	1800.0	1102.3	3988.5	2302.0	1636.6	1982.1	-2495.3

Table 4.2.: Gaugino masses, the decomposition of the lightest neutralino and selected observables corresponding to the three reference scenarios of Tab. 4.1. All masses are given in GeV.

	$m_{\tilde{\chi}_1^0}$	$m_{\tilde{\chi}_2^0}$	$m_{\tilde{\chi}_3^0}$	$m_{\tilde{\chi}_4^0}$	$m_{\tilde{\chi}_1^\pm}$	$m_{\tilde{\chi}_2^\pm}$	$Z_{1\tilde{B}}$	$Z_{1\tilde{W}}$	$Z_{1\tilde{H}_1}$	$Z_{1\tilde{H}_2}$	m_{h^0}	$\Omega_{\tilde{\chi}_1^0}h^2$	BR$(b\to s\gamma)$
I	738.2	802.4	1288.4	1294.5	802.3	1295.1	-0.996	0.049	-0.059	0.037	126.3	0.1243	$3.0\cdot10^{-4}$
II	698.9	850.5	854.0	1940.2	845.6	1940.4	-0.969	0.012	-0.187	0.162	125.2	0.1034	$3.2\cdot10^{-4}$
III	1106.7	1114.9	1855.0	1865.6	1109.6	1856.3	0.046	-0.082	0.706	-0.702	126.0	0.1190	$3.2\cdot10^{-4}$

Our three representative scenarios I to III are now given in Tab. 4.1. Further important characteristics of these scenarios such as gaugino masses, the decomposition into gauge eigenstates and previously introduced observables are presented Tab. 4.2. As already stated above, these have been obtained using `SPheno 3.2.3` and `micrOMEGAs-2.4.1` with the standard `CalcHEP` implementation of the MSSM. As the only slight changes we set the light quark masses to zero, $m_u = m_d = m_s = 0$, and include a lower bound on the squark width $\Gamma_{\tilde{q}} > 0.01$ GeV. These modifications turn out to be necessary to stabilize the numerical evaluation of the NLO corrections, which are described further below. We checked that this does not influence the final relic density. As shown in Tab. 4.2, the selected scenarios fulfill the constraints above mentioned within the uncertainties required. A distinct analysis of the contributing (co)annihilation channels for each of the three scenarios is given in Tab. 4.3. We list all gaugino annihilation channels into light and heavy quarks, which contribute at least 0.1% to the thermally averaged total annihilation cross section. In Tab. 4.4, we further decompose the tree level into different subchannel contributions from the $s-$, $t-$ and $u-$channels as shown in Fig. 4.2. All results are given at a center of mass momentum $p_{\rm cm} = 100$ GeV, the region where the thermal distribution in the integrand of Eq. (3.39) roughly peaks for the parameter sets considered. We group the contributions from the s-channel scalar exchange (contribution denoted s_S), the s-channel contribution from vector boson exchange (s_V) and the exchange of squarks in the t- and u-channels (t/u). The contributions from the corresponding squared matrix elements are denoted $s_S \times s_S$, $s_V \times s_V$ and $t/u \times t/u$, while their interference terms are denoted by $s_S \times s_V$, $s_S \times t/u$, and $s_V \times t/u$. Negative numbers in Tab. 4.4 refer to destructive interferences. We perform all calculations in the Feynman gauge. Hence, we have to include the exchange of associated Goldstone bosons, which become the longitudinal polarization states of the particular massive vector boson. In Tab. 4.4 these Goldstone boson contributions are subsumed under the scalar s-channel exchange.
We now turn to the discussion of the three representative scenarios I-III:

- **Scenario I**: Scenario I is dominated by the coannihilation of the neutralino LSP $\tilde{\chi}_1^0$ with the lighter chargino $\tilde{\chi}_1^\pm$ into heavy quarks (see Tab. 4.3). This channel contributes to the total annihilation cross section by far the most, as its impact lies at approximately 43%. This is the case although this channel is Boltzmann suppressed via the mass splitting $m_{\tilde{\chi}_1^\pm} - m_{\tilde{\chi}_1^0}$ compared to the annihilation of the LSP. The next important channel happens to be the coannihilation between the LSP and the

Table 4.3.: Most relevant gaugino (co)annihilation channels into quarks in the reference scenarios of Tab. 4.1. Channels which contribute less than 0.1% to the thermally averaged cross section are not shown.

		Scenario I	Scenario II	Scenario III
$\tilde{\chi}_1^0\tilde{\chi}_1^0 \to$	$t\bar{t}$	1.4%	15.0%	–
	$b\bar{b}$	9.1%	5.9%	–
	$c\bar{c}$	–	0.1%	–
	$u\bar{u}$	–	0.1%	–
$\tilde{\chi}_1^0\tilde{\chi}_2^0 \to$	$t\bar{t}$	2.5%	12.0%	3.3%
	$b\bar{b}$	23.0%	6.9%	1.6%
	$c\bar{c}$	–	–	1.3%
	$s\bar{s}$	–	–	1.7%
	$u\bar{u}$	–	–	1.3%
	$d\bar{d}$	–	–	1.7%
$\tilde{\chi}_1^0\tilde{\chi}_3^0 \to$	$t\bar{t}$	–	9.1%	–
	$b\bar{b}$	–	5.3%	–
$\tilde{\chi}_2^0\tilde{\chi}_2^0 \to$	$b\bar{b}$	0.2%	–	–
$\tilde{\chi}_1^0\tilde{\chi}_1^\pm \to$	$t\bar{b}$	43.0%	40.0%	0.8%
	$c\bar{s}$	–	–	8.5%
	$u\bar{d}$	–	–	8.5%
$\tilde{\chi}_2^0\tilde{\chi}_1^\pm \to$	$t\bar{b}$	0.4%	–	0.4%
	$c\bar{s}$	0.9%	–	4.6%
	$u\bar{d}$	0.9%	–	4.6%
$\tilde{\chi}_1^\pm\tilde{\chi}_1^\pm \to$	$t\bar{t}$	0.2%	–	3.2%
	$b\bar{b}$	0.6%	–	2.7%
	$c\bar{c}$	0.2%	–	2.3%
	$s\bar{s}$	0.2%	–	1.4%
	$u\bar{u}$	0.2%	–	2.3%
	$d\bar{d}$	0.2%	–	1.4%
Total		83.0%	94.4%	51.6%

Table 4.4.: Sub-processes for the most important channels of Tab. 4.3 (more than 2%) contributing individually at least 0.1% at $p_{\mathrm{cm}} = 100$ GeV.

	$s_V \times s_V$	$s_V \times s_S$	$s_S \times s_S$	$s_V \times t/u$	$s_S \times t/u$	$t/u \times t/u$
Scenario I						
$\tilde{\chi}_1^0\tilde{\chi}_1^0 \to b\bar{b}$	–	–	90.5%	–	9.1%	0.4%
$\tilde{\chi}_1^0\tilde{\chi}_2^0 \to t\bar{t}$	–	0.1%	27.7%	0.1%	3.8%	33.8%
$\tilde{\chi}_1^0\tilde{\chi}_2^0 \to b\bar{b}$	–	–	96.1%	–	3.8%	0.1%
$\tilde{\chi}_1^0\tilde{\chi}_1^+ \to t\bar{b}$	2.8%	–	79.1%	-4.4%	11.4%	1.1%
Scenario II						
$\tilde{\chi}_1^0\tilde{\chi}_1^0 \to t\bar{t}$	–	–	3.2%	0.5%	1.3%	95.0%
$\tilde{\chi}_1^0\tilde{\chi}_1^0 \to b\bar{b}$	–	–	93.5%	–	6.4%	0.1%
$\tilde{\chi}_1^0\tilde{\chi}_2^0 \to t\bar{t}$	–	–	91.5 %	-0.1%	7.9%	0.7%
$\tilde{\chi}_1^0\tilde{\chi}_2^0 \to b\bar{b}$	–	–	99.8%	–	0.2%	–
$\tilde{\chi}_1^0\tilde{\chi}_3^0 \to t\bar{t}$	–	–	97.8%	–	2.1%	0.1%
$\tilde{\chi}_1^0\tilde{\chi}_3^0 \to b\bar{b}$	–	–	100.0%	–	–	–
$\tilde{\chi}_1^0\tilde{\chi}_1^+ \to t\bar{b}$	0.1%	–	84.0%	-0.5%	14.0%	2.4%
Scenario III						
$\tilde{\chi}_1^0\tilde{\chi}_1^+ \to c\bar{s}/u\bar{d}$	100.4%	–	–	-0.4%	–	–
$\tilde{\chi}_2^0\tilde{\chi}_1^+ \to c\bar{s}/u\bar{d}$	100.0%	–	–	–	–	–
$\tilde{\chi}_1^0\tilde{\chi}_2^0 \to t\bar{t}$	16.2%	–	1.0%	-111.2%	-2.7%	196.7%
$\tilde{\chi}_1^+\tilde{\chi}_1^- \to t\bar{t}$	46.2%	–	3.1%	-52.9%	-4.4%	108.0%
$\tilde{\chi}_1^+\tilde{\chi}_1^- \to b\bar{b}$	21.6%	–	0.7%	-131.4%	-0.4%	209.5%
$\tilde{\chi}_1^+\tilde{\chi}_1^- \to c\bar{c}/u\bar{u}$	100.2%	–	–	-0.2%	–	–

second lightest neutralino $\tilde{\chi}_2^0$ into bottom quarks, which contribut to $\langle\sigma_{\mathrm{eff}}v\rangle$ by 23%, whereas annihilation of the lightest neutralino into quarks turns out to be only the third most important channel contributing in total to $\langle\sigma_{\mathrm{eff}}v\rangle$ by roughly 10.5%. This hierarchy of processes can be explained with a view on Tab. 4.4. It is apparent that the s-channel scalar exchange is actually the most important contribution to the tree-level cross section. This can be traced back to s-channel resonances connected to the exchange of the pseudoscalar Higgs A^0 and the charged Higgs $H^\pm$ with masses $m_{A^0} = 1592.9$ GeV and $m_{H^\pm} = 1595.1$ GeV, which both lie very close to the total mass of the incoming particle pairs $m_{\tilde{\chi}_1^0} + m_{\tilde{\chi}_2^0} \approx m_{A^0}$ and $m_{\tilde{\chi}_1^0} + m_{\tilde{\chi}_1^\pm} \approx m_{H^\pm}$ ($m_{\tilde{\chi}_1^0} + m_{\tilde{\chi}_1^\pm} = 1540.5$ GeV and $m_{H^\pm} = 1595.1$ GeV, see Tab. 4.2). In contrast, the LSP with mass $2m_{\tilde{\chi}_1^0} = 1476.4$ GeV is already further away from the A^0-resonance and, hence, its annihilation through the s-channel exchange of the pseudoscalar Higgs is kinematically suppressed. One can also observe that the annihilation of the two lightest neutralinos into down-type quarks is enhanced compared to the corresponding channel into up-type quarks. This can be traced back to a sizeable $\tan\beta$, which is already large enough to favor bottom quarks in the final state due to a $\tan\beta$-enhanced bottom Yukawa coupling (see Tab. 4.2). Finally note that although kinematically even closer to the A^0-resonance ($2m_{\tilde{\chi}_2^0} \approx 2m_{\tilde{\chi}_1^\pm} \approx 1600$ GeV), the pair annihilation of the lighter chargino and of the second lightest neutralino do not sizeably contribute as their impacts on $\langle\sigma_{\mathrm{eff}}v\rangle$ turn out to be highly suppressed by the Boltzmann factor Eq. (3.58).

- **Scenario II**: Scenario II mainly differs from scenario I by a lower higgsino mass parameter μ and a much larger wino mass M_2. Their interplay modifies the composition of the lightest neutralino, which results in an increased higgsino admixture (see $Z_{1\tilde{H}_1}$ and $Z_{1\tilde{H}_2}$ in Tab. 4.2). Compared to scenario I, the hierarchy of dominant coannihilation channels is quite similar. The total annihilation cross section is still dominated by the coannihilation of the lightest neutralino $\tilde{\chi}_1^0$ with the lighter

chargino $\tilde{\chi}_1^\pm$ through the s-channel exchange of a $H^\pm$ which contributes to $\langle\sigma_{\text{eff}}v\rangle$ by 40%. However, the order of $\tilde{\chi}_1^0$-$\tilde{\chi}_1^0$ annihilation and $\tilde{\chi}_1^0$-$\tilde{\chi}_2^0$ is reversed, which contribute to $\Omega_{\tilde{\chi}_1^0}$ by 21.1% and by 18.9% in total. This can be ascribed to a larger mass gap between the LSP and $\tilde{\chi}_2^0$ compared to scenario I, which leads to a larger Boltzmann suppression of the $\tilde{\chi}_1^0\tilde{\chi}_2^0$ coannihilation process compared to the $\tilde{\chi}_1^0$ annihilation. Moreover, in scenario II, $\tan\beta = 6.6$ happens to be only roughly half as large as in scenario I. This gives rise to a decreased suppression/enhancement of up/down type Yukawa couplings, as can be seen in the increased importance of the top quark final state in Tab. 4.3. The $\tilde{\chi}_1^0$ annihilation is dominated by the t-channel exchange of the lighter top squark $\tilde{t}_1$ as apparent in Tab. 4.4. This can be traced back to a much lighter $\tilde{t}_1$ compared to scenario I ($m_{\tilde{t}_1} = 874.8$ GeV against $m_{\tilde{t}_1} = 1009.0$ GeV in scenario I) and in turn to a smaller propagator suppression. For the $\tilde{\chi}_1^0$-$\tilde{\chi}_2^0$ channel, the stop exchange turns out to be less relevant. Here, the kinematical configuration leads to a total mass of the incoming particles being very close to the resonance of the heavier CP-even Higgs boson, $m_{\tilde{\chi}_1^0} + m_{\tilde{\chi}_2^0} = 1549.4$ GeV and $m_{H^0} = 1567.1$ GeV. This yields a dominant contribution of the H^0 s-channel exchange. Since the mass gap between $\tilde{\chi}_1^0$ and the third neutralino is much smaller than in scenario I, there is still another non-negligible contribution due to the coannihilations between the LSP and the third lightest neutralino $\tilde{\chi}_3^0$. This process proceeds dominantly through the s-channel exchange of scalars. As previously seen, this can be ascribed to the kinematic situation close to the H^0-resonance ($m_{\tilde{\chi}_1^0}+m_{\tilde{\chi}_3^0} = 1552.9$ GeV$\approx m_{H^0}$). Finally, the vector exchange of Z and $W^\pm$ bosons in the s-channel turns out to be almost negligible for both scenario I as well as for scenario II. On the one hand, this is due to the kinematic situation, which suppresses the exchange of the comparatively light vector bosons ($m_Z, m_{W^\pm} \ll m_{\tilde{\chi}_1^0}$). On the other hand, this can be ascribed to the dominantly bino-like nature of the lighter neutralino, which suppresses any couplings to vector bosons as there is, for example, no bino-bino-Z coupling.

- **Scenario III**: Scenario III is quite diverse from the scenarios described so far. Here, the pMSSM-11 parameter set yields a dominantly higgsino-like LSP and a mass degeneracy between the two lightest neutralinos and the lightest chargino, which results in the spectrum of relevant (co)annihilation channels as shown in Tab. 4.3. As a consequence, the LSP-pair annihilation is basically negligible, whereas coannihilation with the second lightest neutralino and the lighter chargino as well as chargino-pair annihilation turn out to be the dominant processes. Moreover, the configuration at this parameter point leads to final states with first and second-generation quarks that are dominant, while contributions from third-generation quarks only amount by 12% overall. Tab. 4.4 shows that, in contrast to the two scenarios described above, all (co)annihilation proceeds through the t- and u-channel squark exchange as well as through the s-channel exchange of vector bosons. The former are driven by a, compared to the involved gauginos, relatively light $\tilde{t}_1$ ($m_{\tilde{t}_1} = 1664.2$ GeV) and, hence, by a numerically less suppressed squark propagator. The latter becomes sizeable due to the higgsino nature of the lighter gauginos whose annihilation can now proceed, e.g., through the higgsino-higgsino-Z vertex. This configuration also leads to an increased importance of destructive interferences between the squark exchange and the s-channel vector contributions. Finally, the exchange of the heavier Higgs turns out to be negligible as their resonances already lie below the total mass of the incoming particles (e.g., $m_{\tilde{\chi}_1^0} + m_{\tilde{\chi}_1^\pm} > m_{H^\pm} \sim m_{A^0} = 1951.4$ GeV).

This completes the introduction of the (co)annihilation of gauginos into light and heavy quarks at the tree level. The actual existence of scenarios with sizeable contributions from a large variety of different gaugino (co)annihilation processes can be seen as the original motivation for the work presented here, especially since these regions of important gaugino (co)annihilation turn out to stretch over wide ranges of the pMSSM-11 parameter space, as described in the following chapters.

4.3. QQ2xx: Squark (Co)Annihilation into Electroweak Final States

4.3.1. The Tree Level

The following section and especially all results shown in the context of `QQ2xx` rely on the publication [2]. This section is conceptually closely related to the previous chapter about gaugino (co)annihilation.

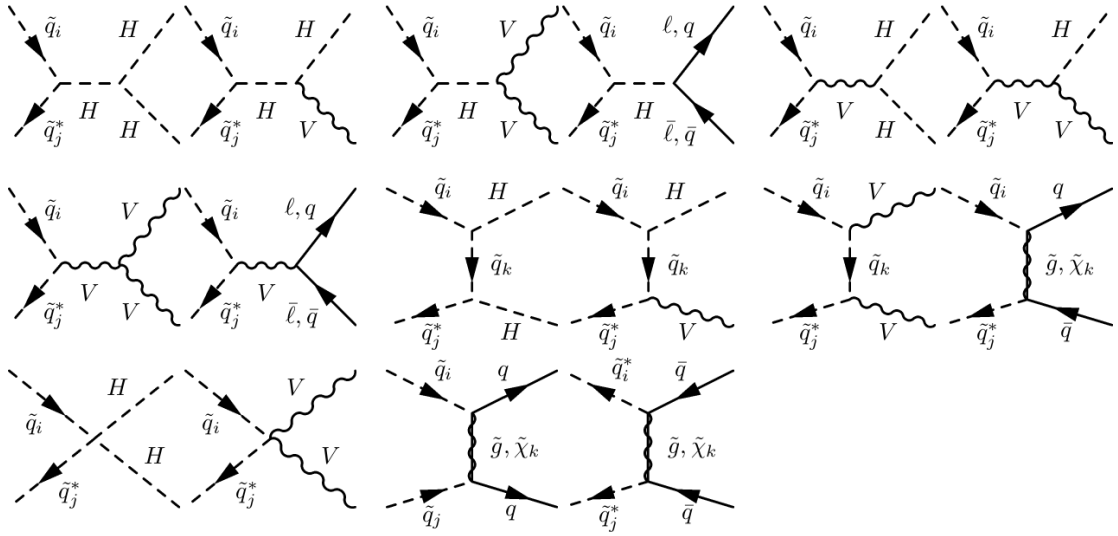

Figure 4.4.: Tree-level diagrams of squark (co)annihilation processes included in `QQ2xx` with $H \in \{\mathrm{h}^0, \mathrm{H}^0, \mathrm{A}^0, \mathrm{H}^\pm\}$, $V \in \{G, \gamma, Z, W^\pm\}$ and q/ℓ can be any quark/lepton. $\tilde{\chi}_k \in \{\tilde{\chi}_k^0, \tilde{\chi}_k^\pm\}$ depending on the initial-state net charge. u-channel diagrams ar not explicitly shown but can be obtained through crossing of final states in the corresponding t-channel graphs.

The `QQ2xx` software package covers all squark-antisquark (co)annihilations into arbitrary SM-final states at tree level as depicted in Fig. 4.4. Depending on the initial-state net electric charge, the corresponding cross sections get contributions from the s-channel exchange of one of the five Higgs-bosons h^0, H^0, A^0 and $H^\pm$ as well as through the s-channel vector exchange of a photon, Z- or $W^\pm$-boson. Moreover, additional contributions come from the t- and u- channel exchange of scalar quarks in case of bosonic as well as of gluinos and neutralinos/charginos (again depending on the initial-state net charge) in case of fermionic final states. Finally, contributions arise due to quartic (quartic=four external particles) couplings of squarks with Higgs or vector bosons as well as from (anti)squark+(anti)squarks pairs going into two (anti)quarks. In contrast to the case of gauginos, these new quartic

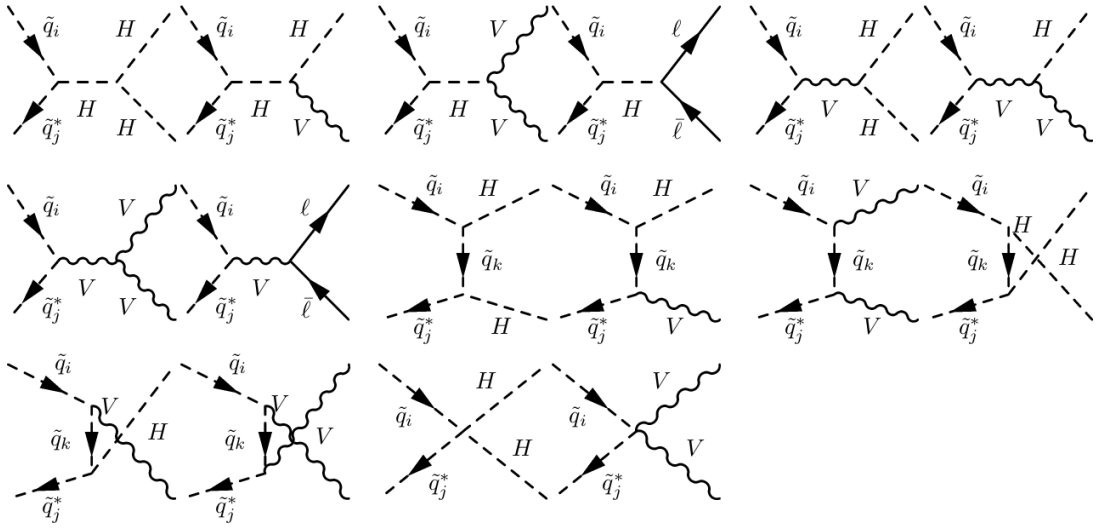

Figure 4.5.: Tree-level diagrams of squark (co)annihilation processes, whose higher-order corrections are included in `QQ2xx`. Here $H = \mathrm{h}^0, \mathrm{H}^0, \mathrm{A}^0, \mathrm{H}^\pm$, $V = \gamma, \mathrm{Z}, \mathrm{W}^\pm$ and ℓ can be any lepton.

couplings arise since we only encounter scalars in the initial state. As a coupling of four boson possesses an overall mass dimension equal to four, such interaction terms turn out to be renormalizable (see Sec. 5.1.1), whereas fermions, which posses a mass dimension [fermion] $= \frac{3}{2}$, cannot pair up with two bosons to form a quartic coupling without violating renormalizability. Therefore, we do not encounter such interactions in the gaugino (co)annihilations of part Sec. 4.2. Finally, note that all tree-level cross sections included in `QQ2xx` have been cross checked with `CalcHEP` replacing effective couplings and running masses in `CalcHEP` and `QQ2xx` if necessary. We found an agreement with a precision of $1/10^4$ or better for all processes considered.
Besides the pure tree level, the `QQ2xx` package also includes the full SUSY-QCD $\mathcal{O}(\alpha_s)$ corrections for a subset of the processes above shown in Fig. 4.5, namely for squark (co)annihilation going into EW final states (i.e. leptons, EW vectors and Higgs bosons)

$$\tilde{q}_i\tilde{q}_j^* \to VV, \tag{4.8}$$
$$\tilde{q}_i\tilde{q}_j^* \to VH, \tag{4.9}$$
$$\tilde{q}_i\tilde{q}_j^* \to HH, \tag{4.10}$$
$$\tilde{q}_i\tilde{q}_j^* \to \ell\bar{\ell}. \tag{4.11}$$

The condition for these corrections to have a sizable impact on the calculation of $\Omega_{\tilde{\chi}_1^0}$ remains the same as in the gaugino (co)annihilation case, i.e, the mass of the (co)annihilating squark has to be close to the LSP mass to evade a large Boltzmann suppression. Due to the considerations of Sec. 2.6.3, it turns out that *the lighter stop $\tilde{t}_1$ is realized as the NLSP over wide ranges of the pMSSM parameter space.* In addition, there is ample theoretical and phenomenological motivation, which give hints on a light stop. We shortly present a few of them in the following

4.3.2. Motivations for a Light Stop

- **A light stop and the relic density**: It turns out that for most of the MSSM parameter space, the neutralino annihilation cross section alone is actually too small to

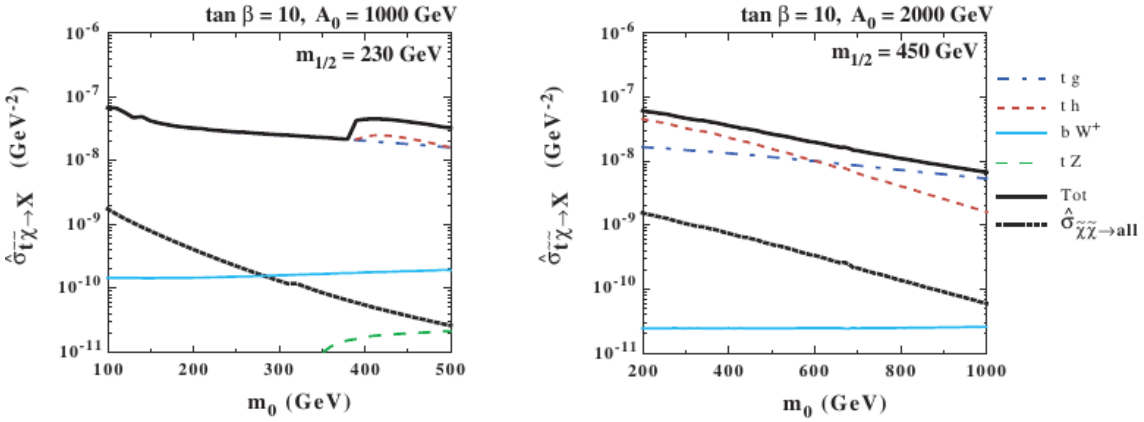

Figure 4.6.: Contribution of $\tilde{\chi}_1\tilde{t}_1$ coannihilation to $\langle\sigma_{\text{eff}}v\rangle \approx a + \frac{1}{2}bx$ at $x = 1/23$ for different final states as a function of the SUSY-breaking universal scalar mass m_0 (note that m_0 does not equal the neutralino mass here). Furthermore, the universal gaugino mass $m_{\frac{1}{2}}$ as well as the universal trilinear A_0 coupling (a) $m_{\frac{1}{2}} = 230$ GeV, $A_0 = 1000$ GeV and (b) $m_{\frac{1}{2}} = 450$ GeV, $A_0 = 2000$ GeV are varied. The total cross section as well as the associated contributions from neutralino annihilation are also shown. Figure taken from [171].

yield efficient annihilation of neutralinos in order to meet the cosmologically favored relic density Eq. (3.57)

$$\Omega h^2 \propto \frac{1}{\langle\sigma_{\text{eff}}v\rangle} \tag{4.12}$$

within the experimental uncertainty. To circumvent an associated overproduction of neutralino LSPs, the total annihilation cross section of $\langle\sigma_{\text{eff}}v\rangle$ Eq. (3.38) needs to be enhanced by additional mechanisms, e.g., by resonant neutralino annihilation within Higgs-funnel regions [144] or by efficient coannihilation. Both can be obtained by choosing an appropriate MSSM-parameter set.

As described in Sec. 3.4.4, coannihilation becomes phenomenologically relevant if the mass of the coannihilating particle, typically the NLSP, is close to the mass of the neutralino LSP to avoid a large Boltzmann suppression. Besides the heavier gauginos presented above, it turns out that the lighter top squark $\tilde{t}_1$ is a suitable candidate as it happens to be the NLSP for many MSSM scenarios. Hence, it can significantly contribute to the total annihilation cross section potentially driving the relic density to the right ballpark as favored by cosmology [171]. This is explicitly shown in Fig. 4.6 and Fig. 4.7 for several cMSSM (constrained MSSM) scenarios, where the different contributions to the partial wave expansion of the total, thermally averaged annihilation cross section

$$\langle\sigma_{\text{eff}}\rangle \approx a + \frac{1}{2}bx \tag{4.13}$$

with $x = T_{\text{freeze}}/m_\chi$ are shown. It is apparent that stop annihilation can sizeably contribute to Eq. (4.13) and can even overcome the contributions of neutralino annihilation as well as the ones from the corresponding stop coannihilation by far.Hence, although the presented scenarios are already excluded by the LHC, these plots serve well to exemplify the potential importance of $\tilde{t}_1$ (co)annihilation in terms of neutralino DM and to emphasize the importance of $\tilde{t}_1\tilde{t}_1^*$ annihilation for the neutralino relic density.

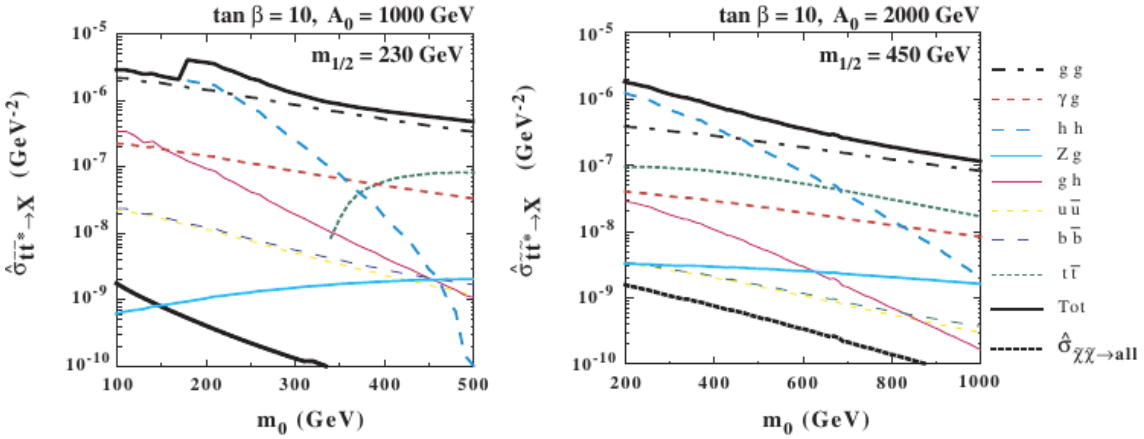

Figure 4.7.: Same as Fig. 4.6, but for $\tilde{t}_1\tilde{t}_1^*$ annihilation. Figure taken from [171].

- **A light stop at colliders**: To keep SUSY models natural, one is led to the assumption that SUSY breaking should take place at around 1 TeV to not reintroduce the problem of fine-tuning. This is of particular interest for the third generation squarks as they turn out to give large radiative corrections to m_{h^0} (see Sec. 2.2.1) and, in turn, are especially affected by this bound. But as the LHC moves on to exclude larger and larger pieces of the MSSM-parameter space with increasing energy and higher integrated luminosity, the non-observance of sparticles puts pressure on these low scale SUSY models and tends to shift the SUSY breaking scale toward higher and higher values. However, one can circumvent this constraint via so called compressed SUSY-mass spectra [172, 173]. These assume a compressed mass hierarchy in the SUSY sector in order that the different sparticle masses lie very close to each other. These scenarios may then evade detection while staying relatively light since the identification of SUSY events at the LHC takes place by the observance of signatures connected to the decay chains of SUSY-particle going into the LSP, i.e., going into SM-particles plus missing energy as the lightest neutralino is typically able to escape the detector unhinderedly[4]. However, when the sparticles produced in proton-proton collision lie close in mass to the LSP, e.g., for a mass splitting $\Delta_{m_{\tilde{t}_1-\tilde{\chi}_1^0}} = m_{\tilde{t}_1} - m_{\tilde{\chi}_1^0} < m_t$, certain decay products tend to be very soft (or even non-existent, if the available energy difference $\Delta_{m_{\tilde{t}_1-\tilde{\chi}_1^0}}$ turns out to be too small) and may therefore exacerbate detection. Hence, compressed spectra with a light third squark generation can allow for low scale SUSY while still evading the LHC exclusion bounds. Consequently, this argues for a stop mass close to the LSP mass if the fine-tuning problem is taken seriously.

- **A light stop in the light of a $\mathbf{m_{h^0} \approx 125}$ GeV Higgs**: The existence of a light stop gets further support from the LHC discovery of a new boson with a mass of $m \approx 125$ GeV [5, 6, 174]. If we interpret this as the light "SM-like" Higgs boson h^0, its squared MSSM tree-level mass (see Eq. (2.107))

$$m^2_{h^0,\text{tree}} = \frac{1}{2}\left[m^2_{A^0} + M^2_Z - \{(m^2_{A^0} + M^2_Z)^2 - 4M^2_Z m^2_{A^0}\cos^2 2\beta\}^{1/2}\right] \tag{4.14}$$

needs to be enhanced, e.g., by a large stop-loop contribution. In the decoupling limit

[4] Here, we assume a neutralino LSP which is stable on cosmological time scales as necessary for CDM and as guaranteed, e.g., via imposing R-parity.

Table 4.5.: Input parameters for the three selected reference scenarios in the pMSSM. All values except $\tan\beta$ are given in GeV.

	$\tan\beta$	μ	m_{A^0}	M_1	M_2	M_3	$M_{\tilde{q}_{1,2}}$	$M_{\tilde{q}_3}$	$M_{\tilde{u}_3}$	$M_{\tilde{\ell}}$	T_t
Ia	16.3	2653.1	1917.9	750.0	1944.1	5832.4	3054.3	2143.7	1979.0	2248.3	-3684.1
Ib	16.3	2653.1	1917.9	989.0	1944.1	5832.4	3054.3	2143.7	2159.0	2248.3	-3684.1
II	27.0	2650.8	1441.5	1300.0	1798.4	1744.8	2189.7	2095.3	1388.0	1815.5	-4097.9

$m_{A^0} \gg m_Z$ this takes the form [175, 176]

$$m_{h^0}^2 \;\approx\; m_Z^2 \cos^2 2\beta + \frac{3g^2 m_t^4}{8\pi^2 m_{W^\pm}^2}\left[\ln\left(\frac{M_{\text{SUSY}}^2}{m_t^2}\right) + \frac{X_t^2}{M_{\text{SUSY}}^2}\left(1 - \frac{X_t^2}{12 M_{\text{SUSY}}^2}\right)\right], \quad (4.15)$$

where $X_t = A_t - \mu\tan\beta$ and $M_{\text{SUSY}} = \sqrt{m_{\tilde{t}_1} m_{\tilde{t}_2}}$. For these contributions to become sufficiently large while still keeping the theory natural $|X_t| \approx \sqrt{6}\, M_{\text{SUSY}}$ needs to be fulfilled which maximizes the stop-loop contributions at fixed M_{SUSY}. This in turn hints toward a sizable A_t and, hence, toward a large stop mass splitting $m_{\tilde{t}_1} \ll m_{\tilde{t}_2}$ (see Eq. 2.131) driving $\tilde{t}_1$ to be rather light.

To draw a final conclusion, of the different squark-(co)annihilation channels, which contribute to the neutralino relic density, annihilation of the lighter stop $\tilde{t}_1$ turns out to be of main interest as it is a natural NLSP over wide ranges of the MSSM parameter space. Moreover, there is ample motivation why SUSY, if realized in nature, may come with a light stop $\tilde{t}_1$. Therefore, the focus of the subsequent analyses lies on $\tilde{t}_1$ annihilation.

4.3.3. The Representative Scenarios

We now move on to the introduction of our representative scenarios, which we use to investigate on the impact of our higher-order corrections on Ω_{CDM}. For this purpose, we reuse the parameter points we found in the pMSSM-11 parameter scan described in Ch. 4.2. However, the constraints imposed on the collection of scenarios are slightly changed although their motivation remains the same (see Sec. 4.2):

$$0.1145 \leq \Omega_{\text{CDM}} h^2 \leq 0.1199 \quad (4.16)$$

$$120 \text{ GeV} \leq m_{h^0} \leq 130 \text{ GeV} \quad (4.17)$$

$$2.56 \cdot 10^{-4} \leq \text{BR}(b \to s\gamma) \leq 4.54 \cdot 10^{-4} \quad (4.18)$$

$$|a_\mu| < 288 \cdot 10^{-11} \quad (4.19)$$

The last constraint limits the SUSY corrections $\delta a_\mu = a_\mu^{\text{exp}} - a_\mu^{\text{theo}}$ to the muon g-factor g_μ with $a_\mu = (g_\mu - 2)/2$ taken from Ref. [177]. We expect the SUSY corrections of the particular pMSSM-11 scenario to improve this discrepancy.

Beside these limits on important observables, we require the representative scenarios to provide a rich spectrum of squark-annihilation channels into EW final states as described above to demonstrate the impact of our NLO corrections. Based on our scans of the pMSSM-11 parameter, we choose the three scenarios presented in Tab. 4.5. Note that we have introduced two scenarios, named Ia and Ib, which only differ by the choice of the two parameters M_1 and $m_{\tilde{u}_3}$. As the shift in these two parameters effects the lighter stop mass $m_{\tilde{t}_1}$ as well as the mass $m_{\tilde{\chi}_1^0}$ of the neutralino-LSP, this has far reaching consequences as

Table 4.6.: Physical squark, neutralino, chargino and Higgs masses, the bino ($\tilde{B}$) contribution to $\tilde{\chi}_1^0$, the decomposition of $\tilde{t}_1$ into left- and right-handed parts, and selected observables corresponding to the reference scenarios of Tab. 4.5. All masses are given in GeV.

	$m_{\tilde{\chi}_1^0}$	$m_{\tilde{t}_1}$	$m_{\tilde{t}_2}$	$m_{\tilde{b}_1}$	$m_{\tilde{\chi}_2^0}$	$m_{\tilde{\chi}_1^\pm}$	m_{h^0}	m_{H^0}	$m_{H^\pm}$	$\lvert Z_{\tilde{\chi}^0,1\tilde{B}}\rvert^2$	$\lvert Z_{\tilde{t},1L}\rvert^2$	$\lvert Z_{\tilde{t},1R}\rvert^2$	BR($b \to s\gamma$)	δa_μ	$\Omega_{\tilde{\chi}_1^0}h^2$
Ia	758.0	826.1	1435.1	1260.5	1986.7	1986.8	128.8	1917.4	1919.6	0.9996	0.27	0.74	$3.1 \cdot 10^{-4}$	$284 \cdot 10^{-11}$	0.1146
Ib	999.6	1079.6	1543.4	1265.8	1986.8	1986.9	129.4	1917.9	1919.6	0.9995	0.55	0.46	$3.1 \cdot 10^{-4}$	$284 \cdot 10^{-11}$	0.1193
II	1306.3	1363.0	2128.8	2055.2	1826.9	1827.1	124.6	1440.7	1443.6	0.9992	0.08	0.92	$3.1 \cdot 10^{-4}$	$279 \cdot 10^{-11}$	0.1209

Table 4.7.: Most relevant stop annihilation channels into EW final states of the reference scenarios in Tab. 4.5.

		Scenario Ia	Scenario Ib	Scenario II
$\tilde{t}_1\tilde{t}_1^* \to$	h^0h^0	46.1%	15.9%	11.3%
	h^0H^0	–	46.6%	11.1%
$\tilde{t}_1\tilde{t}_1^* \to$	ZA^0	–	4.0%	7.4%
	$W^\pm H^\mp$	–	4.2%	13.6%
$\tilde{t}_1\tilde{t}_1^* \to$	ZZ	8.7%	4.3%	7.4%
	W^+W^-	12.5%	2.7%	13.6%
Total		67.3%	77.7%	64.4%

we show further below. Masses and mixings, which become relevant in the phenomenological analysis, as well as the values of the above observables are given in Tab. 4.6. They have been obtained using `micrOMEGAs 2.4.1` with the standard `CalcHEP` [164] implementation of the MSSM. In addition, we adopt some slight changes on the CalcHEP model files to render the evaluation of the higher-order corrections numerically stable. They are discussed later in the context of the corresponding higher-order corrections, when their motivation becomes clearer. However, it turns out that these changes do not have a large impact on the final result.

In order to better understand the origin and impact of the radiative corrections in our scenarios, we dissect all scenarios and show which processes are of particular importance in which parameter point. We therefore present the contributions of the different (co)annihilation channels to the thermally averaged total cross section in Tab. 4.7, where channels have to contribute at least 1% to $\langle\sigma_{\text{eff}}v\rangle$ to be listed. One sees that especially stop annihilation can largely contribute to the relic density covering a broad variety of different EW SM-final states. Hence, it is apparent that the full set of processes presented in Eqs. (4.8)-(4.11) can become relevant[5]. We also show all remaining, sizable contributions to $\langle\sigma_{\text{eff}}v\rangle$, which are not corrected in this work as they do not subsume under the processes listed in the Eqs. (4.8) to (4.11) in Tab. 4.8. Furthermore, as in the case of gaugino (co)annihilation, in Tab. 4.9 we present a decomposition of the tree-level cross sections considered into the different subchannels as given in Fig. 4.5. We group the contributions from quartic couplings (contribution denoted as Q), s-channel scalar exchange (denoted s_S), and the squark exchange in the t- and u-channels (t/u). The vector contributions s_V to the s-channel is absent in Tab. 4.9 as they turn out to be negligible within our reference scenarios (see below). The corresponding contributions from the squared matrix elements are denoted as $Q \times Q$, $s_S \times s_S$ and $t/u \times t/u$, while the interference terms are denoted as

[5]The case of fermionic final states is a bit more peculiar and is discussed further below. However, it turns out that even these final states can contribute sizeably, e.g., in the vicinity of s-channel resonances.

Table 4.8.: Most relevant (co)annihilation channels which are not included within the corrections of this work for the reference scenarios of Tab. 4.5. Channels which contribute less than 1% to the thermally averaged cross section are not shown.

	Scenario Ia	Scenario Ib	Scenario II
$\tilde{\chi}_1^0\tilde{t}_1 \to h^0 t$	10.8%	5.3%	1.4%
$\tilde{\chi}_1^0\tilde{t}_1 \to gt$	5.8 %	2.8%	6.3%
$\tilde{\chi}_1^0\tilde{t}_1 \to Zt$	1.2%	1.7%	–
$\tilde{t}_1\tilde{t}_1 \to tt$	–	–	7.7%
$\tilde{t}_1\tilde{t}_1^* \to h^0 g$	1.5%	1.0%	–
$\tilde{t}_1\tilde{t}_1^* \to H^0 g$	–	1.3%	–
$\tilde{t}_1\tilde{t}_1^* \to \gamma g$	–	–	1.8%
$\tilde{t}_1\tilde{t}_1^* \to b\bar{b}$	1.5%	1.6%	–
$\tilde{t}_1\tilde{t}_1^* \to t\bar{t}$	5.3%	1.5%	–
$\tilde{t}_1\tilde{t}_1^* \to gg$	4.3%	3.9%	12.3%
Total	30.4 %	19.1%	29.5%

$Q \times s_S$, $Q \times t/u$ and $s_S \times t/u$. Negative values again refer to destructive interferences. The percentages in Tab. 4.9 are obtained for the center-of-mass momentum of the incoming particles $p_{\text{cm}} = 200$ GeV, which is roughly the region where the thermal distribution in the integrand of Eq. (3.39) peaks for the scenarios presented here. All calculations are performed in the 't Hooft-Feynman gauge. Moreover, we follow the treatment of external vector bosons as presented in App. B of Ref. [178] and App. C of Ref. [179]. Hence, we replace the sum over polarizations of final-state vectors by $-g_{\mu\nu}$ and add the contributions of Goldstone bosons and Faddeev-Popov ghosts to correct for the corresponding wrong counting of physical polarization states. Before we turn to the discussion of the unique characteristics of each of the three representative scenarios, we firstly give some more general statements. First of all, note that since the incoming scalar-antiscalar configuration is CP-even and since all relevant interactions are CP-conserving, every intermediate and final state has to be CP-even, too. This limits all possible final states such that pseudoscalar Higgs bosons can appear only in pairs or together with a suitable vector boson and are otherwise partial-wave suppressed (see Tab. 4.7). The same argument prohibits any exchange of pseudoscalars in the s-channel. Finally, any s-wave annihilation through the s-channel exchange of vector bosons is forbidden due to conservation of total angular momentum (see Tab. 4.9), whereas p-wave annihilation through the s-channel vector exchange is possible but again partial-wave suppressed. These statements follow solely from the general physics of the initial states and the model under consideration and are basically scenario independent. Further scenario dependent investigations for each of the chosen models are given in the following.

- **Scenario Ia**: In scenario Ia, $\tilde{t}_1$ annihilation into EW final states contributes by 67.3% to $\Omega_{\tilde{\chi}_1^0}h^2$. The dominant contribution stems from the h^0h^0 final state (46.1%), whereas final states that include one or more of the heavier Higgs bosons H^0, A^0, $H^\pm$, are already too heavy to be kinematically accessible. One also encounters a relative dominance of the Higgs-Higgs final state over the vector-vector final states, where the latter contribute by roughly 21% to the relic density. This dominance can be traced back to the fact that the Higgs coupling to scalar top quarks is actually enhanced compared to all other relevant couplings, e.g., the gauge interactions of EW vector bosons to squarks. It is caused by a large top mass and a large trilinear coupling

Table 4.9.: Sub-processes for the channels of Tab. 4.7 contributing individually at least 0.1% at $p_{\mathrm{cm}} = 200$ GeV.

		$Q \times Q$	$Q \times s_S$	$Q \times t/u$	$s_S \times s_S$	$s_S \times t/u$	$t/u \times t/u$
Scenario Ia							
$\tilde{t}_1\tilde{t}_1^* \to$	h^0h^0	0.7%	-0.2%	-17.5%	–	2.4%	114.6%
	ZZ	2.7%	-0.3%	-37.7%	-4.8%	4.2%	135.9%
	W^+W^-	2.2%	-0.4%	-32.7%	-6.1%	6.1%	131.0%
Scenario Ib							
$\tilde{t}_1\tilde{t}_1^* \to$	h^0h^0	2.1%	-0.2%	-32.9%	–	1.5%	129.6%
	h^0H^0	–	–	0.6%	–	-0.6%	100.0%
	ZA^0	–	–	2.3%	-21.7%	10.3%	109.0%
	$W^\pm H^\mp$	–	–	1.8%	-35.4%	32.9%	100.8%
	ZZ	5.1%	-0.3%	-54.5%	-5.3%	4.3%	150.7%
	W^+W^-	6.6%	-1.2%	-52.4%	-19.2%	18.7%	147.7%
Scenario II							
$\tilde{t}_1\tilde{t}_1^* \to$	h^0h^0	8.0%	-0.4%	-72.2%	–	1.8%	162.7%
	h^0H^0	–	–	2.4%	–	-0.6%	98.2%
	ZA^0	–	–	3.0%	-2.1%	1.4%	97.7%
	$W^\pm H^\mp$	–	–	2.9%	-1.8%	0.8%	98.1%
	ZZ	11.9%	-0.3%	-92.6%	-3.5%	3.1%	181.4%
	W^+W^-	11.4%	-0.3%	-90.1%	-3.1%	3.0%	179.2%

$A_t \propto T_t$, where the large A_t is needed to achieve a sizable stop-loop contribution to m_{h^0} as discussed in the previous section. This enhancement is of special importance for the t- and u-channels where the enhanced stop-Higgs/Goldstone-boson coupling enters twice. This results in large contributions and explains the overall dominance of the t- and u-subchannels as given in Tab. 4.9. Although the massive vector final states get contributions from Goldstone bosons, which give rise to couplings as large as the usual Higgs couplings, their corresponding t- and u-channels contributions are further suppressed by large propagators. This is due the fact that G^0 as a pseudoscalar only couples light and heavy squark mass eigenstates. Furthermore, the charged Goldstone boson $G^\pm$ connects up- and down-type squarks which, in scenario Ia, leads to contributions of t- and u-channel diagrams where the exchanged particle is much heavier than the lighter stop $\tilde{t}_1$. This finally results in an overall propagator suppression of the Goldstone boson contributions to vector-vector final states relative to, e.g., the h^0h^0 final state.

- **Scenario Ib**: In scenario Ib, we correct diagrams that in total contribute to $\Omega_{\tilde{\chi}_1^0}h^2$ by 77.7%. The situation is quite similar to scenario Ia, except for the lightest stop, which is heavy enough so that the heavier Higgs bosons are now kinematically accessible, too. As the final state has to be CP-even, the only additional, sizeable contributions stem from the h^0H^0, ZA^0 as well as from the $W^\pm H^\mp$ final states (see Tab. 4.7). Comparing the scenarios Ia and Ib, one encounters a shift of the main contribution to the relic density from the h^0h^0 final state to the h^0H^0 final state. This is the most important channel of scenario Ib contributing to $\Omega_{\tilde{\chi}_1^0}h^2$ by 46.6%. This shift is mainly driven by the dominant t- and u-channel contributions in Tab. 4.9. The special feature of the h^0H^0 final state is that it features $m_{h^0} + m_{H^0} \approx 2m_{\tilde{t}_1}$. Moreover, since the dominant contribution to any cross section relevant to $\Omega_{\tilde{\chi}_1^0}h^2$ is due to the region $\sqrt{s} \approx 2m_{\tilde{t}_1}$, the final-state Higgs bosons h^0H^0 cannot have large momenta. For the h^0H^0 final states, the t- and u-channel propagators are therefore close to their mass shells, whereas for the h^0h^0 final state these propagators can still be far

off their mass shells. This even outweighs the larger accessible phase space of the h^0h^0 pair and translates into the h^0H^0 final state being the leading contribution.

- **Scenario II**: In scenario II, 64.4% of the contributions to $\Omega_{\tilde{\chi}_1^0}h^2$ are affected by our corrections. The mass difference between the squarks and the heavier Higgs boson leads to the same structure of relevant processes as in scenario Ib but, in contrast to the two scenarios encountered previously, scenario II is chosen in order that it gets roughly equal contributions from all possible vector and Higgs boson combinations in the final state.

In Tab. 4.7, one further encounters an absence of final states containing one or more photons. These comparatively low contributions can be traced back to the fact that the photon as the massless ($\rightarrow$ no coupling to the electrically neutral Higgs sector) gauge boson of the Abelian $U(1)$ ($\rightarrow$ no coupling to any other electrically neutral gauge boson) possesses no s-channel contributions to $\tilde{t}_1\tilde{t}_1^*$ annihilation. In addition, since the photon can not be longitudinally polarized, there are no Goldstone boson contributions to photons in the final state, which turned out to be the dominant contributions to the ZZ and W^+W^- final states as explained above. Finally, as the photon coupling to sfermions is diagonal in the squark mass eigenbasis, the $\tilde{t}_1$ annihilation lacks all contributions of $\tilde{t}_2$-exchange in the t- and u-channel. All together, this results in the absence of final states containing one or two photons as shown in Tab. 4.7. Any other (co)annihilation channels such as, e.g., coannihilation with heavier neutralinos, charginos, sbottoms, etc., turn out to be irrelevant in our scenarios Ia/b and II as the mass gaps between all these particles and the lightest neutralino turn out to be too large already (see Tab. 4.6), which prevents these particles from significantly altering $\Omega_{\tilde{\chi}_1^0}h^2$ due to a large Boltzmann suppression (see Eq. (3.58)).

This ends the introductory discussion of the two different sub-projects connected to this thesis, gaugino (co)annihilation into quarks (`ChiChi2qq`) and squark (co)annihilation into electroweak SM final states (`QQ2xx`). We now move on to the main part of this thesis, the inclusion of the corresponding higher-order corrections of $\mathcal{O}(\alpha_s)$ and (partly) beyond. However, their evaluation makes it mandatory to introduce new calculational methods. Therefore, we start with the discussion of the higher-order corrections on quite general grounds, providing the necessary calculational tools, before we move on to the explicit calculation of the relevant $\mathcal{O}(\alpha_s)$ corrections for each of the sub-projects above mentioned.

5. Calculation of Higher-Order Corrections

In the course of higher-order calculations, one typically encounters infinities at interim stages or in final results, which make it mandatory to have completely new calculational methods at hand to render expressions numerically evaluable or to even obtain physically meaningful results. In terms of NLO calculations, there are the prominent examples of the so-called *soft* (= low momentum) and *collinear* (= small angle) [180] as well as *ultraviolet* (UV, high momentum) [181] divergences, which are deeply connected to the arising integrations over unconstrained momenta.
The appearance of UV-divergences makes it necessary to introduce the methods of *regularization* and *renormalization*, where roughly speaking, in the step of regularization the infinities are rendered finite by the use of a certain regularization procedure such that the infinities manifest themselves as poles in a variable specific to the particular regularization scheme. In the subsequent step of renormalization, these poles are subtracted by so-called counterterms, which need to be defined within a certain *renormalization scheme*.
In contrast to UV-divergences, soft and collinear divergences actually appear only at interim stages and can typically be made to cancel in the final result of appropriately (here sufficiently *inclusive*, see below) defined observables. However, a numerical evaluation of soft and collinear divergent amplitudes turns out to be far from trivial as the different divergences reside in distinct integrands, which have to be integrated over different phase spaces. As each of these integrals is ill defined, it is not possible to evaluate them separately numerically. This makes it mandatory to follow a similar road of regularization and clever subtraction of soft and collinear divergences as in the UV case.

5.1. Virtual Corrections and the Treatment of UV Divergences

5.1.1. The Appearance of UV-Divergences

Due to integrations over unconstrained momenta, divergent loop integrals are often encountered in terms of higher-order corrections. A typical N-loop amplitude I_N can be grasped in the generic form [12]

$$I_N \propto \int d^4q_1 d^4q_2 ... d^4q_N \; \frac{F(q_1, q_2, ..., q_N)}{(\not{q}_1 - m_1)...(q_j^2 - m_j^2)...q_N^2}, \tag{5.1}$$

with an arbitrary polynomial $F(q_1, q_2, ..., q_N)$, which is nonsingular in the internal momenta q_i. For every loop, there is a potentially divergent four-momentum integral, whose divergence (convergence) may be softened (enhanced) by additional powers of q_i in the denominator from internal propagators. Roughly speaking, this integral converges if there are more powers of q_i in the denominator than in the numerator for every $i \in \{1, 2, .., N\}$. One can then introduce the *superficial degree of divergence*

$$D = \#\text{ of momenta in numerator} - \#\text{ of momenta in denominator}, \tag{5.2}$$

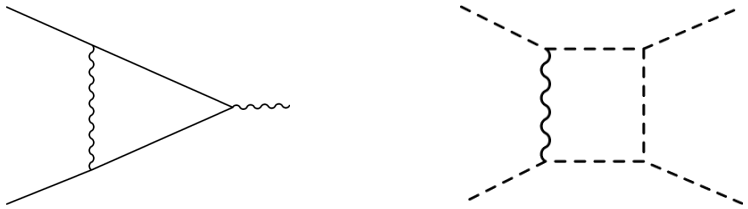

Figure 5.1.: Degree of divergence D for the triangle [$D = 0 \rightarrow$ UV divergent], and the box diagram [$D = -2 \rightarrow$ UV-convergent].

which quantifies if the numbers of factors of q_i in the nominator outweighs the number of q_i in the denominator or not. In turn, the superficial degree of divergence of the integrand can be related to the number of vertices and external particles (propagators) of the associated Feynman (sub)diagram as well as to derivatives attached to the vertices under consideration. Hence, one can express D completely by

$$D = 4 - N_b - \frac{3}{2}N_f - \sum \Delta_i V_i. \tag{5.3}$$

Here, we introduced the definitions

$$\Delta_i := 4 - b_i - \frac{3}{2}f_i - d_i \tag{5.4}$$

as well as

- $N_f :=$ # of external fermion propagators,
- $N_b :=$ # of external boson propagators,
- $V_i :=$ # of vertices of type i,
- $b_i :=$ # of bosons attached to the vertex of type i,
- $f_i :=$ # of fermions attached to the vertex of type i,
- $d_i :=$ # of derivatives in a vertex of type i.

The artificial degree of divergence D allows to assess already at the level of Feynman diagrams, if a NLO correction is UV divergent (see Fig. 5.1 for two examples). Note that it is well possible that a diagram γ with $D(\gamma) > 0$ turns out to be convergent, e.g., because of certain cancellations of divergent parts due to some symmetries. Moreover, a diagram with $D(\gamma) = 0$ is expected to diverge logarithmically, while there are also cases, in which an Feynman amplitude with a vanishing degree of divergence $D(\gamma) = 0$ turns out to be convergent[1]. Hence, the superficial degree of divergence should be used with care. A statement which one can, however, draw is the following: *Diagrams turn out to be* ***UV-finite*** *if $D(\gamma) < 0$ for every one-particle irreducible[2] subdiagram γ of the particular Feynman diagram.* In addition, dimensional analysis of some Lagrangian reveals that the quantity Δ_i of a vertex i equals the mass dimension of the associated coupling constant g_i. Hence, following Eq. 5.3, for $\Delta_i < 0$, the degree of divergence D becomes more and

[1] An example is the trivial diagram without any propagators or loops. This possesses a vanishing superficial degree of divergence $D(\gamma) = 0$ while being UV-convergent.

[2] The term 'one-particle irreducible" here refers to diagrams that cannot be split into two by cutting a single internal propagator

more positive the more loops and, in turn, vertices one adds to a particular Feynman diagram. This worsens the UV-behavior of the diagram by introducing new divergent structures with every higher order in perturbation theory. Therefore, it is possible to categorize the renormalizability of a theory footing only the dimensionality Δ_i of their coupling constants:

1. **Super-renormalizable** ($\Delta_i > 0$): The theory is finite with no divergences.
2. **Renormalizable** ($\Delta_i = 0$) : Only a finite number of amplitudes (substructures) diverges such that a finite number of countertems is sufficient to render the theory UV-finite. However, divergences occur at all orders in perturbation theory.
3. **Non-renormalizable** ($\Delta_i < 0$): Structurally new divergences arise with every higher loop order such that an infinite set of counterterms is necessary to render the theory UV-finite to all orders in perturbation theory.

The theories analyzed in the context of this work fall within the framework of (non-)Abelian gauge theories, which subsume under the category "renormalizable". Hence, it is possible to cancel all UV divergences that we encounter at the one-loop level by the proper definition of just a finite number of counterterms. How this is done is presented in greater detail in Sec. 5.1.5 further below.
So far, we have treated the general case of N-loop calculations, pointing out that these are potentially ill defined, i.e., divergent due to contributions from the region of large internal momenta. However, we found that not every loop diagram has to be ultraviolet divergent. Nevertheless, in order to gain some physically meaningful results, the procedures of regularization and renormalization are introduced in the following.

5.1.2. The Procedure of Regularization

After the identification of divergent amplitudes, the next step to obtain a physically meaningful result is the *regularization* of divergent integrals.
Basically speaking, ***regularization*** *is the process whereby an ill defined correction to some amplitude gets separated into a singular (or infinite part, when the limit of the unregularized theory is restored) and a nonsingular (or finite part within the original theory) part.*
The regularization schemes relevant to this work are the so-called *Dimensional Regularization* (DReg) and *Dimensional Reduction* (DRed) [182] schemes. These regularization schemes turn out to be especially appealing within the work presented here as they can be either used to regularize UV as well as soft and collinear divergences simultaneously. They will be presented in greater detail in the following.
Using DReg or DRed, the integral Eq. (5.1) gets analytically continued from four to $D < 4$ (UV) or $D > 4$ (soft and collinear) spacetime dimensions

$$\int \mathrm{d}^4 q_i \to \mu^{4-D} \int \mathrm{d}^D q_i. \tag{5.5}$$

In Eq. (5.5), we have introduced an additional mass scale μ, the so-called renormalization scale, which is needed to keep the mass dimensions on the left and right hand side equally. In the UV region, these regularization methods are inspired by the fact that lowering the dimension of the integrand can render an initially divergent integral finite, e.g.,

$$\int_a^\infty \frac{1}{r^2}\mathrm{d}^3 r \to \text{ linearly divergent}, \quad \int_a^\infty \frac{1}{r^2}\mathrm{d}^2 r \to \text{ logarithmically divergent}, \tag{5.6}$$

$$\int_a^\infty \frac{1}{r^2} \mathrm{d}r \to \text{ finite.} \tag{5.7}$$

Going from four to $D < 4$ dimension, this results in poles of the form $1/(4\text{-}D)$ in order that infinites get restored in the limit $D \to 4$. On the other hand, this argument can be turned around yielding a lift of soft divergences $q_i \to 0$ for the exchange of some massless particle i if the powers of q_i in the numerator are raised using $D > 4$.
Although physically rather unintuitive compared to, e.g., the *cutoff-scheme* [12] or the *Pauli-Villars scheme* [183], the methods of DRed and DReg are especially appealing as they neither violate Lorentz invariance nor the Ward-Takahashi or Slavnov-Taylor identities (the quantum field theoretical manifestation of (non)Abelian gauge symmetries) nor unitarity of the S-matrix (at least in the non-super-symmetric case (see Ref. [182])). Even though DReg and DRed both work in $D \neq 4$ dimensions, there is still an important difference between these two regularization schemes. As we work within supersymmetric models (up to some explicit SUSY breaking), observables are expected to be symmetric under the exchange of bosons (fermions) and their corresponding fermionic (bosonic) superpartners. This makes it mandatory to treat (s)fermions as well as (s)bosons equally within the considered regularization scheme. Whereas in DRed vector bosons as well as fermions are understood as four-dimensional objects, this is not the case within DReg, in whose terms vectors are taken as $D = 4 - 2\epsilon$-dimensional. Hence, within DRed, the four dimensional vectors can just be decomposed into a D-dimensional object plus so-called ϵ-scalars [184] to draw the connection to DReg. As in DRed, DReg keeps all fermions in four dimensions so that these ϵ-scalars turn out to be the only difference between these two regularization schemes. However, the different treatment of fermions and vectors within DReg results in a mismatch between bosonic and fermionic degrees of freedom (more explicitly, between gauge bosons and their corresponding fermionic superpartners, the so-alled gauginos) and, in consequence, to an explicit though somehow artificial breaking of global SUSY invariance. Although this mismatch within DReg can indeed be corrected via the introduction of supersymmetry restoring counterterms, whose existence is always guaranteed by the renormalizability of supersymmetric gauge theories, their evaluation turns out to be quite involved as these counterterms do not originate from multiplicative renormalization as known from the typically encountered UV-counterterms [185] (see Sec. 5.1.5 below). Hence, DRed is typically used to calculate higher-order corrections within supersymmetric theories. The treatment of DRed can now be specified as follows:

- All four-momenta, space time coordinates and the metric tensor $g_{\mu\nu}$ are analytically continued to $D = 4 - 2\epsilon$ dimensions (e.g. $g^\mu_\mu = D$).
- The Gamma-matrices γ^μ are still 4×4 matrices with the anti-commutation relation $\{\gamma^\mu, \gamma^\nu\} = 2g^{\mu\nu}\mathbb{1}$.
- All vector bosons as well as all fermions are kept in four dimensions.

Note that the definition of γ_5 in D dimensions[3] is quite peculiar [186]. The problem can be traced back to the incompatibility between the anti-commutation relation

$$\{\gamma^\mu, \gamma_5\} = 0 \tag{5.8}$$

and the relation

$$\mathrm{Tr}(\gamma^\mu\gamma^\nu\gamma^\rho\gamma^\sigma\gamma_5) \neq 0 \tag{5.9}$$

[3] γ_5 is needed in the context of theories, containing chiral fermions such as the EW part of the SM.

in $D \neq 4$ dimensions, where the latter is often considered to be mandatory to find

$$\mathrm{Tr}(\gamma^\mu\gamma^\nu\gamma^\rho\gamma^\sigma\gamma_5) = 4i\epsilon^{\mu\nu\rho\sigma} \tag{5.10}$$

in the limit $D \to 4$. Here, we follow a strategy outlined in [186], called the quasi self-chiral scheme, where the "naive dimension regularization scheme" (NDR) is used. Hence, we keep the anti-commutation relation Eq. (5.8) but drop the trace relation Eq. (5.9)[4]. To complete this section about regularization we finally give a first glimpse onto an actual calculation where DReg/DRed is used.
The starting point is the potentially soft as well as UV divergent-expression

$$\int \mathrm{d}^D q \frac{1}{(q^2)^\alpha}, \tag{5.11}$$

which may arise within a Feynman diagram by the propagator of some massless boson, e.g., a gluon ($\alpha = 1$). After the so-called Wick rotation of the four vectors' time component

$$q_0 \to iq_0, \tag{5.12}$$

which corresponds to a transformation from Minkowski to Euclidean coordinates, Eq. (5.40) takes the form

$$\int \mathrm{d}^D q \frac{1}{(q^2)^\alpha} = i(-1)^\alpha \int \mathrm{d}q_E \frac{1}{(q_E^2)^\alpha}. \tag{5.13}$$

The subscript E stands for a vector in an euclidean space ($q_E \cdot q_E = \sum_{i=0}^{3} q_{E,i}^2$). As the integrand of Eq. (5.41) does not depend on the angles, one can already perform the angular integral over the D-dimensional solid angle. This simplifies to

$$\Omega_D = \int_{\Omega_D} \mathrm{d}\Omega_D = \frac{2\pi^{D/2}}{\Gamma(D/2)}. \tag{5.14}$$

In Eq. (5.14), the definition of the Γ-function

$$\Gamma(z) = \int_0^\infty \mathrm{d}t\, t^{z-1}e^{-t}, \tag{5.15}$$

valid for $\mathcal{R}(z) > 0$, has been used. By further substituting

$$q_E \to q_E^2, \tag{5.16}$$

Eq. (5.13) can be brought to the form

$$\int \mathrm{d}^D q \frac{1}{(q^2)^\alpha} = i(-1)^\alpha \frac{\pi^{D/2}}{\Gamma(D/2)} \int_0^\infty \mathrm{d}q_E^2 (q_E^2)^{D/2-1-\alpha}. \tag{5.17}$$

From Eq. (5.17), it can be deduced that the integral is ultraviolet divergent for $D > 2\alpha$ and soft divergent for $D \to D' < 2\alpha$. This means that there is no region in D, where the integral can be properly defined. Therefore, one can split the integration into two regions $q_E^2 > \Lambda^2$ and $q_E^2 < \Lambda^2$, as

$$\int \mathrm{d}^D q \frac{1}{(q^2)^\alpha} = i(-1)^\alpha \frac{\pi^{D/2}}{\Gamma(D/2)} \left(\int_0^{\Lambda^2} \mathrm{d}q_E^2 (q_E^2)^{D/2-1-\alpha} + \int_{\Lambda^2}^\infty \mathrm{d}q_E^2 (q_E^2)^{D/2-1-\alpha} \right). \tag{5.18}$$

[4]Note that, since traces of this order in the gamma-matrices appear in our case only in $2 \to 2$ calculations with the rank-four Levi-Civita symbol contracted with external momenta, these expressions yield zero anyway due to conservation of total momentum.

After performing these two integrations separately, one is left with

$$\int \mathrm{d}^D q \frac{1}{(q^2)^\alpha} = i(-1)^\alpha \frac{2\pi^{D/2}}{\Gamma(D/2)} \left(\frac{\Lambda^{D'-2\alpha}}{D'-2\alpha} - \frac{\Lambda^{D-2\alpha}}{D-2\alpha} \right) \tag{5.19}$$

$$= i(-1)^\alpha \frac{\pi^{2-\epsilon}}{\Gamma(2-\epsilon)} \left(\frac{\Lambda^{-2\epsilon_{\mathrm{IR}}}}{\epsilon_{\mathrm{IR}}} - \frac{\Lambda^{-2\epsilon_{\mathrm{UV}}}}{\epsilon_{\mathrm{UV}}} \right), \tag{5.20}$$

where

$$\epsilon_{\mathrm{IR,UV}} = \frac{4-D}{2} \tag{5.21}$$

has been introduced. One sees that in the limit $D, D' \to 4$, these two kinds of divergences actually cancel each other, yielding

$$\int \mathrm{d}^4 q \frac{1}{(q^2)^\alpha} = 0, \tag{5.22}$$

which justifies the definition

$$\int \mathrm{d}^D q \frac{1}{(q^2)^\alpha} = 0 \tag{5.23}$$

in D-dimensional calculus for any α. This integral, which is proportional to the scalar integral $\mathbf{B_0}(0,0,0,)$ ($\alpha = 2$), which will be introduced later, serves as a first example of dimensionally regularized soft and UV divergences.
In the next chapter, we discuss the appearance and treatment of UV divergences in the context of NLO calculations. There, we outline one of the most important calculational methods used within this work, the so-called *Passarino-Veltman-reduction*.

5.1.3. The Passarino-Veltman Reduction

As already mentioned above, the `DM@NLO` project is primarily concerned with the effect of NLO corrections. A central method in this context is the so-called *Passarino-Veltman-reduction* [168]. Its central statement is that it is possible to decompose an arbitrary N-point tensor-integral

$$T^N_{\mu_1,\mu_2,...,\mu_M}(p_1,...,p_{N-1},m_0,...,m_{N-1}) = \frac{(2\pi\mu)^{4-D}}{i\pi^2} \int d^D q \frac{q_{\mu_1}...q_{\mu_M}}{D_0 D_1 ... D_{N-1}} \tag{5.24}$$

with

$$D_0 = (q^2 - m_0^2 + i\epsilon), \;\; D_i = ((q+p_i)^2 - m_i^2 + i\epsilon) \;\; (i = 1,...N-1) \tag{5.25}$$

as shown in Fig. 5.2 into a finite collection of scalar integrals named $\mathbf{A_0}$, $\mathbf{B_0}$, $\mathbf{C_0}$ and $\mathbf{D_0}$. Defining

$$\int_q := \frac{(2\pi\mu)^{4-D}}{i\pi^2} \int \mathrm{d}^D q, \tag{5.26}$$

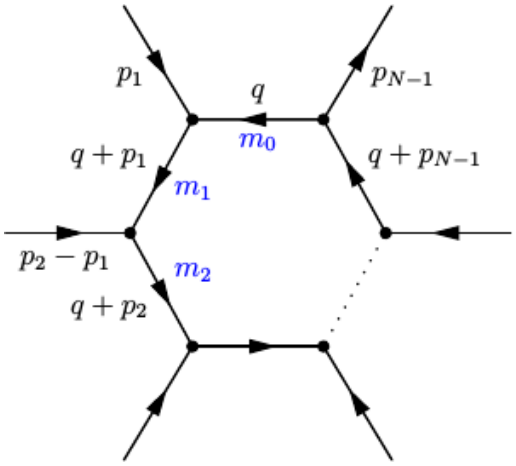

Figure 5.2.: Feynman representation of N-point tensor integrals. Figure taken from Ref. [55].

these scalar integrals take the form

$$\mathbf{A_0}(m_0^2) = \int_q d^D q \frac{1}{D_0}, \tag{5.27}$$

$$\mathbf{B_0}(p_1^2, m_0^2, m_1^2) = \int_q d^D q \frac{1}{D_0 D_1}, \tag{5.28}$$

$$\mathbf{C_0}(p_1^2, (p_1-p_2)^2, p_2^2, m_0^2, m_1^2, m_2^2) = \int_q d^D q \frac{1}{D_0 D_1 D_2}, \tag{5.29}$$

$$\mathbf{D_0}(p_1^2, (p_2-p_1)^2, (p_3-p_2)^2, p_3^2, p_2^2, (p_1-p_3)^2, m_0^2, m_1^2, m_2^2, m_3^2) = \int_q d^D q \frac{1}{D_0 D_1 D_2 D_3}, \tag{5.30}$$

where we have chosen the arguments of the scalar integrals in close correspondence with Ref. [207] following the convention depicted in Fig. 5.2. The starting point of the Passarino-Veltman reduction is the decomposition of an arbitrary tensor integral $\mathbf{T}^i$ (i=1,2,3,...) in terms of Lorentz-tensors of appropriate rank, e.g.,

$$B^\mu = p_1^\mu B_1, \tag{5.31}$$

$$C^\mu = p_1^\mu C_1 + p_2^\mu C_2, \tag{5.32}$$

$$A^{\mu\nu} = g^{\mu\nu} A_2, \tag{5.33}$$

$$B^{\mu\nu} = g^{\mu\nu} B_{00} + p_1^\mu p_1^\nu B_{11}, \tag{5.34}$$

$$C^{\mu\nu} = g^{\mu\nu} C_{00} + p_1^\mu p_1^\nu C_{11} + (p_1^\mu p_2^\nu + p_1^\nu p_2^\mu) C_{12} + p_2^\mu p_2^\nu C_{22}, \tag{5.35}$$

...

with the redefinition $T^1 \to A$, $T^2 \to B$, $T^3 \to C$, $T^4 \to D$, ... corresponding to one-, two-, three-, four-, ... point tensor-integrals[5]. Here, A_i, B_i, B_{ij}, ... can be understood as coefficients in a basis expansion of the N-point tensor-integral spanned by all possible Lorentz tensors, which can be symmetrically (under the exchange of Lorentz indices)

[5]Note that for a consistent use of the tensor decomposition Eqs. (5.31) to (5.35), one has to fix the signs of the momenta according to the signs in the propagator D_i of Eq. (5.25), e.g., $p_1 \to -p_1$, where the latter depends on the assignment of momenta to the particular Feynman diagram.

composed out of the external momenta p_i^μ and the metric tensor $g^{\mu\nu}$[6]. These A_i, B_i, B_{ij}, ... defined in Eq. (5.31) and following contain the integrations over the unconstrained momenta q_i of Sec. 5.1.1 and can be fully reduced to the scalar integrals $\mathbf{A_0}$, $\mathbf{B_0}$, $\mathbf{C_0}$ and $\mathbf{D_0}$ mentioned above (see e.g. [181] for explicit examples). The steps to follow here are basically

1. Contraction of the tensor-integral with all possible tensors of appropriate rank which can be build from external momenta and the metric tensor.

2. Extension of the arising numerator in the contracted tensor-integral to cancel propagators in the denominator.

3. Solve the arising system of linear equations from the different contractions of point 1 for the tensor coefficients.

For example, B^μ of Eq. (5.31) can be decomposed into the scalar integrals $\mathbf{A_0}$ and $\mathbf{B_0}$ as follows: First of all, one has to contract Eq. (5.31) with $p_{1\mu}$, the only Lorentz-vector available, as stated under point 1. This yields

$$p_1^2 B_1 = \int_q \frac{p_1 \cdot q}{(q^2 - m_0^2)[(q+p_1)^2 - m_1^2]}. \tag{5.36}$$

The next step, following point 2, is a clever extension of the numerator of the integrand to cancel propagators in the denominator

$$\begin{aligned} p_1^2 B_1 &= \int_q \frac{[(q+p_1)^2 - m_1^2] - (q^2 - m_0^2) - (p_1^2 - m_1^2 + m_0^2)}{2(q^2 - m_0^2)[(q+p_1)^2 - m_1^2]} \\ &= \frac{1}{2}\int_q \frac{1}{q^2 - m_0^2} - \frac{1}{2}\int_q \frac{1}{(q+p_1)^2 - m_1^2} - \frac{1}{2}\int_q \frac{p_1^2 - m_1^2 + m_0^2}{(q^2 - m_0^2)[(q+p_1)^2 - m_1^2]}. \end{aligned} \tag{5.37}$$

This finally results into a decomposition of the tensor coefficient B_1 in terms of the scalar integrals $\mathbf{A_0}$ and $\mathbf{B_0}$ of the form

$$B_1(p_1^2, m_0, m_1) = \frac{1}{2p_1^2}\left[\mathbf{A_0}(m_0) - \mathbf{A_0}(m_1) + (p_1^2 - m_1^2 + m_0^2)\mathbf{B_0}(p_1^2, m_0, m_1)\right]. \tag{5.38}$$

The same can be done for, e.g., $C^\mu(p_1, p_2, m_0, m_1, m_2)$ of Eq. (5.32), which results in

$$\begin{aligned} \begin{pmatrix} C_1 \\ C_2 \end{pmatrix} =& \frac{1}{2}\begin{pmatrix} p_1^2 & p_1 p_2 \\ p_1 p_2 & p_2^2 \end{pmatrix}^{-1} \\ & \begin{pmatrix} \mathbf{B_0}(p_2^2, m_0^2, m_2^2) - \mathbf{B_0}((p_1 - p_2)^2, m_1, m_2) - f_1 \mathbf{C_0}(p_1^2, p_2^2, m_0^2, m_1^2, m_2^2) \\ \mathbf{B_0}(p_1^2, m_0^2, m_2^2) - \mathbf{B_0}((p_1 - p_2)^2, m_1, m_2) - f_2 \mathbf{C_0}(p_1^2, p_2^2, m_0^2, m_1^2, m_2^2) \end{pmatrix} \end{aligned} \tag{5.39}$$

with the definition $f_i = p_i^2 - m_i^2 + m_0^2$ $(i = 1, 2)$.
Via dimensional analysis of their integrands (see Sec. 5.1.1), it turns out that both $\mathbf{A_0}$ and $\mathbf{B_0}$ are UV divergent. Hence, Feynman graphs, which contain N-point integrals that can be ascribed to some linear combination including any of these two integrals, are actually ill defined. In the next chapter, we will discuss the actual calculation of some of the scalar integrals defined in the Eqs. (5.27)-(5.30) and show how to explicitly single out their UV divergent parts.

[6] The appearance of the Levi-Civita symbol turns out to be forbidden by the symmetry of the integrand under the exchange of different momenta.

5.1.4. The Scalar Integrals in Dimensional Regularization

In the following, we present the explicit extraction of UV-poles for the scalar integrals $\mathbf{A_0}$ and $\mathbf{B_0}$ within DRed/DReg .
The starting point in the calculation of $\mathbf{A_0}$ Eq. (5.27) is the integral

$$I_N = \int \mathrm{d}^D q \frac{1}{(q^2 - A + i\epsilon)^N}, \tag{5.40}$$

which for $N = 1$ reduces to $\mathbf{A_0}$ except for a factor $(2\pi\mu)^{4-D}/(i\pi^2)$. After the Wick rotation of the four vectors' time component, Eq. (5.40) takes the form

$$\mathbf{A_0} = i(-1)^N \int \mathrm{d}^D q_E \frac{1}{(q_E^2 + A - i\epsilon)^N}, \tag{5.41}$$

where the subscript E stands for the euclidean metric ($q_E \cdot q_E = \sum_{i=0}^{3} q_{E,i}^2$) as already introduced above. The angular integral over the D-dimensional solid angle can again be performed following Eq. (5.14). Substituting

$$q_E \to q_E^2 := x \tag{5.42}$$

followed by

$$x \to y(A - i\epsilon), \tag{5.43}$$

Eq. (5.41) then takes the form

$$\mathbf{A_0} = i(-1)^N \frac{\pi^{D/2}}{\Gamma(D/2)} (A - i\epsilon)^{D/2-N} \int_0^\infty \mathrm{d}y \frac{y^{D/2-1}}{(1+y)^N}. \tag{5.44}$$

This can be solved using the Beta function

$$B(D/2, N - D/2) := \int_0^\infty \mathrm{d}y \; y^{D/2-1}(1+y)^{-N} = \frac{\Gamma(D/2)\Gamma(N - D/2)}{\Gamma(N)} \tag{5.45}$$

such that one ends up with the important result

$$I_N = i(-1)^{N/2} \pi^{D/2} \frac{\Gamma(N - D/2)}{\Gamma(N)} (A - i\epsilon)^{D/2-N}, \tag{5.46}$$

where again $I_1 \propto \mathbf{A_0}$.
To finally evaluate the poles of $\mathbf{A_0}$ in the limit $D \to 4$, one still needs to know the behavior of the Γ-function $\Gamma(z)$ for $z \to 0$. In this case, the Γ-function can be expanded as

$$\Gamma(z) = \frac{1}{z} - \gamma_E + \frac{1}{2}\left(\gamma_E^2 + \frac{\pi^2}{6}\right) z + \mathcal{O}(z^2) \tag{5.47}$$

where γ_E is the Euler-Mascheroni constant. Together with the useful identities

$$\Gamma(1 + z) = z\Gamma(z), \tag{5.48}$$
$$\Gamma(1 - z) = -z\Gamma(-z), \tag{5.49}$$
$$\Gamma(1/2) = \sqrt{\pi}, \tag{5.50}$$

these are all ingredients needed to identify potential singularities in the definition of $\mathbf{A_0}$. Hence, after setting $D = 4 - 2\epsilon$ and $N = 1$, the expansion in ϵ of Eq. (5.46) up to terms of $\mathcal{O}(\epsilon)$ results in

$$\mathbf{A_0} = m^2 \left(\Delta - \ln\left(\frac{m^2 - i\epsilon}{\mu^2}\right) + 1 + \mathcal{O}(\epsilon)\right) \tag{5.51}$$

with

$$\Delta = \frac{1}{\epsilon} - \gamma_E + \ln(4\pi), \tag{5.52}$$

which reveals a single UV-pole in the four-dimensional limit $\epsilon \to 0$.
Solving the scalar integral $\mathbf{B_0}$ as defined in Eq. (5.28) turns out to be more involved. As it includes some new tricks in its evaluation, we sketch the most important steps in the estimation of its UV-pole structure in the following. Making use of the so-called Feynman-trick

$$\frac{1}{A_1 A_2 ... A_n} = \int_0^1 \mathrm{d}x_1 ... \mathrm{d}x_n \;\; \delta\left(\sum_{i=1}^{n} x_i - 1\right) \frac{(n-1)!}{[x_1 A_1 + x_2 A_2 + ... x_n A_n]^n} \tag{5.53}$$

for $n = 2$, it is possible to bring the integrand of Eq. (5.28) to a structure of the form of I_2 Eq. (5.40)

$$\frac{1}{D_0 D_1} = \int_0^1 \mathrm{d}x \Big\{ (q^2 - m_0^2 + i\epsilon)(1-x) + [(q+p_1)^2 - m_1^2 + i\epsilon]x \Big\}^{-2} \tag{5.54}$$

$$= \int_0^1 \mathrm{d}x \Big\{ \underbrace{(q + xp_1)^2}_{:=q'} \underbrace{- x^2 p_1^2 + x(p_1^2 - m_1^2 + m_0^2) - m_0^2}_{=:-A} + i\epsilon] \Big\}^{-2}. \tag{5.55}$$

Hence, $\mathbf{B_0}$ can be rewritten as

$$\mathbf{B_0} = \frac{(2\pi\mu)^{4-D}}{i\pi^2} \int_0^1 \mathrm{d}x \underbrace{\int \mathrm{d}^D q' (q'^2 - A + i\epsilon)^{-2}}_{=I_2(A)}. \tag{5.56}$$

One can now use the result Eq. (5.46) and following to separate the UV-pole, which results in

$$\mathbf{B_0} = \Delta - \int_0^1 \mathrm{d}x \;\; \ln\left(\frac{x^2 p_1^2 - (x(p_1^2 - m_1^2 + m_0^2) + m_0^2 - i\epsilon}{\mu^2}\right) + \mathcal{O}(\epsilon) \tag{5.57}$$

with Δ as defined in Eq. (5.52). After a somehow lengthy calculation of the x-integration and clever grouping of logarithms, Eq. (5.57) can finally be brought to the concise form

$$\begin{aligned}\mathbf{B_0}(p_1^2, m_0^2, m_1^2) =& \Delta - \ln\left(\frac{m_0 m_1}{\mu^2}\right) + 2 + \frac{m_0^2 - m_1^2}{p_1^2} \ln\frac{m1}{m_0} \\ & \sqrt{\frac{\lambda(p_1^2, m_0^2, m_1^2) + 4i\pi^2\epsilon}{2p_1^2}} \Big[\ln\left(1 - \frac{1}{x_1}\right) - \ln\left(1 - \frac{1}{x_2}\right) \Big] + \mathcal{O}(\epsilon)\end{aligned} \tag{5.58}$$

with

$$x_{1,2} = \frac{1}{2p_1^2}\left(p_1^2 - m_1^2 + m_0^2 \pm \sqrt{(p_1^2 - m_1^2 - m_0^2)^2 - 4m_0^2 m_1^2 + 4ip_1^2\epsilon}\right). \tag{5.59}$$

This completes the calculation of $\mathbf{B_0}$.
However, in many cases general solutions such as Eq. (5.58) do not provide reliable results for arbitrary argument sets as they do not smoothly converge, e.g., in the limit when certain masses are zero or become equal (compare, e.g., Eq. (5.19) and Eq. (5.58)). In these cases, one has to step back from Eq. (5.58) and recalculate the parameter integral Eq. (5.57) with this new parameter set. Hence, another difficulty beside the actual calculation is to cover all special solutions of scalar integrals Eqs. (5.27) - (5.30) for the different

argument sets needed in the NLO calculations. An extensive collection of scalar integrals for various parameter sets can be found in Refs. [188–190]. The ones we need have been implemented within the `DM@NLO`-package and cross checked with the publically available code `LoopTools` [187]. Note that the correct comparison of `DM@NLO` and `LoopTools` makes it mandatory to include a conversion factor

$$\frac{1+\pi^2\epsilon^2/6}{\Gamma(1+\epsilon)(4\pi)^\epsilon}. \tag{5.60}$$

Here, the part $\propto \epsilon^2$ becomes relevant only if the integral under consideration contains double poles due to simultaneously soft and collinear divergent terms. This turns out to be relevant, e.g., for integrals needed in the implementation of gaugino annihilation into light/massless quarks extended by a gluon exchanged between the final-state quarks. Such integrals arise in the context of `ChiChi2qq`.

5.1.5. Renormalization

So far, we have described the regularization of divergent integrals and identified the form of the arising singularities. The final step left is to render the initially ill defined Feynman amplitudes UV finite, even in the limit of a removed regulator. This is done via so-called *multiplicative renormalization*, in whose terms the arising singularities get completely absorbed into so-called *bare* couplings, wave functions, mixings and masses of the initial Lagrangian $\mathcal{L}_0$ (in the following bare quantities are furnished with the subscript 0). This is done in a way that leaves the symmetries of the initial $\mathcal{L}_0$ intact. The final UV-finite Feynman amplitudes are then comprehensively expressed in terms of so-called *renormalized* parameters, which are connected to the bare parameters by a multiplicative renormalization constant [181], e.g.,

$$A_0^\mu = \sqrt{Z_A}A^\mu,\ \psi_0 = \sqrt{Z_\psi}\psi,\ \phi_0 = \sqrt{Z_\phi}\phi \quad \leftarrow \text{Renormalization of wave functions,} \tag{5.61}$$

$$m_{0,f} = Z_m^f m_f = m_f + \delta m_f \quad \leftarrow \text{Renorm. of fermion masses,} \tag{5.62}$$

$$m_{0,b}^2 = Z_m^b m_b^2 = m_b^2 + \delta m_b^2 \quad \leftarrow \text{Renorm. of boson masses,} \tag{5.63}$$

$$\lambda_0 = Z_\lambda \lambda = \lambda + \delta\lambda \quad \leftarrow \text{Renorm. of coupling constant,} \tag{5.64}$$

$$\Theta_0 = Z_\Theta \Theta = \Theta + \delta\Theta \quad \leftarrow \text{Renorm. of mixing angles.} \tag{5.65}$$

The perturbative expansion of the renormalization constants

$$Z_i = 1 + \delta Z_i = 1 + \mathcal{O}(\lambda) \tag{5.66}$$

(in this case $\lambda \to \alpha_\mathrm{s}$) leads to the introduction of new terms in the initial bare Lagrangian, the so-called counterterms

$$\mathcal{L}_0 = \underbrace{\mathcal{L}_0|_{A_0\to A,\psi_0\to\psi,\ldots}}_{=\mathcal{L}_\mathrm{ren}} + \underbrace{\delta\mathcal{L}}_{\text{counterterms}}. \tag{5.67}$$

These counterterms, collectively summarized as $\delta\mathcal{L}$ in Eq. (5.67), are defined in such a way, that they exactly cancel the previously encountered UV singularities of Sec. 5.1.4 order by order in perturbation theory. As this requirement only fixes the counterterms up to some nonsingular part, their complete form is freely adjustable to a certain extent. A specific choice for these nonsingular parts corresponds to picking a certain *renormalization scheme*. In the subsequent sections we make use of a mixture of the two schemes

called *on-shell* and $\overline{DR}$ renormalization schemes, leaving us with a hybrid on-shell/$\overline{\text{DR}}$ scheme, which shares some important features with a renormalization scheme previously introduced in Ref. [191]. The on-shell and the $\overline{\text{DR}}$ renormalization scheme are presented while we go through renormalization of the different particle sectors of the MSSM relevant to this work.
These new terms in $\delta\mathcal{L}$ result in an extended set of Feynman rules, which can be understood as new sorts of interactions. They hence leave us with an additional set of diagrams. These new diagrams supplement the set of Feynman diagrams as derived form $\mathcal{L}_{\text{ren}}$, whose Feynman rules match the Feynman rules of $\mathcal{L}_0$, but with all parameters replaced by their renormalized counterparts as defined in Eqs. (5.61)- (5.65). In the following, we mark the insertion of counterterms within a Feynman graph by a cross (see, e.g, Fig. 5.3). Finally note that it is far from trivial that all arising divergences can be entirely absorbed into the available parameter set of the bare Lagrangian order by order in perturbation theory. Theories that fulfill these criteria are called renormalizable as already discussed in Sec. 5.1.1. Fortunately, nature seems to favor renormalizable theories.

The Quark Sector

The bare Lagrangian of the massive quark sector takes the form

$$\mathcal{L}_0^{\text{quark}} = \bar{q}_{0,j}\delta_{ij}(i\partial\!\!\!/ - m_{q_{0,i}})q_{0,i}, \tag{5.68}$$

where i, j are indices in generation space and account for potential flavor mixing. We can now substitute the bare fields and the bare mass in $\mathcal{L}_0^{\text{quark}}$ by their renormalized counterparts via the replacements

$$q_{0,i} \to (\delta_{ij} + \frac{1}{2}\delta Z_{ij}^{q,L}P_L + \frac{1}{2}\delta Z_{ij}^{q,R}P_R)q_j, \tag{5.69}$$

$$m_{q_{0,i}} \to m_{q_i} + \delta m_{q_i}, \tag{5.70}$$

which can be deduced from Eq. (5.61) and Eq. (5.62) together with Eq. (5.66). Hence, we introduce distinct renormalization constants for each chirality

$$\begin{pmatrix} q_{0,i}^L \\ q_{0,i}^R \end{pmatrix} = \begin{pmatrix} \delta_{ij} + \frac{1}{2}\delta Z_{ij}^{q,L} & 0 \\ 0 & \delta_{ij} + \frac{1}{2}\delta Z_{ij}^{q,R} \end{pmatrix} \begin{pmatrix} q_j^L \\ q_j^R \end{pmatrix}. \tag{5.71}$$

After the replacements Eqs. (5.69) and (5.70), the bare Lagrangian Eq. (5.68) up to one-loop order takes the form

$$\begin{aligned} \mathcal{L}_0^{\text{quark}} =& \underbrace{\bar{q}_j\delta_{ij}(i\partial\!\!\!/ - m_{q_i})q_i + \frac{1}{2}\bar{q}_i i\partial\!\!\!/ \left(\delta Z_{ij}^{q,L}P_L + \delta Z_{ij}^{q,R}P_R\right) q_j}_{\mathcal{L}_{\text{ren}}^{\text{quark}}} \\ &\underbrace{\begin{aligned} &- \frac{1}{2}\bar{q}_i m_{q_i}\left(\delta Z_{ij}^{q,L}P_L + \delta Z_{ij}^{q,R}P_R\right) q_j \\ &+ \frac{1}{2}\bar{q}_j i\partial\!\!\!/ \left((\delta Z^{q,L})_{ji}^* P_L + (\delta Z^{q,R})_{ji}^* P_R\right) q_i \\ &- \frac{1}{2}\bar{q}_j m_{q_i}\left((\delta Z^{q,L})_{ji}^* P_R + (\delta Z^{q,R})_{ji}^* P_L\right) q_i \\ &- \delta m_{q_i}\bar{q}_i q_i. \end{aligned}}_{\delta\mathcal{L}^{\text{quark}}} \end{aligned} \tag{5.72}$$

We fix the counterterms in $\delta\mathcal{L}^{\text{quark}}$ within the on-shell renormalization scheme. As a starting point serves the one particle irreducible two-point function $\hat{\Gamma}_{ij}^q$ (the inverse of the

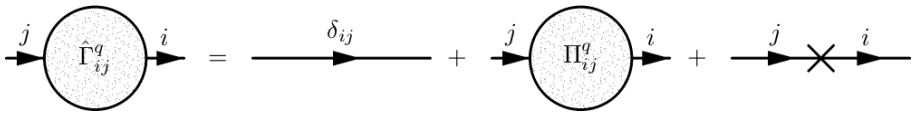

Figure 5.3.: Renormalized two-point function for quark mixing with definition of indices.

two-point Green function) depicted in Fig. 5.3. It can be related to the S-matrix element $\mathcal{M}$ via the *LSZ-reduction formula* [12]

$$\mathcal{M}^q = i\bar{u}_i(p)\hat{\Gamma}^q_{ij}u_j(p). \tag{5.73}$$

Here, the hat symbolizes that $\hat{\Gamma}^q_{ij}$ is a renormalized quantity containing both divergent loop corrections as well as the associated counterterms. $\hat{\Gamma}^q_{ij}$ can be expressed in terms of the renormalized quark self energy $\hat{\Pi}^q_{ij}$

$$\hat{\Gamma}^q_{ij} = \delta_{ij}(\not{p} - m_{q_i}) + \hat{\Pi}^q_{ij}(p^2). \tag{5.74}$$

According to the common structure of fermionic propagators, we decompose the renormalized self energy $\hat{\Pi}^q_{ij}$ as

$$\hat{\Pi}^q_{ij}(p) = \not{p}P_L\hat{\Pi}^{q,L}_{ij}(p^2) + \not{p}P_R\hat{\Pi}^{q,R}_{ij}(p^2) + \hat{\Pi}^{q,SL}_{ij}(p^2)P_L + \hat{\Pi}^{q,SR}_{ij}(p^2)P_R, \tag{5.75}$$

where $\hat{\Pi}^{q,L/R}$ and $\hat{\Pi}^{q,SL/SR}$ stand for the decomposition of $\hat{\Pi}^q_{ij}$ into a vector ($\propto \not{p}$) and a scalar part ($\propto \mathbb{1}$). Following Eq. (5.72), $\hat{\Pi}^{q,L/R}$ and $\hat{\Pi}^{q,SL/SR}$ can be expressed by the divergent self-energy contributions subsumed under $\Pi^{q,L/R}$ and $\Pi^{q,SL/SR}$ and the counterterms from $\delta\mathcal{L}^{\text{quark}}$ as

$$\hat{\Pi}^{q,L/R}_{ij} = \Pi^{q,L/R}_{ij} + \frac{1}{2}\left(\delta Z^{q,L/R}_{ij} + \delta(Z^{q,L/R})^*_{ji}\right), \tag{5.76}$$

$$\hat{\Pi}^{q,SL/SR}_{ij} = \Pi^{q,SL/SR}_{ij} - \frac{1}{2}\left(m_{q_i}\delta Z^{q,L/R}_{ij} + m_{q_j}\delta(Z^{q,R/L})^*_{ji}\right) - \delta_{ij}\delta m_{q_i}. \tag{5.77}$$

The final task is to fix the counterterms within the on-shell scheme. The associated renormalization conditions can be grasped into the form

$$\Re\left[\hat{\Gamma}^q_{ij}(p^2)\right]u_{q_j}(p)|_{p^2=m^2_{q_j}} = \Re\left[\hat{\Pi}^q_{ij}(p^2)\right]u_{q_j}(p)|_{p^2=m^2_{q_j}} = 0, \tag{5.78}$$

$$\lim_{p^2\to m^2_{q_i}} \frac{1}{\not{p} - m_{q_i}}\Re\left[\hat{\Gamma}^q_{ii}(p)\right]u_{q_i}(p) = u_{q_i}(p). \tag{5.79}$$

The first condition Eq. (5.78) taken at $i = j$ fixes the renormalized mass to the physical mass, i.e., to the real part of the propagator pole, requiring any real mass correction to vanish at $p^2 = m^2_{q_j}$. For $i \neq j$, Eq. (5.78) prohibits any mixing of different quark flavors induced by the self energy graphs collected under $\Pi^q_{ij}(p^2)$ for $\hat{\Pi}^q_{ij}(p^2)$. Finally, the second condition Eq. (5.79) requires the real part of the propagator residue to be one. Plugging the Eqs. (5.74), (5.75), (5.76) and (5.77) into the Eqs. (5.78) and (5.79), one finds that

the above on-shell renormalization conditions adjust the counterterms to

$$\delta m_{q_i}^{\rm OS} = \frac{1}{2}\Re\left[m_{q_i}(\Pi_{ii}^{q,L}(m_{q_i}^2)+\Pi_{ii}^{q,R}(m_{q_i}^2))+\Pi_{ii}^{q,SL}(m_{q_i}^2)+\Pi_{ii}^{q,SR}(m_{q_i}^2)\right], \tag{5.80}$$

$$\begin{aligned}\delta(Z^{q,L/R})_{ij}^{\rm OS} =& \frac{2}{m_{q_i}^2-m_{q_j}^2}\Re\Big[m_{q_j}^2\Pi_{ij}^{q,L/R}(m_{q_j}^2)+m_{q_i}m_{q_j}\Pi_{ij}^{q,R/L}(m_{q_j}^2)\\ &+m_{q_i}\Pi_{ij}^{q,SL/SR}(m_{q_j}^2)+m_{q_j}\Pi_{ij}^{q,SR/SL}(m_{q_j}^2)\Big] \qquad \text{for} \quad i\neq j,\end{aligned} \tag{5.81}$$

$$\begin{aligned}\delta(Z^{L/R})_{ii}^{\rm OS} =& \Re\Big[-\Pi_{ii}^{q,L/R}(m_{q_i}^2)+\frac{1}{2m_{q_i}}\left[\Pi_{ii}^{q,SL/SR}(m_{q_i}^2)-\Pi_{ii}^{q,SR/SL}(m_{q_i}^2)\right]\\ &-m_{q_i}\frac{\partial}{\partial p^2}\Big[m_{q_i}\Big(\Pi_{ii}^{q,L/R}(p^2)+\Pi_{ii}^{q,R/L}(p^2)\Big)+\Pi_{ii}^{q,SL/SR}(p^2)\\ &+\Pi_{ii}^{q,SR/SL}(p^2)\Big]\Big|_{p^2=m_{q_i}^2}\Big].\end{aligned} \tag{5.82}$$

The Eqs. (5.80) - (5.82) fix all the counterterms in $\delta\mathcal{L}^{\rm quark}$ yielding a UV-finite result with all renormalization constants defined in the on-shell scheme. Since we do not take the mixing of different flavors into account one can set $i=j$, e.g., in Eq. (5.71) in the following. Furthermore, due to the renormalization condition Eq. (5.78), this mixing is not reintroduced by higher-order corrections.

After this general introduction, we move on to the actual renormalization of the up and down type quarks. The wave function renormalization follows from the Eqs. (5.81) and (5.82). However, due to the different characteristics of the quarks, we choose to renormalize their masses within different renormalization schemes.

Due to its relatively large mass, the top-quark decays quickly after its production and, hence, cannot form any bound states. Its mass is directly measurable such that it seems reasonable to fix the renormalized mass to this physical mass $(m_t)^{\rm OS} = 172.3$ GeV[7] using of the on-shell scheme Eq. (5.80)

$$\delta m_t^{\rm OS} = \frac{1}{2}\Re\left[m_t(\Pi_{33}^{q,L}(m_t)+\Pi_{33}^{q,R}(m_t))+\Pi_{33}^{q,SL}(m_t)+\Pi_{33}^{q,SR}(m_t)\right]. \tag{5.83}$$

The situation turns out to be quite different for the bottom quark, which happens to be long-lived enough to hadronize. Its mass cannot be directly measured but needs to be deduced within a certain theoretical framework. We therefore choose to renormalize the bottom mass as well as all quarks of the first and second generation within the $\overline{\rm DR}$ scheme related to the use of DRed as introduced in Sec. 5.1.2. The $\overline{\rm DR}$ scheme fixes the counterterms by the simple requirement that they have to subtract Δ as defined in Eq. (5.52) from the radiative corrections. It takes the general form

$$\delta m_q^{\overline{\rm DR}} = (-2)\frac{\alpha_{\rm s}C_F}{4\pi}m_q^{\overline{\rm DR}}\Delta. \tag{5.84}$$

Note that Eq. (5.84) vanishes in the limit of a vanishing quark mass $m_q \to 0$ (see chiral symmetry, Sec. 2.2.1). Quark masses of the first and second generation are renormalized within the $\overline{DR}$-scheme. However, these only become relevant in the context of `ChiChi22qq`, where we set the $\overline{\rm DR}$ masses of the u-, d- and s-quark to zero. We keep the charm quark as massive only, where we use the $\overline{MS}$-mass throughout as provided by `micrOMEGAs` (see SPA-convention). This slight numerical inconsistency does not spoil renormalization. Moreover, it has no large impact on the final result due to the smallness of the charm-quark mass

[7] Note that the top-mass renormalized in the $\overline{\rm DR}$ scheme yields $m_t^{\overline{\rm DR}} = 161.6$ GeV, which is quite a difference.

compared to the top-quark mass[8] and the relevant energy scale of the processes under consideration.
The treatment of the bottom quark mass m_b is more elaborated and deserves our special attention. Its evaluation is therefore outlined in the following section.

5.1.6. The Treatment of m_b

In the following, we provide a quite careful treatment of the bottom quark mass. This is motivated by the fact that its mass appears in the bottom-Yukawa coupling, which enters, i.a., the s-channel Higgs exchange for gaugino (co)annihilation into bottom quarks. As this channel can yield large contributions to the total (co)annihilation cross section of gauginos, for example within the so-called Higgs-funnel regions as discussed in Sec. 4.2, a precise estimation can be of great importance for an accurate evaluation of $\Omega_{\tilde{\chi}_1^0}$.
The mass parameter $m_b(m_b)$ is typically extracted in the $\overline{\rm MS}$ renormalization scheme[9] from the SM analysis of Υ sum rules [192]. To obtain the corresponding $\overline{\rm DR}$ value within the MSSM taken at a scale $\mu = Q$ (typically Q$\sim \mathcal{O}$(1 TeV)) from the $\overline{\rm MS}$ bottom mass calculated within the SM at the renormalization scale $\mu = m_b$, one has to go through the following steps of recalculation:

$$m_b^{\overline{\rm MS},{\rm SM}}(m_b) \overset{(1)}{\to} m_b^{\overline{\rm MS},{\rm SM}}(Q) \overset{(2)}{\to} m_b^{\overline{\rm DR},{\rm SM}}(Q) \overset{(3)}{\to} m_b^{\overline{\rm DR},{\rm MSSM}}(Q). \tag{5.85}$$

In step (1), we use the SM three-loop renormalization group equation for five active quarks flavors to evolve the bottom mass from the scale m_b to the scale Q [193], which leaves us $m_b^{\overline{\rm MS},{\rm SM}}(Q)$. In a second step, we convert $m_b^{\overline{\rm MS},{\rm SM}}(Q)$ to the corresponding $\overline{\rm DR}$ mass using the two-loop relation

$$\begin{aligned} m_b^{\overline{\rm DR},{\rm SM}}(Q) \; = m_b^{\overline{\rm MS},{\rm SM}}(Q) \Bigg[1 - \frac{\alpha_e}{\pi}\frac{1}{4}C_F + \left(\frac{\alpha_{\rm s}^{\overline{\rm MS}}}{\pi}\right)^2 \frac{11}{192}C_A C_F - \frac{\alpha_{\rm s}^{\overline{\rm MS}}}{\pi}\frac{\alpha_e}{\pi}\left(\frac{1}{4}C_F^2 + \frac{3}{32}C_A C_F\right) \\ + \left(\frac{\alpha_e}{\pi}\right)^2 \left(\frac{3}{32}C_F^2 + \frac{1}{32}C_F T_F n_f\right) + \dots \Bigg] \end{aligned} \tag{5.86}$$

as provided in Ref. [194]. The dots indicate corrections of higher orders, which are not relevant here, n_f is the number of active quark flavors and $T_F = \frac{1}{2}$, $C_A = 3$ as well as $C_F = 4/3$ are QCD colorfactors. In Eq. (5.86), we have also introduced a so-called evanescent coupling α_e. It arises due to the decomposition of the four dimensional gluon as common to DRed into a D-dimensional part and an ϵ-scalar $\alpha_{\rm s} g^{(4)} \bar{q} q \to \alpha_{\rm s} g^{(D)} \bar{q} q + \alpha_e \epsilon_g \bar{q} q$ as mentioned in Sec. 5.1.2. There, it was stated that the contributions of ϵ-scalars just account for the difference between DRed an DReg in order that their appearance in Eq. (5.86) is not unexpected. α_e, taken in the SM, now relates to the strong coupling renormalized in the

[8] Due to $m_t/m_c \sim 40$, resonant annihilation through a s-channel Higgs into up-typ quarks is, at least for the scenarios relevant here, always dominated by the top quark contribution.
[9] The $\overline{\rm MS}$ renormalization scheme is the pendant of the $\overline{\rm DR}$ scheme but for DReg instead of DRed (see Sec. 5.1.2).

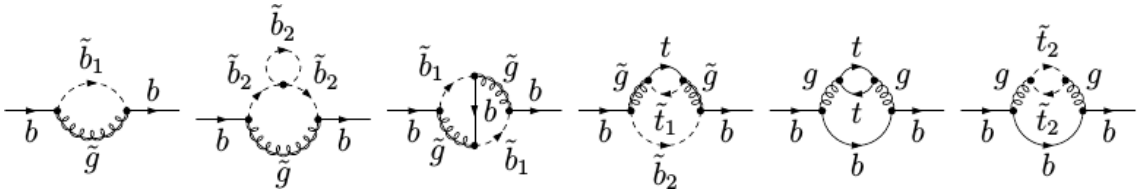

Figure 5.4.: Sample of top-quark and SUSY-QCD corrections to the bottom mass up to two-loop. Fig. taken from Ref. [195].

$\overline{\text{DR}}$ scheme in the MSSM via [195]

$$\alpha_e = \alpha_{\text{s}}^{\overline{\text{DR}},\text{MSSM}}\left[1+\frac{\alpha_{\text{s}}^{\overline{\text{DR}},\text{MSSM}}}{\pi}\left\{-T_F\frac{L_t}{2}+\frac{C_A}{4}\left(2+L_{\tilde{g}}+\sum_{i=1,2}\left(L_{\tilde{g}}-L_{\tilde{q}_i}\right)\frac{m^2_{\tilde{q}_i}}{m^2_{\tilde{g}}-m^2_{\tilde{q}_1}}\right)\right.\right.$$
$$+\frac{C_F}{4}\left(\sum_{i=1,2}\left(-1-2L_{\tilde{g}}+2L_{\tilde{q}_i}+\left(-L_{\tilde{g}}+L_{\tilde{q}_i}\right)\frac{m^2_{\tilde{q}_i}}{m^2_{\tilde{g}}-m^2_{\tilde{q}_i}}\right)\right.$$
$$\left.\left.\left.\times\frac{m^2_{\tilde{q}_i}}{m^2_{\tilde{g}}-m^2_{\tilde{q}_i}}+(-3-2L_{\tilde{g}})+\mathcal{O}(\epsilon)\right)\right\}\right]. \tag{5.87}$$

Here, we make use of the shorthand notation $L_i = \ln(Q^2/m_i^2)$ and, again, $\epsilon = (4-D)/2$. The third and last step in Eq. (5.85) involves the conversion of the bottom mass calculated within the SM with $n_f = 5$ light quarks to the bottom mass estimated within the MSSM with $n_f = 6$. This step requires the addition of threshold corrections to the bottom mass from top quark as well as from SUSY-QCD loops as depicted in Fig. 5.4. Following Ref. [195], this can be achieved using

$$m_b^{\overline{\text{DR}},\text{SM}}(Q) \;=\; \zeta_{m_\text{b}}\, m_b^{\overline{\text{DR}},\text{MSSM}}(Q)\,, \tag{5.88}$$

where the coefficient ζ_{m_b}, expanded in terms of the strong coupling, takes the form

$$\zeta_{m_\text{b}} \;=\; 1+\left(\frac{\alpha_{\text{s}}^{\overline{\text{DR}}}}{\pi}\right)\zeta_b^{(1)}+\left(\frac{\alpha_{\text{s}}^{\overline{\text{DR}}}}{\pi}\right)^2\zeta_b^{(2)}+\mathcal{O}(\alpha_{\text{s}}^3)\,. \tag{5.89}$$

The one and two-loop decoupling coefficients $\zeta_b^{(1)}$ and (the very lengthy) $\zeta_b^{(2)}$ can again be found in Ref. [195]. After inverting Eq. (5.88), we are finally left with the required $m_b^{\overline{\text{DR}},\text{MSSM}}(Q)$, which has been used throughout our analyses. Note again that we do not go through this procedure for the quarks of the first and second generation.

This ends the discussion of the quark sector of the MSSM. Before we go on and provide the same for the squark sector, we shortly discuss how to improve on the bottom-Yukawa coupling by the incorporation of additional higher-order corrections providing a short view on the use of effective couplings.

The Effective Treatment of the Bottom-Yukawa Coupling

As already explained above, the bottom-Yukawa coupling can become phenomenologically important so that its exact calculation is of large interest. The bottom Yukawa coupling can be improved via the inclusion of additional higher-order EW, QCD and SUSY-QCD

corrections. Leading QCD and top-quark induced corrections are known up to $\mathcal{O}(\alpha_s^4)$ [196] up to date. These corrections can be included in the form of an effective Yukawa coupling via

$$\left[h_b^{\overline{\text{MS}},\text{QCD},\text{H}}(Q)\right]^2 = \left[h_b^{\overline{\text{MS}},\text{H}}(Q)\right]^2 \left[1 + \Delta_{\text{QCD}} + \Delta_t^{\text{H}}\right] \tag{5.90}$$

for each Higgs H=h^0, H^0, A^0. The QCD corrections Δ_{QCD} are explicitly given by

$$\begin{aligned}\Delta_{\text{QCD}} =& \frac{\alpha_\text{s}(Q)}{\pi} C_F \frac{17}{4} + \frac{\alpha_s^2(Q)}{\pi^2}\left[35.94 - 1.359\, n_f\right] \\ &+ \frac{\alpha_s^3(Q)}{\pi^3}\left[164.14 - 25.77\, n_f + 0.259\, n_f^2\right] \\ &+ \frac{\alpha_s^4(Q)}{\pi^4}\left[39.34 - 220.9\, n_f + 9.685\, n_f^2 - 0.0205\, n_f^3\right].\end{aligned} \tag{5.91}$$

The top-quark induced corrections Δ_t^Φ for each Higgs boson H read

$$\Delta_t^h = c_h(Q)\left[1.57 - \frac{2}{3}\ln\frac{Q^2}{m_t^2} + \frac{1}{9}\ln^2\frac{m_b^2(Q)}{Q^2}\right], \tag{5.92}$$

$$\Delta_t^H = c_H(Q)\left[1.57 - \frac{2}{3}\ln\frac{Q^2}{m_t^2} + \frac{1}{9}\ln^2\frac{m_b^2(Q)}{Q^2}\right], \tag{5.93}$$

$$\Delta_t^A = c_A(Q)\left[\frac{23}{6} - \ln\frac{Q^2}{m_t^2} + \frac{1}{6}\ln^2\frac{m_b^2(Q)}{Q^2}\right], \tag{5.94}$$

with

$$\left\{c_h(Q),\ c_H(Q),\ c_A(Q)\right\} = \frac{\alpha_\text{s}^2(Q)}{\pi^2}\left\{\frac{1}{\tan\alpha\tan\beta},\ \frac{\tan\alpha}{\tan\beta},\ \frac{1}{\tan^2\beta}\right\}. \tag{5.95}$$

As we provide a full $\mathcal{O}(\alpha_\text{s})$ calculation, we exclude the one-loop parts from the above corrections as they are already consistently provided by our NLO result.
It is well known that within the MSSM, higher-order corrections of the bottom-Yukawa coupling can be enhanced for large $\tan\beta$ or large A_b, eventually spoiling the perturbative series in α_s. Therefore, we include these corrections that can be resumed to all orders in perturbation theory [165, 197]. They can be incorporated in the Yukawa couplings Eq. (5.90) via

$$h_b^{\text{MSSM},h}(Q) = \frac{h_b^{\overline{\text{MS}},\text{QCD},h}(Q)}{1+\Delta_b}\left[1 - \frac{\Delta_b}{\tan\alpha\tan\beta}\right], \tag{5.96}$$

$$h_b^{\text{MSSM},H}(Q) = \frac{h_b^{\overline{\text{MS}},\text{QCD},H}(Q)}{1+\Delta_b}\left[1 + \Delta_b\frac{\tan\alpha}{\tan\beta}\right], \tag{5.97}$$

$$h_b^{\text{MSSM},A}(Q) = \frac{h_b^{\overline{\text{MS}},\text{QCD},A}(Q)}{1+\Delta_b}\left[1 - \frac{\Delta_b}{\tan^2\beta}\right], \tag{5.98}$$

where the resumable part is denoted by Δ_b. Moreover, we include the NNLO corrections to Δ_b, which can be found in Ref. [198]. Note that Δ_b is also known for non-minimal sources of flavor violation [199]. Finally, EW one-loop corrections to the bottom-Yukawa coupling, analytically resumed to all orders, can be found in Ref. [200]. These corrections are also part of the current DM@NLO code.

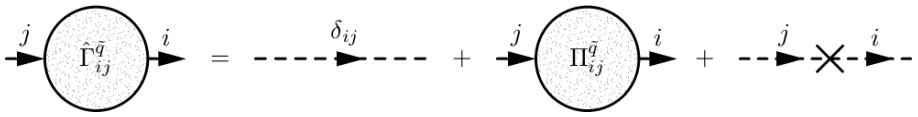

Figure 5.5.: Renormalized two-point function for squark mixing with definition of indices.

The Squark Sector

Starting with the bare Lagrangian of the squark sector

$$\mathcal{L}_0^{\text{squark}} = \partial_\mu \tilde{q}^*_{0,i} \partial^\mu \tilde{q}_{0,i} - m^2_{\tilde{q}_0} \tilde{q}^*_{0,i} \tilde{q}_{0,i}, \tag{5.99}$$

we insert the replacements

$$\tilde{q}_{0,i} \to (\delta_{ij} + \frac{1}{2}\delta Z^{\tilde{q}}_{i,j})\tilde{q}_j, \tag{5.100}$$

$$m^2_{\tilde{q}_{0,i}} \to m^2_{\tilde{q}_i} + \delta m^2_{\tilde{q}_i}, \tag{5.101}$$

which can be deduced from Eq. (5.61) and Eq. (5.63) together with Eq. (5.66). We find that the Lagrangian up to next-to-leading order takes the form

$$\begin{aligned} \mathcal{L}_0^{\text{squark}} =& \underbrace{\partial_\mu \tilde{q}^*_i \partial^\mu \tilde{q}_i - m^2_{\tilde{q}_i} \tilde{q}^*_i \tilde{q}_i}_{\mathcal{L}_{\text{ren}}^{squark}} \\ & \underbrace{\begin{aligned} &+ \frac{1}{2}\delta Z^{\tilde{q}}_{ij} \left(\partial_\mu \tilde{q}^*_i \partial^\mu \tilde{q}_j - m^2_{\tilde{q}_i} \tilde{q}^*_i \tilde{q}_j\right) \\ &+ \frac{1}{2}(\delta Z^{\tilde{q}})^*_{ji} \left(\partial_\mu \tilde{q}^*_j \partial^\mu \tilde{q}_i - m^2_{\tilde{q}_i} \tilde{q}^*_j \tilde{q}_i\right) \\ &- \delta m^2_{\tilde{q}_i} \tilde{q}^*_i \tilde{q}_i. \end{aligned}}_{\delta\mathcal{L}^{\text{squark}}} \end{aligned} \tag{5.102}$$

The double index in $Z^{\tilde{q}}_{ij}$ accounts for additional mixings of squarks, which may be introduced due to higher-order corrections as shown in Fig. 5.5. The subscripts $i, j \in \{1, 2\}$ indicate that we work in the basis of mass eigenstates. Like we already did in the quark sector, we begin with fixing the counterterms in $\delta\mathcal{L}^{\text{squark}}$ within the on-shell renormalization scheme.
The renormalized one particle irreducible 2-point function $\hat{\Gamma}^{\tilde{q}}_{ij}$ is depicted in Fig. 5.5. It is related to the S-matrix element $\mathcal{M}^{\tilde{q}}$ via

$$\mathcal{M}^{\tilde{q}} = i\hat{\Gamma}^{\tilde{q}}_{ij} \tag{5.103}$$

and to the renormalized self energy $\hat{\Pi}^{\tilde{q}}_{ij}$ via

$$\hat{\Gamma}^{\tilde{q}}_{ij} = \hat{\Pi}^{\tilde{q}}_{ij} + (p^2 - m^2_{\tilde{q}_i})\delta_{ij}. \tag{5.104}$$

$\hat{\Pi}_{ij}$ gets contributions from divergent loop diagrams subsumed under Π_{ij} as well as from the counterterms in $\delta\mathcal{L}^{\text{squark}}$ Eq. (5.102) associated to the wave function and mass renormalization constants. Following Eq. (5.102), $\hat{\Pi}^{\tilde{q}}_{ij}$ can be decomposed as

$$\hat{\Pi}^{\tilde{q}}_{ij}(p^2) = \Pi^{\tilde{q}}_{ij} + \frac{1}{2}(p^2 - m^2_{\tilde{q}_i})\delta Z^{\tilde{q}}_{ij} + \frac{1}{2}(p^2 - m^2_{\tilde{q}_j})\delta(Z^{\tilde{q}})^*_{ji} - \delta_{ij}\delta m^2_{\tilde{q}_i}. \tag{5.105}$$

The renormalization conditions in the on-shell scheme require the counterterms to fulfill

$$\Re\left[\hat{\Gamma}^{\tilde{q}}_{ij}(p^2)|_{p^2=m^2_{\tilde{q}_j}}\right] = \Re\left[\hat{\Pi}^{\tilde{q}}_{ij}(p^2)|_{p^2=m^2_{\tilde{q}_j}}\right] = 0, \tag{5.106}$$

$$\lim_{p^2 \to m^2_{\tilde{q}_i}} \frac{1}{p^2 - m^2_{\tilde{q}_i}} \Re\left[\hat{\Gamma}^{\tilde{q}}_{ii}(p^2)\right] = 1, \tag{5.107}$$

which adjust the renormalization constants of Eqs. (5.100) and (5.101) to

$$\delta(m^2_{\tilde{q}_i})^{\text{OS}} = \Re\left[\Pi^{\tilde{q}}_{ii}(m^2_{\tilde{q}_i})\right], \tag{5.108}$$

$$\delta(Z^{\tilde{q}})^{\text{OS}}_{ij} = \frac{2\Re\left[\Pi^{\tilde{q}}_{ij}(m^2_{\tilde{q}_j})\right]}{m^2_{\tilde{q}_i} - m^2_{\tilde{q}_j}}, \quad \text{for } i \neq j, \tag{5.109}$$

$$\delta(Z^{\tilde{q}})^{\text{OS}}_{ii} = -\Re\left[\frac{\partial\Pi^{\tilde{q}}_{ii}(p^2)}{\partial p^2}|_{p^2=m^2_{\tilde{q}_i}}\right] = -\Re\left[\dot{\Pi}^{\tilde{q}}_{ii}(m^2_{\tilde{q}_i})\right]. \tag{5.110}$$

The first two results arise from condition Eq. (5.106). They fix the renormalized mass to the physical mass, i.e., to the real part of the propagator pole, requiring any real mass correction to vanish at $p^2 = m^2_{\tilde{q}_i}$ (Eq. (5.108)). They further prohibit any mixing of squark mass eigenstates due to the self energy graphs collected under $\Pi^{\tilde{q}}_{ij}(p^2)$ (Eq. (5.109)). The third condition Eq. (5.110) stems from the renormalization condition Eq. (5.107). It requires the real part of the propagator residue to be one, which can be seen by looking at the expansion of the propagator in terms of the renormalized self energy

$$\frac{1}{p^2 - m^2_{\tilde{q}_i}} + \frac{1}{p^2 - m^2_{\tilde{q}_i}}\hat{\Pi}_{ii}(p^2)\frac{1}{p^2 - m^2_{\tilde{q}_i}} = \frac{1}{p^2 - m^2_{\tilde{q}_i}}\left(1 + \frac{\hat{\Pi}_{ii}(p^2)}{p^2 - m^2_{\tilde{q}_i}}\right). \tag{5.111}$$

Due to the mixing of squarks, it actually turns out that the renormalization of squark masses is not that straight forward but has to be discussed in conjunction with all other parameters appearing in the tree-level squark matrix Eq. (2.131) and Eq. (2.134)

$$\begin{pmatrix} m^2_{\tilde{q}_1} & 0 \\ 0 & m^2_{\tilde{q}_2} \end{pmatrix} = \tag{5.112}$$

$$\mathbf{U}^{\tilde{q}}\begin{pmatrix} \mathcal{M}^2_{\tilde{q}} + M^2_{Z^0}(T^{\tilde{q}}_{3L} - Q_q \sin^2\Theta_W)\cos 2\beta + \boldsymbol{m}^2_q & \boldsymbol{m}_q(A_{\tilde{q}} - \mu(\tan\beta)^{-2T^{\tilde{q}}_{3L}}) \\ (A_{\tilde{q}} - \mu(\tan\beta)^{-2T^{\tilde{q}}_{3L}})\boldsymbol{m}_q & \mathcal{M}^2_{\tilde{u},\tilde{d}} + Q_q M^2_{Z^0}\cos 2\beta \sin^2\Theta_W + \boldsymbol{m}^2_{q_i} \end{pmatrix}(\mathbf{U}^{\tilde{q}})^\dagger.$$

Here, we redefined $A_{\tilde{q}} \to -A_{\tilde{q}}$ to match the definitions of Ref. [147]. As stated in Sec. 2.6.3, the up and down type sectors of left-handed squarks are intertwined by the $SU(2)_L$-symmetry, which leads to the introduction of a common soft breaking mass $\mathcal{M}^2_{\tilde{q}}$. Therefore, the renormalization of both sectors has to be considered simultaneously. It turns out that from the eleven parameters $\mathcal{M}^2_{\tilde{q}}$, $\mathcal{M}^2_{\tilde{u}}$, $\mathcal{M}^2_{\tilde{d}}$, $A_{\tilde{u}}$, $A_{\tilde{d}}$, $\Theta_{\tilde{u}}$, $\Theta_{\tilde{d}}$, $m^2_{\tilde{u}_1}$, $m^2_{\tilde{u}_2}$, $m^2_{\tilde{d}_1}$ and $m^2_{\tilde{d}_2}$, which appear in the up and down type squark mass-matrices Eq. (5.112), only five are completely independent and can be considered as input parameters. Hence, their counterterms can be adjusted freely. The rest is fixed by the requirement that Eq. (5.112) holds true even at the one-loop order. For the particular choice of the five independent parameters out of the above set, it is important to think about the regions of parameters space that are of particular interest to the analyses performed in the context of `DM@NLO`. As we consider (co)annihilation of 3rd generation squarks, in particular of the top squark, which, due to the Boltzmann suppression Eqs. (3.59a) and (3.59b), happens to be extremely sensitive to the lighter stop-mass $m^2_{\tilde{t}_1}$ [10], it seems reasonable to take the up-type squark mass $m^2_{\tilde{u}_1}$ as an input parameter and to renormalize it in the on-shell scheme. We also treat the down-type squark masses $m^2_{\tilde{d}_1}$ and $m^2_{\tilde{d}_2}$ as input parameters and renormalize them on-shell, whereas the heavier up squark mass $m^2_{\tilde{u}_2}$, which is typically much heavier[11] and,

[10] The masses $m_{\tilde{t}_1}$ and $m_{\tilde{b}_1}$ play an important role in the gaugino (co)annihilation Sec. 4.2, where they can appear in the corresponding t- and u-channel propagators.

[11] At least, this is the case in the scenarios investigated here, which typically feature a large mixing proportional to the quark mass and in turn a large mass splitting in the 3rd-generation squark sector.

hence, less sensitive to radiative corrections, is treated as a dependent parameter. We take the trilinear couplings $A_{\tilde{u}}$ and $A_{\tilde{d}}$ as input parameters since, e.g., the Higgs coupling to squarks, which can become important to squark annihilation within the Higgs-funnel regions of the MSSM-parameter space, depends sensitively on $A_{\tilde{u}}$ and $A_{\tilde{d}}$. As it turns out that in the on-shell scheme $A_{\tilde{b}}$ can be subject to potentially large higher-order corrections

$$\delta A_{\tilde{b}} = \frac{1}{m_{\mathrm{b}}}\left[-(A_{\tilde{b}} - \mu^* \tan\beta)\delta m_{\mathrm{b}} + ...\right] \tag{5.113}$$

as discussed in Ref. [201], which render the perturbative expansion in α_{s} unreliable if $|A_{\tilde{b}} - \mu^* \tan\beta|$ happens to be large, we choose to renormalize the trilinear couplings within the $\overline{\mathrm{DR}}$-scheme. This leaves us with a hybrid $\overline{\mathrm{DR}}$/on-shell scheme with the input parameters

$$(m^2_{\tilde{u}_1})^{\mathrm{OS}},\ (m^2_{\tilde{d}_1})^{\mathrm{OS}},\ (m^2_{\tilde{d}_2})^{\mathrm{OS}},\ A_{\tilde{u}}^{\overline{\mathrm{DR}}}\ A_{\tilde{d}}^{\overline{\mathrm{DR}}} \tag{5.114}$$

and the dependent parameters

$$m^2_{\tilde{u}_2},\ \mathcal{M}^2_{\tilde{q}},\ \mathcal{M}^2_{\tilde{u}},\ \mathcal{M}^2_{\tilde{d}},\ \Theta_{\tilde{u}},\ \Theta_{\tilde{d}}. \tag{5.115}$$

The next step is to specify the corresponding counterterms according to the above choice. The counterterms for the squark masses renormalized in the on-shell scheme follow from Eq. (5.108), whereas the counterterms of the trilinear couplings $A_{\tilde{q}}^{\overline{\mathrm{DR}}}$ ($q \in \{u, d\}$ for up and down type) take the form

$$\begin{aligned}\delta A_{\tilde{q}}^{\overline{\mathrm{DR}}} = \frac{1}{m_q}\Big[&U^{\tilde{q}}_{11}U^{\tilde{q}}_{12}(\delta m^2_{\tilde{q}_1})^{\overline{\mathrm{DR}}} + U^{\tilde{q}}_{21}U^{\tilde{q}}_{22}(\delta m^2_{\tilde{q}_2})^{\overline{\mathrm{DR}}} + (U^{\tilde{q}}_{21}U^{\tilde{q}}_{12} + U^{\tilde{q}}_{11}U^{\tilde{q}}_{22})(m^2_{\tilde{q}_1} - m^2_{\tilde{q}_2})\delta\Theta_{\tilde{q}}^{\overline{\mathrm{DR}}} \\ &- \frac{\delta m_q^{\overline{\mathrm{DR}}}}{m_q}(U^{\tilde{q}}_{11}U^{\tilde{q}}_{12}m^2_{\tilde{q}_1} + U^{\tilde{q}}_{21}U^{\tilde{q}}_{22}m^2_{\tilde{q}_2})\Big].\end{aligned} \tag{5.116}$$

Just like in the case of the bottom mass, the $\delta A_{\tilde{q}}^{\overline{\mathrm{DR}}}$ counterterm is defined to cancel the Δ defined in Eq. (5.52) including the singularity, which arises through radiative contributions to the trilinear couplings. The counter terms for the squark masses and mixings in Eq. (5.116) are for $i \neq j$ (i.e. $i = 1 \to j = 2$, $i = 2 \to j = 1$)

$$\begin{aligned}(\delta m^2_{\tilde{q}_i})^{\overline{\mathrm{DR}}} =&\frac{\alpha_{\mathrm{s}}C_F}{4\pi}\frac{c_\epsilon}{\epsilon}\Big[((U^{\tilde{q}}_{i1})^2 - (U^{\tilde{q}}_{i2})^2)^2 m^2_{\tilde{q}_i} - m^2_{\tilde{q}_i} + (U^{\tilde{q}}_{21}U^{\tilde{q}}_{11} - U^{\tilde{q}}_{22}U^{\tilde{q}}_{12})^2 m^2_{\tilde{q}_j} \\ &+ 8m_q m_{\tilde{g}} U^{\tilde{q}}_{i1}U^{\tilde{q}}_{i2} - 4m^2_{\tilde{g}} - 4m^2_q\Big]\end{aligned} \tag{5.117}$$

and

$$\begin{aligned}(\delta\Theta_{\tilde{q}})^{\overline{\mathrm{DR}}} =&\frac{\alpha_{\mathrm{s}}C_F}{4\pi}\frac{c_\epsilon}{\epsilon}\frac{1}{m^2_{\tilde{q}_1} - m^2_{\tilde{q}_2}}\Big[(U^{\tilde{q}}_{21}U^{\tilde{q}}_{11} - U^{\tilde{q}}_{22}U^{\tilde{q}}_{12})\Big(((U^{\tilde{q}}_{11})^2 - (U^{\tilde{q}}_{12})^2)^2 m^2_{\tilde{q}_1} \\ &+ ((U^{\tilde{q}}_{21})^2 - (U^{\tilde{q}}_{22})^2)^2 m^2_{\tilde{q}_2}\Big) + 4m_q m_{\tilde{g}}(U^{\tilde{q}}_{11}U^{\tilde{q}}_{22} + U^{\tilde{q}}_{12}U^{\tilde{q}}_{21})\Big].\end{aligned} \tag{5.118}$$

Here, we introduce c_ϵ defined by

$$c_\epsilon := \Gamma(1+\epsilon)(4\pi)^\epsilon \tag{5.119}$$

(see also Eq. (5.84) for the definition of $\delta m_q^{\overline{\mathrm{DR}}}$). As already mentioned above, the dependent counterterms are fixed by the requirement that Eq. (5.112) should hold even at the one-loop order. Taking the trace and determinant of both sides of Eq. (5.112) in the up- and down-squark sector, this yields the required identities for fixing the soft breaking

masses $\mathcal{M}^2_{\tilde{q}}$ and $\mathcal{M}^2_{\tilde{u}}$, $\mathcal{M}^2_{\tilde{d}}$ in terms of the input parameters and other parameters of the mass matrices such as μ and $\tan\beta$, which do not receive any QCD-corrections and, hence, do not require renormalization. However, as the corresponding counterterms never appear in any vertex, we do not calculate them. By further diagonalizing the right hand side of Eq. (5.112), again for both the up- and the down-squark sector, the recovered eigenvalues can be identified with the chosen input masses $m^2_{\tilde{t}_1}$, $m^2_{\tilde{b}_1}$, $m^2_{\tilde{b}_2}$ and the dependent mass $m^2_{\tilde{t}_2}$. These identities can then be used to fix the counterterms of the remaining mixing angles $\Theta_{\tilde{q}}$

$$\delta\Theta_{\tilde{q}} = \frac{\delta m_q(A_{\tilde{q}} - \mu(\tan\beta)^{-2T^{\tilde{q}}_{3L}} + m_q\delta A_{\tilde{q}} - U^{\tilde{q}}_{11}U^{\tilde{q}}_{12}(\delta m^2_{\tilde{q}_1} - \delta m^2_{\tilde{q}_2})}{(U^{\tilde{q}}_{21}U^{\tilde{q}}_{12} + U^{\tilde{q}}_{11}U^{\tilde{q}}_{22})(m^2_{\tilde{q}_1} - m^2_{\tilde{q}_2})}. \tag{5.120}$$

The last counterterm still missing is the mass counterterm for the heavier up-type squark $\delta m_{\tilde{u}_2}$. It takes the form

$$\begin{aligned}\delta m^2_{\tilde{u}_2} = \frac{1}{U^{\tilde{u}}_{21}U^{\tilde{u}}_{12}}\Big[&(U^{\tilde{u}}_{21}U^{\tilde{u}}_{12} + U^{\tilde{u}}_{11}U^{\tilde{u}}_{22})\Big((U^{\tilde{d}}_{11})^2\delta m^2_{\tilde{d}_1} + (U^{\tilde{d}}_{21})^2\delta m^2_{\tilde{d}_2}\\ &+ 2U^{\tilde{d}}_{11}U^{\tilde{d}}_{21}(m^2_{\tilde{d}_1} - m^2_{\tilde{d}_2})\delta\Theta_{\tilde{d}} - 2m_d\delta m_d\\ &- (U^{\tilde{u}}_{11})^2\delta m^2_{\tilde{u}_1} + 2m_u\delta m_u\Big) - 2U^{\tilde{u}}_{11}U^{\tilde{u}}_{21}\Big(\delta m_u(A_{\tilde{u}} - \mu/\tan\beta)\\ &+ m_u\delta A_{\tilde{u}} - U^{\tilde{u}}_{11}U^{\tilde{u}}_{12}\delta m^2_{\tilde{u}_1}\Big)\Big].\end{aligned} \tag{5.121}$$

Using all the relations above, we finally end up with a scheme that cancels all UV-divergences that we encounter during the calculation of the one-loop corrections to the Born-level processes listed in Sec. 4.2 and Sec. 4.3.
This section is closed with a short comment on the renormalization scheme presented here. Eqs. (5.118) and (5.120) make evident that the mixed $\overline{\text{DR}}$/on-shell scheme stated above leads to difficulties if $m^2_{\tilde{q}_2} \to m^2_{\tilde{q}_1}$, which correspond to a small squark mixing angle $\Theta_{\tilde{q}} \to 0$. Unfortunately, there is no renormalization scheme known by now which is well defined for the entire MSSM parameter space. Since scenarios with light third generation squarks favor a large mixing and, in turn, a large mass splitting, the renormalization scheme presented here turns out to be an appropriate choice for the parameter combinations that we expect to encounter throughout our analyses.
Moreover, we include the wave function renormalization constant for external and internal particles at each vertex and propagator of a Feynman diagram. Although the wave function renormalization constants for internal particles have to drop out of the final result, this distribution over the Feynman graphs allows for a better check of our results as it renders the vertex correction as well as the propagator corrections UV-finite separately.
Further note that we use the strong coupling $\alpha_s^{\overline{\text{DR}},\text{MSSM}}(Q)$ defined in the $\overline{\text{DR}}$ scheme at scale Q within the MSSM. However, since α_s enters the calculation of corrections to the processes presented in the Secs. 4.2 and 4.3 starting at NLO, the inclusion of the corresponding counterterms is only a NNLO effect. It is therefore beyond the scope of this work.

We finally need to know how to construct the counterterm of functions V that depend on more than one renormalized parameter A_i ($i \in \{1,..,n\}$). Following the guideline of perturbative renormalization, it turns out that these counterterms can be evaluated by an expansion of V in the counterterms (i.e. here in orders of α_s), which yields

$$\delta V(A_1, A_2, ..., A_n) = \sum_{i=1}^{n} \frac{\partial V(A_i)}{\partial A_i}\delta A_i. \tag{5.122}$$

Examples of such functions $V(A_1, ..., A_n)$, whose counterterms are evaluated by Eq. (5.122), are couplings, which may depend on masses, mixings, coupling constants, etc. as well as propagators, which depend on the propagator mass and on the wave function renormalization constants of attached external and internal particles (see statement above).

5.1.7. The Treatment of α_s

This section deals with the treatment of the strong coupling α_s. Although certain steps in its recalculation turn out to be of NNLO for the processes investigated here[12], we give a concise overview of its treatment within `DM@NLO` for the sake of completeness. The estimation of α_s follows quite similar lines as in the case of the bottom quark mass m_b encountered previously. The strong coupling is extracted from experimental data as $\alpha_s^{\overline{\rm MS},{\rm SM},n_f=5}(m_Z^2)$ and, hence, needs to be converted into the required $\alpha_s^{\overline{\rm DR},{\rm MSSM},n_f=6}(Q)$ following the steps

$$\alpha_s^{\overline{\rm MS},{\rm SM},n_f=5}(M_Z^2) \overset{(1)}{\to} \alpha_s^{\overline{\rm MS},{\rm SM},n_f=5}(Q) \overset{(2)}{\to} \alpha_s^{\overline{\rm DR},{\rm SM},n_f=5}(Q) \overset{(3)}{\to} \alpha_s^{\overline{\rm DR},{\rm MSSM},n_f=6}(Q). \quad (5.123)$$

In the first step, we run the strong coupling with $n_f = 5$ active quark flavors within the $\overline{\rm MS}$ scheme from the scale $\mu = M_Z$ up to the scale $\mu = Q$ by the N^{m}LO renormalization group equation

$$\frac{{\rm d}\alpha_{\rm s}}{{\rm d}\ln\mu^2} = \beta_{{\rm N}^m{\rm LO}}(\alpha_{\rm s}) = -\sum_{k=0}^{m} \alpha_{\rm s}^{k+2}\beta_k. \quad (5.124)$$

Here, we use the shorthand notation $\alpha_{\rm s} = \alpha_s^{\overline{\rm MS},{\rm SM},n_f=5}/4\pi$. The above expansion coefficients β_k of the β-function of QCD at $k = 3$, i.e., at N^{3}LO (= NNNLO) take the form [202]

$$\beta_0 = 11 - 2/3 n_f, \quad (5.125)$$
$$\beta_1 = 102 - 38/3 n_f, \quad (5.126)$$
$$\beta_2 = 2857/2 - 5033/18 n_f + 325/54 n_f^2, \quad (5.127)$$
$$\beta_3 = 29243.0 - 6946.30 n_f + 405.089 n_f^2 + 1093/729 n_f^3. \quad (5.128)$$

In the second step, we convert the strong coupling defined in the $\overline{\rm MS}$ scheme to its $\overline{\rm DR}$ value. Following Ref. [203], $\alpha_{\rm s}^{\overline{\rm MS}}$ and $\alpha_{\rm s}^{\overline{\rm DR}}$ are related by

$$\alpha_s^{\overline{\rm DR}} = \alpha_s^{\overline{\rm MS}} \left[1 + \frac{\alpha_s^{\overline{\rm MS}}}{\pi}\frac{C_A}{12} + \left(\frac{\alpha_s^{\overline{\rm MS}}}{\pi}\right)^2 \left(\frac{11}{72}C_A^2 - \frac{1}{8}C_F T_F n_f\right) \right], \quad (5.129)$$

where it is implicitly understood that all couplings are evaluated at the same scale within the SM and for $n_f = 5$. We finally transform the strong coupling of the SM with $n_f = 5$ to the strong coupling evaluated in the MSSM and including top quark effects ($n_f = 6$). To do so, we need to correct for the different μ-dependent running of $\alpha_{\rm s}$ within (SM, $n_f = 5$) compared to (MSSM, $n_f = 6$) up to the scale Q. Just as in the case of the bottom mass, this is obtained at two-loop accuracy by adding the threshold corrections from diagrams as shown in Fig. 5.6. This last step, which yields the final $\alpha_s^{\overline{\rm DR},{\rm MSSM},n_f=6}(Q) = \alpha_s^{\rm full}$, can be written as

$$\alpha_s^{\rm full} = \alpha_s^{\overline{\rm DR}} \left[1 - \frac{\alpha_s^{\overline{\rm DR}}}{\pi}\zeta_1 + \left(\frac{\alpha_s^{\overline{\rm DR}}}{\pi}\right)^2 (2\zeta_1^2 - \zeta_2) \right]. \quad (5.130)$$

[12] For the processes under consideration, α_s first enters the calculation at the one-loop order.

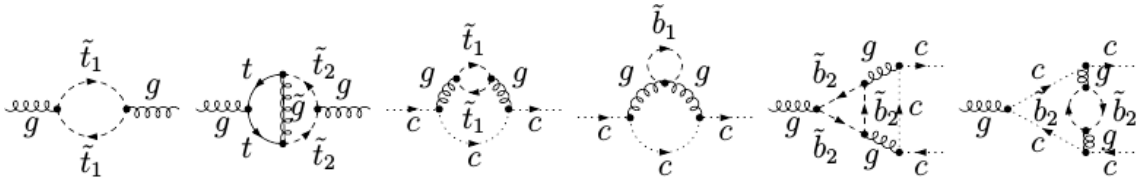

Figure 5.6.: Sample of top-quark, ghost (c) and SUSY-QCD corrections to the strong coupling constant up to two-loop. Fig. taken from Ref. [195].

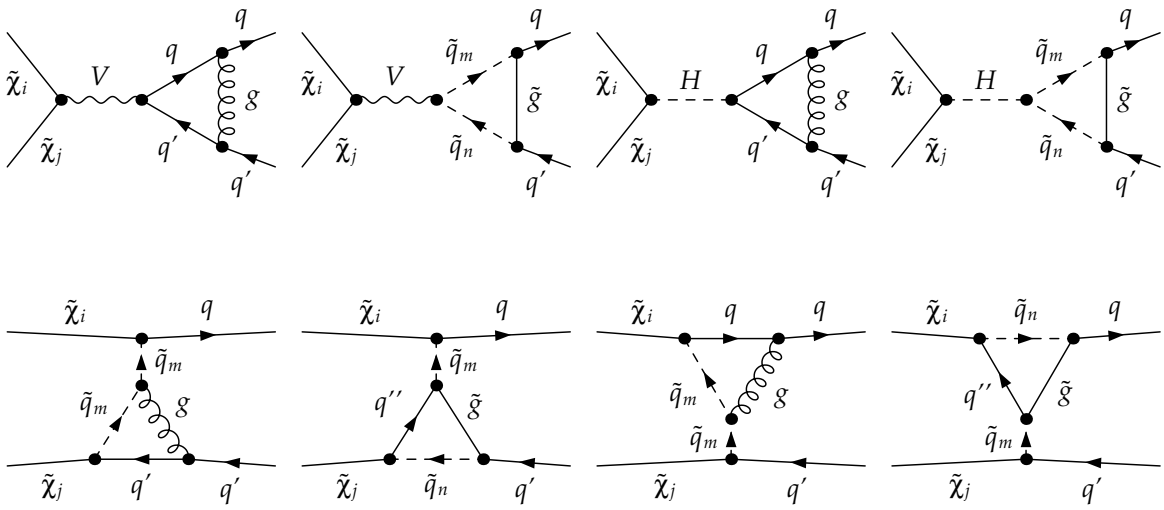

Figure 5.7.: s- and t-channel vertex corrections to the gaugino (co)annihilation processes as included in `ChiChi2qq` [1]. u-channel contributions can be obtained via crossing of the corresponding t-channels.

The decoupling coefficients ζ_1 and (the very long) ζ_2 can again be found in Ref. [195]. Although not needed here (see Sec. 5.1.6), we finally give the resulting $\overline{DR}$-counterterm for α_s^{full} for the sake of completeness. It takes the form

$$\delta\alpha_s^{\text{full}} = \frac{\alpha_s^{\text{full}}}{8\pi}\Delta\left[n_f - 3C_A\right]. \tag{5.131}$$

5.1.8. ChiChi2qq: The Virtual Corrections

The virtual $\mathcal{O}(\alpha_s)$ corrections to gaugino (co)annihilation cover all possible tree-level diagrams of Fig. 4.2 extended by the exchange of additional gluons, gluinos, quarks and squarks. The resulting diagrams of $\mathcal{O}(\alpha_s)$ are shown in the Figs. 5.7 to 5.10. They are most commonly categorized into vertex- (Figs. 5.7), propagator- (Fig. 5.8) box-corrections (Fig. 5.9) and the corresponding counterterms (Fig. 5.10) as outlined in the Secs. 5.1.5 and 5.1.6. Their mathematical expressions are then contracted with the complex conjugate of the different tree-level amplitudes in order to yield the contributions of the virtual $\mathcal{O}(\alpha_s)$ corrections to the overall squared matrix element. This contribution averaged/summed

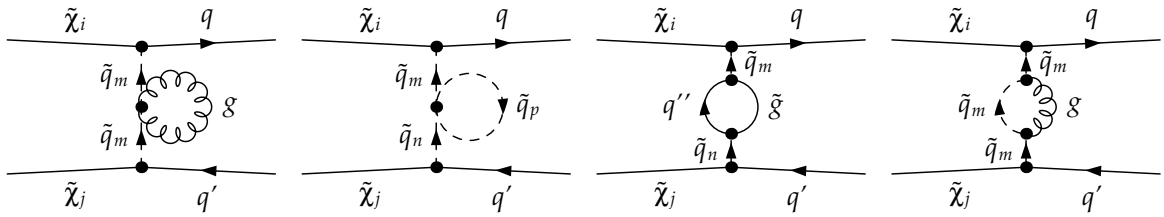

Figure 5.8.: t-channel propagator corrections to the gaugino (co)annihilation processes as included in `ChiChi2qq` [1]. u-channel contributions can be obtained via crossing of the corresponding t-channels.

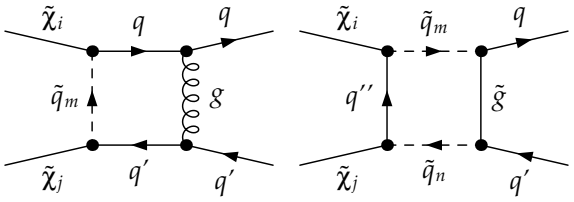

Figure 5.9.: Box diagrams of gaugino (co)annihilation processes as included in `ChiChi2qq` [1]. u-channel contributions can be obtained via crossing of the corresponding t-channels.

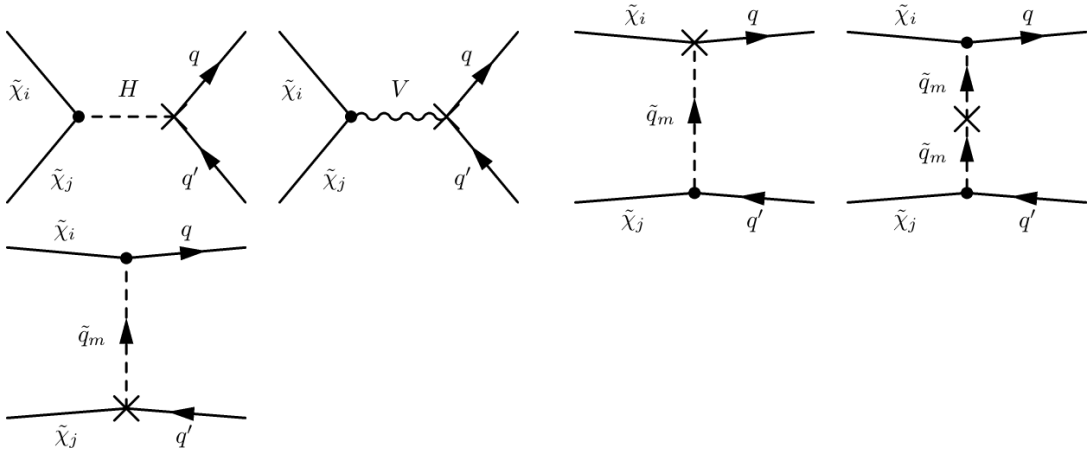

Figure 5.10.: The counterterms of gaugino (co)annihilation processes as included in `ChiChi2qq` [1]. u-channel contributions can be obtained via crossing of the corresponding t-channels.

over initial-/final-state colors and spins s takes the form

$$\begin{aligned}2\Re\left\{\overline{(\mathcal{M}^{\text{Born}})^\dagger \mathcal{M}^{\text{Virt}}}\right\} =& \frac{1}{4}\sum_{\text{color}_{\text{out}}}\sum_{s_{\text{in, out}}} 2\Re\Big\{ \left(\mathcal{M}_s^{\text{Born}}\right)^\dagger \mathcal{M}_s^{\text{Virt}} + \left(\mathcal{M}_t^{\text{Born}}\right)^\dagger \mathcal{M}_t^{\text{Virt}} \\ &+ \left(\mathcal{M}_u^{\text{Born}}\right)^\dagger \mathcal{M}_u^{\text{Virt}} - \left(\mathcal{M}_s^{\text{Born}}\right)^\dagger \mathcal{M}_t^{\text{Virt}} \\ &+ \left(\mathcal{M}_s^{\text{Born}}\right)^\dagger \mathcal{M}_u^{\text{Virt}} - \left(\mathcal{M}_t^{\text{Born}}\right)^\dagger \mathcal{M}_u^{\text{Virt}} \Big\} \qquad (5.132) \\ =& \frac{1}{2} C_F N_C \sum_{s_{\text{in, out}}} \Re\Big\{ \left(\mathcal{M}_s^{\text{Born}}\right)^\dagger \mathcal{M}_s^{\text{Virt}} + \left(\mathcal{M}_t^{\text{Born}}\right)^\dagger \mathcal{M}_t^{\text{Virt}} \\ &+ \left(\mathcal{M}_u^{\text{Born}}\right)^\dagger \mathcal{M}_u^{\text{Virt}} - \left(\mathcal{M}_s^{\text{Born}}\right)^\dagger \mathcal{M}_t^{\text{Virt}} \\ &+ \left(\mathcal{M}_s^{\text{Born}}\right)^\dagger \mathcal{M}_u^{\text{Virt}} - \left(\mathcal{M}_t^{\text{Born}}\right)^\dagger \mathcal{M}_u^{\text{Virt}} \Big\}, \qquad (5.133)\end{aligned}$$

where we suppress all spin correlations between each two matrix elements. In Eq. (5.132), we have included the relative minus signs connected to the ordering of fermion fields in the particular amplitude according to Fig. 4.3.
The general calculational method of the virtual corrections has been outlined in the Secs. 5.1.2 to 5.1.5. Furthermore, the corrections to the bottom mass and the effective treatment of its Yukawa coupling as explained in the Secs. 5.1.5 and 5.1.6 turn out to be of particular importance as we encounter large contributions from gaugino (co)annihilation into bottom final states. But since the particular calculation of the virtual corrections has not been subject to this work, we do not go into greater detail.

5.1.9. QQ2xx: The Virtual Corrections

The calculation of the virtual corrections to the processes Eq. (4.8)-(4.11) is one of the main parts of this work. They are presented in more detail in the following.
For the tree-level as well as for the virtual corrections, we rely on the Born-level conventions as shown in Fig. 5.11. The contribution of the virtual corrections to the overall squared matrix element at $\mathcal{O}(\alpha_s)$ averaged/summed over initial-/final-state colors, spins s and polarizations λ takes the form

$$\begin{aligned}2\Re\left\{\overline{(\mathcal{M}^{\text{Born}})^\dagger \mathcal{M}^{\text{Virt}}}\right\} =& \frac{1}{N_c^2 S}\sum_{\text{color}_{\text{in}}}\sum_{s_{\text{out}},\lambda_{\text{out}}} \\ & 2\Re\Big\{ \Big[\mathcal{M}_Q^{\text{Born}} + \mathcal{M}_s^{\text{Born}} + \mathcal{M}_t^{\text{Born}} + \mathcal{M}_u^{\text{Born}}\Big]^\dagger \\ & \Big[\mathcal{M}^{\text{prop}} + \mathcal{M}^{\text{vertex1}} + \mathcal{M}^{\text{vertex2}} + \mathcal{M}^{\text{box}}\Big]\Big\}, \qquad (5.134)\end{aligned}$$

where we suppress the Lorentz-, spin- and color structures, which connect each two matrix elements in Eq. (5.134). We have also introduced the symmetry factor S, which accounts for identical particles in the final state. It equals two, if the two final-state particles are identical, and equals one, otherwise. The different Feynman amplitudes which contribute to $\mathcal{M}^{\text{Virt}}$ are then obtained via inserting gluon, quark, squark and gluino loops into the Born level diagrams depicted in Fig. (4.5). But there also arise additional diagrams, which do not have a direct Born-level equivalent. Further note that we do not encounter any gluino loops to quartic couplings (see Fig. 5.16), as a vertex with two fermions and two bosons would possess a mass dimension larger than four and would hence be non-renormalizable.

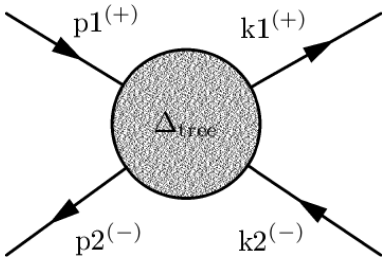

Figure 5.11.: Conventions used in the calculation of $2 \to 2$ processes included in `QQ2xx`. p_1 and p_2 are ingoing momenta, k_1 and k_2 are outgoing. The arrows on the outer legs indicate the assignment of particles and antiparticles (and/or the sign of corresponding electric charges).

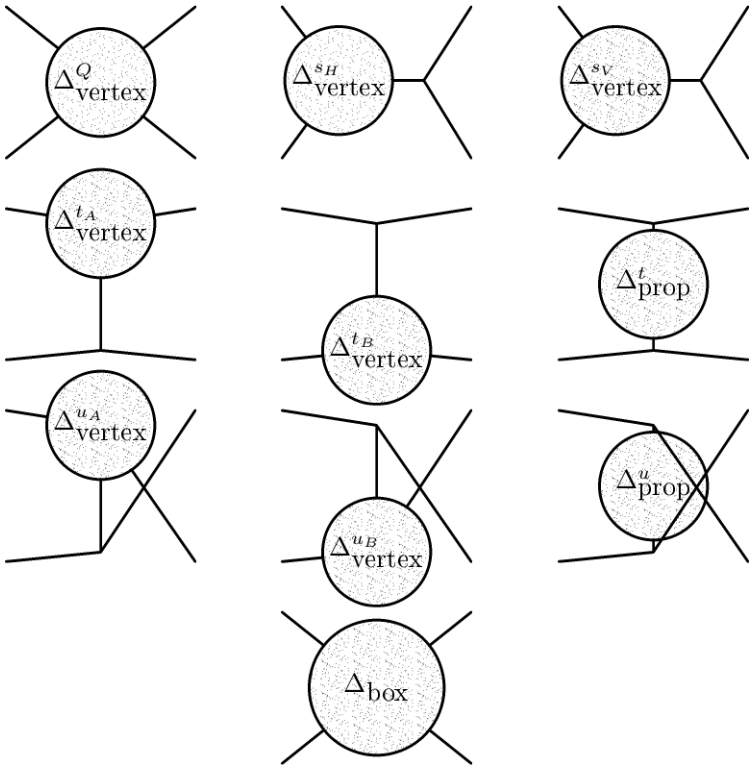

Figure 5.12.: Conventions used for the naming of the different types of virtual corrections for squark (co)annihilation into EW final states as given in the Eqs. (4.8)-(4.11).

We give the general form of the higher-order corrections in Fig. (5.12). There, we also present the naming of the different $\mathcal{O}(\alpha_s)$ contributions that are used in the following.

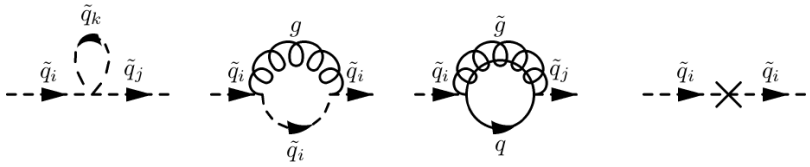

Figure 5.13.: The different propagator corrections that subsume under the associated general amplitudes in Fig. 5.12.

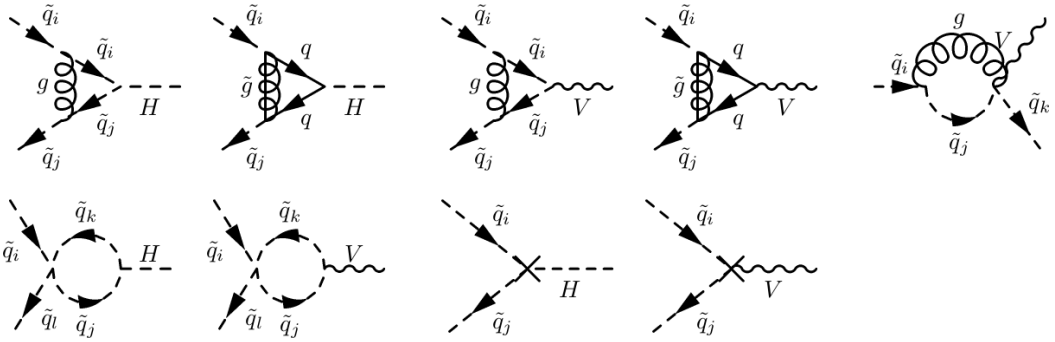

Figure 5.14.: The different vertex insertions that subsume under the associated general diagrams in Fig. 5.12.

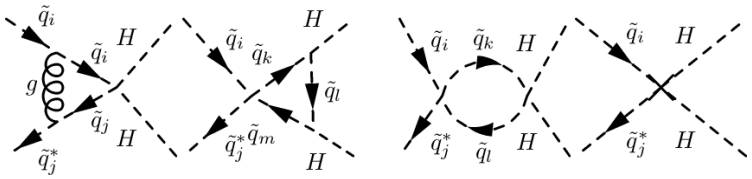

Figure 5.15.: The different irreducible vertex corrections for the Higgs-Higgs final states that subsume under the associated general amplitudes in Fig. 5.12. The u-channel contributions can be obtained via crossing of the corresponding t-channels.

The concrete propagator and vertex insertions as well as additional NLO corrections are shown in the Figs. 5.13 to 5.18. Their calculation, regularization and renormalization follows the explanations of Sec. 5.1. However, as these calculations have been a big part of the work connected to this thesis, we go through the different contributions in a bit more detail.

The Propagator Corrections

We start with the propagator corrections $\mathcal{M}_t^{\text{prop}}$ and $\mathcal{M}_u^{\text{prop}}$, which subsume under

$$\mathcal{M}^{\text{prop}} = \mathcal{M}_t^{\text{prop}} + \mathcal{M}_u^{\text{prop}} \tag{5.135}$$

of Eq. (5.134). These can be obtained via substituting the corrections depicted in Fig. 5.13 for Δ_{prop}^t and Δ_{prop}^u of Fig. 5.12. Note that the pure gluon loop does not contribute

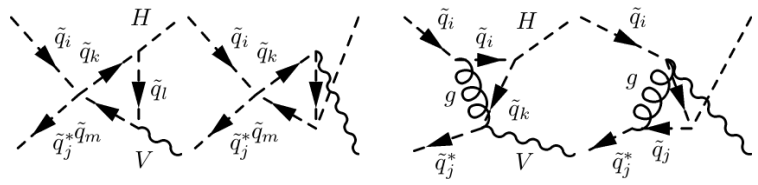

Figure 5.16.: The different irreducible vertex corrections for the vector-Higgs final states that subsume under the associated general amplitudes in Fig. 5.12.

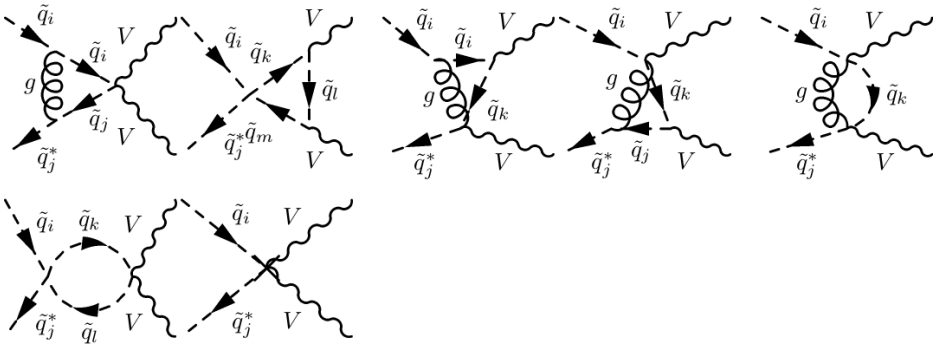

Figure 5.17.: The different irreducible vertex corrections for the vector-vector final states that subsume under the associated general amplitudes in Fig. 5.12. The u-channel contributions can be obtained via crossing of the corresponding t-channels.

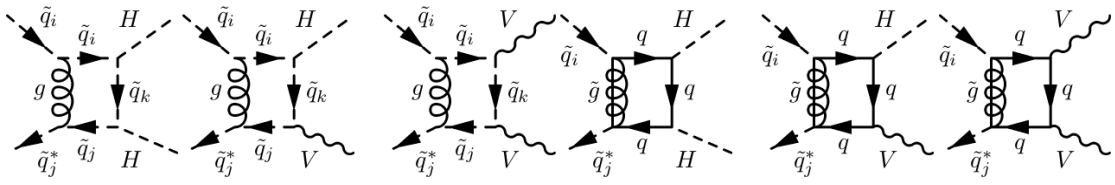

Figure 5.18.: The different box corrections that subsume under the associated general amplitudes in Fig. 5.12. The u-channel contributions can be obtained via crossing of the corresponding t-channels.

as it is proportional to $\mathbf{A}_0(0) = 0$.
As we only encounter corrections to squark propagators that are scalars, these corrections completely factorize from the Born-level cross sections. We can simply calculate the corresponding expression by the replacements

$$\mathcal{M}_t^{\text{Born}} \to \sum_{l,k} \frac{(\Delta^t_{\text{prop}})_{lk}}{t - m^2_{\tilde{q}_l}} \mathcal{M}^{\text{Born}}_{t,k} = \mathcal{M}_t^{\text{prop}}, \tag{5.136}$$

$$\mathcal{M}_u^{\text{Born}} \to \sum_{l,k} \frac{(\Delta^u_{\text{prop}})_{lk}}{u - m^2_{\tilde{q}_l}} \mathcal{M}^{\text{Born}}_{u,k} = \mathcal{M}_u^{\text{prop}}, \tag{5.137}$$

with Mandelstam variables $t = (p_1 - k_1)^2$ and $u = (p_1 - k_2)^2$ (see Fig. 5.11). Note that the squark mass eigenstate, which runs into the propagator correction, can in principle differ from the outgoing squark mass eigenstate (see the fixing of the squark-propagator counterterm Eq. 5.109 and the subsequent discussion). Hence, one has to separately sum over ingoing and outgoing mass eigenstates $\tilde{q}_k$ and $\tilde{q}_l$. As we attach the wave function renormalization constants also to internal lines, the full propagator corrections Eqs. (5.136) and (5.137) take the general form (see Eq. (5.105) and Fig. 5.5)

$$\begin{aligned}(\Delta^{\text{x}}_{\text{prop}})_{lk} =& \sum_{m,n} \Big[\frac{x - m^2_{\tilde{q}_l}}{2} \Big(- (\delta Z^{\tilde{q}})^*_{lm} \delta_{nk} - \delta_{lm} \delta Z^{\tilde{q}}_{nk} \Big) \delta_{mn} + \delta_{lm} (\delta m^2_{\tilde{q}} \delta_{mn} - \frac{i}{(4\pi)^2} \Pi^{\tilde{q}}_{mn}(x)) \delta_{nk} \Big] \\ =& \Big[- \frac{x - m^2_{\tilde{q}_l}}{2} \Big((\delta Z^{\tilde{q}})^*_{lk} + \delta Z^{\tilde{q}}_{lk} \Big) + \delta m^2_{\tilde{q}} \delta_{lk} - \frac{i}{(4\pi)^2} \Pi^{\tilde{q}}_{lk}(x) \Big]. \end{aligned} \tag{5.138}$$

$\Pi^{\tilde{q}}_{lk}$ stands for the different insertions corresponding to the first three diagrams of Fig. 5.13 where we already pulled a factor $i/(4\pi)^2$ out of the propagator corrections. These insertions have been calculated as outlined in the Secs. 5.1.3 and 5.1.4, whereas the counterterms δZ and δm^2 are calculated according to Sec. 5.1.6. Our results coincide with the results given in Ref. [207]. Moreover, we verify that the implemented Eq. (5.138) yields a UV-finite result.

The Vertex Corrections 1

In this section, we discuss the corrections that are obtained by inserting the $\mathcal{O}(\alpha_s)$ corrections depicted in Fig. 5.14 for $\Delta^{s_H}_{\text{vertex}}$, $\Delta^{s_V}_{\text{vertex}}$, $\Delta^{t_A}_{\text{vertex}}$, $\Delta^{t_B}_{\text{vertex}}$, $\Delta^{u_A}_{\text{vertex}}$ and $\Delta^{u_B}_{\text{vertex}}$ of Fig. 5.12. The Δ^x_{vertex} ($x \in \{s_H, s_V, t_A, t_B, u_A, u_B\}$) symbolize the different sorts of radiative corrections to the squark-squark-Higgs as well as to the squark-squark-vector vertex. These enter the corresponding matrix elements

$$\mathcal{M}^{\text{vertex1}} = \mathcal{M}^{\text{vertex1}}_{s_H} + \mathcal{M}^{\text{vertex1}}_{s_V} + \mathcal{M}^{\text{vertex1}}_{t_A} + \mathcal{M}^{\text{vertex1}}_{t_B} + \mathcal{M}^{\text{vertex1}}_{u_A} + \mathcal{M}^{\text{vertex1}}_{u_B} \tag{5.139}$$

of Eq. (5.134). We can obtain the matrix elements $\mathcal{M}^{\text{vertex1}}_x$ from the corresponding Born level matrix elements $\mathcal{M}^{\text{Born}}_x$ by replacing the Born-level couplings in $\mathcal{M}^{\text{Born}}_x$ by so-called general couplings. These replacements in D dimensions are of the form

$$\mu^{\frac{4-D}{2}} V^{H,x}_{\text{Born}} \to \mu^{\frac{4-D}{2}} V^{H,x}_{\text{Virt}} \tag{5.140}$$

for the $\tilde{q}^*_l H \tilde{q}_k$-vertex and of the form

$$\mu^{\frac{4-D}{2}} (V^{V,x}_{\text{Born}})_{lk} (p_k + p_l)^\mu \to \mu^{\frac{4-D}{2}} \Big((V^{V,x,+}_{\text{Virt}})_{lk} (p_k + p_l)^\mu + (V^{V,x,-}_{\text{Virt}})_{lk} (p_k - p_l)^\mu \Big) \tag{5.141}$$

for the $\tilde{q}_l^* V \tilde{q}_k$-vertex. Note that the decompositions on the right hand sides of Eq. (5.140) and Eq. (5.141) are already exhaustive in terms of linearly independent Lorentz structures of appropriate rank that can be formed out of the available Lorentz tensors. The replacements Eq. (5.140) and (5.141) in $\mathcal{M}_x^{\text{Born}}$ are sufficient to end up with a convenient form for $\mathcal{M}_x^{\text{vertex}}$ in which we can grasp all the corrections of Fig. 5.14. The expression for the effective couplings can now be written as

$$\begin{aligned}(V_{\text{Virt}}^{H,x})_{lk} =& \sum_{m,n} \Big[\frac{1}{2}\Big((\delta Z^{\tilde{q}})^*_{lm}\delta_{nk} + \delta_{lm}\delta Z^{\tilde{q}}_{nk}\Big)\Big(V_{\text{Born}}^{H,x}\Big)_{mn} \\ &+ \delta_{lm}\left((\delta V_{\text{Born}}^{H,x})_{mn} + \frac{i}{(4\pi)^2}\Pi_{mn}^{H,x}\right)\delta_{nk}\Big] \\ =& \sum_{m,n} \Big[\frac{1}{2}\Big((\delta Z^{\tilde{q}})^*_{lm}\delta_{nk} + \delta_{lm}\delta Z^{\tilde{q}}_{nk}\Big)\Big(V_{\text{Born}}^{H,x}\Big)_{mn}\Big] \\ &+ (\delta V_{\text{Born}}^{H,x})_{lk} + \frac{i}{(4\pi)^2}\Pi_{lk}^{H,x} \end{aligned} \tag{5.142}$$

for the $\tilde{q}_l^* H \tilde{q}_k$-vertex Eq. (5.140) and

$$\begin{aligned}\Big(V_{\text{Virt}}^{V,x,+}\Big)_{lk} =& \sum_{m,n} \Big[\frac{1}{2}\Big((\delta Z^{\tilde{q}})^*_{lm}\delta_{nk} + \delta_{lm}\delta Z^{\tilde{q}}_{nk}\Big)\Big(V_{\text{Born}}^{V,x}\Big)_{mn} \\ &+ \delta_{lm}\left((\delta V_{\text{Born}}^{V,x})_{mn} + \frac{i}{(4\pi)^2}\Pi_{mn}^{V,x,+}\right)\delta_{nk}\Big] \\ =& \sum_{m,n} \Big[\frac{1}{2}\Big((\delta Z^{\tilde{q}})^*_{lm}\delta_{nk} + \delta_{lm}\delta Z^{\tilde{q}}_{nk}\Big)\Big(V_{\text{Born}}^{V,x}\Big)_{mn}\Big] \\ &+ (\delta V_{\text{Born}}^{V,x})_{lk} + \frac{i}{(4\pi)^2}\Pi_{lk}^{V,x,+} \end{aligned} \tag{5.143}$$

$$\Big(V_{\text{Virt}}^{V,x,-}\Big)_{lk} = \frac{i}{(4\pi)^2}\sum_{m,n}\delta_{ln}\Pi_{mn}^{V,x,-}\delta_{nk} = \frac{i}{(4\pi)^2}\Pi_{lk}^{V,x,-} \tag{5.144}$$

for the $\tilde{q}_l^* V \tilde{q}_k$-vertex Eq. (5.141). We have again included the wave function renormalization constants $Z^{\tilde{q}}$ for every squark $\tilde{q}$ attached to the particular vertex as described in Sec. 5.1.5. Further note that, since the counterterms in Eq. (5.142) and Eq. (5.143) only multiply the kinematic structures of the the Born-level $\propto (p_k + p_l)^\mu$, multiplicative renormalizability guarantees that all UV-poles reside in $V_{\text{Virt}}^{V,x,+}$ of Eq. (5.141), whereas $V_{\text{Virt}}^{V,x,-}$ remains UV-finite. The vertex counterterms $\delta V_{\text{Born}}^{H/V,x}(\Theta_{\tilde{q}}, m_q, ...)$ can then be obtained via Eq. (5.122). There, the $\Theta_{\tilde{q}}$ dependence on the squark mixing angle enters as we still have to transform the original vertices $\hat{V}$, typically given in a basis of squark-interaction eigenstates, into a basis of squark-mass eigenstates according to

$$V = \mathbf{U}^{\tilde{q}}(\Theta_{\tilde{q}})\,\hat{V}\left(\mathbf{U}^{\tilde{q}}(\Theta_{\tilde{q}})\right)^\dagger \tag{5.145}$$

as explained in Sec. 2.6.3. The arising counterterms $\delta\Theta$, δm_q etc. can then be calculated as outlined in Sec. 5.1.5. $\Pi_{lk}^{H/V,x,\pm}$ includes the different insertions that correspond to the first seven diagrams of Fig. 5.14, divided by a factor $i/(4\pi)^2$, which we pulled out of the vertex corrections. Moreover, we decomposed the full correction according to Eq. (5.141). All insertions haven been calculated as outlined in the Secs. 5.1.3 and 5.1.4. Note that the contributions to $\Pi_{lk}^{H/V,x,\pm}$ can be calculated on quite general grounds such that only the kinematics have to be adjusted according to the corresponding $x \in \{s_H, s_V, t_A, t_B, u_A, u_B\}$. The general results of the insertions have been cross checked completely with the results given in Ref. [207].

The Vertex Corrections 2

The Feynman diagrams of the Figs. 5.15 to 5.17 differ from the vertex corrections considered before, as they connect all four external particles and, hence, cannot be reduced to simple insertions plugged into the Born-level matrix element $\mathcal{M}^{\text{Born}}$. They therefore correspond to diagrams of the type Δ_{box} of Fig. 5.12. The full contribution to $\mathcal{M}^{\text{vertex2}}$ of

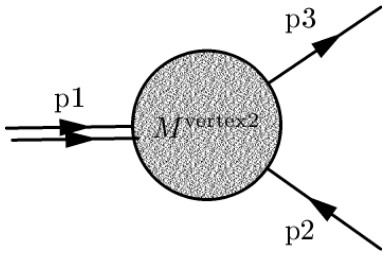

Figure 5.19.: The conventions used for the calculation of general amplitudes subsumed under $\mathcal{M}^{\text{vertex2}}$. Here, the momentum p_1 corresponds to the sum of momenta of the two external particles attached to the same (quartic) vertex and the arrows on the lines indicate the momentum flow.

the depicted diagrams can be written as

$$\begin{aligned}
\mathcal{M}_{ab}^{\text{vertex2}} =& \sum_{m,n} \Big[\frac{1}{2} \Big((\delta Z^{\tilde{q}})^*_{lm} \delta_{nk} + \delta_{lm} \delta Z^{\tilde{q}}_{nk} \Big) \Big(V_{\text{Born}}^{(ab),Q} \Big)_{mn} \\
&+ \delta_{lm} \left((\delta V_{\text{Born}}^{(ab),Q})_{mn} + \frac{i}{(4\pi)^2} \Pi^{(ab)}_{mn} \right) \delta_{nk} \Big] \\
=& \sum_{m,n} \Big[\frac{1}{2} \Big((\delta Z^{\tilde{q}})^*_{lm} \delta_{nk} + \delta_{lm} \delta Z^{\tilde{q}}_{nk} \Big) \Big(V_{\text{Born}}^{(ab),Q} \Big)_{mn} \Big] \\
&+ (\delta V_{\text{Born}}^{(ab),Q})_{lk} + \frac{i}{(4\pi)^2} \Pi^{(ab)}_{lk},
\end{aligned} \tag{5.146}$$

where we suppressed the Lorentz structure, which depends on the specific final state ab ($a, b \in \{H, V\}$). The vertices $V_{\text{Born}}^{(a,b),Q}$ are the quartic couplings of Fig. 4.5, which are nonzero only if ($a = b = H, V$), and

$$\delta V_{\text{Born}}^{(a,b),Q} = \delta \left[\mathbf{U}^{\tilde{q}}(\Theta^{\tilde{q}}) \hat{V}_{\text{Born}}^{(a,b),Q} \left(\mathbf{U}^{\tilde{q}}(\Theta^{\tilde{q}}) \right)^\dagger \right] \tag{5.147}$$

are the corresponding counterterms as defined in Eq. (5.122). Except for the counterterms, all diagrams of Fig. 5.15 to Fig. 5.17 are subsumed under $\Pi^{(ab)}_{lk}$. According to their Lorentz structures, these can be decomposed into the general amplitudes

$$\Pi^{(HH)} = A_0 \tag{5.148}$$

for the Higgs-Higgs final states (Fig. 5.15),

$$\left(\Pi^{(VH)} \right)^\mu = (A_0 p_1^\mu + A_1 p_3^\mu) \tag{5.149}$$

for the Vector-Higgs final states (Fig. 5.16) and

$$\left(\Pi^{(VV)} \right)^{\mu\nu} = (A_0 g^{\mu\nu} + A_1 p_1^\mu p_1^\nu + A_2 p_1^\mu p_3^\nu + A_3 p_3^\mu p_1^\nu + A_4 p_3^\mu p_3^\nu) \tag{5.150}$$

for the vector-vector final states (Fig. 5.17) with kinematics chosen according to Fig. 5.19. Note that the above decomposition into Lorentz tensors of appropriate rank is already exhaustive. This is because all external momenta attached to $\Pi^{(ab)}$ are on-shell. Hence, we can eliminate one external momentum via overall four-momentum conservation. Moreover, in the Figs. 5.15 to 5.17, there are always at least two external momenta attached to a single vertex as indicated by the double arrow in order that we can replace these two momenta by their sum, leaving us with at most two independent four momenta. The matrix elements of the virtual corrections, decomposed as in Eqs. (5.148) to (5.150), can then be contracted with the Born-level matrix element following Eq. (5.134). The explicit results for the coefficients A_i ($i \in \{0, ..., 4\}$) are finally obtained by the calculation of the diagrammatic expressions of the radiative corrections and decomposition of the arising results according to the general amplitudes given above. The coefficients of the Feynman diagrams shown in Fig. 5.15 to Fig. 5.17 can be found in App. A.

The Box Corrections

The Box corrections are depicted in Fig. 5.18. Similar to the vertex2 corrections of the previous subsection, the box corrections connect all four external particles. The general

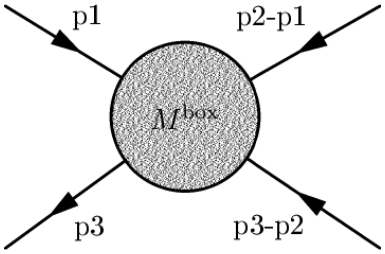

Figure 5.20.: The conventions used for the calculation of diagrams subsumed under $\mathcal{M}^{\text{box}}$.

Lorentz structure of the corresponding general amplitudes is a bit more complex as we encounter three independent external momenta, which form the general amplitudes. We choose the following decomposition:

$$\mathcal{M}^{\text{box}}_{(HH)} = \frac{i}{(2\pi)^4} A_0 \tag{5.151}$$

for the Higgs-Higgs final states,

$$\left(\mathcal{M}^{\text{box}}_{(VH)}\right)^{\mu} = \frac{i}{(2\pi)^4} \left(A_0 p_1^{\mu} + A_1 p_2^{\mu} + A_2 p_3^{\mu}\right) \tag{5.152}$$

for the Vector-Higgs final states and

$$\begin{aligned}\left(\mathcal{M}^{\text{box}}_{(VV)}\right)^{\mu\nu} = \frac{i}{(2\pi)^4} \Big(& A_0 g^{\mu\nu} + A_1 p_1^{\mu} p_1^{\nu} + A_2 p_1^{\mu} p_2^{\nu} + A_3 p_2^{\mu} p_1^{\nu} \\ & + A_4 p_1^{\mu} p_3^{\nu} + A_5 p_3^{\mu} p_1^{\nu} + A_6 p_2^{\mu} p_2^{\nu} \\ & + A_7 p_2^{\mu} p_3^{\nu} + A_8 p_3^{\mu} p_2^{\nu} + A_9 p_3^{\mu} p_3^{\nu} \Big)\end{aligned} \tag{5.153}$$

for the vector-vector final states (Fig. 5.17), where the kinematics have been chosen according to Fig. 5.20. The coefficients of the Feynman diagrams shown in Fig. 5.18 can be partly found in App. A.

5.2. Real Corrections and the Treatment of Soft and Collinear Divergences

5.2.1. Kinematics and Cross Sections

In this section, we present the so-called *real corrections*, which are, compared to the virtual corrections discussed in the previous sections, another kind of $\mathcal{O}(\alpha_s)$ corrections. Following Ref. [207], we provide a comprehensive overview of the most important formulas and conventions used in the calculation of the real-radiation amplitudes.
In the present case, the real correction arise due to the radiation of an additional gluon off a colored particle stemming from the original Born-level process. The nomenclature

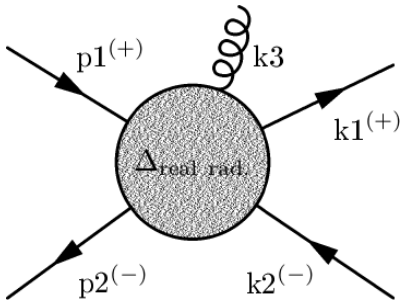

Figure 5.21.: Conventions used in the calculation of $2 \to 3$ processes.

used throughout the calculations is shown in Fig. 5.21. We choose the parametrization of external four momenta according to Fig. 5.22. Hence, the four momenta can be expressed by

$$(p_1^\mu)^\intercal = \frac{\sqrt{s}}{2}\left(1+\mu_{p_1}^2-\mu_{p_2}^2, 0, 0, \sqrt{(1-\mu_{p_1}^2-\mu_{p_2}^2)^2-4\mu_{p_1}^2\mu_{p_2}^2}\right), \tag{5.154}$$

$$(p_2^\mu)^\intercal = \frac{\sqrt{s}}{2}\left(1-\mu_{p_1}^2+\mu_{p_2}^2, 0, 0, -\sqrt{(1-\mu_{p_1}^2-\mu_{p_2}^2)^2-4\mu_{p_1}^2\mu_{p_2}^2}\right), \tag{5.155}$$

$$(k_3^\mu)^\intercal = \frac{\sqrt{s}}{2}\left(x_3, \sqrt{x_3^2-4\mu_{k_3}^2}\sin\Theta, 0, \sqrt{x_3^2-4\mu_{k_3}^2}\cos\Theta\right), \tag{5.156}$$

$$(k_1^\mu)^\intercal = \frac{\sqrt{s}}{2}\left(x_1, \sqrt{x_1^2-4\mu_{k_1}^2}\vec{n}^\intercal\right) \tag{5.157}$$

with

$$\vec{n}^\intercal = (\cos\xi\sin\Theta + \sin\xi\sin\eta\cos\Theta, \sin\xi\cos\eta, \cos\xi\cos\Theta - \sin\xi\sin\eta\sin\Theta)\,. \tag{5.158}$$

In the Eqs. (5.154) to (5.157), we make use of the definitions

$$x_i = \frac{2k_i^0}{\sqrt{s}}, \quad \mu_i = \frac{m_i}{\sqrt{s}} \tag{5.159}$$

in order that in these new variables energy conservation is expressed by

$$2 = x_1 + x_2 + x_3. \tag{5.160}$$

k_2^μ follows from overall momentum conservation

$$k_2^\mu = p_1^\mu + p_2^\mu - k_1^\mu - k_3^\mu. \tag{5.161}$$

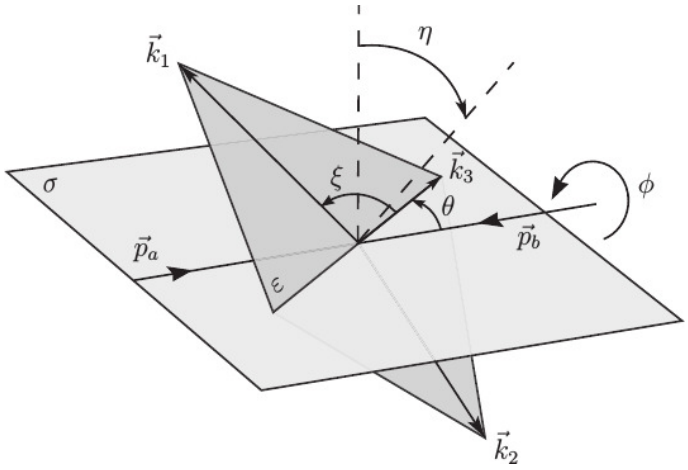

Figure 5.22.: Parametrization of the $2 \to 3$ phase space for $\vec{p}_a \to \vec{p}_1$, $\vec{p}_b \to \vec{p}_2$. Figure taken from Ref. [207].

The three-particle phase space with external momenta k_1, k_2, k_3 takes the form

$$\int \mathrm{d}\Gamma^{(3)} = \int \frac{\mathrm{d}^4k_1}{(2\pi)^4}\frac{\mathrm{d}^4k_2}{(2\pi)^4}\frac{\mathrm{d}^4k_3}{(2\pi)^4}(2\pi)\delta(k_1^2 - m_{k_1}^2)(2\pi)\delta(k_2^2 - m_{k_2}^2)(2\pi)\delta(k_3^2 - m_{k_3}^2) \\ \Theta(k_1^0)\Theta(k_2^0)\Theta(k_3^0)(2\pi)^4\delta^4(p_1 + p_2 - k_1 - k_2 - k_3), \tag{5.162}$$

where (overall) energy-momentum conservation is explicitly assumed. By using the above parametrization and integrating out the δ-functions, the phase space Eq. (5.162) can be rewritten as

$$\int \mathrm{d}\Gamma^{(3)} = \frac{s}{32}\frac{1}{(2\pi)^5}\int \mathrm{d}x_1\mathrm{d}\eta\mathrm{d}x_3\mathrm{d}\cos\Theta\mathrm{d}\phi. \tag{5.163}$$

The corresponding integration boundaries now take the form

$$\eta \in (0, 2\pi), \quad \phi \in (0, 2\pi), \quad \Theta \in (0, \pi), \tag{5.164}$$

$$(x_3)^{\min} = 2\mu_{k_3}, \quad (x_3)^{\max} = 1 - (\mu_{k_1} + \mu_{k_2})^2 + 2\mu_{k_3} \tag{5.165}$$

and

$$(x_1)^{\max}_{\min} = \frac{1}{2\bar{\tau}}\left[\bar{\sigma}(\bar{\tau} + \mu_+\mu_-) \pm \sqrt{x_3^2 - 4\mu_{k_3}^2}\sqrt{(\bar{\tau} - \mu_+^2)(\bar{\tau} - \mu_-^2)}\right] \tag{5.166}$$

where we introduced the definitions

$$\bar{\sigma} := 2 - x_3, \quad \bar{\tau} := 1 - x_3 + \mu_{k_3}^2, \quad \mu_\pm := \mu_{k_1} \pm \mu_{k_2}. \tag{5.167}$$

Moreover, the angle ξ can now be expressed by

$$\cos\xi = \frac{(2 - x_1 - x_3)^2 + 4\mu_{k_1}^2 + 4\mu_{k_3}^2 - 4\mu_{k_2}^2 - x_1^2 - x_3^2}{2\sqrt{x_1^2 - 4\mu_{k_1}^2}\sqrt{x_3^2 - 4\mu_{k_3}^2}}. \tag{5.168}$$

These are the basic ingredients needed for the calculation of real-radiation amplitudes and the evaluation of the corresponding cross section σ_{R}. A more process dependent discussion is given further below, in which we consider the real corrections in the context of `ChiChi2qq` and `QQ2xx`. In the following, we discuss the intimate intertwining between the real and virtual corrections and introduce additional methods that are necessary to render the full NLO cross section σ_{NLO} numerically evaluable.

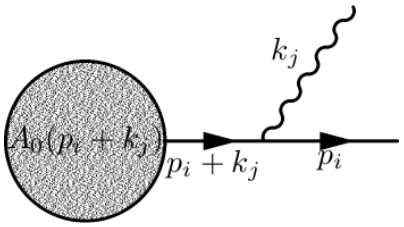

Figure 5.23.: Radiation of a massless particle j with momentum k_j off an internal particle ij with momentum $p_i + k_j$ running out of a hard process $\mathcal{A}_0(p_i + k_j)$.

5.2.2. The Appearance of Soft and Collinear Divergences

Since in this work we study the $\mathcal{O}(\alpha_s)$ corrections of gaugino (co)annihilation into quarks as well as of stop annihilation into EW SM particles, we need to know how to handle the previously mentioned soft and collinear (or quasi-collinear) divergences connected to the exchange of virtual gluons (see Sec. 5.1.2). This investigation leads to the introduction of so-called *inclusive* cross sections, which cover both virtual as well as real corrections.
The cross section up to NLO can be written as [204]

$$\sigma = \int_m \mathrm{d}\sigma_B + \sigma_{\mathrm{NLO}}, \tag{5.169}$$

where $\int_m \mathrm{d}\sigma_B$ is the differential Born-level cross-section integrated over the m-particle phase space (in our case $m = 2$) and σ_{NLO}, i.a., includes all $\mathcal{O}(\alpha_s)$ virtual corrections as discussed in Sec. 5.1. Considered a general 1-loop integral I (compare, e.g., Eq. (5.24)) as it typically arises in the calculation of σ_{Virt}, we can grasp it in the form

$$I = \int \mathrm{d}^4 q N(p_i, q, m_n) \prod_{i=1}^{l} \frac{i}{(k_i^2 - m_i^2) + i\epsilon}, \tag{5.170}$$

where the momenta k_i are linear combinations of internal and external momenta q and p_i

$$k_i = q + \sum_{n=1}^{i-1} \eta_{in} p_n \tag{5.171}$$

and the coefficients η_{in} can take the values $+1$ or -1 depending on the relative orientation (incoming or outgoing) of the associated momentum. The problem of soft and collinear divergences is now connected to propagators that can become singular in certain physical regions of the phase space. An arbitrary propagator with nomenclature as given in Fig. 5.23 is proportional to

$$\propto \frac{1}{(p_i + k_j)^2 - m_{ij}^2} = \frac{1}{E_i E_j (1 - \beta_i \cos(\Theta_{ij}))}. \tag{5.172}$$

Here, we define

$$\beta_i := \sqrt{1 - \frac{m_{ij}^2}{E_i^2}}. \tag{5.173}$$

If the particle radiated off the internal line is taken as massless, expression Eq. (5.172) turns out to be divergent in the limit $E_j \to 0$, the so-called soft limit, as the denominator in Eq. (5.172) goes to zero. If the particle ij is massless ($m_{ij} \to 0$), too, there is yet

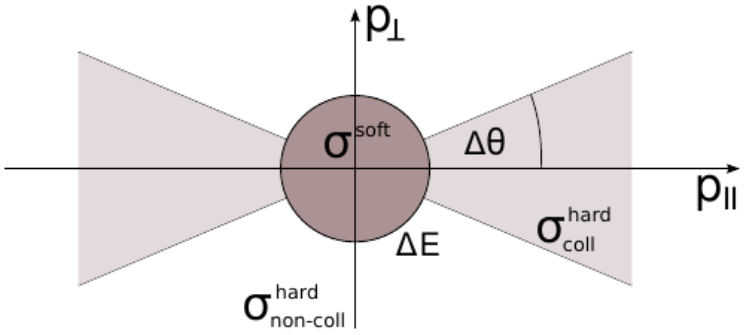

Figure 5.24.: The phase space of the radiated particle, dissected into soft and collinear regions. Figure taken from [55].

another kinematic region, where the denominator can become zero. This is the collinear limit $\Theta_{ij} \to 0$ ($\cos(\Theta_{ij}) \to 1 \Leftrightarrow k_{j,\perp} \to 0$), i.e., when the parent particle ij splits in two particles radiated off nearly parallel to each other. Making use of, e.g., DRed, integration over these regions of phase space introduces single as well as double poles $\frac{1}{\epsilon}$ and $\frac{1}{\epsilon^2}$ in the virtual corrections, of which the latter can appear in the overlap regions of soft and collinear singularities (see Fig. 5.24). In addition, there may arise so-called quasi-collinear divergences, i.e., terms of the form $\ln(\frac{m_{ij}}{\sqrt{s}})$, which can be understood as collinear divergences, regularized by the mass of the parent particle m_{ij}. If m_{ij} happens to be much smaller than the CMS energy of the associated process $m_{ij} \ll \sqrt{s}$, these quasi-collinear divergences blow up eventually spoiling perturbativity of the virtual corrections. Hence, even after regularization of UV-divergences, the virtual corrections may still be ill defined. However, there are theorems by *Bloch and Nordsieck* (BN-theorem) [205] and by *Kinoshita, Lee and Nauenberg* (KLN-theorem) [206] which may help us out here. They state that for a sufficiently inclusive quantity, e.g., the cross section σ_{NLO} defined as

$$\sigma_{\mathrm{NLO}} = \int_{m+1} \mathrm{d}\sigma_{\mathrm{R}} + \int_{m} \mathrm{d}\sigma_{\mathrm{Virt}}, \tag{5.174}$$

which covers the full $\mathcal{O}(\alpha_s)$ corrections including both virtual (m-particle final state) as well as real ($m+1$-particle final state) corrections[13], all soft singularities of σ_{Virt} cancel order by order in perturbation theory in the sum with poles of same analytic form but opposite sign stemming from the real corrections σ_{R} (BN-theorem). Following the *KLN-theorem*, the same holds true for (quasi)collinear divergences caused by final-state radiation, whereas in the case of initial-state radiation the (quasi)collinear regions must be treated with special care[14]. Therefore, in principle, Eq. (5.174) is finite. But this statement is only valid *after* summing up both integrated parts. Note that this intimate intertwining between real and virtual corrections is not accidental but can be inferred from

[13] Note that the divergences encountered here are actually physical. But since the energy as well as spatial resolution and covering of the full solid angle around the collision point of a detector are limited, one typically measures inclusive cross sections, which contain both virtual corrections as well as real-radiation processes and, hence, are soft and collinear finite.

[14] The appearance of initial-state radiation in the collinear regime leads to momenta running into the hard process of σ_{R}, which differ from the momenta going into σ_{Virt} by the momentum of the radiated particle. Since in the collinear region the latter may happen to be hard, the shift in the momenta can be sizable and may lead to uncanceled collinear divergences (see Fig. 5.25). However, due the factorizability of the remaining collinear poles as guaranteed by the KLN-theorem, these can always be separated and absorbed into, e.g., the partition function (pdf) of an incoming Hadron.

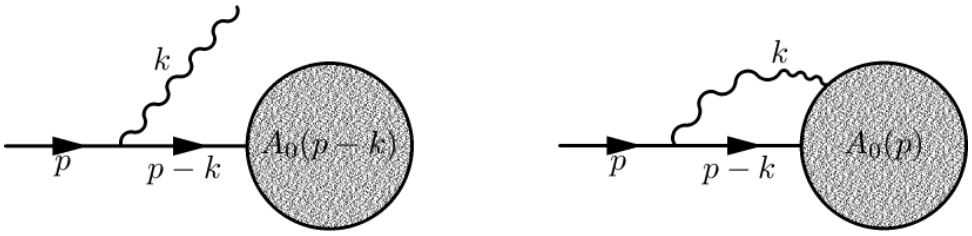

Figure 5.25.: Real (figure on the left) and virtual (figure on the right) corrections by radiation off a particle with momentum p running into the hard process $\mathcal{A}_0(p-k)$ (figure on the left) or $\mathcal{A}_0(p)$ (figure on the right).

the optical theorem

$$2\Im\left\{\mathcal{M}(p_1p_2 \to k_1k_2)\right\} = \sum_n \left(\prod_{i=1}^{n} \int \frac{1}{2E_i}\frac{\mathrm{d}^3q_i}{(2\pi)^3}\right) \mathcal{M}^*(k_1k_2 \to \{q_i\})\mathcal{M}(p_1p_2 \to \{q_i\}) \times (2\pi)^4\delta^{(4)}(p_1 + p_2 - \sum_i q_i). \tag{5.175}$$

This relates the matrix element of internal loops with momenta q_i to the same diagram but cut through internal lines in any possible way (sum over n) and with every cut line put on-shell (see also the Cutkosky cutting rule Ref. [12]). Taking $p_1 = k_1$ and $p_2 = k_2$, the latter can then be related to the squared matrix element of the associated real corrections. Note again that n can correspond to any set of possible final states depending on the chosen cut such that the real corrections are just a part of the final states on the right hand side of Eq. (5.175) for $p_1 = k_1$ and $p_2 = k_2$ (see also App. C). This motivates the intertwining mentioned above and even allows to identify at the level of diagrams already (more precisely, on the level of squared matrix elements), which parts of σ_{R} and σ_{Virt}, added up, provide a soft and collinear finite result[15] [181]. This is exemplified in Fig. 5.26. As a consequence of the complexity of the arising integrands in Eq. (5.174), it is usually impossible to solve the integrations in a completely analytic way. Hence, Eq. (5.174) is typically evaluated numerically. But as in this case the m-particle- and $(m+1)$-particle phase space are again evaluated separately, the theorems above do not apply so that one runs into the problems of soft and collinear ill defined amplitudes again. Therefore, the numerical evaluation of Eq. (5.174) is far from trivial. There are approaches that carry out only a small part of the phase space-integrations in Eq. (5.174) analytically, namely the integration over soft and (quasi)collinear regions of the phase space, while the regular part of the integrals is evaluated numerically. Two of these approaches are presented in the following.

5.2.3. The Phase-Space Slicing Method

In this section, we present the so-called *phase-space slicing method*, which we use to render the squark (co)annihilation numerically evaluable in the soft region.
The phase space slicing method isolates the soft and collinear divergences in the real corrections by slicing the $2 \to 3$ phase space into soft, collinear, soft-collinear divergent and regular parts using cuts ΔE and $\Delta\Theta$ on the energy of the radiated gluon as well as on

[15] At least, these divergences cancel up to some collinear singularities connected to initial-state radiation as stated above.

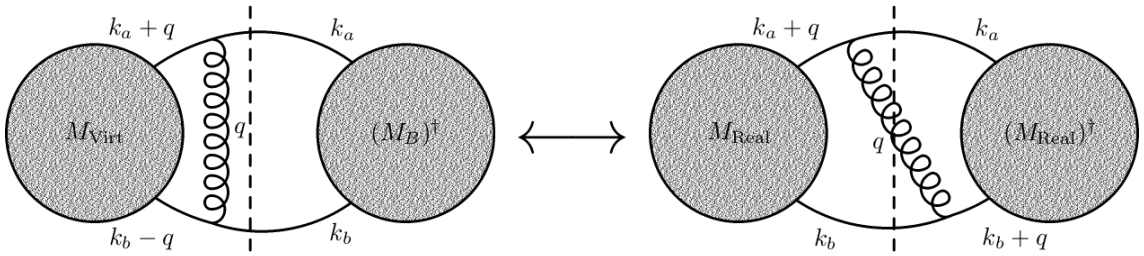

Figure 5.26.: Correlation between virtual and real corrections.

the relative angle Θ_{ij} as defined below Eq. (5.172) (see Fig. 5.24). Since for this work only the treatment of the soft divergences in terms of phase space slicing is of further interest, we solely concentrate on this case. A comprehensive study and treatment of the collinear regime in the context of phase space slicing can be found in Ref. [148] and references therein.
Starting point is the splitting of the real cross section according to

$$\sigma_{\text{R}} = \sigma_{\text{R}}^{\text{soft}}(\Delta E, D) + \sigma_{\text{R}}^{\text{hard}}(\Delta E). \tag{5.176}$$

After choosing an appropriate cut ΔE on the gluon energy, all soft divergences reside in the soft part $\sigma_{\text{R}}^{\text{soft}}(\Delta E, D)$, regularized by, e.g., DRed with $D > 4$ as introduced in Sec. 5.1.2. $\sigma_{\text{R}}^{\text{hard}}(\Delta E)$ remains free of any soft divergence and can, hence, be integrated numerically without any further effort.
The main idea behind this splitting is to analytically integrate $\mathrm{d}\sigma_{\text{R}}^{\text{soft}}(\Delta E, D)$ over the associated single gluon phase space connected to the soft singularities (see Fig. 5.24) in D dimensions by using the soft limit to simplify the integrands. The analytic integration over the gluon-phase space then yields the expected soft divergences but regularized by the DRed-parameter ϵ as introduced in Ch. 5.1.2. If everything works out as guaranteed by the BN-theorem, these poles cancel against poles of the same analytic form but opposite sign from the virtual corrections, such that the sum of σ_{Virt} and $\sigma_{\text{R}}^{\text{soft}}(\Delta E, D)$ is infrared finite.
Starting point of the soft photon approximation used in $\sigma_{\text{R}}^{\text{soft}}(\Delta E, D)$ is the general expression for a matrix element

$$\mathcal{M} = \mathcal{M}_0 \otimes (-ig_s \mathbf{T}^a)) \frac{i(2p-k)^\mu}{((p-k)^2 - m^2)} \epsilon_\mu^a(k) \tag{5.177}$$

($g_s := \sqrt{4\pi\alpha_s}$). Eq. (5.177) describes the radiation of a gluon with polarization vector ϵ off a scalar particle going into a hard process $\mathcal{A}_0(p-k)$ as shown in the left diagram of Fig. 5.25. The $\mathbf{T}^a$ ($a \in 1, ...8$) are half of the Gell-Mann matrices, the generators of the fundamental $SU(3)_{\text{C}}$[16]. Eq. (5.177) also describes the setup relevant to later calculations, where we use the phase space slicing method to render initial-state gluon radiation off incoming squarks suitable for numerical evaluations. In the soft limit $|\vec{k}| \ll |\vec{p}|$ and, hence, for a massless gluon $k^\mu \ll p^\mu$ Eq. (5.177) simplifies to

$$\mathcal{M} = -\mathcal{M}_0(p) \otimes (g_s \mathbf{T}^a) \frac{p \cdot \epsilon^a}{(p \cdot k)}. \tag{5.178}$$

[16] To keep things a bit clearer, we do not explicitly write out the color correlations between the scalars and the hard part of the amplitude $\mathcal{A}_0(p-k)$, which we symbolize by $\otimes$ in the following. However, this correlation should be kept in mind for explicit calculations.

Note that this factorization even holds true for radiation off spinors and vectors, because in the soft limit one finds that the spin-dependent part actually drops out of $\mathcal{M}$. Since final-state radiation also only differs from Eq. 5.178 by a relative sign, the most general expression for gluon radiation from initial and final states can be written as

$$\mathcal{M} = (-g_s)\mathcal{M}_0 \otimes \sum_i (\pm)\mathbf{T}^a \frac{p_i \cdot \epsilon^a}{p_i \cdot k}. \tag{5.179}$$

As the differential cross section is proportional to the absolute value squared of $\mathcal{M}$, we are left with the result

$$\overline{|\mathcal{M}|^2} = \sum_{spin} |\mathcal{M}_0|^2 \times (-g_s^2) C_F \left[\frac{p_1^2}{(p_1 \cdot k_3)^2} + \frac{p_2^2}{(p_2 \cdot k_3)^2} - \frac{2 p_1 \cdot p_2}{(p_1 \cdot k_3)(p_2 \cdot k_3)} \right] \tag{5.180}$$

where Eq. (5.180) is a fully averaged quantity already, i.e., averaged over incoming and summed over outgoing spins, gluon-polarizations λ ($\sum_\lambda \epsilon_\mu^{*\lambda}(k_3)\epsilon_\nu^\lambda(k_3) = -g_{\mu\nu}$) and colors. Moreover, we replaced the color sum by the overall color factor $C_F = 4/3$ ($\frac{1}{N_c}\sum_{i,j} \mathbf{T}_{ij}^a \mathbf{T}_{ji}^a = C_F$) as it is valid for squark annihilation going into a color singlet, which is the case of relevance here. In Eq. (5.180), we also made use of the overall color conservation, which implies

$$\sum_i \mathbf{T}_i = 0, \tag{5.181}$$

where i runs over all colored particles involved in the process[17]. As we later use dimensional regularization to regularize the soft poles, we need the D-dimensional cross section of a three-particle final state. It takes the form

$$\sigma = \int_{|\vec{k}_3| \leq \Delta E} \frac{\mathrm{d}^{D-1}k_1}{(2\pi)^{D-1} 2k_1^0} \frac{\mathrm{d}^{D-1}k_2}{(2\pi)^{D-1} 2k_2^0} \frac{\mathrm{d}^{D-1}k_3}{(2\pi)^{D-1} 2E_3} \frac{1}{2S} (2\pi)^D \delta^{(D)}(p_1 + p_2 - k_1 - k_2 - k_3) \overline{|\mathcal{M}|^2}. \tag{5.182}$$

$2S$ is the flux factor and ΔE limits the integration over the gluon momentum k_3 to its soft region, where the approximation $|\vec{k_3}| \ll |\vec{p}|$ (see Fig. 5.23 with $k \to k_3$) is valid. In the soft gluon approximation, the argument of the δ-function simplifies to $p_1 + p_2 - k_1 - k_2 - k_3 \to p_1 + p_2 - k_1 - k_2$ such that one is left with

$$\sigma_{\text{soft}} = \frac{1}{2S} \int \mathrm{d}\Gamma_2 \times \int_{|\vec{k}_3| \leq \Delta E} \frac{\mathrm{d}^{D-1}k_3}{(2\pi)^{D-1} 2E_3} \overline{|\mathcal{M}|^2}. \tag{5.183}$$

Here, $\mathrm{d}\Gamma_2$ is the D-dimensional $2 \to 2$ phase space element

$$\mathrm{d}\Gamma_2 = \frac{\mathrm{d}^{D-1}k_1}{(2\pi)^{D-1} 2k_1^0} \frac{\mathrm{d}^{D-1}k_2}{(2\pi)^{D-1} 2k_2^0} (2\pi)^D \delta^{(D)}(p_1 + p_2 - k_1 - k_2). \tag{5.184}$$

Combining Eq. (5.180) and Eq. (5.183), one already sees that the cross section Eq. (5.182) in the soft gluon approximation nicely factorizes such that it can be rewritten in differential form as

$$\left(\frac{\mathrm{d}\sigma}{\mathrm{d}\Gamma_2} \right)_{\text{soft}} = \left(\frac{\mathrm{d}\sigma}{\mathrm{d}\Gamma_2} \right)_0 \times \int_{|\vec{k}_3| \leq \Delta E} \frac{\mathrm{d}^{D-1}k_3}{(2\pi)^{D-4} 2E_3} T \tag{5.185}$$

[17] Note that an incoming antiparticle corresponds to an outgoing particle. Hence, it contributes with a relative minus to the color sum.

and $(\mathrm{d}\sigma/\mathrm{d}\Gamma_2)_0$ is the differential Born-level cross section in D dimensions. Following Eq. (5.180), in the case of pure initial-state radiation (the case relevant for us) T takes the form

$$T = -\frac{g_s^2 \mu^{4-D}}{8\pi^3} C_F \left[\frac{p_1^2}{(p_1 \cdot k_3)^2} + \frac{p_2^2}{(p_2 \cdot k_3)^2} - \frac{2 p_1 \cdot p_2}{(p_1 \cdot k_3)(p_2 \cdot k_3)} \right]. \tag{5.186}$$

In Eq. (5.186), we attached the soft factorization scale μ to the strong coupling $\alpha_s = g_s^2/(4\pi)$ following the reasoning given in Sec. 5.1.2. Hence, by defining the integral

$$I_{ab} = \mu^{4-D} \int_{|\vec{k}_3| \leq \Delta E} \frac{\mathrm{d}^{D-1} k_3}{(2\pi)^{D-4} 2E_3} \frac{2a \cdot b}{(a \cdot k_3)(b \cdot k_3)}, \tag{5.187}$$

we can grasp our final result in the concise form

$$\left(\frac{\mathrm{d}\sigma}{\mathrm{d}\Gamma_2} \right)_{\text{soft}} = - \left(\frac{\mathrm{d}\sigma}{\mathrm{d}\Gamma_2} \right)_0 \times \frac{g_s^2 C_F}{16\pi^3} \left(I_{p_1^2}(\Delta E) + I_{p_2^2}(\Delta E) - 2 I_{p_1 p_2}(\Delta E) \right), \tag{5.188}$$

where according to the above derivation, the integral I_{ab} matches the soft singularities connected to the real-radiation amplitude with gluon radiation off the initial-/final-state particle with momentum a contracted with the complex conjugated real-radiation diagram with gluon radiation off the initial-/final-state particle with momentum b. Details on the calculation of the last missing piece of Eq. (5.188), the integrals I_{ab}, are quite lengthy and can be found in Ref. [207, 208]. However, for our purposes we only need the two special cases $a = b$ and $\vec{a} = -\vec{b}$ (all calculations are performed in the CMS). In the former case, the integral I_{ab} takes the form

$$I_{a^2} = 2\pi \Big\{ \Delta_{IR} + \ln \frac{4\Delta E^2}{\mu^2} + \frac{a^0}{|\vec{a}|} \ln \Big(\frac{a^0 - |\vec{a}|}{a^0 + |\vec{a}|} \Big) \Big\}. \tag{5.189}$$

In the latter case, I_{ab} can be expressed by

$$\begin{aligned} I_{ab} = \frac{2\pi(a \cdot b)}{(a^0 + b^0)|\vec{p}|} \Big\{ & \frac{1}{2} (\Delta_{IR} + \ln \frac{4\Delta E^2}{\mu^2}) \ln \frac{a^0 + |\vec{p}|}{a^0 - |\vec{p}|} - \frac{1}{4} \ln^2 \frac{a^0 + |\vec{p}|}{a^0 - |\vec{p}|} - \mathrm{Li}_2 \Big(\frac{2|\vec{p}|}{a^0 + |\vec{p}|} \Big) \\ & \frac{1}{2} (\Delta_{IR} + \ln \frac{4\Delta E^2}{\mu^2}) \ln \frac{b^0 + |\vec{p}|}{b^0 - |\vec{p}|} - \frac{1}{4} \ln^2 \frac{b^0 + |\vec{p}|}{b^0 - |\vec{p}|} - \mathrm{Li}_2 \Big(\frac{2|\vec{p}|}{b^0 + |\vec{p}|} \Big) \Big\} \end{aligned} \tag{5.190}$$

with $\vec{a} = -\vec{b} = \vec{p}$ and

$$\Delta_{IR} = \frac{1}{\epsilon_{IR}} + \gamma_E - \log 4\pi, \tag{5.191}$$

where we define $\epsilon_{IR} := (D-4)/2$. In Eq. (5.190), Li_2 is the dilogarithm defined as

$$\mathrm{Li}_2(z) = - \int_0^z \frac{\ln(1-t)}{t} \mathrm{d}t. \tag{5.192}$$

The only thing left for the calculation of the phase space slicing are the $2 \to 2$ kinematics in D dimensions, which we apply in the soft limit in Eqs. (5.186)-(5.190). For the CMS we choose the following convention:

$$p_1 = (E_1, ..., 0, 0, |\vec{p}_1|), \tag{5.193}$$

$$p_2 = (E_2, ..., 0, 0, -|\vec{p}_2|), \tag{5.194}$$

$$k_1 = (E_3, ..., 0, \sin\Theta |\vec{k}_1|, \cos\Theta |\vec{k}_1|), \tag{5.195}$$

$$k_2 = (E_4, ..., 0, -\sin\Theta |\vec{k}_2|, -\cos\Theta |\vec{k}_2|) \tag{5.196}$$

with

$$E_1 = \frac{s + m_1^2 - m_2^2}{2\sqrt{s}}, \quad E_2 = \frac{s - m_1^2 + m_2^2}{2\sqrt{s}}, \quad E_3 = \frac{s + m_3^2 - m_4^2}{2\sqrt{s}}, \quad E_4 = \frac{s - m_3^2 + m_4^2}{2\sqrt{s}}, \tag{5.197}$$

$$|\vec{p}_1| = |\vec{p}_2| = \frac{\sqrt{\lambda(s, m_1^2, m_2^2)}}{2\sqrt{s}}, \quad |\vec{k}_1| = |\vec{k}_2| = \frac{\sqrt{\lambda(s, m_3^2, m_4^2)}}{2\sqrt{s}} \tag{5.198}$$

and the so-called Källén function

$$\lambda(x, y, z) = x^2 + y^2 + z^2 - 2xy - 2xz - 2yz. \tag{5.199}$$

Including this last part, we have everything at hand we need to perform the phase space slicing on the initial-state gluon radiation off an incoming squark pair going into EW final states.

5.2.4. The Dipole-Subtraction Method

We now proceed to the so-called *dipole-subtraction method*, a second method that can be used to bring Eq. (5.174) to a numerically evaluable form.
The dipole-subtraction method renders the integrands in Eq. (5.174) separately non singular by adding and subtracting an auxiliary cross section σ_{A}. Within DRed, Eq. (5.174) can be rewritten as

$$\sigma_{\mathrm{NLO}} = \int_{m+1} \mathrm{d}\sigma_{\mathrm{R}} + \int_m \mathrm{d}\sigma_{\mathrm{Virt}} = \int_{m+1} [\mathrm{d}\sigma_{\mathrm{R}}|_{\epsilon=0} - \mathrm{d}\sigma_{\mathrm{A}}|_{\epsilon=0}] + \int_m [\mathrm{d}\sigma_{\mathrm{Virt}} + \int_1 \mathrm{d}\sigma_{\mathrm{A}}]|_{\epsilon=0}, \tag{5.200}$$

where the second step is, roughly speaking, just a very sophisticated way of adding a zero. On the right hand side of Eq. (5.200), the $(m+1)$-particle phase space integral is now factorized into the m-particle phase space integral times the integration over the one-particle phase space of the radiated gluon. Further note that in the first term on the right hand side of Eq. (5.200), the limit $\epsilon \to 0$ has already been applied at the integrand level as the associated soft and collinear singularities first arise during the integration over the $(m+1)$-particle phase space. $\mathrm{d}\sigma_A$ is now constructed in such a way that it correctly matches up all soft and (quasi)collinear singularities that arise in the integrands of the $(m+1)$- as well as of the m-particle phase space integrals in Eq. (5.200). For this cancellation to work out correctly, $\mathrm{d}\sigma_A$ has to fulfill certain requirements:

1. $\mathrm{d}\sigma_A$ has to possess the same pointwise singular behavior like $\mathrm{d}\sigma_{\mathrm{R}}$ in D dimensions, smoothly (i.e., avoiding double counting of singularities) reproducing the associated soft and (quasi)collinear terms in the singular regions.

2. $\mathrm{d}\sigma_A$ has to be analytically integrable over the one particle phase space of the gluon (see Eq. (5.200)) yielding the same single and double pole structure (but with opposite sign) as $\mathrm{d}\sigma_{\mathrm{Virt}}$.

If $\mathrm{d}\sigma_{\mathrm{A}}$ fulfills these two requirements, it will act as a local counterterm for $\mathrm{d}\sigma_{\mathrm{R}}$, rendering the sum $[\mathrm{d}\sigma_{\mathrm{R}}|_{\epsilon=0} - \mathrm{d}\sigma_{\mathrm{A}}|_{\epsilon=0}]$ soft as well as collinear well defined and, hence, numerically evaluable even in $D = 4$ dimensions. Moreover, $\int_1 d\sigma_{\mathrm{A}}$ cancels the poles in the virtual corrections such that $[\mathrm{d}\sigma_{\mathrm{Virt}} + \int_1 \mathrm{d}\sigma_{\mathrm{A}}]|_{\epsilon=0}$ is soft and collinear finite, too. Furthermore, it matches all quasi-collinear terms and prevents the real as well as virtual contributions from separately blowing up for $m_{ij} \ll \sqrt{s}$.

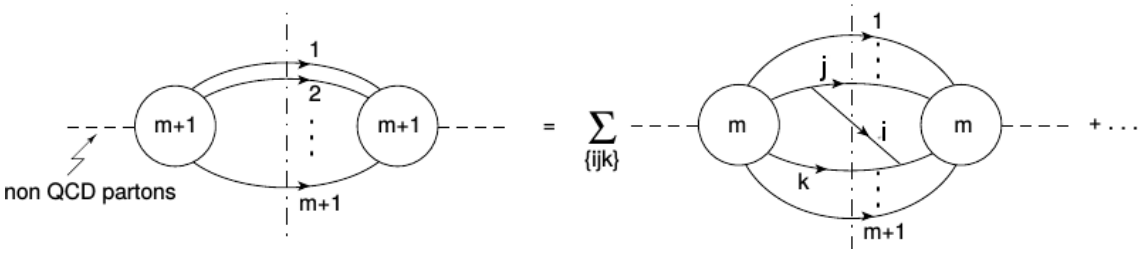

Figure 5.27.: The dipole structure for a $(x \to m+1)$-process, which mimics the factorization of the $(x \to m+1)$-matrix element in the singular regions into a $(x \to m)$-process with subsequent splitting of the emitter particle $\tilde{ij} \to i+j$. Figure originally taken from Ref. [180].

The attraction of this method relies on the observation that the singular behavior of the $(m+1)$-particle matrix element $\mathcal{M}_{m+1} = \mathcal{M}_{\mathrm{R}}$ turns out to be universal, i.e., independent with respect to the details of the matrix element $\mathcal{M}_m = \mathcal{M}_{\mathrm{B}}$. This allows for a process independent construction of the $\mathrm{d}\sigma_{\mathrm{A}}$ (up to a factor $|\mathcal{M}_{\mathrm{B}}|^2$) and especially for a process independent evaluation of $\int_1 \mathrm{d}\sigma_{\mathrm{A}}$ (see Eq. (5.200)). Therefore, most of the calculational steps presented in the following can be done once and for all.
We later use the dipole-subtraction method to render the gaugino (co)annihilation into light and heavy quarks numerically evaluable. There, the final-state (anti)quarks as well as squarks in the t- and u-channel turn out to be the only partons (i.e. colored particles) in the process. Since the t- and u-channel propagator squarks do not lead to any soft or collinear divergences as they are massive and typically far off the mass-shell, in the following, we solely concentrate on radiation off final-state partons, i.e., on processes with no initial-state partons.
To be able to construct the required $\mathrm{d}\sigma_{\mathrm{A}}$, more information about the exact structures of the real and virtual corrections in the soft and collinear regions is needed. Therefore, we start with the construction of bras and kets in the helicity and color space spanned by all partons involved in the process

$$|1,...,m\rangle_m = (|c_1,...,c_m\rangle \otimes |s_1,...,s_m\rangle) \cdot \mathcal{M}_m^{c_1,...,c_m;s_1,...s_m}(k_1,...,k_m). \tag{5.201}$$

Here, $\mathcal{M}_m^{c_1,...,c_m;s_1,...s_m}(k_1,...,k_m)$ is the matrix element that describes the production of m final-state partons with colors c_i and helicities s_i. The indices of all other uncolored particles involved in the process are suppressed, which also is the case throughout the rest of this section. We can then express the square of color correlated tree-amplitudes summed over all colors and parton helicities $|\mathcal{M}_m^{i,j}|^2$ by

$$\begin{aligned}|\mathcal{M}_m^{i,j}|^2 =& {}_m\langle 1,...,m|\mathbf{T}_i\mathbf{T}_j|1,...m\rangle_m \\ & [\mathcal{M}_m^{a_1,...,b_i,...,b_j,...a_m}(k_1,...,k_m)]^* T^c_{b_i a_i} T^c_{b_j a_j} \mathcal{M}_m^{a_1,...,a_i,...,a_j,...a_m}(k_1,...,k_m).\end{aligned} \tag{5.202}$$

In Eq. (5.202), we have $T^c_{b_i a_i} = i f_{b_i c a_i}$ (color-charge matrix in the adjoint representation of the $\mathfrak{su}(3)_{\mathrm{C}}$ with structure constants f_{bac}), if i is a gluon, and $T^c_{b_i a_i} = t^c_{b_i a_i}$ (color-charge matrix in the fundamental representation of the $\mathfrak{su}(3)_{\mathrm{color}}$), if i is a quark (if i is an antiquark, then $T^c_{b_i a_i} = \bar{t}^c_{b_i a_i} = -t^c_{b_i a_i}$). It further follows directly from construction that, assuming overall color conservation in each process, all vectors in this space have to be color singlets

$$\sum_{i=1}^{m} \mathbf{T}_i |1,...,i,..m\rangle_m = 0. \tag{5.203}$$

Using the above definitions, we can express the squared matrix elements of $(m+1)$ final-state partons summed over the corresponding helicities and colors as

$$|\mathcal{M}_{m+1}|^2 = {}_{m+1,\ldots,1}\langle||\rangle_{m+1,\ldots,1}. \tag{5.204}$$

In the soft limit of some momentum $(k_i)_\mu \to \lambda(k_i)_\mu$ ($\mu \in \{0,1,2,3\}$), $\lambda \to 0$ [180], one finds

$${}_{m+1,\ldots,1}\langle||\rangle_{m+1,\ldots,1} \to -\frac{g_s^2}{\lambda^2}\ {}_{m,\ldots,1}\langle|[\mathbf{J}^\mu(k_i)]^\dagger \mathbf{J}_\mu(k_i)|\rangle_{m,\ldots,1}, \tag{5.205}$$

where only the most singular terms $\mathcal{O}(1/\lambda^2)$ are kept. The right hand side of Eq. (5.205) has been obtained by simply removing the particle i from $\mathcal{M}_{m+1}$. $\mathbf{J}_\mu(k_i)$ is the so-called *eikonal current* for the emission of a soft gluon with momentum k_i. Its explicit form is

$$\mathbf{J}_\mu(k_i) = \sum_{j\neq i} \mathbf{T}_j \frac{k_j}{k_i \cdot k_j}. \tag{5.206}$$

The square yields

$$[\mathbf{J}^\mu(k_i)]^\dagger \mathbf{J}_\mu(k_i) = \sum_{j\neq i}\sum_{k\neq i,j} \mathbf{T}_j \mathbf{T}_k \left(\frac{k_j \cdot k_k}{(k_i \cdot k_j)(k_i \cdot k_k)} - \frac{k_j^2}{(k_i \cdot k_j)^2} \right), \tag{5.207}$$

where Eq. (5.181)/Eq. (5.203) have been used. Plugging Eq. (5.207) into Eq. (5.205), we rediscover the result Eq. (5.180) (Eq. (5.179)) from the previous section, but written in terms of final-state radiation. Note again that this factorization is only strictly valid in the limit $(k_i)_\mu \to 0$ in order that away from this limit, the factorization has to be used with care. Furthermore, Eq. (5.207) can become collinear divergent if the momentum k_i is parallel either to k_j or k_k ($k_i \cdot k_j \to 0$, $k_i \cdot k_k \to 0$).
In the (quasi)collinear region things look a bit different. One can express the momenta k_i and k_j through the Sudakov parametrization [180]

$$p_i^\mu = z p^\mu + k_\perp^\mu - \frac{k_\perp^2 + z^2 m_{ij}^2 - m_i^2}{z} \frac{n^\mu}{2p\cdot n}, \tag{5.208}$$

$$p_j^\mu = (1-z) p^\mu - k_\perp^\mu - \frac{k_\perp^2 + (1-z)^2 m_{ij}^2 - m_j^2}{1-z} \frac{n^\mu}{2p\cdot n}, \tag{5.209}$$

where $p^2 = 0$ is a light-like vector and n^μ is an auxiliary light-like vector necessary to specify the transverse component of $k_\perp$ ($k_\perp^2 < 0$, ($k_\perp \cdot p = k_\perp \cdot n = 0$). The invariant mass of the i-j pair then takes the form

$$(k_i + k_j)^2 = -\frac{k_\perp^2}{z(1-z)} + \frac{m_i^2}{z} + \frac{m_j^2}{1-z}. \tag{5.210}$$

If one further performs the rescaling $k_\perp \to \lambda k_\perp$, $m_i \to \lambda m_i$, $m_j \to \lambda m_j$ and $m_{ij} \to \lambda m_{ij}$, the collinear limit is recovered for $\lambda \to 0$. In this limit, the $(m+1)$-parton matrix element behaves like

$${}_{m+1,\ldots,1}\langle||\rangle_{m+1,\ldots,1} \to \frac{1}{\lambda^2}\mu^{2\epsilon} \frac{2g_s^2}{(k_i+k_j)^2 - m_{ij}^2} {}_{m,\ldots,1}\langle|\hat{P}_{(ij),i}(z,k_\perp;\epsilon)|\rangle_{m,\ldots,1}, \tag{5.211}$$

where terms less singular than $1/\lambda^2$ have again been omitted. In Eq. (5.211), the right hand side is obtained by replacing the two particles i and j by the single particle $\tilde{ij}$. The

kernel $\hat{P}_{(ij),i}(z, k_\perp; \epsilon)$ is the so-called D-dimensional generalized *Altarelli-Parisi splitting kernel* (generalized from the collinear to the quasicollinear case) [210]. It is a matrix in the helicity space of the parton $\tilde{ij}$ and, hence, acts on the spin of $\tilde{ij}$. Therefore, Eq. (5.211) factorizes only up to some spin correlation between the splitting kernel and the remaining squared m-particle matrix element $|\mathcal{M}_m|^2$. In the relevant case of gluon radiation off some (anti)quark q ($\bar{q}$), $\hat{P}_{(ij),i}(z, k_\perp; \epsilon)$ acting on the helicity of the particle $\tilde{ij}$ s, s' takes the form

$$\langle s|\hat{P}_{(ij),i}(z, k_\perp; \epsilon)|s'\rangle = \delta_{ss'} C_F \left[\frac{1+(1-z^2)}{z} - \epsilon z - \frac{m_q^2}{p_g \cdot p_q}\right]. \tag{5.212}$$

This completes the short investigation on the singular behavior of the real-radiation matrix element $|M_{\mathrm{R}}|$ in the soft and collinear limit specified to the case of gluon radiation off final-state quarks. These limits are needed when we construct the dipoles.
The dipole expansion of the square of a real final-state radiation matrix element $|M_{\mathrm{R}}|^2$ can be grasped in its most general form as

$$|M_{\mathrm{R}}|^2 = \sum_{i,j} \sum_{k \neq i,j} \mathcal{D}_{ij,k} + ... = \mathcal{D}_{gq,\bar{q}} + \mathcal{D}_{g\bar{q},q} + ..., \tag{5.213}$$

where i, j and k run over all final-state partons and the dots stand for additional soft as well as collinear finite terms. Eq. (5.213) encodes the singular structure of the squared real-radiation matrix element in different regions of phase space as a summation over so-called emitter-spectator pairs, singled out over the m Born-level external partons in all possible ways. The final $(m+1)$-parton configuration is then reached in a second step, where the emitter $\tilde{ij}$ splits into two final-state particles i and j (i.e., in the present case into a (anti)quark plus an additional gluon) as shown in Fig. 5.27, while the spectator k is needed to maintain total-momentum conservation. Both, Eq. (5.213) as well as Fig. 5.27 embody the observation that the matrix element $\mathcal{M}_{m+1}$ can, with respect to its soft and collinear terms, always be considered as being obtained by the insertion of the radiated particle i over all possible external legs of the Born-level matrix element $\mathcal{M}_{\mathrm{B}}$. This crucial insight translates into the factorization of dipoles according to [18]

$$\mathcal{D}_{ij,k} = \mathbf{V}_{ij,k}(k_i, \tilde{k}_{ij}, \tilde{k}_k) \otimes |M_{\mathrm{B}}(\tilde{k}_{ij}, \tilde{k}_k)|^2, \tag{5.214}$$

which mimics the two step-process of the Born-level production of an emitter-spectator pair with momenta $\tilde{k}_{ij}$ and $\tilde{k}_k$, subsequently followed by the emitter-decay described by the $\mathbf{V}_{ij,k}$ (see Fig. 5.28). The $\mathbf{V}_{ij,k}$ are matrices in color and helicity space of the emitter-spectator pair and depend on the momenta of the final-state particles i, j and k. In addition, the $\otimes$ symbols the associated helicity and color correlations between $\mathbf{V}_{ij,k}$ and $|M_{\mathrm{B}}(\tilde{k}_{ij}, \tilde{k}_k)|^2$. Due to the factorization of Eq. (5.214), the $\mathbf{V}_{ij,k}$ are basically independent of the Born-level-cross section. Therefore, they need to be calculated only once for each splitting-processes.
Now, with regard of point 1 above, $\mathrm{d}\sigma_{\mathrm{A}}$ has to approximate $\mathrm{d}\sigma_{\mathrm{R}}$ in the soft and collinear limit. Hence, one can rewrite the general structure of the associated matrix element of $\mathrm{d}\sigma_{\mathrm{A}}$ as

$$|M_A|^2 = \sum_{i,j} \sum_{k \neq i,j} \mathcal{D}_{ij,k} = \sum_{i,j} \sum_{k \neq i,j} \mathbf{V}_{ij,k}(k_i, \tilde{k}_{ij}, \tilde{k}_k) \otimes |M_B(\tilde{k}_{ij}, \tilde{k}_k)|^2. \tag{5.215}$$

[18] See, e.g., the factorization in the soft limit exemplified in Sec. (5.2.3).

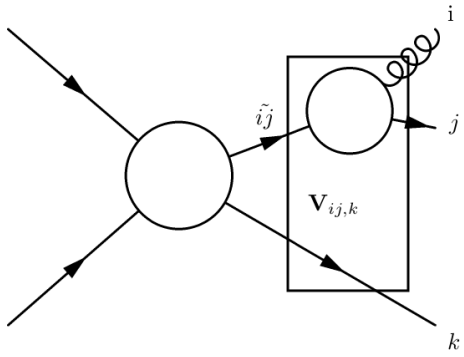

Figure 5.28.: Factorization of a $2 \to 3$ process in the soft and collinear limit with the emitter-spectator correlating matrix element $\mathbf{V}_{ij,k}$.

For the relevant case without initial-state partons the $\mathcal{D}$'s of Eqs. (5.214) and (5.215) can be written as

$$\mathcal{D}_{ij,k} \;=\; -\frac{1}{(k_i+k_j)^2-m_{ij}^2}\;{}_m\langle ...,\tilde{ij},...,\tilde{k},...|\frac{\mathbf{T}_k\cdot\mathbf{T}_{ij}}{\mathbf{T}_{ij}^2}V_{ij,k}|...,\tilde{ij},...,\tilde{k},...\rangle_m. \tag{5.216}$$

For the relevant case of gaugino (co)annihilation into quarks with additional gluon radiation, i.e., for a (anti)quark-emitter and an antiquark (quark)-spectator, we can be even more explicit. Since in the present case the quark-antiquark pair forms a color singlet, the color structure in Eq. (5.216) reduces to one[19]. This simplifies Eq. (5.216) to

$$\mathcal{D}_{ij,k} \;=\; -\frac{1}{(k_i+k_j)^2-m_{ij}^2}V_{ij,k}(k_i,\tilde{k}_{ij},\tilde{k}_k)\otimes|M_B(\tilde{k}_{ij},\tilde{k}_k))|^2. \tag{5.217}$$

Here, the $\otimes$ still accounts for helicity correlations between $V_{ij,k}$ and $|M_B(\tilde{k}_{ij},\tilde{k}_k))|^2$, which, however, vanish after integrating $V_{ij,k}$ over the gluon phase space [204]. After averaging over incoming and summing over outgoing color states [211], the color factors from the (anti)quark-gluon vertices of the squared amplitude become

$$\frac{1}{N_c}\sum_{efgh}(T_k^a)_{ef}(T_{ij}^a)_{gh}\delta_{eh}=\frac{1}{N_c}\sum_{fg}\frac{1}{2}(N_c-\frac{1}{N_c})\delta_{fg}=\frac{N_c^2-N_c}{2N_c}=C_F, \tag{5.218}$$

where summation over a is implicitly assumed. The $V_{ij,k}$ of Eq. (5.217) has to be chosen such that according to point 1 it reproduces the singular part of $\mathcal{M}_R$ in the soft and collinear limit (Eq. (5.205) and Eq. (5.212)). In addition, it has to feature a convenient form for its analytic integration over the one particle phase space as demanded by point 2 above. The authors of Ref. [204] chose to express $V_{ij,k}$ in the case of (anti)quark-gluon splitting as

$$\begin{aligned}\langle s|V_{ij,k}|s'\rangle \;&=8\pi\alpha_s\mu^{2\epsilon}\;C_F\{\frac{2}{1-\tilde{z}_j(1-y_{ij,k})}-\frac{\tilde{v}_{ij,k}}{v_{ij,k}}[1+\tilde{z}_j+\frac{m_q^2}{k_ik_j}+\epsilon(1-\tilde{z}_j)]\}\delta_{ss'}\\ &=\langle V_{ij,k}\rangle\delta_{ss'},\end{aligned} \tag{5.219}$$

where $i=g$, $j=q$ (or $\bar{q}$) and $k=\bar{q}$ (or q) and s, s' are helicities in the helicity space of the emitter. Moreover, μ is the dimensional regularization scale. We further made use

[19]Note, that we assign the color charges of the Born-level amplitude to the emitter and spectator.

of Eq.(5.218). For remaining definitions see App. B. The appearance of $\delta_{ss'}$ signals that there is no helicity flip induced by the radiated gluon, i.e., $V_{ij,k}$ takes diagonal form in the helicity space of the emitter.
Another important observation is that Eq.(5.214) allows for a factorizable mapping of the of the $(m+1)$-particle phase space onto the m-particle phase space represented by the emitter- and spectator-momenta $\tilde{k}_{ij}(k_i, q_j, k_k)$ and $\tilde{k}_k(k_i, q_j, k_k)$. For the case of final-state radiation with no initial-state partons, we use the mapping [204]

$$\tilde{k}_k^\mu = \frac{\sqrt{\lambda(Q^2, m_{ij}^2, m_k^2)}}{\sqrt{\lambda(Q^2, (k_i+k_j)^2, m_k^2)}}(k_k^\mu - \frac{Q\cdot k_k}{Q^2}Q^\mu) + \frac{Q^2+m_k^2-m_{ij}^2}{2Q^2}Q^\mu \tag{5.220}$$

and

$$\tilde{k}_{ij}^\mu = Q^\mu - \tilde{k}_k^\mu \tag{5.221}$$

with

$$Q = k_i + k_j + k_k, \tag{5.222}$$

which is symmetric under $i \leftrightarrow j$. For further definitions see App. B. Making use of the definitions Eqs. (5.220)-(5.222), the phase space element of a three-particle final state in D dimensions (see Eq. (5.162))

$$\begin{aligned}\mathrm{d}\Gamma^{(3)} = \frac{\mathrm{d}^D k_1}{(2\pi)^D}\frac{\mathrm{d}^D k_2}{(2\pi)^D}\frac{\mathrm{d}^D k_3}{(2\pi)^D}(2\pi)\delta(k_1^2-m_{k_1}^2)(2\pi)\delta(k_2^2-m_{k_2}^2)(2\pi)\delta(k_3^2-m_{k_3}^2)\\ \Theta(k_1^0)\Theta(k_2^0)\Theta(k_3^0)(2\pi)^D\delta^D(P-k_i-k_j-k_k)\end{aligned} \tag{5.223}$$

with overall four-momentum P factorizes according to

$$\mathrm{d}\Gamma^{(3)}(k_i,k_j,k_k,Q) = \mathrm{d}(\tilde{k}_{ij},\tilde{k}_k,Q)\ \mathrm{d}k_i(\tilde{k}_{ij},\tilde{k}_k)\ \Theta\left(1-\frac{m_i}{\sqrt{Q^2}}-\frac{m_j}{\sqrt{Q^2}}-\frac{m_k}{\sqrt{Q^2}}\right) \tag{5.224}$$

(note that $Q^2 = s$ for a three-particle final state ($m = 2$)). For more details, e.g., the explicit form of $\mathrm{d}k_i(\tilde{k}_{ij},\tilde{k}_k)$, see Ref. [204]. This factorization of the phase space element allows for an analytic integration of $\mathrm{d}\sigma_\mathrm{A}$ over the one particle-phase space spanned by k_i independent of $M_i^\mathrm{B}(\tilde{k}_{ij},\tilde{k}_k)$ (see Eq. (5.214)). This is an important result as it allows to perform the necessary analytical integration $\int_1 \mathrm{d}\sigma_A$ just once and for all.
Let us now turn to the *virtual dipole-contributions* of Eq. (5.200), where exactly this property turns out to be of great use. The virtual dipole can be rewritten at NLO as [204]

$$\begin{aligned}\int_m \Big[\mathrm{d}\sigma_\mathrm{Virt} + \int_1 \mathrm{d}\sigma_\mathrm{A}\Big]\Big|_{\epsilon=0} &= \int_m \Big[\mathrm{d}\sigma_\mathrm{Virt} + \mathrm{d}\sigma^B \otimes \mathbf{I}_m\Big]\Big|_{\epsilon=0}\\ &= \int \mathrm{d}\mathbf{\Phi}_m\Big[2\Re\left\{(\mathrm{M}^B)^\dagger \mathcal{M}^\mathrm{NLO}\right\}\\ &\quad +{}_m\langle|\mathbf{I}_m(\epsilon,\mu^2;\{k_a,m_a\}]|\rangle_m\Big]\Big|_{\epsilon=0},\end{aligned} \tag{5.225}$$

where a runs over all Born-level final-state partons and $\mathrm{d}\mathbf{\Phi}_m(k_1,...,k_m,P)$ is the m-particle phase space element already including flux factors and spin averaging. Following Eq. (5.225), $\mathbf{I}_m$ is then defined as

$$\mathbf{I}_m = \sum_\mathrm{dipoles}\int_1 \mathrm{d}V_\mathrm{dipole} = \sum_j \sum_{k\neq i,j}\left(\int \mathrm{d}k_i(\tilde{k}_{ij},\tilde{k}_k)\frac{\langle V_{ij,k}\rangle}{(k_i+k_j)^2-m_{ij}^2}\right)_{\substack{\tilde{ij}\to j\\ \tilde{k}\to k}}, \tag{5.226}$$

where the replacement of momenta on the right hand side is performed *after* the integral has been evaluated. For the particular case of (anti)quark-gluon splitting, $\langle V_{ij,k}\rangle$ is defined in Eq. (5.219). The actual calculation of the integral Eq. (5.226) is quite involved. Therefore, we only state the final result. Following Ref. [204] again, $\mathbf{I}_m$ in Eq. (5.226) takes the form

$$\begin{aligned}\mathbf{I}_m(\epsilon,\mu^2;\{k_a,m_a\}) &= -\frac{g_s^2}{8\pi^2}\frac{(4\pi)^\epsilon}{\mathbf{\Gamma}(1-\epsilon)}\sum_j\frac{1}{\mathbf{T}_j^2}\sum_{k\neq j}\mathbf{T}_j\cdot\mathbf{T}_k\\ &\quad\times\Big[\mathbf{T}_j^2(\frac{\mu^2}{s_{jk}})^\epsilon\left(\mathcal{V}_j(s_{jk},m_j,m_k;\epsilon)-\frac{\pi^2}{3}\right)\\ &\quad+\mathbf{\Gamma}_j(\mu,m_j,\{m_F\};\epsilon)\\ &\quad+\gamma_j\ln\frac{\mu^2}{s_{jk}}+\gamma_j+\mathrm{K}_j+O(\epsilon)\Big],\end{aligned}\tag{5.227}$$

where in the present case j can be either the quark or the antiquark of the Born level cross section considered (in either case $j=q$ such that only the momenta k_j and k_k have to be fixed in agreement with the kinematics in $\mathcal{M}^{\mathrm{B}}$). The necessary definitions can again be found in App. B. One can further decompose $\mathcal{V}_j$ of Eq. (5.227) into a (j↔k)-symmetric and a soft as well as (quasi)collinear singular (S) and a $(j\leftrightarrow k)$-non symmetric and a soft as well as (quasi)collinear nonsingular (NS) part

$$\mathcal{V}_j(s_{jk},m_j,m_k;\epsilon)=\mathcal{V}^{(\mathrm{S})}(s_{jk},m_j,m_k;\epsilon)+\mathcal{V}_j^{(\mathrm{NS})}(s_{jk},m_j,m_k).\tag{5.228}$$

Here, the subscript j indicates that $\mathcal{V}_j^{(\mathrm{NS})}$ depends on whether the parton j is a gluon or a(n) (anti)quark. As we also deal with light quarks in the final state, we encounter numerical instabilities of the relevant dipoles when the mass of a final-state quark drops far below the CMS energy $m_q\ll\sqrt{s}$. To circumvent this problem, we set the light quark masses m_u, m_d, m_s to zero. This in turn makes it necessary to also take the associated $\mathcal{V}^{(\mathrm{S})}$ and $\mathcal{V}^{(\mathrm{NS})}$ into account, which distinguish between massive and massless partons. All necessary $\mathcal{V}_j^{(\mathrm{S})}(s_{jk},m_j,m_k;\epsilon)$ and $\mathcal{V}_j^{(\mathrm{NS})}(s_{jk},m_j,m_k)$ for every possible mass configuration are provided in App. B. Moreover, one has to expand the prefactor in Eq. (5.227) in ϵ to obtain the right structure of singular and finite (in the limit $\epsilon\to 0$) terms by the multiplication with the singular terms in $\mathcal{V}_j$ and Γ_j.
Putting everything together, these are all necessary building blocks for the construction of $\mathrm{d}\sigma_A$ as well as of $\int_1\mathrm{d}\sigma_A$ to render the σ_{NLO} of Eq. (5.200) suitable for a numerical evaluation. Finally note that for the following numerical investigations, the dimensional regularization scale μ introduced in this chapter, which drops out of the final σ_{NLO}, is set to be equal to the renormalization scale.

5.2.5. ChiChi2qq: The Real Corrections

The real radiation amplitudes connected to gaugino (co)annihilation can be understood as the tree-level graphs of Fig. 4.2 extended by the radiation of an additional gluon as shown in Fig. 5.29. Since only the final states as well as t- and u-channel propagators carry color, these turn out to be the only legs or internal lines to which the additional gluon can be attached. The polarization (λ), spin and color summed (over final states)/averaged (over

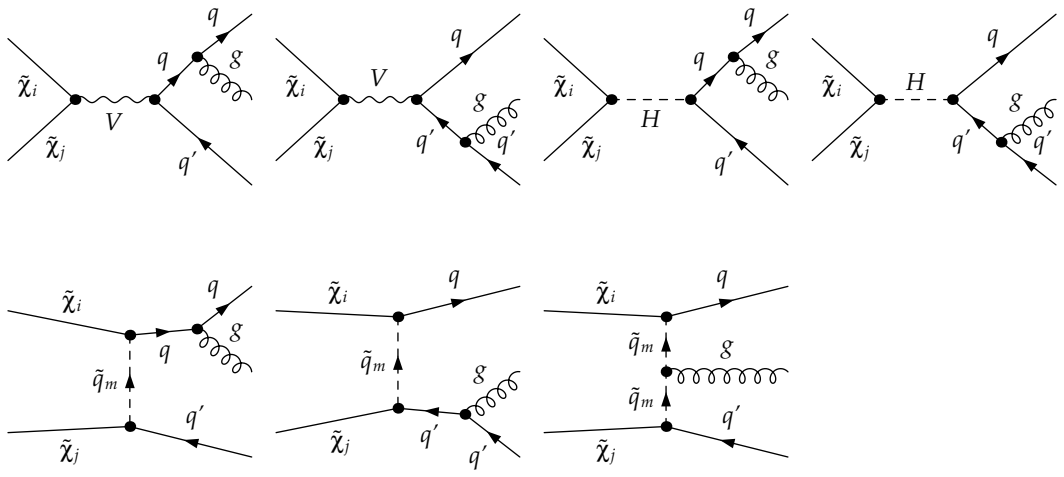

Figure 5.29.: Real radiation corrections to gaugino (co)annihilation processes as included in `ChiChi2qq` [1]. u-channel contributions can be obtained through crossing of the corresponding t-channels.

initial states) squared matrix element can be written as

$$\begin{aligned}\overline{|\mathcal{M}^{\mathrm{R}}|^2} = &\sum_{i,j} t^a_{ij} t^a_{ji} \sum_{\lambda} (\epsilon^a_\lambda)^*_\mu (\epsilon^a_\lambda)_\nu \Big[\left(\mathcal{M}^{\mathrm{R}}_s\right)^{\dagger,\mu} \mathcal{M}^{\mathrm{R},\nu}_s + \left(\mathcal{M}^{\mathrm{R}}_t\right)^{\dagger,\mu} \mathcal{M}^{\mathrm{R},\nu}_t + \left(\mathcal{M}^{\mathrm{R}}_u\right)^{\dagger,\mu} \mathcal{M}^{\mathrm{R},\nu}_u \\ &- 2\Re\left\{\left(\mathcal{M}^{\mathrm{R}}_s\right)^{\dagger,\mu} \mathcal{M}^{\mathrm{R},\nu}_t\right\} + 2\Re\left\{\left(\mathcal{M}^{\mathrm{R}}_s\right)^{\dagger,\mu} \mathcal{M}^{\mathrm{R},\nu}_u\right\} - 2\Re\left\{\left(\mathcal{M}^{\mathrm{R}}_t\right)^{\dagger,\mu} \mathcal{M}^{\mathrm{R},\nu}_u\right\} \Big] \end{aligned} \tag{5.229}$$

$$\begin{aligned} = &- C_F N_c \Big[|\mathcal{M}^{\mathrm{R}}_s|^2 + |\mathcal{M}^{\mathrm{R}}_t|^2 + |\mathcal{M}^{\mathrm{R}}_u|^2 \\ &+ 2\Re\left\{(\mathcal{M}^{\mathrm{R}}_s)^\dagger \mathcal{M}^{\mathrm{R}}_t\right\} - 2\Re\left\{(\mathcal{M}^{\mathrm{R}}_s)^\dagger \mathcal{M}^{\mathrm{R}}_u\right\} - 2\Re\left\{(\mathcal{M}^{\mathrm{R}}_t)^\dagger \mathcal{M}^{\mathrm{R}}_u\right\} \Big]. \end{aligned} \tag{5.230}$$

Here, the relative minus signs between the different squared matrix elements, which arise by appropriately contracting the different fermion fields in the amplitude according to Fig. 4.3, are already included. We also suppress all color and spin structures connected to final-state particles that are already present at the Born level in Eq. (5.229) (see Eq. (5.132) for greater detail). However, we explicitly write out the Lorentz and color structure connected to the radiated gluon. The latter collapses into C_F owing to the fact that the incoming particles are color singlets. In Eq. (5.230) we further make use of the polarization sum

$$\sum_{\lambda} (\epsilon_\lambda)^{\dagger,\mu} \epsilon^\nu_\lambda \to -g^{\mu\nu}, \tag{5.231}$$

where it has to be paid attention to the fact that this identity holds true only if the Ward-Takahashi or Slavnov-Taylor identities are imposed [12]. This insight can become relevant if one checks for the positivity of the associated squared amplitudes. The convention for the kinematics as well as the phase space integration are used as outlined in Sec. 5.2.1. In addition, there arise subtleties in the calculation of the real-radiation amplitudes that are connected to the nature of the incoming neutralinos. As already stated in Sec. 4.2, neutralinos as Majorana fermions do not carry any fermion number. Hence, one can assign an arbitrary fermion flow to the neutralino lines, which can be understood as fixing a convention for the application of the Feynman rules (i.e., the assignment of u- and v-spinors).

After this choice, there may arise clashing arrows within a Feynman diagram as well as in the contraction of different (s-, t-, u-channel) amplitudes[20]. The appearance of clashing arrows within a Feynman diagram is connected to the fact that Majorana fermions as selfconjugated particles feature Wick contractions, which differ from conventional contractions known for Dirac fermions. Moreover, we also encounter clashing arrows in the case of charginos owing to fact, that the assignment of particle and antiparticle and, hence, the assignment of the (anti)fermion flow is arbitrary to a certain extend. A pair of clashing arrows may be associated with a spinor structure of the form $u(p)v^{\intercal}(p)$, e.g.. It is then not possible to apply the common spin sums for Dirac fermions [12]

$$\sum_s u^{(s)}(p)\bar{u}^{(s)}(p) = \not{p} + m, \quad \sum_s v^{(s)}(p)\bar{v}^{(s)}(p) = \not{p} - m, \tag{5.232}$$

which makes it mandatory to introduce new spin sums as given in Ref. [212]. However, we use a set of transformations outlined in Ref. [213], which allows to transform the bilinears $\bar{\chi}'\Gamma\chi$ for some spinors χ, $\chi' \in \{u, v\}$ and $\Gamma \in \{1, i\gamma_5, \gamma^\mu, \gamma^\mu\gamma_5, \sigma^{\mu\nu}\}$ in such a way that we end up with a convenient form to evaluate the corresponding squared amplitudes using Eq. (5.232) solely. The only necessary ingredients are the spinor identities

$$v = C\bar{u}^{\intercal}, \;\; u = C\bar{v}^{\intercal} \tag{5.233}$$

with the charge conjugation matrix C ($C^\dagger = C^{-1}$, $C^{\intercal} = -C$) as well as

$$C\Gamma C^{-1} = \eta\Gamma \tag{5.234}$$

with

$$\eta = \begin{cases} 1, & \text{if } \Gamma \in \{1, i\gamma_5, \gamma^\mu\gamma_5\} \\ -1, & \text{if } \Gamma \in \{\gamma^\mu, \sigma^{\mu\nu}\} \end{cases}.$$

Note that these transformations apply equally well to Majorana as well as to Dirac spinors. The concrete calculation of the corresponding squared amplitudes are performed half-automatically using Feyncalc [214] to simplify the Dirac algebra and the kinematics. The resulting expressions are finally implemented into the `Fortran` code `ChiChi2qq`.
Within `ChiChi2qq`, we further rely on the dipole-subtraction method of Sec. 5.2.4 to render the integral over the phase space of the radiated gluon numerically evaluable. The resulting $2 \to 3$ cross section σ_{R} is than added to the virtual cross section σ_{Virt} as defined in Eq. (5.200) in order to cancel the soft and (quasi)collinear divergences as explained in Ch. 5.2. We finally verify that

$$\int_3 [d\sigma_{\mathrm{R}}|_{\epsilon=0} - d\sigma_{\mathrm{A}}|_{\epsilon=0}] \tag{5.235}$$

as well as

$$\int_2 \left[d\sigma_{\mathrm{Virt}} + \int_1 d\sigma_{\mathrm{A}}\right]\Big|_{\epsilon=0} \tag{5.236}$$

are indeed soft as well as collinear finite. This turns out to be a nice cross check as it connects both the $2 \to 3$ matrix element as well as the virtual corrections in the singular regions of the phase space to the Born-level matrix element times the corresponding dipoles following Eq. (5.215) and Eq. (5.225).

[20] Note that this subtlety of course also arises in the tree-level calculation and in the calculation of the virtual corrections.

5.2.6. QQ2xx: The Real Corrections

In this section, we outline the calculation of the real corrections associated with the processes of Eqs. (4.8) to (4.11) and describe how to handle the singularities connected to Sec. 5.2.

The real corrections diagrams that arise in the context of squark (co)annihilation into electroweak final states are depicted in Fig. 5.30. They are obtained by attaching a single final-state gluon to every colored particle in the diagrams of Fig. 4.5. Moreover, since there exist quartic couplings of two squarks together with an electroweak vector boson and an additional gluon, one can also attach the additional gluon to a squark-squark-vector boson vertex as exemplified in the last diagram of Fig. 5.30.

The differential cross section of the real corrections $\mathrm{d}\sigma_{\mathrm{R}}$ is then proportional to the polarization- (λ), spin- and color-summed (over final states)/averaged (over initial states) squared matrix element

$$\begin{aligned}\overline{|\mathcal{M}^{\mathrm{R}}|^2} =& \frac{1}{N_c}\sum_{i,j} t^a_{ij} t^a_{ji} \sum_{\lambda} (\epsilon^a_\lambda)^*_\mu (\epsilon^a_\lambda)_\nu \left[\mathcal{M}^{\mathrm{R}}_{Q,1} + \mathcal{M}^{\mathrm{R}}_{Q,2} + \mathcal{M}^{\mathrm{R}}_{s} + \mathcal{M}^{\mathrm{R}}_{t} + \mathcal{M}^{\mathrm{R}}_{u}\right]^{\dagger,\mu} \\ & \left[\mathcal{M}^{\mathrm{R}}_{Q,1} + \mathcal{M}^{\mathrm{R}}_{Q,2} + \mathcal{M}^{\mathrm{R}}_{s} + \mathcal{M}^{\mathrm{R}}_{t} + \mathcal{M}^{\mathrm{R}}_{u}\right]^{\nu} \qquad (5.237) \\ =& - C_F \left[\mathcal{M}^{\mathrm{R}}_{Q,1} + \mathcal{M}^{\mathrm{R}}_{Q,2} + \mathcal{M}^{\mathrm{R}}_{s} + \mathcal{M}^{\mathrm{R}}_{t} + \mathcal{M}^{\mathrm{R}}_{u}\right]^{\dagger,\mu} \\ & \left[\mathcal{M}^{\mathrm{R}}_{Q,1} + \mathcal{M}^{\mathrm{R}}_{Q,2} + \mathcal{M}^{\mathrm{R}}_{s} + \mathcal{M}^{\mathrm{R}}_{t} + \mathcal{M}^{\mathrm{R}}_{u}\right]_{\mu}. \qquad (5.238)\end{aligned}$$

Here, we subsume all real radiation diagrams under $\mathcal{M}_{Q,1}$, which already possess a quartic coupling at the Born level, whereas $\mathcal{M}_{Q,2}$ includes all diagrams where the additional gluon is attached to a three particle vertex. Note that the only fermions, which we encounter throughout our calculations of the real corrections are final-state leptons as shown in the last diagram of Fig. 5.30. As squark (co)annihilation into leptons can only proceed through the s-channel at leading order, we do not have to pay attention to relative minus signs between the different squared matrix elements connected to an appropriate contraction of fermion fields, as opposed to the case of gaugino (co)annihilation of Sec. 5.2.5. In Eq. (5.237), we further suppress all Lorentz and spin structures as well as symmetry factors connected to final-state particles that are already present at the Born level (see Eq. (5.134) for greater detail). However, we explicitly write out the Lorentz and color-structure connected to the radiated gluon. In Eq. (5.238), one can completely collapse the color structure into C_F due to the fact that all of the Born-level final-state particles are color singlets. We also make use of the polarization sum Eq. (5.231)

$$\sum_{\lambda} (\epsilon_\lambda)^{\dagger,\mu} \epsilon^\nu_\lambda \to -g^{\mu\nu}. \qquad (5.239)$$

The conventions used and concrete calculations of the different amplitudes as well as of the real radiation cross section σ_{R} follow the lines presented in Sec. 5.2.1. Again, all calculations are performed in the 't Hooft-Feynman gauge in order that we have to keep track of Goldstone bosons. Moreover, we use the replacement Eq. (5.231) for all external (massive as well as massless) vector bosons. Hence, to correct for this wrong summation over polarizations, we also have to take external Faddeev-Popov ghosts as well as Goldstone bosons into account following the discussion of Ref. [178] (App. B) and Ref. [179] (App. C) (see also the discussion of Sec. 2.6.1).

As already discussed in Sec. 5.2.2, Eq. (5.238) is not suitable for a numerical integration as we encounter soft poles during the integration over the gluon phase space connected to the gluon-radiation off an incoming (anti)squark. However, we do not encounter any

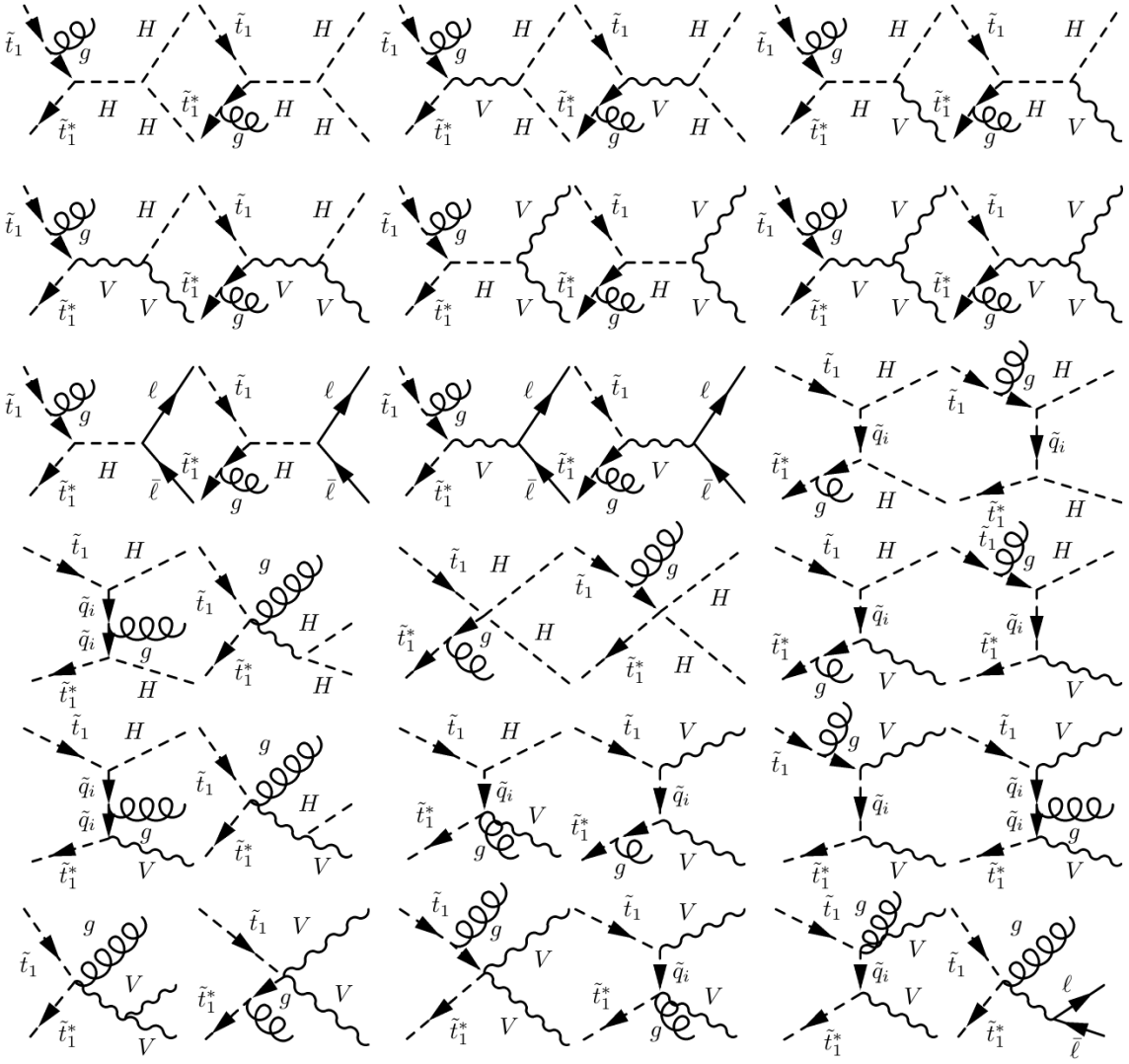

Figure 5.30.: Diagrams depicting the real gluon emission corrections of $\mathcal{O}(\alpha_s)$ to the stop-annihilation processes shown in Fig. 4.5. Again, $V = \gamma, Z^0, W^\pm$ and $H = h^0, H^0, A^0, H^\pm$. The corrections to the u-channel processes are not explicitly shown, as they can be obtained by crossing from the corresponding t-channel diagrams.

(quasi)collinear divergences as the only colored particles at the Born-level are massive squarks with masses typically of the order $m_{\tilde{q}} \sim \sqrt{s}$. We cure the problem of soft singularities via the phase-space slicing method outlined in Sec. 5.2.3. One can perform several cross checks, which foot on the intimate intertwining between the soft singularities of the real and virtual corrections as stated by the BN-theorem and as discussed in Sec. 5.2.2. Since the soft-gluon contributions, which match the poles in the real as well as in the virtual part, once on the integrand level ($\to \mathrm{d}\sigma_{\mathrm{R}}$) and once after integration over the gluon phase space ($\to \mathrm{d}\sigma_{\mathrm{Virt}}$), are connected to the $2 \to 2$ tree-level cross section (see Eq. (5.185)), this, moreover, allows to include the Born-level amplitudes into this cross check. Now, since $\sigma_{\mathrm{soft}}(\Delta E, D)$ as defined in Eq. (5.188) features the same soft singularities as σ_{R}, the BN-theorem $\sigma_{\mathrm{NLO}}^{\text{infr. safe}}$ guarantees the cancellation of all soft singularities in the sum

$$\sigma_{\mathrm{NLO}}^{\text{infr. safe}} = \left(\sigma_{\mathrm{Virt}} + \sigma_{\mathrm{soft}}(\Delta E, D)\right)|_{D\to 4} \tag{5.240}$$

in the limit of a removed regulator. Hence, a first check is the validation of the actual cancellation of all soft poles between the virtual part and the integrated soft gluon part in the sum of Eq. (5.240). Furthermore, it follows from the discussion below Eq. (5.188) together with the correspondence of virtual and real corrections as given in Fig. 5.26 that the result Eq. (5.188) even allows for a *diagram wise* validation of Eq. (5.240). This entanglement is not conducted easily within the Dipole-subtraction method. We verified that, within our implementation, the cancellation of soft poles works out as expected.
In addition, the final sum of the soft-gluon approximation and the regular part of the $2 \to 3$ integration has to be independent of the unphysical cutoff parameter ΔE. This is a second cross check, which turns out to be particularly nice as it relates the $2 \to 2$ tree-level cross section to the $2 \to 3$ cross section of the real radiation via Eq. (5.185). An example

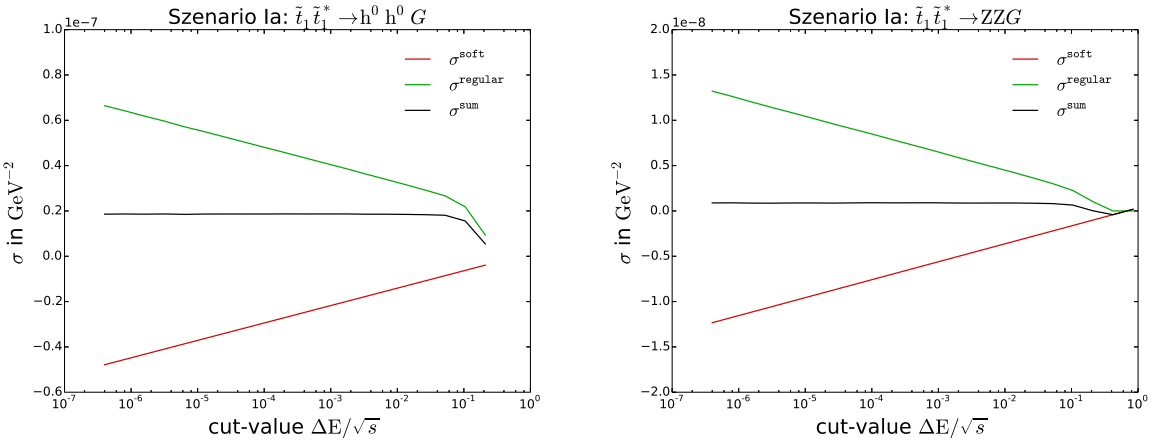

Figure 5.31.: Cutoff dependence of sliced $2 \to 3$ cross section at $p_{\mathrm{cm}} = 100$ GeV. The left plot shows the different contributions of the regular and soft-divergent part as well as the total sum in dependence of the cutoff $\Delta E/\sqrt{s}$ for stop-annihilation into $\mathrm{h}^0\mathrm{h}^0 G$ final states and the right plot shows the same but for the ZZG-final state.

of what this cutoff independence can numerically look like is given in Fig. 5.31 for the two processes $\tilde{t}_1\tilde{t}_1^* \to \mathrm{h}^0\mathrm{h}^0 G$ and $\tilde{t}_1\tilde{t}_1^* \to \mathrm{ZZ}G$ of scenario Ia as introduced in Ch. (4.3.3). The regular part of the $2 \to 3$ total cross section (green) as well as the soft-photon approximation (red) and the sum of both (black) are plotted against $\Delta E/\sqrt{s}$. It is apparent that the total sum is basically cutoff independent for the cutoff region shown here. However, this

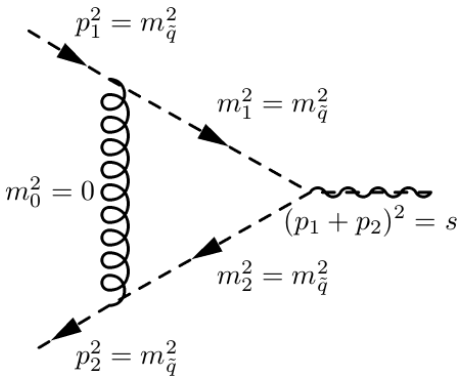

Figure 5.32.: Gluon corrections, e.g., to the s-channel annihilation of a $\tilde{t}_1\tilde{t}_1^*$-pair.

independence breaks down if one goes to much lower or to much larger values of $\Delta E/\sqrt{s}$. In the former case, this breakdown can be traced back to the original numerical instability, which gets reintroduced if a too low ΔE is taken. In the latter case, the cutoff dependence signifies that the soft gluon approximation is used up to inappropriately high values of ΔE. Hence, from this perspective, it turns out that a "good" choice of the cutoff scale is mandatory to obtain reliable results for the full $2 \to 3$ cross section. For what follows, we choose a cutoff value of $\Delta E/\sqrt{s} = 5 \cdot 10^{-6}$, which falls into the cutoff independent regime for the processes under consideration.
As a final cross check we can numerically compare the $2 \to 3$-cross sections with `CalcHEP` for specific processes. As `CalcHEP` provides analytic expressions for squared $2 \to 3$ amplitudes, we are able to compare our results for certain channels by copying the corresponding analytic squared amplitudes from `CalcHEP` into our code (translating the `CalcHEP` convention into ours) and to evaluate both numerically. Comparing the `CalcHEP` amplitudes with our implementation, we find a numerical agreement at the cross section level (σ_{R}) of better than 0.1 % for the processes under consideration.

5.3. Coulomb Corrections

In the previous sections, we have discussed the different methods and techniques that arise in the context of NLO calculations. However, the trust in the accuracy of NLO corrections relies on the concept of perturbativity and its applicability to the particular calculation. It is well known that an expansion in terms of some small parameter $P < 1$ (in the present case this is the strong coupling α_{s}), does not necessarily yield a (quickly) convergent series but can feature large higher-order corrections. One example of such non-perturbative corrections are the so-called *Coulomb* or *Sommerfeld corrections* firstly discussed in Ref. [215].
During the calculation of the $\mathcal{O}(\alpha_{\mathrm{s}})$ corrections to squark (co)annihilation, we encounter diagrams of the form depicted in Fig. 5.32, where a gluon is exchanged between an incoming squark-antisquark pair of equal mass $m_{\tilde{q}}$. It turns out that, following the road outlined in Sec. 5.1.3, the corresponding mathematical expression includes the scalar integral $\mathbf{C_0}(m_{\tilde{q}}^2, s, m_{\tilde{q}}^2, 0, m_{\tilde{q}}^2, m_{\tilde{q}}^2)$ as introduced in Eq. (5.29). $\mathbf{C_0}(m_{\tilde{q}}^2, s, m_{\tilde{q}}^2, 0, m_{\tilde{q}}^2, m_{\tilde{q}}^2)$ with this particular argument set can be written as

$$\mathbf{C_0}(m_{\tilde{q}}^2, s, m_{\tilde{q}}^2, 0, m_{\tilde{q}}^2, m_{\tilde{q}}^2) = \frac{1}{2} F_1 \left(\Delta_{IR} + \ln \frac{s}{\mu^2} \right) + \frac{1}{2} F_2 \tag{5.241}$$

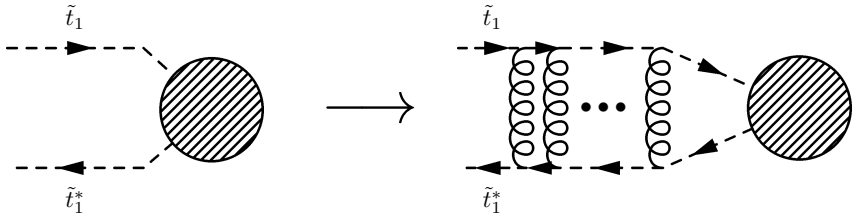

Figure 5.33.: Ladder diagram for a LO Coulomb potential.

with Δ_{IR} as defined in Eq. (5.191) and

$$F_1 := \frac{2}{s\beta_m} \ln\left(\frac{\beta_m - 1}{\beta_m + 1}\right), \tag{5.242}$$

$$F_2 := \frac{2}{s\beta_m}\Big[\ln\left(\frac{\beta_m - 1}{\beta_m + 1}\right) \ln\frac{m_{\tilde{q}}^2 \beta_m^2}{-s} - 2\mathrm{Li}_2\left(\frac{\beta_m - 1}{2\beta_m}\right) + 2\mathrm{Li}_2\left(\frac{\beta_m + 1}{2\beta_m}\right)\Big]. \tag{5.243}$$

The prefactor $\frac{2}{s\beta_m}$ of the above defined F_1 and F_2 with

$$\beta_m = \sqrt{1 - \frac{4m_{\tilde{q}}^2}{s}} \tag{5.244}$$

tends to diverge in the limit $\beta_m = v/2 \to 0$, i.e., when the relative velocity of the incoming squark-antisquark pair v approaches zero ($v \to 0 \Leftrightarrow \frac{4m_{\tilde{q}}^2}{s} \to 1$). Hence, we find that higher-order corrections can feature prefactors $\sim 1/v$, which can lead to a strong enhancement of these presumably small (compared to the LO) contributions[21]. The above enhancement of higher-order corrections can be traced back to the exchange of so-called potential gluons, i.e., gluons with momentum $k \sim \mathcal{O}(p_{\mathrm{cm}})$, between the incoming squarks[22]. As the squarks relevant to the thermal production of DM moved at non-relativistic energies during freeze-out with $E_{\mathrm{kin},\tilde{q}} \approx T_{\mathrm{freeze-out}} \ll m_{\tilde{q}}$ (see Eq. (3.39) as well as the thermal distribution presented in Fig. 5.34 below), the characteristic v is actually expected to be quite small, eventually reaching the regime

$$\alpha_{\mathrm{s}}/v \gtrsim \mathcal{O}(1). \tag{5.245}$$

Since the exchange of n potential gluons comes with a correction factor $(\alpha_{\mathrm{s}}/v)^n$, it turns out that terms of $\mathcal{O}(\alpha_{\mathrm{s}})$ and beyond are not necessarily suppressed but can even be enhanced compared to the leading order. This so-called Coulomb enhancement of higher-order corrections can spoil the perturbativity of Feynman amplitudes expanded in terms of α_s. Hence, it can become mandatory to add up the exchange of gluons to all orders in perturbation theory, leading to the inclusion of so-called ladder diagrams as depicted in Fig. 5.33. This resummation can be implemented within the framework of non-relativistic QCD (NRQCD) [218]. In the following, we consider the case of multiple gluon exchange between a color singlet formed by particles of equal mass. This is the case relevant to this work as the opposite case of unequal masses typically turns out to be largely Boltzmann suppressed in DM calculations (at least for the representative scenarios of Sec.

[21] The divergence at $v \to 0$ is the well-known Coulomb singularity, which signals the production of a squark-antisquark quasi-bound state, a so-called squarkonium.

[22] The exchange of gluons with momentum $k \sim p_{\mathrm{cm}}$ leaves the incoming squarks basically on-shell and, hence, avoids a large suppression of the corresponding amplitude by subsequent (off-shell) squark propagators.

4.3.3). Moreover, we provide the formulas which allow to sum the Coulomb corrections of $\mathcal{O}((\alpha_s/v)^n)$ and $\mathcal{O}(\alpha_s(\alpha_s/v)^n)$ to all orders in perturbation theory, i.e., for arbitrary n, as shown in Fig. 5.33.
The Coulomb corrected result can be grasped in the form

$$\sigma^{\text{Coul}}\big(\tilde{q}\tilde{q}^* \to \text{EW}\big) = \frac{4\pi}{v m_{\tilde{q}}^2} \Im\Big\{ G^{[1]}\big(\mathbf{r}=0; \sqrt{s} + i\Gamma_{\tilde{q}}\big)\Big\} \times \sigma^{\text{LO}}\big(\tilde{q}\tilde{q}^* \to \text{EW}\big). \tag{5.246}$$

Here, $\sigma^{\text{LO}}(\tilde{q}\tilde{q}^* \to \text{EW})$ is the annihilation cross section of the squark-antisquark color singlet into EW final states and $G^{[1]}\big(\mathbf{r}; \sqrt{s} + i\Gamma_{\tilde{q}}\big) = G^{[1]}\big(\mathbf{r}, \mathbf{r}'=0; \sqrt{s} + i\Gamma_{\tilde{q}}\big)$ stands for the color-singlet Greens function of the Schrödinger equation at $\mathbf{r}' = 0$. The prefactor $4\pi/(v m_{\tilde{q}}^2)$ is chosen in order that $\sigma^{\text{Coul}}\big(\tilde{q}\tilde{q}^* \to \text{EW}\big) \to \sigma^{\text{LO}}\big(\tilde{q}\tilde{q}^* \to \text{EW}\big)$ in the limit $\alpha_s \to 0$. Derivations of Eq. (5.246) can be found in the Refs. [219, 228, 229]. However, the final result is spin independent and can therefore be applied in equal ways to the case of quarks and squark. We also provide a concise overview of the derivation of Eq. (5.246) in App. C.
Eq. (5.246) governs the dynamics of the would-be squarkonium evaluated at distance $\mathbf{r}$. More precisely, $G^{[1]}\big(\mathbf{r}; \sqrt{s} + i\Gamma_{\tilde{q}}\big)$ is the solution to

$$\Big[H^{[1]} - \big(\sqrt{s} + i\Gamma_{\tilde{q}}\big)\Big] G^{[1]}\big(\mathbf{r}; \sqrt{s} + i\Gamma_{\tilde{q}}\big) = \delta^{(3)}(\mathbf{r}), \tag{5.247}$$

where $H^{[1]}$ is the Hamilton operator of the squark-antisquark system

$$H^{[1]} = -\frac{1}{m_{\tilde{q}}}\Delta + 2m_{\tilde{q}} + V^{[1]}(\mathbf{r}). \tag{5.248}$$

The Coulomb potential $V^{[1]}(\mathbf{r})$ can be written at NLO as [220, 221]

$$\tilde{V}^{[1]}(\vec{q}) = -\frac{4\pi\alpha_s(\mu_G) C^{[1]}}{\vec{q}^2} \times \left[1 + \frac{\alpha_s(\mu_G)}{4\pi}\left(\beta_0 \ln\frac{\mu_G^2}{\vec{q}^2} + a\right)\right] \tag{5.249}$$

with

$$\begin{aligned} C^{[1]} =& C_F = \frac{4}{3}, \;\; C_A = 3, \\ a =& \frac{31}{9} C_A - \frac{20}{9} T_f n_f, \\ \beta_0 =& \frac{11}{3} C_A - \frac{4}{3} T_f n_f \end{aligned} \tag{5.250}$$

and $T_f = \pm\frac{1}{2}$ is the third component of the weak isospin. The zero-distance NLO Greens function is known in compact analytic form. It takes the form

$$G^{[1]}(0; \sqrt{s} + i\Gamma_{\tilde{q}}) = \frac{C^{[1]}\alpha_s(\mu_G) m_{\tilde{q}}^2}{4\pi} \times \Big[g_{\text{LO}} + \frac{\alpha_s(\mu_G)}{4\pi} g_{\text{NLO}} + \dots\Big], \tag{5.251}$$

where its UV-divergence at $\mathbf{r} = 0$ is removed via $\overline{\text{MS}}$-subtraction [222]. We work with $n_f = 5$ massless quark flavors since the typical energy scale of the potential gluon, here $\mathcal{O}(p_{\text{cm}}) \approx \mathcal{O}(100 \;\; \text{GeV})$ (see Fig. 5.34), is still too low to neglect the top quark mass m_t [223]. Hence, we ignore all top-quark effects in the potential Eq. (5.249)[23]. However,

[23] As we expect the SUSY particles to be rather heavy, we, hence, also neglect all gluino and squark corrections in the potential.

following Ref. [224] we include additional top quark effects into the strong coupling α_s, which we renormalize in the $\overline{\text{MS}}$-scheme. Additional definitions used in Eq. (5.251) are

$$\begin{aligned} g_{\text{LO}} &= -\frac{1}{2\kappa} + L - \psi^{(0)}, \\ g_{\text{NLO}} &= \beta_0 \Big[L^2 - 2L(\psi^{(0)} - \kappa\psi^{(1)}) + \kappa\psi^{(2)} + (\psi^{(0)})^2 - 3\psi^{(1)} - 2\kappa\psi^{(0)}\psi^{(1)} \\ &\quad + 4\ {}_4F_3(1,1,1,1;2,2,1-\kappa;1) \Big] + a\Big[L - \psi^{(0)} + \kappa\psi^{(1)} \Big] \end{aligned} \tag{5.252}$$

and

$$\kappa = \frac{iC^{[1]}\alpha_s(\mu_G)}{2v}, \tag{5.253}$$

$$v = \sqrt{\frac{\sqrt{s} + i\Gamma_{\tilde{q}} - 2m_{\tilde{q}}}{m_{\tilde{q}}}}, \tag{5.254}$$

$$L = \ln \frac{i\mu_G}{2m_{\tilde{q}}v}. \tag{5.255}$$

Here, $\psi^{(n)} = \psi^{(n)}(1-\kappa)$ is the n-th derivative of $\psi(z) = \gamma_E + \mathrm{d}/\mathrm{d}z \ln\Gamma(z)$ and ${}_4F_3(1,1,1,1;2,2,1-\kappa;1)]$ is a hypergeometric function. The latter is discussed in greater detail in App. D. Considering μ_G for the NLO Greens function Eq. (5.246), it turns out that μ_G can be chosen independently from the renormalization scale μ introduced in Ch. 5. Since the Coulomb corrections are related to the exchange of potential gluons with momentum $|\mathbf{p}| \approx m_{\tilde{q}}v$, taking μ_G of the order

$$\mu_G \ \sim \ m_{\tilde{q}}v \tag{5.256}$$

is expected to be a natural choice. On the other hand, α_s taken at a very low scale μ_G may reach the non-perturbative regime

$$\alpha_s(\mu_G) \gtrsim 1 \tag{5.257}$$

as it approaches its Landau pole in the integration over the thermal distribution Eq. (3.39). Hence, we define μ_G to be [225]

$$\mu_G \ = \ \max\{C^{[1]}m_{\tilde{q}}\alpha_s(\mu_G), 2m_{\tilde{q}}v\}, \tag{5.258}$$

where $\mu_G = C^{[1]}m_{\tilde{q}}\alpha_s(\mu_G)$ corresponds to twice the inverse Bohr radius (see Eq. (5.253)). In Ref. [226], it has been shown for the color singlet top-antitop pair production near threshold that with μ_G set to this characteristic (s)quarkonium-energy scale, the Greens function possesses a well convergent perturbative series, whereas for lower values logarithms of the scale μ_G can blow up and again spoil perturbativity. The masses of the incoming squarks do actually not depend on μ_G, since we use the associated on shell masses (at least for the case relevant here, i.e., for $\tilde{q} = \tilde{t}_1$) as specified in Sec. 5.1.6. One could use another scale in Eq. (5.258), for example the typical SUSY-QCD-choice $\mu_G \sim m_{\tilde{q}}$. It would then become advantageous to resum terms of the order $\mathcal{O}(\alpha_s \log^n v)$ in the same way as the $\mathcal{O}((\alpha_s/v)^n)$ and $\mathcal{O}(\alpha_s(\alpha_s/v)^n)$ contributions. Methods that account for the resummation of these potentially large logarithms have been developed within velocity non-relativistic QCD (vNRQCD). These can be found, e.g., in Ref. [216].
Since we add the Coulomb corrections to our full NLO calculation, we have to avoid a double counting of contributions that are partly included in the Greens function as well

as in our full NLO result (see, e.g., the first diagram of Fig. 5.18). We therefore subtract the $\mathcal{O}(\alpha_s)$ corrections from the Greens function Eq. (5.251)

$$\Im\Big\{G^{[1]}\big(0;\sqrt{s}+i\Gamma_{\tilde{q}}\big)\Big\} = m_{\tilde{q}}^2\Im\Big\{\frac{v}{4\pi}\Big[i+\frac{\alpha_s(\mu_G)C^{[1]}}{v}\Big(\frac{i\pi}{2}+\ln\frac{\mu_G}{2m_{\tilde{q}}v}\Big)+\mathcal{O}(\alpha_s^2)\Big]\Big\}, \quad (5.259)$$

which is obtained by expanding Eq. (5.251) up to $\mathcal{O}(\alpha_s^2)$.
There are still additional subtleties arising in the context of the Coulomb corrections, which we want to address shortly in the following. Since Eq. (5.252) is only an expansion around the leading-order bound-state poles, it induces poles in the Greens function of the general form $\big[\alpha_s E_n^{\rm LO}/(E_n^{\rm LO}-\sqrt{s}-i\Gamma_{\tilde{q}})\big]^k$ (k=1,2 at NLO). These differ from an exact treatment by an $\mathcal{O}(\alpha_s^2)$ correction [220, 227]. However, this difference becomes relevant near the associated bound-state poles only, whose production is suppressed by the non-zero temperature during freeze-out[24]. Hence, there is no need for a more elaborated treatment for a precise calculation of $\Omega_{\tilde{\chi}^0}h^2$.
Furthermore, for the above calculations we have implicitly assumed that the amplitudes that enter $\sigma^{\rm LO}$ in Eq. (5.246) do not depend on the momenta of the Coulomb enhanced particles (see also App. C). In the case of dominant s-wave annihilation in the non-relativistic limit, this turns out to be an approximation well justified, but can become misleading for cross sections dominated by higher partial waves. However, these are typically suppressed by orders of v compared to the leading s-wave contribution. Since the contributions to the relic density are typically s-wave dominated (see below for a more detailed discussion), these corrections turn out to be negligible for the aimed level of precision. To be more precise, as we provide a full NLO calculation, the error turns out to be of the order $\mathcal{O}(\alpha_s^2)$ for $\alpha_s \ll v$ and remains of this order relative to the leading $\mathcal{O}((\alpha_s/v)^n)$ Coulomb corrections even in the limit $\alpha_s \gtrsim v$. Therefore, we choose to rely on this simplified treatment. However, the Coulomb factors for arbitrary partial waves for a leading order Coulomb potential can be found the Refs. [228, 229].
In Fig. 5.34, we present cross sections multiplied by the relative velocity for squark annihilation into h^0H^0 and W^+W^- final states. These include the Coulomb corrections to the corresponding tree-level cross sections for two processes of scenario II of Sec. 4.3.3. Note that, though we chose scenario II to present our results, the basic qualitative behavior of the Coulomb corrections is actually scenario independent. We further show the thermal average of Eq. (3.39) in arbitrary units in the two plots, which indicates the thermal weighting of the σv contribution to $\Omega_{\tilde{\chi}^0}h^2$. It is apparent that for both cases the Coulomb corrected σv (green line) steeply rises at low $p_{\rm cm}$ due to the attractive force felt by the squark-antisquark pair (see Eq. (5.249)), while the s-wave dominated tree-level contribution (orange line) is roughly constant as expected[25]. Going to higher $p_{\rm cm}$ values, the $1/v$-enhancement becomes more and more subdominant and the Coulomb corrections turn into a usual perturbative series in α_s. However, we encounter a sizeable splitting between the orange and the green line in the vicinity of the peak of the thermal distribution. Hence, Fig. 5.34 elucidates the relevance of these corrections for a precise estimation of $\Omega_{\tilde{\chi}^0}h^2$.
Moreover, with μ_G set to the renormalization scale $\mu_G = \mu$ and with α_s renormalized according to Sec. 5.1.5, the Coulomb corrections of the order $\mathcal{O}(\alpha_s)$ of Eq. (5.259) should

[24] See also the vanishing weighting factor of the thermal distribution for $v \approx 0$ ($m_{\tilde{q}}v \ll T_{\rm freeze-out}$), e.g., in Fig. 5.34.

[25] σv can be expanded according to $\sigma\ v = a + bv^2 + \mathcal{O}(v^4)$ with a and b being velocity independent. a includes all s-wave contributions at $\mathcal{O}(v^0)$, whereas b includes the leading p-wave contributions, which set in at $\mathcal{O}(v^2)$, as well as the $\mathcal{O}(v^2)$ s-wave contributions.

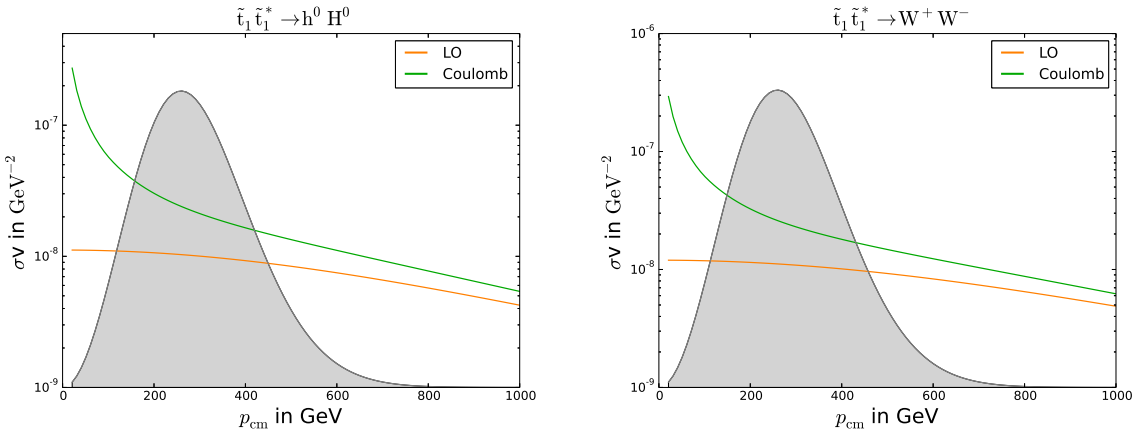

Figure 5.34.: The leading-order (orange line) and the Coulomb-corrected cross section (green line) multiplied with the relative velocity v in dependence of the center-of-mass momentum p_{cm} for two selected channels of scenario II. The gray areas indicate the thermal distribution (in arbitrary units).

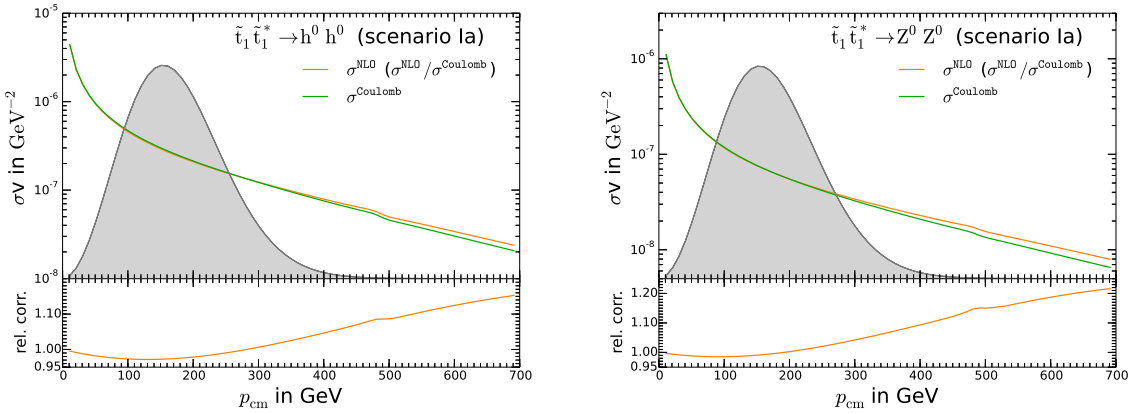

Figure 5.35.: The NLO contributions of the Coulomb enhanced diagrams (orange line) and the Coulomb corrections off $\mathcal{O}(\alpha_s)$ (green line) multiplied by the relative velocity v in dependence of the center-of-mass momentum p_{cm} for two selected channels of scenario Ia. The gray areas indicate the thermal distribution (in arbitrary units). The lower parts of the plots show the corresponding ratios of cross sections (second item in the legends).

actually match the Coulomb enhanced diagrams of the full NLO calculation within the threshold region. This is explicitly checked in Fig. 5.35, where we present the relative deviation between the sum of $\mathcal{O}(\alpha_s)$ contributions of all Coulomb enhanced diagrams (σ^{NLO}) and the $\mathcal{O}(\alpha_s)$ corrections of Eq. (5.259) (σ^{Coulomb}). As expected, we encounter a deviation between these two cross sections of less than 1% at low p_{cm}, whereas toward larger p_{cm} values, the non-Coulomb enhanced terms in the NLO result start to contribute and, hence, increase the difference between σ^{NLO} and σ^{Coulomb} .

5.4. Further Subtleties in the Context of QQ2xx

This section summarizes subtleties, which we encounter in the context of squark (co)annihilation. Since some of the $2 \to 2$ amplitudes that contribute to the final neutralino relic density $\Omega_{\tilde{\chi}_1^0} h^2$ contain a gluon and an unstable electroweak particle X (e.g., a Higgs or a Z-boson) in their final state, we partly double count contributions if we simply add the $2 \to 3$ processes (see the diagrams of the first line of Fig. 5.30) to the Born level cross section. This is because in the case of an on-shell Higgs or vector boson propagator in a $2 \to 3$-process, the $2 \to 3$ amplitude corresponds to the $2 \to 2$-on-shell production of a gluon and a heavy boson X followed by its decay (exemplified in Fig. 5.36). But since the on-shell production is already included within the $2 \to 2$ contributions, this would hence result in the aforementioned double counting. To avoid this double counting, we subtract

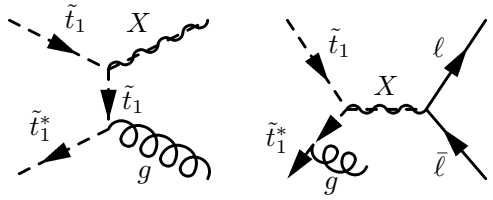

Figure 5.36.: Example for a potential double-counting between $2 \to 2$ and $2 \to 3$ amplitudes for a $\ell\bar{\ell}$ final state.

the $2 \to 2$ matrix element but weighted by the fraction of the EW decay width $\Gamma_{\text{X}\to\text{EW}}$ divided by the total decay width $\Gamma_{\text{X}\to\text{tot}}$ from the $2 \to 2$ matrix element

$$\left|M_{\tilde{t}_1\tilde{t}_1^*\to Xg}\right|^2 \to \left(1 - \frac{\Gamma_{X\to\text{EW}}}{\Gamma_{X\to\text{tot}}}\right) \times \left|M_{\tilde{t}_1\tilde{t}_1^*\to Xg}\right|^2, \tag{5.260}$$

both for a two particle final state. Within our implementation it is, however, possible that in some rare cases a gluon-X final state is corrected as in Eq. (5.260) without taking into account the corresponding $2 \to 3$ amplitude. But as we correct all processes that contribute to $\Omega_{\tilde{\chi}_1^0} h^2$ by more than 1%, we expect this to be a minor error with respect to the aimed level of precision.

Beside the real radiation of soft gluons, we also encounter the radiation of soft photon radiation in the $2 \to 3$ processes that subsume under the EW final states described in Eqs. (4.8) and (4.9), while we integrate over the 3-particle phase space. As for the gluon, the soft photon radiation introduces soft poles to the $2 \to 3$-matrix cross section, which would cancel if one takes into account the corresponding virtual corrections. This would require the inclusion of the corresponding EW corrections into σ_{virt}, which is beyond the scope of this work. Hence, we regulate these divergences with the help of a lower bound on the

photon energy similar to ΔE introduced in Sec. 5.2.3. We check explicitly that this bound does not much alter the final relic density but prevents the phase-space integrations from becoming numerically unstable. This is even more the case as the $2 \to 3$ corrections turn out to be only a small contribution to $\Omega_{\tilde{\chi}_1^0} h^2$ for most of the relevant channels (see Sec. 7.1 below) and channels with photon final states turn out to be even less important (Sec. 4.3.3).

We finally introduce electron and muon masses, $m_e = 5.1 \cdot 10^{-4}$ GeV and $m_\mu = 0.106$ GeV, to keep the photon propagator in the last diagram of Fig. 5.30 away from its mass shell.

To obtain consistent cross checks, all these changes, including the associated lepton-Higgs couplings, are implemented in `CalcHEP` and are used by `micrOMEGAs` in our analysis[26]. Furthermore, as already mentioned in the context of gaugino (co)annihilation, we include a lower bound on the squark widths to stabilize the phase space integration in the vicinity of squark-propagator poles. We choose this bound to be 0.01 GeV. If the value of a particular squark width, by default taken from `micrOMEGAs`, drops below this bound, we set its value to 0.01 GeV and keep the `micrOMEGAs` value, otherwise.

[26] Yukawa couplings proportional to such small masses of course only lead to minor corrections.

6. Gaugino (Co)Annihilation: The Results

Provided all of the components necessary to calculate the virtual and real corrections, we now come to the discussion of the impact of the higher-order corrections included in `ChiChi2qq` on the processes presented in Sec. 4.2 basing on Ref. [1]. A discussion on the cross section level serves as the starting point, followed by an investigation of the impact of the SUSY-QCD corrections on the neutralino relic density $\Omega_{\tilde{\chi}_1^0}$.

6.1. Impact on the Cross Sections

In this section, we discuss the numerical impact of the full $\mathcal{O}(\alpha_s)$-corrections of the Secs. 5.1.8 and 5.2.5 on the different gaugino (co)annihilation cross sections of Eqs. (4.1)-(4.3). Therefore, we go trough the different scenarios presented in Sec. 4.2 and investigate the impact of our higher-order corrections for the channels of Tab. 4.3 in greater detail.
Fig. 6.1 shows two of the most relevant (co)annihilation channels plotted against the CMS-momentum p_{cm} for each of the scenarios of Tab. 4.1. It contains the cross sections at tree level (black dashed line) and at full one-loop (blue solid line) as well as the `micrOMEGAs` result, including the changes reported in Sec. 4.2 (orange solid line). The lower part of each plot shows different ratios between `micrOMEGAs` and our tree-level $\sigma^{\text{MO}}/\sigma^{\text{tree}}$ (black dashed line), between our full correction and `micrOMEGAs` $\sigma^{\text{NLO}}/\sigma^{\text{MO}}$(orange solid line) and between our full result and our tree level $\sigma^{\text{NLO}}/\sigma^{\text{tree}}$ (blue solid line).
The plot in the upper left of Fig. 6.1 presents the cross section for the process $\tilde{\chi}_1^0\tilde{\chi}_1^+ \to t\bar{b}$ of scenario I. One encounters a broad peak around $p_{\text{cm}} \approx 200$ GeV due to a resonance in the s-channel exchange of the H^+ boson, as already discussed in Sec. 4.2. Our tree level deviates from the `micrOMEGAs` result by $\sim 20\%$, whereas our full $\mathcal{O}(\alpha_s)$ corrections decrease this discrepancy relative to `micrOMEGAs` to at most $\sim 10\%$. The former deviation can be traced back to a different treatment of third generation quark masses in `micrOMEGAs` compared to our code, as discussed in Sec. 5.1.5. These enter the important Yukawa couplings as well as $2 \to 2$ kinematics, which results in the observed shift between σ^{tree} and σ^{MO}.
The second plot in the upper row shows the cross section of the process $\tilde{\chi}_1^0\tilde{\chi}_2^0 \to b\bar{b}$ of scenario I. Again, we encounter a broad resonance at $p_{\text{cm}} \approx 200$ GeV. This resonance can be ascribed to the s-channel exchange of the pseudoscalar Higgs A^0, which weights nearly as much as the charged Higgs $m_{A^0} \approx m_{H^\pm}$, whereas the coannihilating particle $\tilde{\chi}_2^0$ fulfills $m_{\tilde{\chi}_2^0} \approx m_{\tilde{\chi}_1^0}$ ($\approx m_{\tilde{\chi}_1^\pm}$) necessary to evade a large Boltzmann suppression. The deviation between `micrOMEGAs` and the tree level reaches here even more than 30%, which is now decreased to roughly 10% by our full NLO result, while the full $\mathcal{O}(\alpha_s)$ corrections yield a shift of roughly 15% relative to our tree level.
Keeping in mind that according to Tab. 4.3, these two processes already contribute to the full annihilation cross section of scenario I by 66%, it already becomes clear at this early stage that the NLO corrections investigated in this work can overcome the current experimental error as stated by the Planck experiment.
In the third and fourth plot of the second row of Fig. 6.1, we present the processes $\tilde{\chi}_1^0\tilde{\chi}_1^+ \to t\bar{b}$ and $\tilde{\chi}_1^0\tilde{\chi}_2^0 \to t\bar{t}$ of scenario II. These two channels already account for 52%

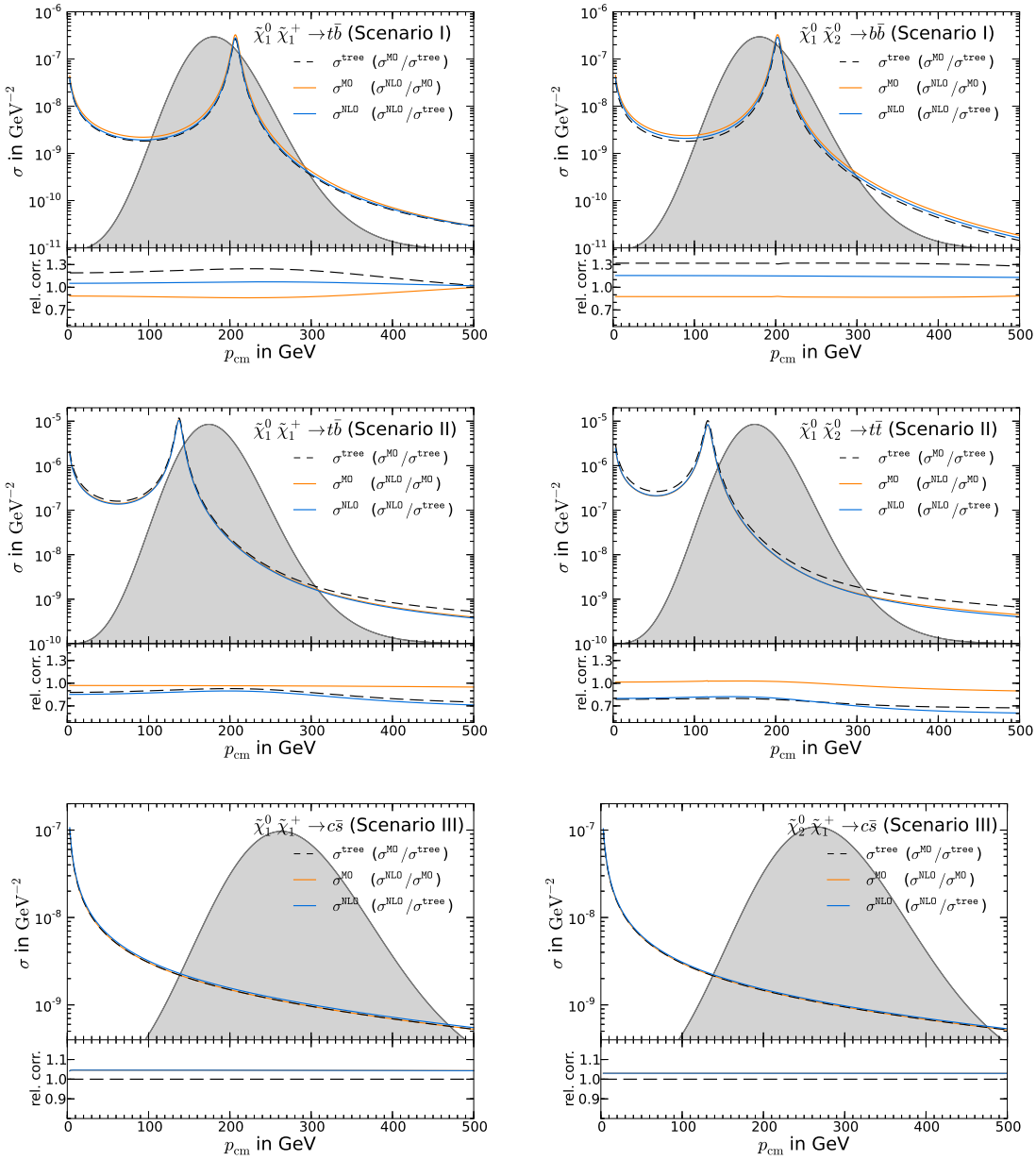

Figure 6.1.: Tree-level (black dashed line), full one-loop (blue solid line) and `micrOMEGAs` (orange solid line) cross sections for selected channels of the scenarios of Tab. 4.1. The upper part of each plot shows the absolute value of σ in GeV^{-2} in dependence of the momentum in the center-of-mass frame p_{cm}. The gray areas indicate the thermal distribution (in arbitrary units). The lower part of each plot shows the corresponding ratios of the cross sections (second item in the legends). Figure taken from [1].

of the full $\langle\sigma_{\text{eff}}\rangle$. Again, both plots feature broad resonances at $p_{\text{cm}} = 120$ GeV and $p_{\text{cm}} = 140$ due to s-channel exchanges of the H^+ and the H^0 boson. In contrary to the previous plots, these resonances differ in their relative p_{cm} position. This can be traced back to a less degenerated mass spectrum (concerning $m_{\tilde{\chi}_1^+} - m_{\tilde{\chi}_2^0}$, $m_{H^0} - m_{H^\pm}$) as compared to scenario I (see Tab. 4.2), which results in the observed small p_{cm}-shift, necessary to hit the resonances within this slightly changed kinematic situation. Our $\mathcal{O}(\alpha_s)$ corrections account for a shift relative to the original tree-level cross section by 10%-30% for the $\tilde{\chi}_1^0\tilde{\chi}_1^+ \to t\bar{b}$ process and even by 20%-40% for the $\tilde{\chi}_1^0\tilde{\chi}_2^0 \to t\bar{t}$ process. Moreover, we encounter a relatively large difference between our tree level and `micrOMEGAs`, whereas the NLO corrections nearly compensate for this deviation, leading to a maximum discrepancy $\sigma_{\text{NLO}}/\sigma_{\text{MO}}$ of only 5% in the case of $\tilde{\chi}_1^0\tilde{\chi}_1^+ \to t\bar{b}$ and of 10% in the case of the $\tilde{\chi}_1^0\tilde{\chi}_2^0 \to t\bar{t}$ channel. This compensation, also visualized by the overlapping orange and blue bands in the particular upper plot, hints toward a good approximation of the higher-order corrections by the effective heavy quark masses, which enter the kinematics as well as important Yukawa couplings.
The remaining two plots of Fig. 6.1 show the channels $\tilde{\chi}_1^0\tilde{\chi}_1^+ \to c\bar{s}$ and $\tilde{\chi}_2^0\tilde{\chi}_1^+ \to c\bar{s}$ for scenario III, which all together contribute to the thermally averaged annihilation cross section by 13.1%. It is apparent that there is no resonance contributing to the cross sections due to reasons already explained in Sec. 4.2. This results in a monotonous dropping of the cross section with raising p_{cm} as required by unitarity. Moreover, one encounters a good agreement between our tree level and the `micrOMEGAs` result, whose deviation turns out to be nearly negligible as depicted by the black dashed line in the associated lower plots lying constantly close to one. This behavior can be traced back to the particular final states. These are now composed of second generation quarks, which are not affected by our renormalization scheme and, hence, agree with `micrOMEGAs`. The full NLO corrections result in deviations of $\sim 5\%$ for the $\tilde{\chi}_1^0\tilde{\chi}_1^+ \to c\bar{s}$ channel and of only $\sim 3\%$ for the $\tilde{\chi}_2^0\tilde{\chi}_1^+ \to c\bar{s}$ channel, relative to `micrOMEGAs` as well as to our tree level. The corrections in scenario III turn out to be quite small compared to the examples of scenario I and II encountered previously. This is due to the relatively heavy SUSY-mass spectrum of scenario III, as can be seen in Tab. 4.2, which leads to the suppression of the higher-order corrections observed here.
Finally note that within our code the widths are always active, whereas in `micrOMEGAs`/`CalcHEP` these are switched on only within a rather narrow interval around the resonance. In order to compare our results to the `micrOMEGAs` implementation, we modify this treatment in `micrOMEGAs` for the plots shown in Fig. 6.1 such that the widths are taken into account over the full p_{cm}. However, for the following calculation of the relic density, we do not include these modifications within `micrOMEGAs/CalcHEP` as their impact on $\Omega_{\tilde{\chi}_1^0}$ is expected to be negligible.

6.2. Impact on the Relic Density

In this section, we investigate the impact of the $\mathcal{O}(\alpha_s)$ corrections on the final DM relic density $\Omega_{\tilde{\chi}_1^0}$. Therefore, we include the full NLO corrections as discussed in Sec. 5.1.8 into `micrOMEGAs`, following the float chart presented in Fig. 4.1. These corrections cover all possible (co)annihilation channels of two gauginos going into any quark-antiquark combination as presented in Eqs. (4.1) -(4.3), in all 102 different processes, not distinguishing between different charge combinations in the chargino sector. All other processes, such as , e.g., squark (co)annihilation or any (co)annihilation into EW final states are left unchanged, which means that for these cases, we take the original `CalcHEP` result at effective

tree level. However, the relevant channels out of the list of corrected processes (Eqs. (4.1) -(4.3)) are actually unknown beforehand as they strongly depend on the particular pMSSM-11 parameter point as defined in Sec. 2.5. Moreover, since the NLO calculations, especially the integration over the three-particle phase space, turn out to be quite time consuming, we correct only those processes that contribute to the full $\langle\sigma_{\text{eff}}v\rangle$ as provided by `CalcHEP` by more than some predefined lower bound, here by more than 2%. Processes that do not pass this bound are kept at tree level using our result instead of `CalcHEP` for consistency.

In the Figs. 6.2 and 6.3, we show the relic density bands as obtained by using `CalcHEP` (orange), our tree-level (gray) and the one-loop corrected result (blue) within the pMSSM-11 giving the region of parameter space as favored by Planck Eq. (4.5) at the 1σ level. We dissect the scenarios into their contributions of different channels represented by the green background in each of the different plots of Fig. 6.2 and 6.3.

Since the gaugino (co)annihilation strongly depends on the different mass splittings of the involved gauginos, which in turn are explicitly dependent on the soft breaking parameters M_1, M_2 and μ as shown in Sec. 2.6.2, we present the relic density bands obtained in the pMSSM planes spanned by different combinations of these parameters scanning around the scenarios I and II as defined in Tab. 4.1.

Starting with Fig. 6.2, we present a scan over the $M_1 - M_2$ plane surrounding scenario I. Since in this scenario the lightest neutralino $\tilde{\chi}_1^0$ is dominated by large bino and wino contributions $Z_{1\tilde{B}}$ and $Z_{1\tilde{W}}$ (see Tab. 4.2), varying these two parameters is expected to sizeably alter the final relic density. The plot in the upper left shows the total contribution of all processes improved by `DM@NLO` in green. These reach up to 80% in the upper left and drop down to 20% in the upper right corner, where EW final states become dominant. The three relic bands, which correspond to the color code defined above, now cut out the cosmologically favored region within the presented parameter plane. The thinness of the lines already shows how constraining the demand that the lightest neutralino should account for the whole DM, actually is. One observes a distinct separation of the full `CalcHEP` result relative to the tree-level and NLO results obtained by `DM@NLO` over large parts of the given parameter plane. However, our higher-order corrections tend to decrease this separation as already observed and discussed at the cross section level in the previous section. Our tree-level and NLO results tend to lie closely together with a separation of maximally 1σ as given by the colored bands. However, the exact separation varies strongly with the particular parameter point in close correspondence to the total contribution of processes corrected by `DM@NLO`. This leads to a strong overlap of all three bands, e.g., in the upper right and lower left, which are regions with relatively low `DM@NLO` contributions, whereas in the upper left of the plot, where `DM@NLO` contributes to the relevant channels by 80%, the distinction of the bands is much more pronounced.

The five remaining plots of Fig. 6.2 state the contributions of different (co)annihilation channels, whose contribution to $\langle\sigma_{\text{eff}}v\rangle$ is given in percent in green. By far the most dominant contribution to $\langle\sigma_{\text{eff}}v\rangle$ over wide parts of the presented $M_1 - M_2$ plane stems from the $\tilde{\chi}_1^0\tilde{\chi}_1^0 \to b\bar{b}$ channel, which reaches up to 80% in the upper left. However, this contribution is decreased to less than 10% toward the lower left corner, where the `DM@NLO` processes still correct by around 60% of the relevant channels. There, the processes $\tilde{\chi}_1^0\tilde{\chi}_2^0 \to b\bar{b}$ and $\tilde{\chi}_1^+\tilde{\chi}_1^0 \to t\bar{b}$ take over contributing to the total annihilation cross section by up to 24% and 45% in the cosmologically preferred region, respectively. The reason for this enhancement can be found in the s-channel resonances due to the exchanges of one of the Higgs bosons A^0 and $H^\pm$ discussed previously (see Sec. 4.2). These resonances lead to the typical kinks in the relic density bands as common to these so-called Higgs funnel regions. Furthermore,

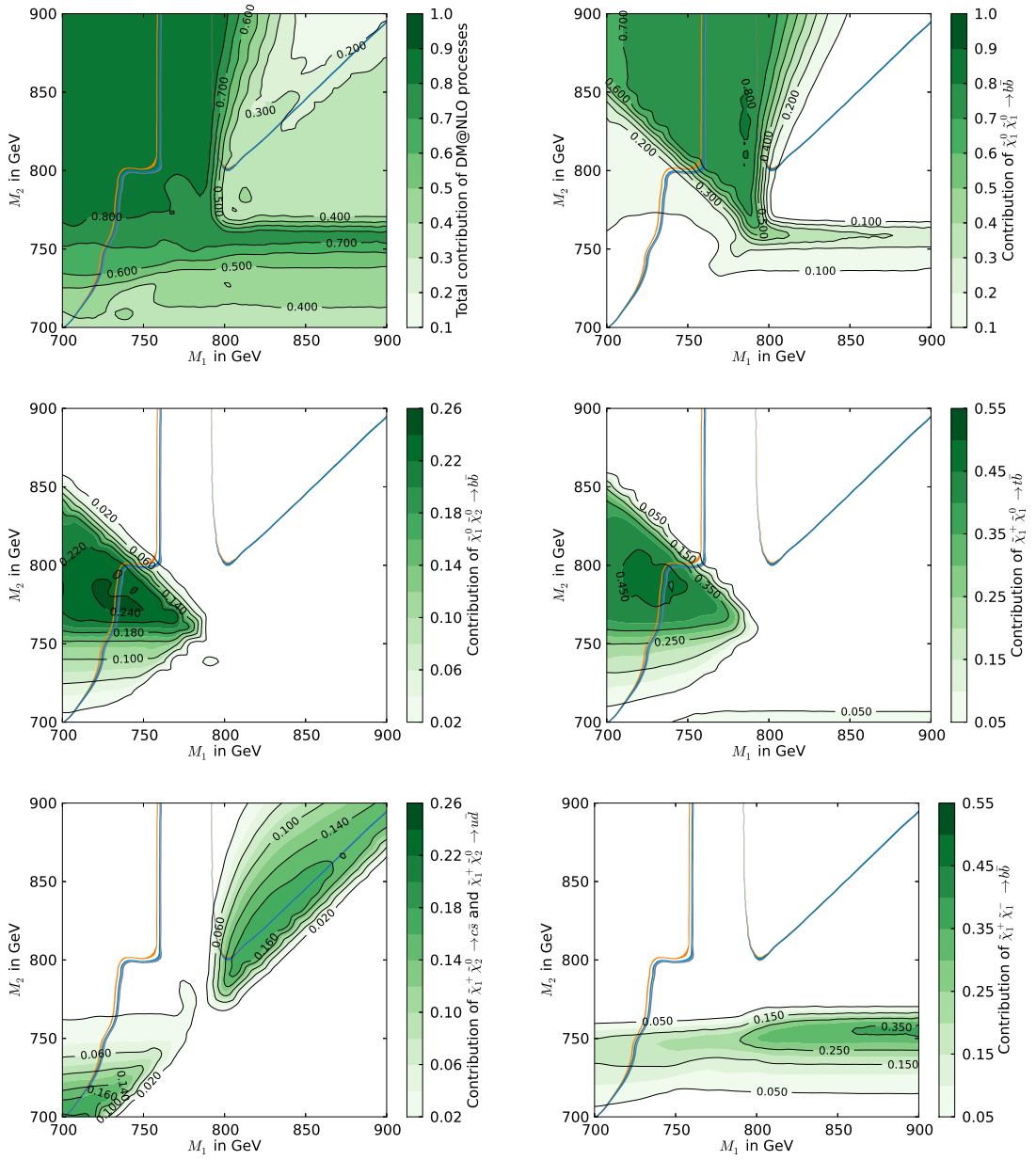

Figure 6.2.: Relative importance of the processes that contribute to the neutralino relic density in the M_1–M_2 plane surrounding scenario I. The three colored lines represent the part of the parameter space that leads to a neutralino relic density compatible with the Planck limits given in Eq. (4.5) using the standard `micrOMEGAs` calculation (orange), our tree-level calculation (gray) and our full one-loop calculation (blue). Figure taken from [1].

the shape of the two contributions turns out to be very similar, which can be traced back to the fact that the particles $\tilde{\chi}_2^0$ and $\tilde{\chi}_1^+$ on the one hand and the Higgs bosons A^0 and $H^\pm$ on the other hand are almost degenerate in mass (see Tab. 4.2 and the discussion in Sec. 4.2). Therefore, coannihilations of $\tilde{\chi}_1^0$ with these two particles become important in the same region of the parameter space.
The plot in the lower left shows the sum of the rather exotic channels $\tilde{\chi}_1^+\tilde{\chi}_2^0 \to c\bar{s}$ and $\tilde{\chi}_1^+\tilde{\chi}_2^0 \to u\bar{d}$. Their individual contributions to the relic density are basically identical, since the main difference, the nonzero mass of the charm quark m_c, is already negligible at the considered energy scale $\sqrt{s} \gtrsim \sqrt{(m_{\tilde{\chi}_1^+})^2 + (m_{\tilde{\chi}_2^0})^2}$. It becomes evident that the sum of these channels with light quarks in the final state accounts for up to 16% in the cosmologically favored region.
We further show the analogous plot for the annihilation channel $\tilde{\chi}_1^+\tilde{\chi}_1^- \to b\bar{b}$ in the lower-right part of Fig. 6.2. This channel constitutes more than 35% outside and roughly 15% inside the cosmologically preferred region. Additional contributions, which are not presented but which contribute by more than the cutoff bound of 2%, are $\tilde{\chi}_1^+\tilde{\chi}_1^0 \to c\bar{s}$, $\tilde{\chi}_1^+\tilde{\chi}_1^0 \to u\bar{d}$, $\tilde{\chi}_1^0\tilde{\chi}_1^0 \to t\bar{t}$ ($\sim 10\%$ each) and $\tilde{\chi}_2^0\tilde{\chi}_2^0 \to b\bar{b}$ ($\sim 5\%$).
Fig. 6.4 contains the corresponding plots for scenario II of Tab. 4.1. Since the lightest neutralino now features beside a large bino component $Z_{1\tilde{B}}$ also sizeable higgsino components $Z_{1\tilde{H}_1}$ and $Z_{1\tilde{H}_2}$ driven by the parameters M_1 and μ (see Sec. 2.6.2), in Fig. 6.3, scans around scenario II in the plane spanned by these two parameters are performed. One encounters a broad overlap between the pure `CalcHEP` result and the $\mathcal{O}(\alpha_s)$-corrected result, signalizing the good approximation of the higher-order corrections by the effective masses and couplings used within `CalcHEP`, as discussed in Sec. 4.2. Moreover, the relic band obtained by our tree level shows a clear spatial deviation from the former two, which indicates a shift of the final relic by more than 1σ due to the higher-order corrections.
The sum of all channels corrected by `DM@NLO` now sums up to more than 90% over large parts of the presented parameter space and drops down to less than 10% in the upper right corner, where (co)annihilation processes with (of) the lighter stop $\tilde{t}_1$, as discussed in the Refs. [2, 147, 148], become relevant. In this case, the largest contributions are due to the channels $\tilde{\chi}_1^0\tilde{\chi}_1^0 \to t\bar{t}$ and $\tilde{\chi}_1^0\tilde{\chi}_1^0 \to b\bar{b}$, whose contribution to $\langle\sigma_{\text{eff}}v\rangle$ reach up to $\sim 60\%$ and $\sim 35\%$ across the scanned $M_1 - \mu$ plane. However, there is yet another region in the center left, similar to scenario I, where the contributions of these channels drop below 20% and 10%, respectively, while the total contribution still remains above 90%. There, the most relevant channels turn out to be $\tilde{\chi}_+^0\tilde{\chi}_1^0 \to t\bar{b}$ ($\sim 45\%$), $\tilde{\chi}_1^0\tilde{\chi}_2^0 \to t\bar{t}$ ($\sim 13\%$), $\tilde{\chi}_1^0\tilde{\chi}_2^0 \to b\bar{b}$ ($\sim 7\%$), $\tilde{\chi}_1^0\tilde{\chi}_3^0 \to t\bar{t}$ ($\sim 9\%$) and $\tilde{\chi}_1^0\tilde{\chi}_3^0 \to b\bar{b}$ ($\sim 5\%$), which are enhanced by the s-channel exchange of the A^0 and $H^\pm$ yielding the characteristic Higgs-funnel kink. It is further apparent that in contrast to scenario I, $t\bar{t}$ final states are dominant in scenario II due to reasons discussed in Sec. 4.2. We even encounter contributions from coannihilation with the third neutralino $\tilde{\chi}_3^0$, which is remarkable, because a quite compressed mass spectrum in the neutralino sector is necessary to avoid a potentially large Boltzmann suppression.
Summarizing the observed contributions to the different gaugino (co)annihilation channels Eqs. (4.1) – (4.3) in the scanned planes around our scenarios I and II, we find a large variety of different processes that sizeably contribute to the final relic density (e.g., we correct between two and twelve gaugino annihilation and coannihilation channels in parallel in scenario I) yielding an overall sum of processes corrected by `DM@NLO` of up to more than 90%. This underlines the importance of the different gaugino (co)annihilation channels, even of the rather exotic ones such as $\tilde{\chi}_1^0\tilde{\chi}_3^0 \to b\bar{b}$ ($\sim 5\%$), and, hence, of their corresponding higher-order corrections for a precise estimation of the final relic density.
To conclude the investigation of the impact of our $\mathcal{O}(\alpha_s)$ corrections on $\Omega_{\tilde{\chi}_1^0}$, in Fig. 6.4, we

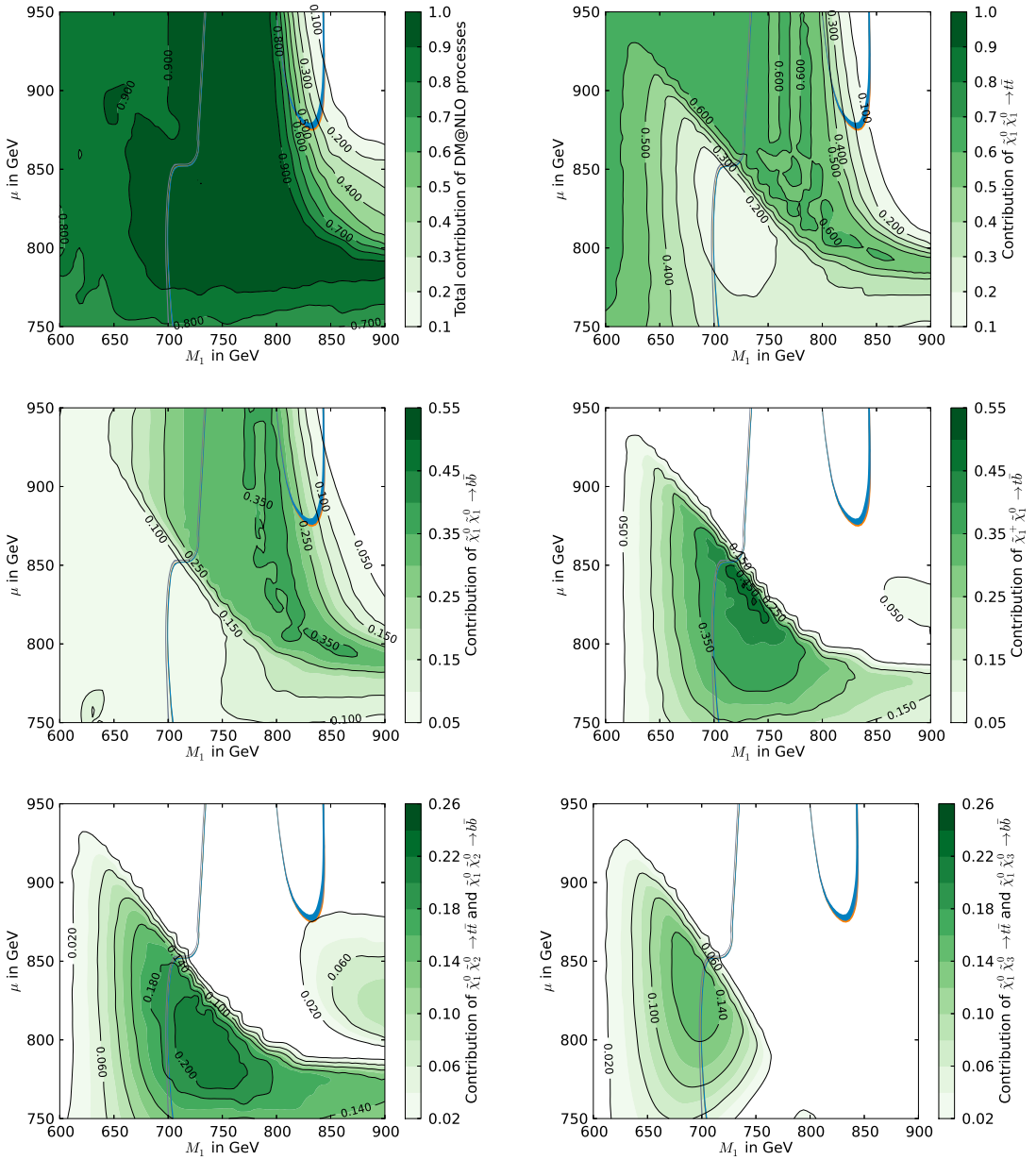

Figure 6.3.: Relative importance of the processes that contribute to the neutralino relic density in the M_1–μ plane surrounding scenario II. The three colored lines represent the part of the parameter space which leads to a neutralino relic density compatible with the Planck limits given in Eq. (4.5) using the standard `micrOMEGAs` calculation (orange), our tree-level calculation (gray) and the full one-loop calculation (blue). Figure taken from [1].

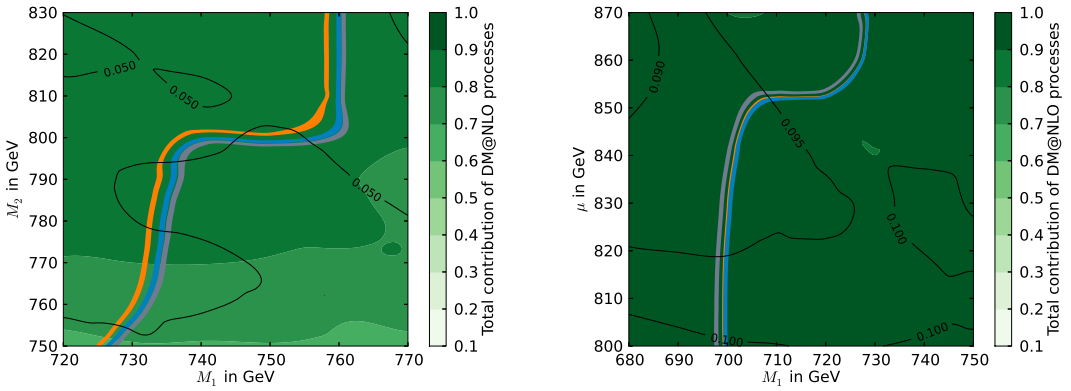

Figure 6.4.: Neutralino relic density in the M_1–M_2-plane surrounding scenario I (left) and the M_1-μ-plane surrounding scenario II (right). The three colored lines represent the part of the parameter space that leads to a neutralino relic density compatible with the Planck limits given in Eq. (4.5). For the orange line, we use the standard `micrOMEGAs` routine, the gray one corresponds to our tree-level calculation and the blue one represents the full one-loop calculation. The black contour lines denote the relative shift between the tree-level and one-loop relic density, i.e. $\left|1 - \Omega_\chi^{\mathrm{NLO}}/\Omega_\chi^{\mathrm{tree}}\right|$. Figure taken from [1].

zoom into parts of the cosmologically favored regions of Fig. 6.2 and Fig. 6.3. The former is shown in the left hand plot of Fig. 6.4. As already mentioned above, the three lines separate completely. This confirms the observations concerning the upper plots of Fig. 6.1, where the cross sections of the channels $\tilde{\chi}_1^0\tilde{\chi}_1^+ \to t\bar{b}$ and $\tilde{\chi}_1^0\tilde{\chi}_2^0 \to b\bar{b}$ are depicted. As these channels dominate the parameter space around scenario I shown in Fig. 6.4 (see also Fig. 6.2), the deviations between the three cross sections propagate through the Boltzmann equation to yield sizeable deviations in the final relic density. This shifts our one-loop result away from the tree-level relic density by roughly 5%, whereas the relic density obtained with `micrOMEGAs` differs by ≈14% from our tree-level result. The right-hand side of Fig. 6.4 shows a detailed view on Fig. 6.3. As already mentioned, the orange and blue lines overlap, which agrees with our results from Sec. 6.1. There, we find that the one-loop corrections of the dominant channels $\tilde{\chi}_1^0\tilde{\chi}_1^+ \to t\bar{b}$ and $\tilde{\chi}_1^0\tilde{\chi}_2^0 \to t\bar{t}$ are well approximated by the effective tree-level calculation from `micrOMEGAs` (see middle part of Fig. 6.1). As a consequence, the relic density determined by `micrOMEGAs` agrees with the full one-loop calculation. The one-loop corrections shift the relic density by roughly 9-10%. Note that the size of the corrections is, hence, larger than in scenario I.

We now turn to the final states with first and second generation quarks. Scanning through the pMSSM-11 parameter space, we find that phenomenologically viable scenarios are quite similar to our reference scenario III, featuring rather heavy squarks of the first and second generation, while those of the third generation are lighter in order to meet the requirement of the 125 GeV Higgs boson. Consequently, the NLO corrections to the annihilation cross section into final states with first and second generation quarks happen to be suppressed by the corresponding large squark masses (in the t- and u-channel) as can be seen in Fig. 6.1 for scenario III. Thus, this correction of the neutralino relic density will be even less important since these final states typically account for far less than 50% of the total cross section, the rest being, e.g., annihilation into third-generation quarks. We therefore do not show extensive studies of the relic density for our scenario III. Note, however, that in

a more general SUSY framework, the situation can be different and the corrections to the (co)annihilation into light quarks can become numerically relevant. Since our numerical code includes $\mathcal{O}(\alpha_s)$ corrections in the most general form, such an investigation within a more general MSSM setup is actually possible.
Let us finally briefly comment on potentially large Sommerfeld enhancement effects (the Coulomb corrections in the case of massless boson exchange) to the processes investigated in this section. As discussed in Sec. 5.3, these can largely alter the corresponding (co)annihilation cross section between two particles at low relative velocity v. The impact of the Sommerfeld enhancement for WIMP dark matter is widely discussed in the literature [230]. Although we have discussed the Coulomb corrections only in the context of gluons, i.e., for strongly interacting, massless particles, the qualitative enhancement at low v is also found for the photon exchange or for the exchange of some massive bosons ϕ, at least, as long as $m_\phi \ll m_{\tilde{\chi}}$ is fulfilled, such that the incoming gauginos $\tilde{\chi}$ can be kept on-shell during the multiple ϕ exchanges. To be more precise, these corrections become relevant when the Bohr radius $1/m_{\tilde{\chi}}$ becomes smaller then the interaction range $1/m_\phi$ or $\alpha_W m_{\tilde{\chi}}/m_\phi \gtrsim 1$, where α_W is the coupling constant between the boson ϕ and the incoming particles. In the MSSM with typical neutralino-LSP masses $m_{\tilde{\chi}_1^0} \lesssim 1$ TeV and with EW bosons with mass $m_\phi \gtrsim \mathcal{O}(100)$GeV (except for the photon), this situation is, however, almost never realized. In particular it is never realized in our representative scenarios I-III in Tab. 4.1. The only case where this may be of certain interest is the case of Coulomb corrections due to the exchange of photons between an incoming chargino pair. In scenario III, we find that chargino annihilation can sizeably contribute to the final DM relic density. The corresponding calculation of the Coulomb corrections follows the exact same lines as for the gluon discussed in Sec. 5.3 where it would be necessary to only replace the couplings and color factors by the corresponding electromagnetic charges[1]. However, as the electromagnetic coupling happens to be much smaller than the strong coupling constant, one would have to go to much smaller velocities to reach the non-perturbative regime

$$\alpha_e/v \gtrsim 1, \tag{6.1}$$

a region, where the Boltzmann suppression may already counteract the Sommerfeld enhancement. As, in addition, the chargino annihilation is still only a subleading contribution ($\sim 10\%$ to $\langle \sigma_{\text{eff}} v \rangle$) we leave this topic for later investigations.

[1]Note that Sec. 5.3 only treats the case of particles with equal masses. Hence, the case of chargino coannihilation between different mass eigenstates would only be (approximately) covered if $m_{\tilde{\chi}_1^\pm} \approx m_{\tilde{\chi}_2^\pm}$. However, the opposite case would of course be highly Boltzmann suppressed and, hence, be rather irrelevant.

7. Squark (Co)Annihilation: The Results

7.1. Impact on the Cross Sections

We now turn to the discussion of the impact of the full corrections of `QQ2xx` for the processes listed in Eqs. (4.8) - (4.11) based on the corresponding discussion of Ref. [2].
Fig. 7.1 presents the cross sections multiplied by the relative velocity v as a function of the center-of-mass momentum p_{cm} for selected annihilation channels of the three reference scenarios presented in Tab. 4.5. We show the cross section at tree level (black dashed line), including the full $\mathcal{O}(\alpha_s)$ corrections as discussed in Secs. 5.1.9 and 5.2.6 (red solid line), with the full corrections including the Coulomb corrections of Sec. 5.3 (blue solid line) and the corresponding value obtained by `micrOMEGAs/CalcHEP` (orange solid line). In the lower part of each plot, we give different ratios between the different cross sections (second item in the legend). The gray shaded regions represent the thermal weighting of the σv contributions to $\langle \sigma_{\text{ann}} v \rangle$ of Eq. (3.39).
Turning to the different graphs, the plot on the upper left of Fig. 7.1 illustrates σv for the process $\tilde{t}_1 \tilde{t}_1^* \to h^0 h^0$, which happens to be the dominant subchannel in scenario Ia. We find that our prediction for the cross section at tree level deviates by roughly 45% from the `micrOMEGAs` result. This deviation can be traced back to a different treatment of couplings as well as different input parameters used within `micrOMEGAs` compared to `DM@NLO`. In particular, `micrOMEGAs` uses the $\overline{\text{DR}}$-top mass $m_{\text{t}}^{\overline{\text{DR}}} = 161.6$ GeV, whereas we take the on-shell top mass $m_{\text{t}}^{\text{OS}} = 172.3$ GeV. As these enter the Yukawa couplings and in turn alter the important t- and u-channels, which happen to be the dominant contributions for most of the corrected processes (see Tab. 4.9), this is the main reason for the observed shift between our tree level and the `micrOMEGAs` result. Note, that this behavior has also been encountered previously in Ch. 6. At low relative velocities of the incoming stops (i.e. at small p_{cm}), the higher-order corrections (red and blue curves) rise steeply due to the Coulomb corrections discussed in Sec. 5.3. For larger values of $p_{\text{cm}} > 400$ GeV, the Coulomb corrections become less relevant turning into a usual perturbative series in α_s, whereas the $2 \to 3$ processes become more and more important due to the enhanced phase space and already start to significantly alter the p_{cm} dependence of the NLO and the full result. Here, the full corrections lead to a change of roughly 35% compared to our tree-level calculation.
Comparing the ratios $\sigma_{\text{full}}/\sigma_{\text{tree}}$ (red line) and $\sigma_{\text{NLO}}/\sigma_{\text{tree}}$ (orange line) in the lower part of the plot within the region favored by the thermal weighting of the integrand in Eq. (3.39) (here between $p_{\text{cm}} = 50$ GeV and $p_{\text{cm}} = 350$ GeV), we observe that the Coulomb corrections significantly contribute even beyond NLO. This observation has already been suggested earlier by Fig. 5.34 in Sec. 5.3. Its contribution at NNLO and higher amounts up to about half of the $\mathcal{O}(\alpha_s)$ contribution. Furthermore, our full result deviates from the tree level by up to 300% and from the `micrOMEGAs` result even by up to a factor of seven to eight within the above interval of high thermal weighting.
In the upper right corner of Fig. 7.1, we show the analogous plot for the process $\tilde{t}_1 \tilde{t}_1^* \to Z^0 Z^0$ of scenario Ia. The difference between our tree level and `micrOMEGAs` amounts up to 60%. This deviation can again be traced back to the different treatment of couplings

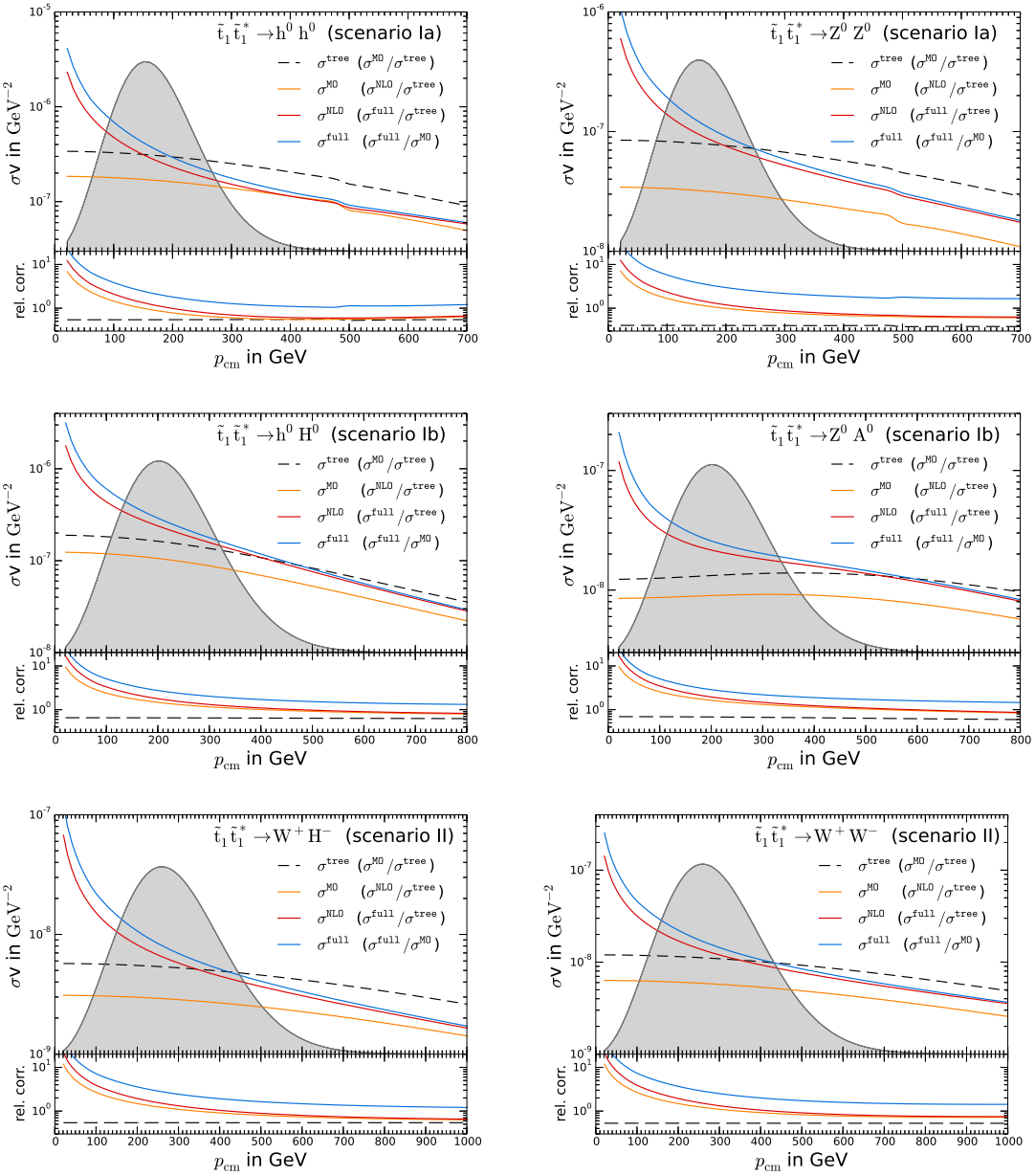

Figure 7.1.: Tree-level (black dashed line), `micrOMEGAs` (orange solid line), NLO ($\mathcal{O}(\alpha_s)$) corrections (red solid line) and full corrections (blue solid line) for selected channels in the scenarios of Tab. 4.5. The upper part of each plot shows σv in GeV^{-2} in dependence of the momentum in the center-of-mass frame p_{cm}. The gray areas indicate the thermal distribution (in arbitrary units). The lower parts of the plots show the corresponding ratios of the cross sections (second item in the legends).

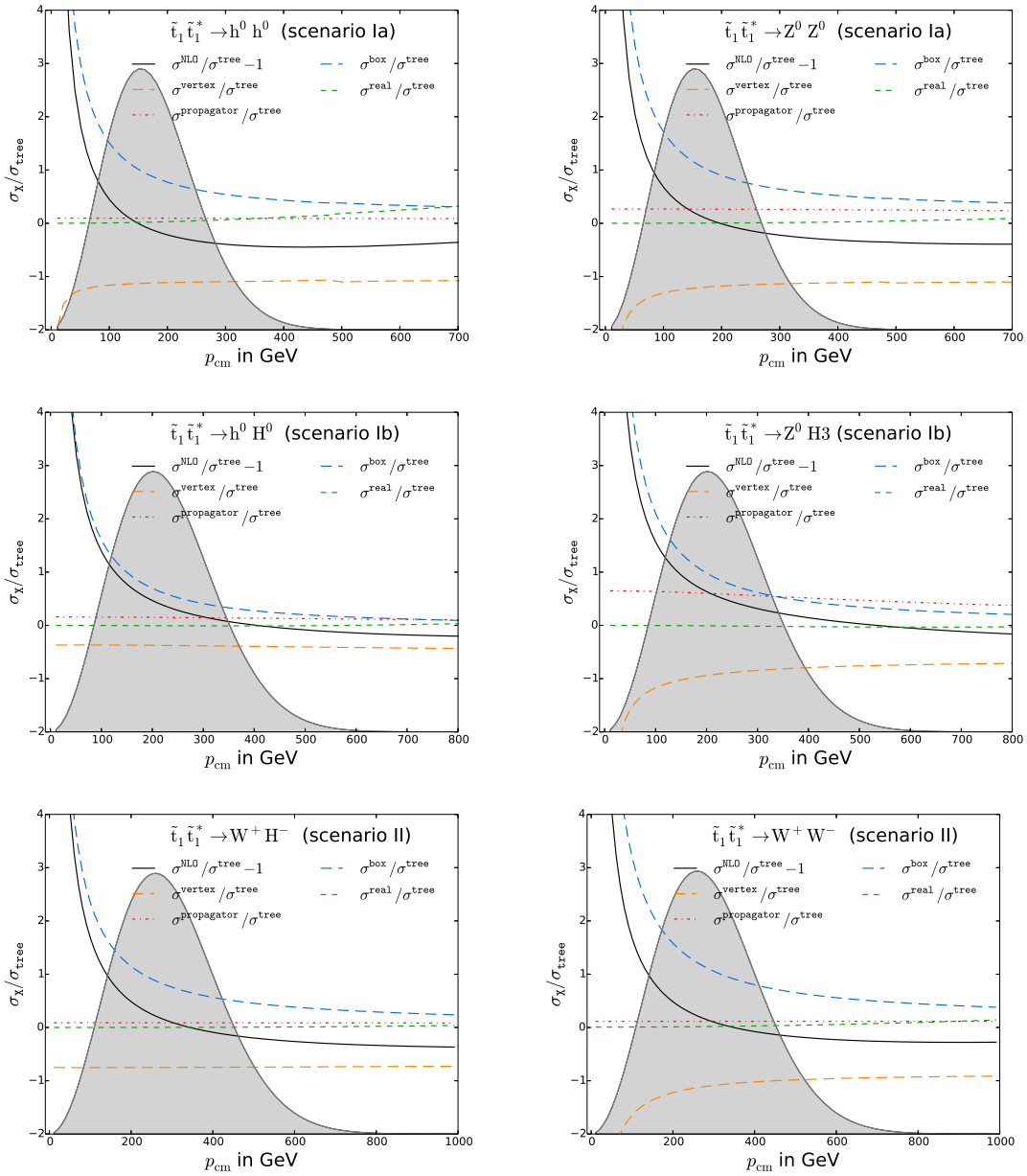

Figure 7.2.: Results for NLO (without tree level, black), vertex (orange), propagator (red), box (blue) and real plus soft-photon corrections (green) of Ch. 5 for selected channels in the scenarios of Tab. 4.5. The plots show ratios of the different corrections over tree-level cross sections dependent on p_{cm}. The gray areas indicate the thermal distribution (in arbitrary units).

and input parameters due to our choice of the renormalization scheme. For small $p_{\rm cm}$, the Coulomb enhancement takes over yielding large corrections of a factor of 10 and more relative to our tree level. Moreover, our full corrections deviate from our tree level by up to a factor of three or four in the important region between $p_{\rm cm} = 50$ GeV and 350 GeV, whereas the ratio between the full result and `micrOMEGAs` gets even larger by another factor of three and more. Since these two final states h^0h^0 and Z^0Z^0 constitute around 55% of the total annihilation cross section $\langle\sigma_{\rm eff}v\rangle$ (see Tab. 4.7), the importance of our corrections to the neutralino relic density is already indicated at this point.
One further encounters small kinks in the upper two plots of Fig. 7.1 around $p_{\rm cm} = 485$ GeV. These are due to a very broad s-channel resonance caused by the heavier CP-even Higgs H^0. Although the pseudoscalar Higgs boson A^0 is similar in mass ($m_{A^0} \approx m_{H^0} =$ 1917.4 GeV), it does not contribute to the s-channel in the case of $\tilde{t}_1\tilde{t}_1^*$ annihilation (see Sec. 4.3.3) as it is CP-odd and, hence, does not couple to two identical squark mass eigenstates.
The remaining four plots show $\tilde{t}_1\tilde{t}_1^* \to h^0H^0$ and $\tilde{t}_1\tilde{t}_1^* \to Z^0A^0$ for scenario Ib and $\tilde{t}_1\tilde{t}_1^* \to W^+H^-$ and $\tilde{t}_1\tilde{t}_1^* \to W^+W^-$ for scenario II. In all four cases, our tree level differs from the `micrOMEGAs` result by 30% to 50%. It may seem to be quite surprising that for Z^0A^0 the deviation between our tree level and `micrOMEGAs` turns out to be only half as large as in the case of Z^0Z^0 final state, although their different contributions can be considered as relatively similar. The larger difference seen in the case of the Z^0Z^0 final state can be traced back to the longitudinal polarized vector bosons, which, in the 't Hooft-Feynman gauge are represented by the Goldstone bosons G^0 (beside the different treatment of the top mass). More accurately, it turns out that the coupling $\tilde{t}_1\tilde{t}_2G^0$ causes the large difference in Fig. 7.1. It is treated differently in `micrOMEGAs` compared to our implementation that uses the proper tree-level coupling. The reason for the shift observed is that this coupling enters the important t- and u-channel contributions twice in the case of Z^0Z^0 but only once, e.g., in the case of the Z^0A^0 final state.
In the last four plots, the Coulomb corrections dominate our higher-order corrections in the region of small $p_{\rm cm}$. For large values of $p_{\rm cm}$, the Coulomb corrections again turn into a usual perturbative series in α_s such that the full $\mathcal{O}(\alpha_s)$ corrections become relevant and give rise to corrections roughly between 15% and 35%. In the region relevant for $\Omega_{\tilde{\chi}_1^0}h^2$, i.e., in the vicinity of the peak of the thermal distribution, the deviation between our full result and our tree level accounts for roughly 50% to 100% and between our full result and `micrOMEGAs` for around 200%.
Fig. 7.2 shows the decomposition of the absolute value of the NLO cross section without the tree-level contributions $\sigma^{\texttt{NLO}}/\sigma^{\texttt{tree}} - 1$ (black) into the various types of UV finite $\mathcal{O}(\alpha_s)$ corrections for each of the processes of Fig. 7.1. More precisely, we show the vertex (orange), propagator (red), box (blue) and real corrections (green) where the latter already includes the soft-gluon contribution as discussed in Sec. 5. The different contributions due to the vertex, box and propagator corrections are already summed up with their appropriate counter terms discussed in Sec. 5, yielding UV-finite results. However, together with the real corrections, these different contributions are separately IR divergent as well as dependent on large logarithms of the associated factorization scale μ (see Sec. 5.2.3). These terms cancel in the final cross section but can lead to an enhancement of each contributions of Fig. 7.2 individually.
Looking at Fig. 7.2, one can clearly identify the subclasses of $\mathcal{O}(\alpha_s)$ corrections which are enhanced by the Coulomb corrections of Sec. 5.3, namely the vertex and box corrections. Only the vertex corrections of the processes $\tilde{t}_1\tilde{t}_1^* \to h^0H^0$ and $\tilde{t}_1\tilde{t}_1^* \to W^+H^-$ show no significant rise at small $p_{\rm cm}$. We find that in these cases, the dominant contributions are

due to the t- and u-channel, which turn out to be much larger than the Coulomb enhanced diagrams sum under the vertex corrections (see Tab. 4.9). Therefore, much smaller values of $p_{\text{cm}} \sim \mathcal{O}(10^{-3}\,\text{GeV})$ have to be considered to see a significant rise in the vertex corrections which is, however, not shown here.
Finally note, that the sum of box and vertex corrections results in a positive correction at low p_{cm}, whereas for large p_{cm} the situation is reversed and the overall corrections are negative. The point where the overall correction changes its sign is approximately given by the point where the dominant contributions of the box and vertex corrections compensate each other. Moreover, the real emission corrections turn out to be subdominant for all cases. They only rise toward larger p_{cm}, where the larger kinematically accessible phase space of the $2 \to 3$ processes enhances the associated total cross sections. However, in those regions, the thermal weighting already yields a suppression too large for these contributions to significantly alter the final relic density.

7.2. Impact on the Relic Density

We now come to the investigation of the impact of our higher-order corrections on the neutralino relic density $\Omega_{\tilde{\chi}_1^0}$. For the following analysis, we use the setup presented in the flow chart Fig. 4.1. The overall number of corrected processes for the relevant case of $\tilde{t}_1\tilde{t}_1^*$ pair annihilation presented in the Eqs. (4.8) to (4.11) amounts to 24 different final states. All other processes that do not sum under the processes listed in Eqs. (4.8) - (4.11) or the processes named in Sec. 5.4 (see Fig. 5.36) are provided by `CalcHEP` at the effective tree level. The actual relevance of each of these different channels for the final $\Omega_{\tilde{\chi}_1^0}$ is *a priori* unknown as it is strongly dependent on the specific parameter point. Hence, each of the 24 processes needs to be considered separately. To optimize the calculational time cost for the evaluation of $\Omega_{\tilde{\chi}_1^0}$, we include a cutoff on the contribution of the different channels to $\langle\sigma_{\text{eff}}\rangle$, similar to the one discussed in Sec. 6.2. We set this bound to 1%. This is in accordance with the current experimental precision of $\Omega_{\tilde{\chi}_1^0}h^2$, which lies at around 2% at 1σ confidence level. All remaining channels are either replaced by our tree level for consistency or are left unchanged, i.e., are calculated via `CalcHEP` at the effective tree level.
In the representative scenarios of Tab. 4.5, the lightest neutralino appears to be bino-like always (see $|Z_{\tilde{\chi}^0,1\tilde{B}}|^2$ in Tab. 4.6) and, hence, its mass is predominantly determined by the bino-mass parameter M_1. Since within our scenarios Ia/b and II, the lightest scalar top quark turns out to possess a large admixture $|Z_{\tilde{t},1R}|^2$ of $\tilde{t}_R$, the superpartner of the right-handed part of the top quark, $m_{\tilde{t}_1}$ is also sensitive to the right-handed supersymmetry breaking parameter $M_{\tilde{u}_3}$. We therefore present our results in the M_1-$M_{\tilde{u}_3}$ plane of the pMSSM-11 parameter space as defined in Sec. 2.5. These two parameters directly influence the important mass splitting $m_{\tilde{\chi}_1^0} - m_{\tilde{t}_1}$ to which the relic density in the stop (co)annihilation region is extremely sensitive.
The Figs. 7.3 and 7.4 show scans around our reference scenarios of Tab. 4.5. Following the color convention introduced in Sec. 6.2, the orange band ($\Omega^{\texttt{MO}}$) refers to the neutralino relic density $\Omega_{\tilde{\chi}_1^0}h^2$ obtained by `micrOMEGAs`/`CalcHEP` and the gray band ($\Omega^{\texttt{tree}}$) indicates the prediction of the relic density $\Omega_{\tilde{\chi}_1^0}h^2$, in which our tree-level calculation replaces the `CalcHEP` result for the processes specified in Eqs. (4.8) - (4.11). Finally, the blue band ($\Omega^{\texttt{full}}$) represents $\Omega_{\tilde{\chi}_1^0}h^2$ as a result of the full calculation discussed in the Secs. 5.1.9, 5.2.6 and 5.3. We add the relic density obtained by our NLO calculation alone in red to Fig. (7.4).

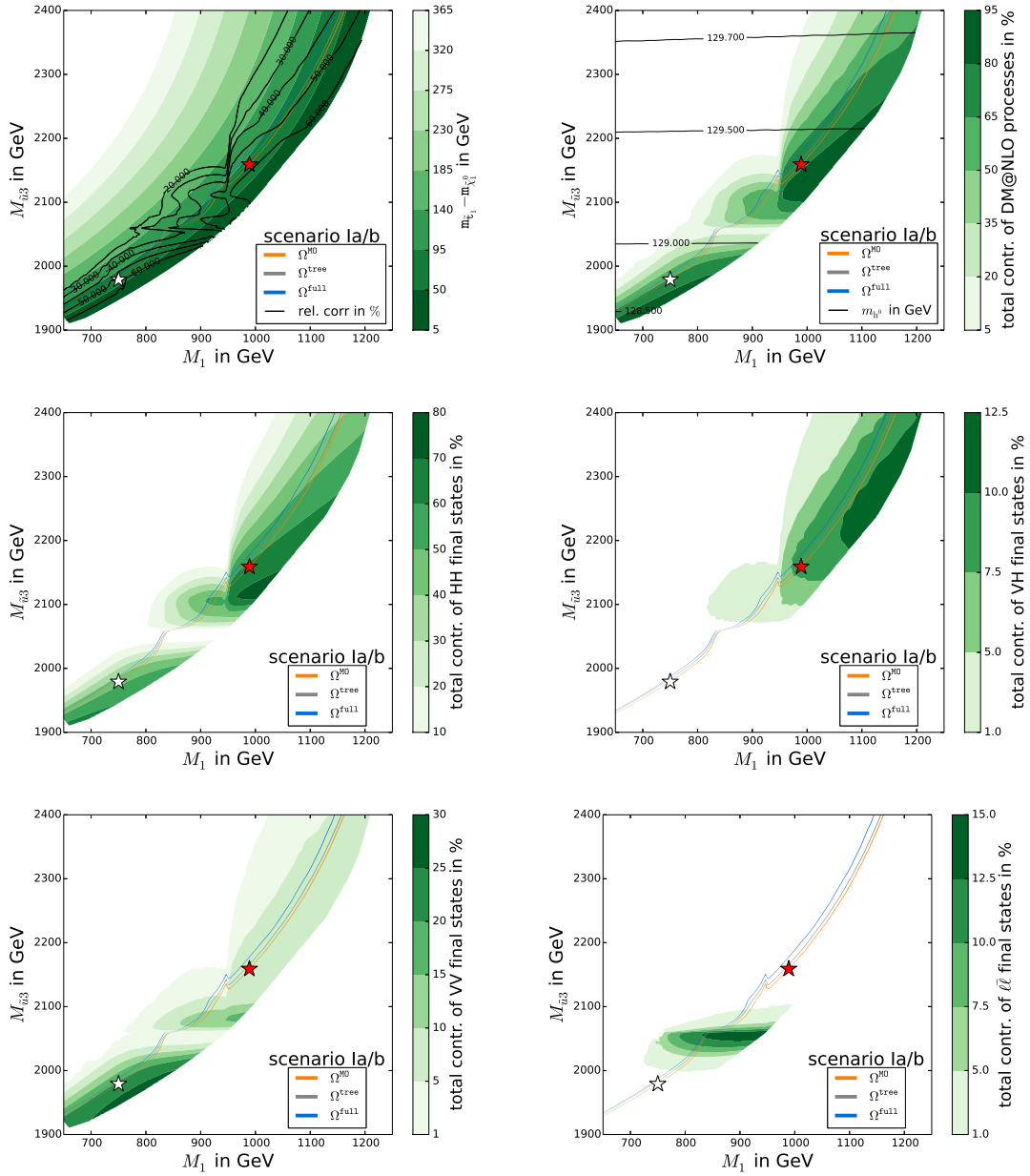

Figure 7.3.: Planck-compatible relic density bands (see Eq. 4.16) in the M_1–$M_{\tilde{u}_3}$ plane surrounding scenario Ia and Ib. The calculation includes `micrOMEGAs` (orange), our tree-level (gray) and our full corrections (blue). The white and red stars mark the positions of our reference scenarios Ia and Ib. The black lines of the plot on the upper left show the deviation between `micrOMEGAs` and our full result in per cent. In the plot on the upper right, the black lines stand for the mass of the lightest Higgs boson m_{h^0} in GeV. For further explanations see the text.

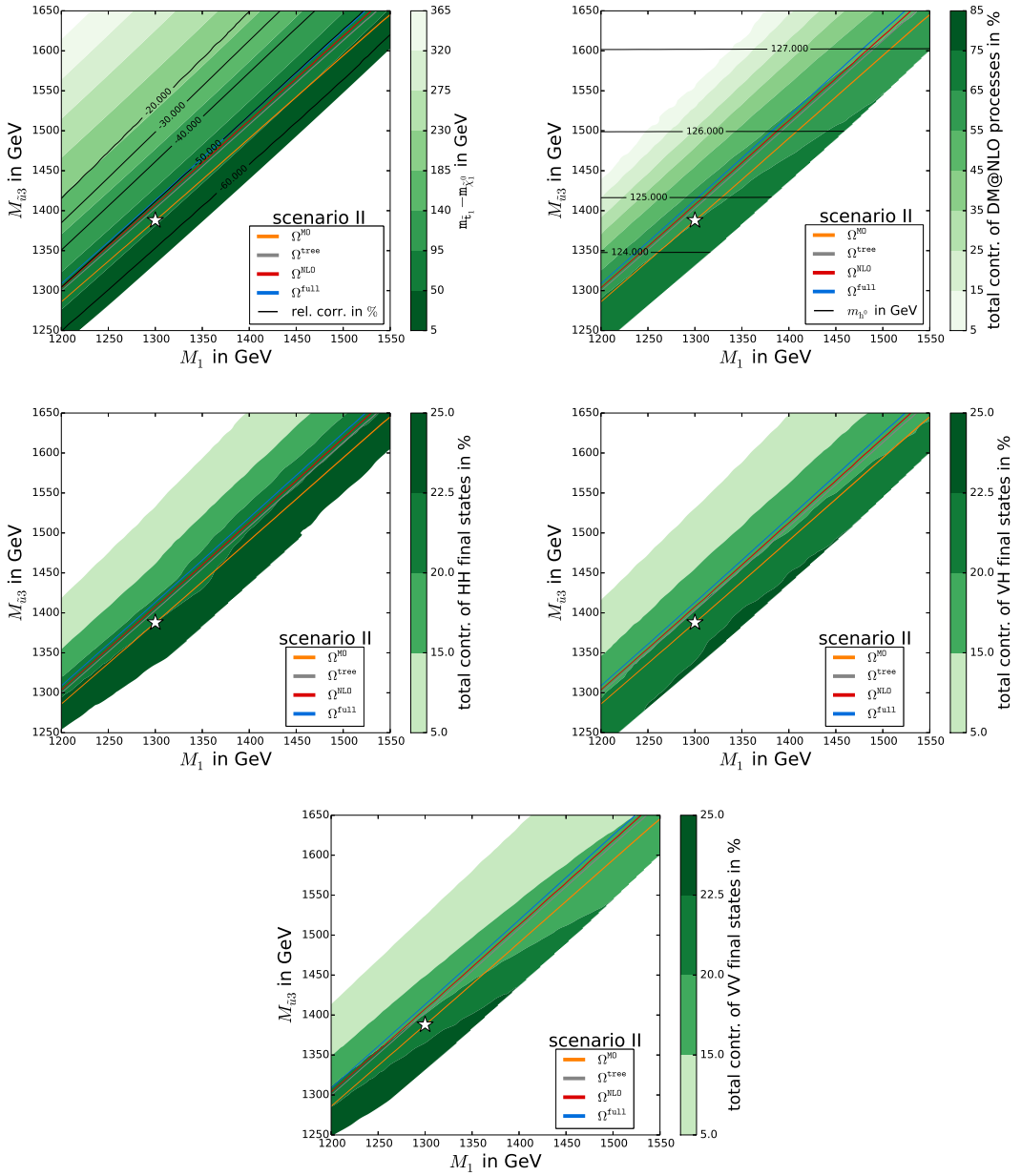

Figure 7.4.: Same as Fig. 7.3 for scenario II. Here, the plot for the $\ell\bar{\ell}$-final states is left out (see text). The NLO result is added in red.

The experimental 1σ-uncertainty of Eq. (4.16) is reflected by the width of the three bands of Fig. 7.3 and Fig. 7.4. Their fineness underlines the impact of the constraining assumption that the lightest neutralino $\tilde{\chi}_1^0$ accounts for the whole cold dark matter in the universe. As evident from the Figs. 7.3 and 7.4, a distinct separation between the bands corresponding to our tree-level result (gray) and the default result of `micrOMEGAs` (orange) can be observed nearly everywhere throughout the $M_1 - M_{\tilde{u}_3}$ plane. This separation becomes even larger when the NLO (red) or full (blue) corrections are taken into account. The black contour lines in the top left plots of Figs. 7.3 and 7.4 quantify the magnitude of the corrections between `micrOMEGAs` and the full result more precisely. They amount up to roughly 50% in Fig. 7.4 and reach even more than 50% in the cosmologically favored region of the corresponding plot of Fig. 7.3 while our fully corrected result deviates by up to 25% from our tree level in Fig. 7.4 and by nearly 40% in Fig. 7.3, respectively. In Fig. 7.4, the importance of the NNLO Coulomb corrections for a precise estimation of the relic density is pointed out. Here, the full result deviates by far more than one standard deviation from our NLO result, which is visualized by the splitting of the associated blue and red bands. This deviation, caused by Coulomb corrections of NNLO and beyond, even exceeds the size of our full NLO corrections. Beside the fact that for $v \approx \alpha_s$ the higher-order Coulomb corrections are roughly of the same size as the leading order Coulomb corrections, this result can be traced back to a cancellation among the NLO contributions to the relic density as shown in Fig. 7.1. By looking at Fig. 7.1, it becomes apparent that the NLO corrections at large v tend to lower the tree-level cross section, whereas for lower v the Coulomb corrections start to sizeably alter the cross section turning the NLO corrections to positive values. Since for certain processes, this transition takes place quite closely to the peak of the thermal distribution as defined in Eq. (3.39), the associated cancellation significantly lowers the total contribution of the NLO corrections to the final relic density. On the contrary, the Coulomb corrections of $\mathcal{O}(\alpha_s^2)$ and beyond yield a throughout positive correction, lacking any kind of cancellation in the thermal integral. This propagates through to the overall large importance of the higher-order Coulomb corrections as observed in Fig. 7.4. Note that this large impact of the $\mathcal{O}(\alpha_s^2)$ Coulomb corrections also increases the scale uncertainty of the final result connected to the unphysical scale μ_G of Eq. (5.258), which drops out of the corresponding $\mathcal{O}(\alpha_s)$ Coulomb corrections[1]. Apart from the corrections discussed above, Figs. 7.3 and 7.4 highlight several regions of parameter space, where stop annihilation into different EW final states become important. The cosmologically preferred region of parameter space lies along a line of almost constant mass difference between the neutralino-LSP and the stop-NLSP as apparent in the plots in the upper left of the Figs. 7.3 and 7.4. For scenario Ia/b, one observes that for higher values of $M_{\tilde{u}_3}$ the processes with Higgs bosons in the final state dominate along the cosmologically favored region, whereas for small $M_{\tilde{u}_3}$ and M_1, the processes with a vector boson in the final state take over and become the most important contributions. This is because for smaller $M_{\tilde{u}_3}$, the stops are lighter and two Higgs bosons in the final state turn out to be no longer kinematically allowed or are at least largely suppressed. The same observation, though less pronounced, holds for scenario II, where one encounters an increasing relevance of vector-vector final states toward lower values of $M_{\tilde{u}_3}$ and M_1 in the last plot of Fig. 7.4.

Although the scenario Ia/b as well as scenario II fulfill the experimental bounds on the Higgs boson mass, only scenario II lies within the vicinity of the experimentally favored m_{h^0} region (see Eq. (4.17)), whereas the scenarios Ia and Ib lie at the edge of this constraint. The mass of the lightest Higgs boson is mainly driven by the $M_{\tilde{u}_3}$ parameter as

[1] Of course, this is valid only apart from the intrinsic scale dependence of the strong coupling $\alpha_s(\mu_G)$.

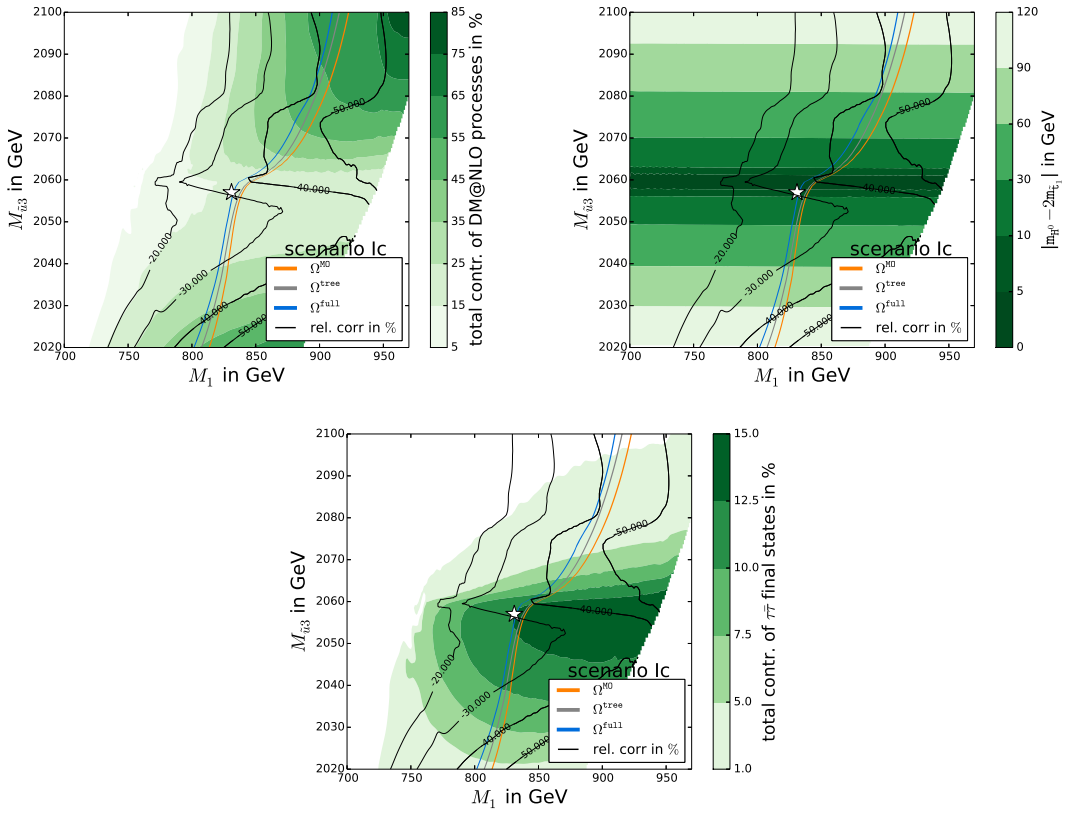

Figure 7.5.: Scan of the scenario Ia/b-plane. The white star marks the position of the scenario Ic ($M_1 = 831$ GeV, $M_{\tilde{u}_3} = 2057$ GeV) further analyzed in Fig. 7.6.

discussed in the Secs. 2.2.1 and 4.3.2, which determines the mass $m_{\tilde{t}_1}$ in our scenarios. Consequently, the parameter $M_{\tilde{u}_3}$ influences the mass splitting between the top quark and its superpartner $\tilde{t}_1$, which in turn enters the mass corrections of the mass of the lightest Higgs boson (see Eq. (4.15)).

Another interesting contribution including electroweak final states, which has not been disussed so far, is the annihilation of scalar top quarks into lepton-antilepton pairs. Although this process is not the leading contribution to the total cross section in any of the representative scenarios, there is a region in the $M_{\tilde{u}_3}$-M_1 plane shown in the bottom-right plot of Fig. 7.3, where the process with $\tau\bar{\tau}$ final state actually contributes to $\langle\sigma_{\text{eff}}\rangle$ by as much as 13%. In order to get a closer look at this, in Fig. 7.5, we zoom into this area of enhanced $\tau\bar{\tau}$ contributions. It turns out that the enhancement of the $\tau\bar{\tau}$ final state is due to an s-channel resonance caused by the heavier Higgs H^0 accompanied by a Yukawa coupling, which, for $\tan\beta = 16.3$, is already large enough to significantly favor the down-type fermions. Interestingly, the corrections to this process are significant enough to cause a shift of the relic density by surprisingly large 20% relative to our tree level and by even more than 30% relative to `micrOMEGAs` despite the fact that its contribution is comparatively low. The reason for this unexpectedly large contribution is that the annihilation into $\tau\bar{\tau}$ proceeds only through an s-channel exchange of vector and Higgs bosons. As pointed out in Fig. 7.2, while for all other final states the corrections from the vertex and the box diagrams tend to cancel each other and lead to a reduction in the total correction, this is not the case for τ-leptons in the final state as they do not feature any box corrections. Thus, this cancellation cannot take place. For further discussion we introduce a fourth

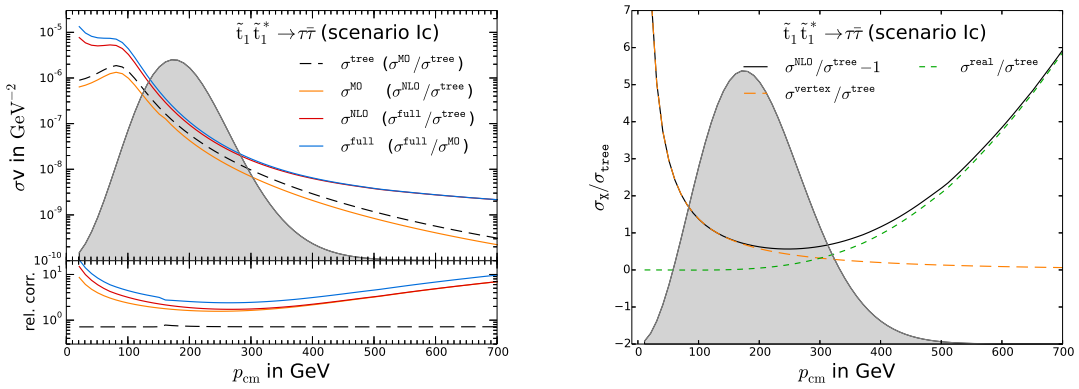

Figure 7.6.: Cross sections and NLO contributions to scenario Ic of Fig. 7.5.

representative scenario Ic marked by the white star in Fig. 7.5. The relevant cross section contributions for this parameter point are shown in greater detail in Fig. 7.6. It becomes evident that, starting from the H^0-resonance at around $p_{\text{cm}} = 80$ GeV (first plot of Fig. 7.6), the corrections to the annihilation into $\tau\bar{\tau}$ are comprised of large Coulomb corrections from the vertex diagrams, whereas for larger p_{cm} the corrections are dominated by the relatively large contributions of the $2 \to 3$ processes (see second plot of Fig. 7.6) due to the phase-space enhancement of the $2 \to 3$ final states. The latter already sets in at much lower p_{cm} because of the small τ-mass. Finally note that the s-wave annihilation through the H^0 of a stop-antistop pair into $\ell\bar{\ell}$ final states is suppressed by a factor of $(m_\ell/m_{\tilde{t}_1})^2$. Therefore, a more elaborate treatment that takes the full Coulomb corrections for the p-wave into account may lead to relative corrections of the particular cross section that are less suppressed than $\mathcal{O}(\alpha_s^2)$ compared to the leading s-wave contribution (see Sec. 5.3). However, as the leptons tend to unfold their main impact on the relic density in the vicinity of the H^0-resonance, this decreases the impact of the p-wave contributions (see plot on the left of Fig. (7.6)), which do not feature the above suppression factor $(m_\ell/m_{\tilde{t}_1})^2$. Hence, we leave this open to further investigations.

Finally note that there is a theoretical uncertainty or "error" for both the `ChiChi2qq` as well as for the `QQ2xx` results due to higher-order corrections not yet included. A common way to give an estimate of the impact of higher-order corrections is to check the dependence of associated observables such as cross sections or the relic density on the unphysical scales, in the present case these are the renormalization scale μ and the scale of the Greens function μ_G. This dependence is expected to be successively decreased by adding higher-order corrections not yet included. More precisely, the scale dependence relies on the interplay between renormalized parameters evaluated at the scale μ via the corresponding RGEs on the one hand and the accuracy of the higher-order virtual corrections in $\mathcal{O}(\alpha_s)$ as calculated in Sec. 5.1 on the other hand. Hence, if one uses the RGEs to evolve the parameters, whose virtual corrections are explicitly included, given at the accuracy of the corresponding virtual corrections, the full result is expected to be scale independent. However, as this is in general not the case here (see Sec. 5.1.5, Sec. 5.1.7 and Sec. 4.1 for the precision of RGEs used for m_b, α_s and for additional parameters estimated by the spectrum calculator used here), we expect a residual scale dependence of observables, which allows to give a rough estimate about the size of the higher-order virtual corrections. Moreover, as we provide strong corrections to processes that do not include the strong coupling α_s

at the Born level, our corrections are the first who allow to test the impact of higher-order strong corrections via the scale dependence of the strong coupling constant.
In order to somehow quantify the size of the higher-order corrections, the renormalization scale and the scale of the Greens function are varied typically between half and twice of their default values. The size of the shifts of observables is then said to quantify the theoretical error. Note, that this has to be handled with special care, because, on the one hand the variation of scales only tests the scale dependent terms and does not allow to give an estimate about the size of scale independent corrections, which are known to be potentially large, too. On the other hand, the size of the variation is completely arbitrary in order that the shift of observables with μ and μ_G is actually not a real error but rather a way to estimate the size of the higher-order corrections. However, we investigate on the scale dependencies in the context of `DM@NLO` in greater detail in a paper which is currently in production.

8. Summary, Conclusions and Outlook

The Standard Model presents a well established theory of particle physics, whose overwhelming success, which relies on the cornerstones of local gauge invariance and renormalizability, substantially influenced our understanding of nature. However, experiments hint toward the existence of a sizeable mass component composed out of non-luminous and non-baryonic matter, whose nature cannot be consistently explained by the Standard Model alone. In this thesis, we have discussed an extended version of the Standard Model, the R-parity conserving minimal supersymmetric Standard Model (MSSM), whose enlarged particle sector provides the lightest neutralino as a viable dark matter candidate. We have further presented the standard calculation of the relic density of thermally produced dark matter, where we have emphasized on the importance of approximate mass degeneracy for efficient coannihilation to evade a large Boltzmann suppression. Moreover, a closer look was taken on the different sources of uncertainties that can enter the estimation of the final DM relic density both on the experimental as well as on the theoretical side. In this regard, we have found that the precise calculation of the thermally averaged effective annihilation cross section $\langle \sigma_{\text{eff}} v \rangle$, as in parts provided by this work, can be of great importance for an exact estimation of the DM relic density competitive with the current experimental accuracy as provided by the WMAP or Planck experiment. However, we have also seen that this should only be understood as one part of a much larger picture of various uncertainties entering the final Ω_{DM}. We have then moved on to introduce the `DM@NLO` project, a software package, which covers the $\mathcal{O}(\alpha_{\text{s}})$ SUSY-QCD corrections for many important (co)annihilation channels within SUSY-QCD. We have further presented two sub-projects of `DM@NLO`, namely

`ChiChi2qq`:Gaugino (co)annihilation into quarks,
`QQ2xx`: Squark (co)annihilation into electroweak final states,

in whose context the work described in this thesis has taken place. We have subsequently turned to the discussion of the corrected channels for each of the above projects and introduced the corresponding representative scenarios within the phenomenological MSSM, in which later investigation of our higher-order corrections took place. After that, we went on to the actual work of this thesis, the estimation of higher-order corrections comprised of virtual, real and Coulomb corrections. We have discussed the theoretical methods to separate the ultraviolet, soft and collinear divergences, which we have encountered in higher loop contributions. To cancel the former, we have introduced a hybrid $\overline{DR}$/on-shell scheme, which has been chosen in order that it ensures numerically stable calculations over wide regions of parameter space. Moreover, we have presented methods that handle soft and (quasi)collinear divergences. These are the phase-space slicing and the dipole-subtraction method. Afterwards, we have introduced the non-perturbative Coulomb corrections, whose contributions are connected the exchange of potential gluons and which have been included into `QQ2xx`. Based on the representative scenarios mentioned above, we have provided extensive studies of our higher-order corrections, both on the cross section level and on the level of the relic density. In the case of gaugino (co)annihilation, we have encountered a large variety of different (co)annihilation channels which turned out to sizeably contribute to the final relic density. We have stated

that both quite common as well as rather exotic initial states such as $\tilde{\chi}_1^0\tilde{\chi}_3^0$ can become important for a precise estimation of $\Omega_{\tilde{\chi}_1^0}$, which provided to $\langle\sigma_{\text{eff}}v\rangle$ partly more than 90%. Concerning the corrections to the (co)annihilation cross sections and the final relic density, we have found that the effective treatment of couplings and masses as provided by `micrOMEGAs` often yields a good approximation of the full NLO calculation. Hence, we have often encountered a broad overlap between the 1σ-bands of our NLO-improved calculation and the standard implementation of `micrOMEGAs`. However, this agreement did not pertain through the whole parameter space such that we found regions, where our corrections yielded a 9% deviation from the `micrOMEGAs` result, largely overcoming the experimental precision of the dark matter relic density. We have further found that the impact of first and second generation quarks on $\Omega_{\tilde{\chi}_1^0}$ is rather low as these channels are typically accompanied by large contributions of heavy quarks and are furthermore suppressed by heavy first and second generation squarks in the t- and u-channel (at least in the scenarios investigated in this work).
In the case of squark (co)annihilation, we have mainly focused on the annihilation of the lighter stop $\tilde{t}_1$, a particle, which turned out to be a quite natural and also phenomenologically well motivated next to lightest supersymmetric particle. In the analyses of the higher-order corrections, we have distinguished between Higgs-Higgs, vector-Higgs, vector-vector and lepton-antilepton final states. As in the case of gauginos, we have found a large variety of different final states from the above list that became relevant in the evaluation of $\Omega_{\tilde{\chi}_1^0}$. We have corrected scenarios where the processes, whose NLO corrections are covered by `QQ2xx`, provided more than 70% to the final $\langle\sigma_{\text{eff}}v\rangle$. The corrections have shifted the tree-level result of $\Omega_{\tilde{\chi}_1^0}$ by far further than the experimental 1σ interval within the cosmologically favored region. Moreover, also the splitting between our full result and `micrOMEGAs` has exceeded the current experimental uncertainty by far. Most noticeable, the Coulomb corrections of $\mathcal{O}(\alpha_s^2)$ and beyond turned out to sizeably alter the relevant cross sections by a factor of four and more within the p_{cm} region of large thermal weight. This has propagated through to the final relic density where we found, that these higher-order Coulomb corrections of $\mathcal{O}(\alpha_s^2)$ can even become larger than the full NLO corrections, whereas the latter suffered from an intrinsic cancellation in the Boltzmann integral of $\langle\sigma_{\text{eff}}v\rangle$ to a certain extend. Compared to the bosonic final states, the leptonic final states have been a bit more special. However, also these final states have given large corrections to the neutralino relic density, e.g., when they are enhanced by a Higgs resonance. These comparatively large contributions have been traced back to the lack of all box contributions and, hence, to the lack of an associated cancellation in the corresponding virtual contributions, which took place for all bosonic final states in the sum of box and vertex corrections.
To provide an overall conclusion, *we have shown that the corrections encountered in this work can become larger than the current experimental uncertainty on the DM relic density provided by WMAP and the Planck satellite. Hence, these corrections play an important role on the way toward a high precision estimation of the DM relic density* Ω_{DM}*. Moreover, we have observed that even the inclusion of rather exotic (co)annihilation channels can become mandatory as various interplays between mass spectra, particle resonances and enhancements or suppressions of couplings may lead to a strongly increased importance of such typically highly Boltzmann suppressed processes.*
An obvious though not straightforward next step in the context `DM@NLO` is the inclusion of strong final states to squark (co)annihilation. We further encountered many regions in the pMSSM, where a combined analysis of all the sub-project of `DM@NLO`, covering gaugino (co)annihilation, neutralino-squark coannihilation and squark (co)annihilation, might

become interesting. We have further mentioned that the higher-order corrections given in this work also possess a theoretical "error", which can basically be understood as an estimate of the yet unknown corrections of $\mathcal{O}(\alpha_s^2)$ and beyond. A hands-on approach to quantify this includes the variation of the Coulomb and renormalization scales μ_G and μ, a topic which will be subject to subsequent publications. Another important project in the context of `DM@NLO` is the inclusion of $\mathcal{O}(\alpha_s)$ radiative corrections to neutralino scattering on nucleons as required in direct detection calculations. Additional future goals are the extension of the `DM@NLO` project by new models beyond the MSSM, e.g., the next-to-minimal supersymmetric Standard Model, as well as the inclusion of stau (co)annihilation, as the lighter stau $\tilde{\tau}_1$, similar to the $\tilde{t}_1$, turns out to be the NLSP for many realizations of the MSSM. It is further planned to include an integration routine into the `DM@NLO` package to solve the Boltzmann equation Eq. (3.36) in order to become independent from public codes such as `micrOMEGAs` or `DarkSUSY` at some point. However, in this regard, it is of course necessary to include many additional relevant (co)annihilation channels, which enter the thermally averaged (co)annihilation cross section $\langle \sigma_{\text{eff}} v \rangle$ of Eq. (3.27) such as annihilation of the lightest neutralino into EW final states.

A. Virtual Corrections

Here, we give the results for the vertex2 and box corrections of Sec. 5.1.9. The arrows on the lines indicate the momentum flow and the momentum at double lines stands for the total momentum of both lines summed up. The box diagrams including a fermion loop lead to rather long expressions and are therefore not given here.

A.1. HH-Final States

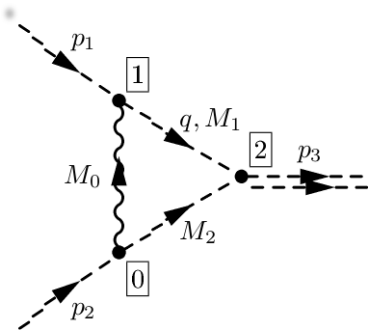

$\boxed{0} : ig_0[q - 2p_3 + p_1]^\alpha$

$\boxed{1} : ig_1[q + p_1]^\beta$

$\boxed{2} : ig_2$

$$\mathbf{B}\left[p_2^2, M_0^2, M_2^2\right], \quad \mathbf{C}\left[p_1^2, p_2^2, p_3^2, M_1^2, M_0^2, M_2^2\right]$$

$$A_0 \;=\; g_0 g_1 g_2 \left[B_0 + M_1^2 C_0 + p_1^2(C_0 - 2C_1) + 2p_3^2 C_2 - 2(p1 \cdot p_3)(C_0 - C_1 + C_2)\right]$$

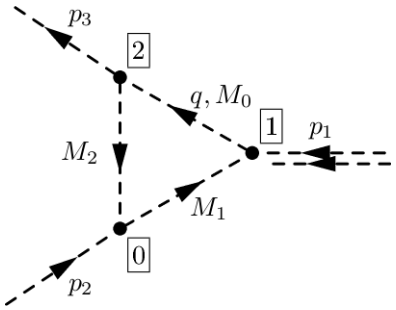

$\boxed{0} : ig_0$
$\boxed{1} : ig_1$
$\boxed{2} : ig_2$

$$\mathbf{C}\left[p_1^2, p_2^2, p_3^2, M_0^2, M_1^2, M_2^2\right]$$
$$A_0 \;=\; -g_0 g_1 g_2 C_0$$

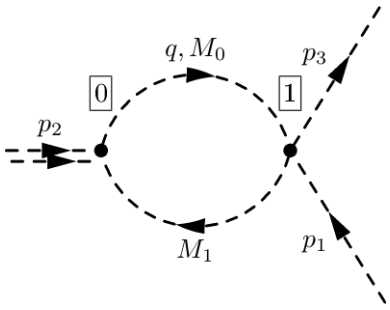

$\boxed{0} : ig_0$
$\boxed{1} : ig_1$

$$\mathbf{B}\left[p_2^2, M_0^2, M_1^2\right]$$
$$A_0 \;=\; g_0 g_1 g_2 B_0$$

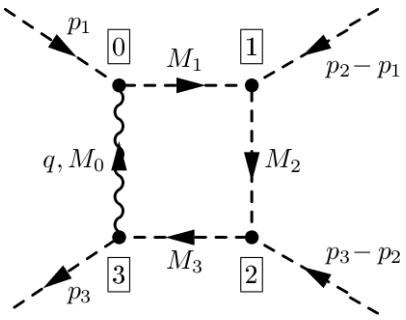

$\boxed{0} : ig_0 \left[q + 2p_1\right]^\alpha$
$\boxed{1} : ig_1$
$\boxed{2} : ig_2$
$\boxed{3} : ig_3 \left[q + 2p_3\right]^\beta$

$\mathbf{C}^{(a)} \left[p_1^2, (p_2 - p_1)^2, p_2^2, M_0^2, M_1^2, M_2^2\right]$, $\mathbf{C}^{(b)} \left[p_2^2, (p_3 - p_2)^2, p_3^2, M_0^2, M_2^2, M_3^2\right]$,
$\mathbf{C}^{(c)} \left[(p_2 - p_1)^2, (p_3 - p_2)^2, (p_3 - p_1)^2, M_1^2, M_2^2, M_3^2\right]$,
$\mathbf{D} \left[p_1^2, (p_2 - p_1)^2, (p_3 - p_2)^2, p_3^2, p_2^2, (p_1 - p_3)^2, M_0^2, M_1^2, M_2^2, M_3^2\right]$

$$A_0 \;=\; -g_0 g_1 g_2 g_3 \left[C_0^{(a)} + C_0^{(b)} - C_0^{(c)} - (M_0^2 - M_1^2 - M_3^2 - 4(p_1 \cdot p_3) + p_1^2 + p_3^2) D_0\right]$$

A.2. VH-Final States

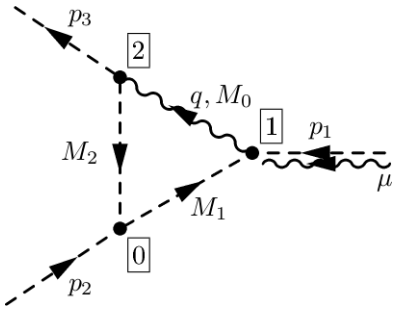

$\boxed{0} : ig_0$

$\boxed{1} : ig_1 g^{\alpha\mu}$

$\boxed{2} : ig_2[q - 2p_3]^\beta$

$$\mathbf{C}\left[p_1^2, p_2^2, p_3^2, M_0^2, M_1^2, M_2^2\right]$$

$$A_0 = -g_0 g_1 g_2 C_1 \qquad A_1 = -g_0 g_1 g_2 \left[2C_0 + C_2\right]$$

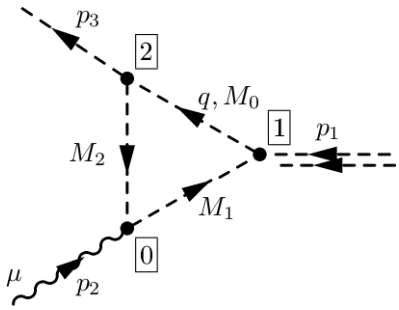

$\boxed{0} : ig_0 \left[2q - p_3 - p_1\right]^\mu$

$\boxed{1} : ig_1$

$\boxed{2} : ig_2$

$$\mathbf{C}\left[p_1^2, p_2^2, p_3^2, M_0^2, M_1^2, M_2^2\right]$$

$$A_0 = g_0 g_1 g_2 \left[C_0 + 2C_1\right] \qquad A_1 = g_0 g_1 g_2 \left[C_0 + 2C_2\right]$$

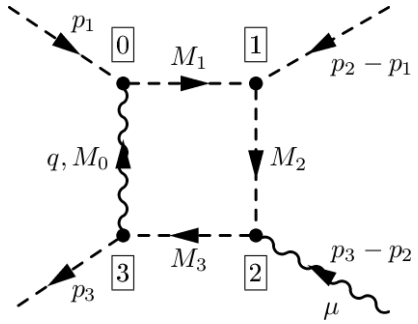

$\boxed{0} : ig_0 \left[q + 2p_1\right]^{\alpha}$
$\boxed{1} : ig_1$
$\boxed{2} : ig_2 \left[2q + p_2 + p_3\right]^{\mu}$
$\boxed{3} : ig_3 \left[q + 2p_3\right]^{\beta}$

$\mathbf{C}^{(a)} \left[p_1^2, (p_2 - p_1)^2, p_2^2, M_0^2, M_1^2, M_2^2\right]$, $\mathbf{C}^{(b)} \left[p_2^2, (p_3 - p_2)^2, p_3^2, M_0^2, M_2^2, M_3^2\right]$,
$\mathbf{C}^{(c)} \left[(p_2 - p_1)^2, (p_3 - p_2)^2, (p_3 - p_1)^2, M_1^2, M_2^2, M_3^2\right]$,
$\mathbf{D} \left[p_1^2, (p_2 - p_1)^2, (p_3 - p_2)^2, p_3^2, p_2^2, (p_1 - p_3)^2, M_0^2, M_1^2, M_2^2, M_3^2\right]$

$$
\begin{aligned}
A_0 &= -2g_0g_1g_2g_3 \left[C_1^{(a)} + C_1^{(c)} + C_2^{(c)} + C_0^{(c)} - (M_0^2 - M_1^2 - M_3^2 - 4(p_1 \cdot p_3) + p_1^2 + p_3^2)D_1\right] \\
A_1 &= -g_0g_1g_2g_3 \Big[2(C_1^{(b)} - C_1^{(c)} + C_2^{(a)}) + C_0^{(a)} + C_0^{(b)} - C_0^{(c)} - (M_0^2 - M_1^2 - M_3^2 - 4(p_1 \cdot p_3) \\
&\qquad + p_1^2 + p_3^2)(2D_2 + D_0)\Big] \\
A_2 &= -g_0g_1g_2g_3 \Big[2(C_2^{(b)} - C_1^{(c)}) + C_0^{(a)} + C_0^{(b)} - C_0^{(c)} - (M_0^2 - M_1^2 - M_3^2 - 4(p_1 \cdot p_3) \\
&\qquad + p_1^2 + p_3^2)(2D_3 + D_0)\Big]
\end{aligned}
$$

A.3. VV-Final States

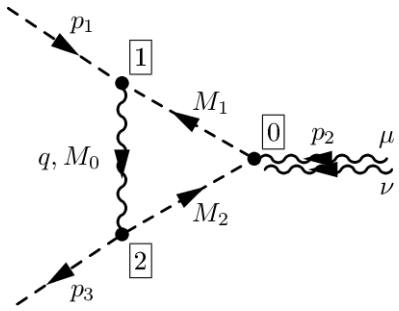

$\boxed{0} : ig_0 g^{\mu\nu}$
$\boxed{1} : ig_1 \left[2p_1 - q\right]^{\alpha}$
$\boxed{2} : ig_2 \left[2p_3 - q\right]^{\beta}$

$$\mathbf{B}\left[p_2^2, M_1^2, M_2^2\right], \quad \mathbf{C}\left[p_1^2, p_2^2, p_3^2, M_0^2, M_1^2, M_2^2\right]$$

$$\begin{aligned} A_0 &= g_0 g_1 g_2 \left[B_0 + M_0^2 C_0 + 2(p_1^2 C_1 + p_3^2 C_2 + (p_1 \cdot p_3)(2C_0 + C_1 + C_2)\right] \\ A_i &= 0 \ \ (i \in \{1,2,3,4\}) \end{aligned}$$

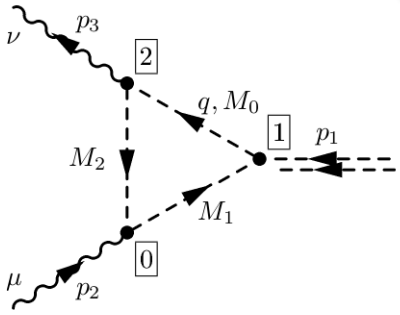

$\boxed{0} : ig_0 \left[2q - p_1 - p_3\right]^{\mu}$
$\boxed{1} : ig_1$
$\boxed{2} : ig_2 \left[2q - p_3\right]^{\nu}$

$$\mathbf{C}\left[p_1^2, p_2^2, p_3^2, M_0^2, M_1^2, M_2^2\right]$$

$$\begin{aligned} A_0 &= -4 g_0 g_1 g_2 C_{00} & A_1 &= -2 g_0 g_1 g_2 \left[C_1 + 2C_{11}\right] \\ A_2 &= -2 g_0 g_1 g_2 \left[C_0 + 2(C_1 + 2C_{12} + C_2)\right] & A_3 &= -2 g_0 g_1 g_2 \left[C_1 + 2C_{12}\right] \\ A_4 &= -g_0 g_1 g_2 \left[C_0 + 4(C_2 + C_{22})\right] \end{aligned}$$

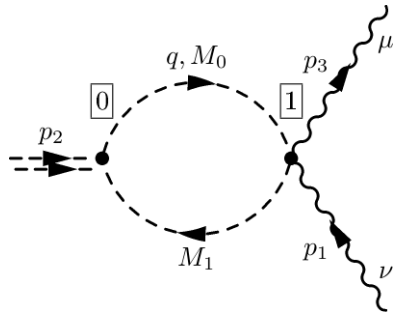

$\boxed{0} : ig_0$

$\boxed{1} : ig_1 g^{\mu\nu}$

$$\mathbf{B}\left[p_2^2, M_0^2, M_1^2\right]$$

$$A_0 \;=\; g_0 g_1 B_0 \qquad\qquad A_i \;=\; 0 \;\; (i \in \{1,2,3,4\})$$

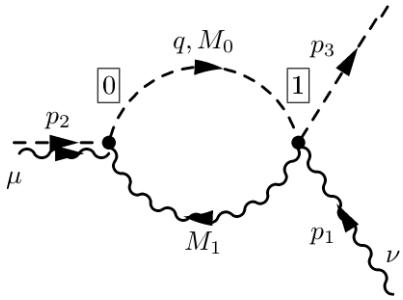

$\boxed{0} : ig_0 g^{\mu\beta}$

$\boxed{1} : ig_1 g^{\nu\alpha}$

$$\mathbf{B}\left[p_2^2, M_0^2, M_1^2\right]$$

$$A_0 \;=\; -g_0 g_1 B_0 \quad A_i \;=\; 0 \;\; (i \in \{1,2,3,4\})$$

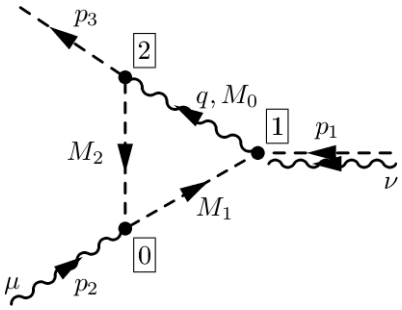

$\boxed{0} : ig_0 \left[2q - p_1 - p_3\right]^\mu$
$\boxed{1} : ig_1 g^{\nu\alpha}$
$\boxed{2} : ig_2 \left[q - 2p_3\right]^\beta$

$$\mathbf{C}\left[p_1^2, p_2^2, p_3^2, M_0^2, M_1^2, M_2^2\right]$$

$$\begin{aligned} A_0 &= 2g_0 g_1 g_2 C_0 & A_1 &= g_0 g_1 g_2 \left[C_1 + 2C_{11}\right] \\ A_2 &= g_0 g_1 g_2 \left[2C_0 + 4C_1 + 2C_{12} + C_2\right] & A_3 &= g_0 g_1 g_2 \left[C_1 + 2C_{12}\right] \\ A_4 &= g_0 g_1 g_2 \left[2C_0 + 5C_2 + 2C_{22})\right] \end{aligned}$$

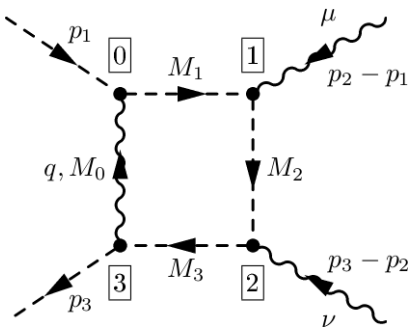

$\boxed{0} : ig_0 \left[2p_1 + q\right]^\alpha$
$\boxed{1} : ig_1 \left[2q + p_1 + p_2\right]^\mu$
$\boxed{2} : ig_2 \left[2q + p_2 + p_3\right]^\nu$
$\boxed{3} : ig_3 \left[2p_3 + q\right]^\beta$

$\mathbf{C}^{(a)}\left[p_1^2, (p_2 - p_1)^2, p_2^2, M_0^2, M_1^2, M_2^2\right]$, $\mathbf{C}^{(b)}\left[p_2^2, (p_3 - p_2)^2, p_3^2, M_0^2, M_2^2, M_3^2\right]$,
$\mathbf{C}^{(c)}\left[(p_2 - p_1)^2, (p_3 - p_2)^2, (p_3 - p_1)^2, M_1^2, M_2^2, M_3^2\right]$,
$\mathbf{D}\left[p_1^2, (p_2 - p_1)^2, (p_3 - p_2)^2, p_3^2, p_2^2, (p_1 - p_3)^2, M_0^2, M_1^2, M_2^2, M_3^2\right]$

$$
\begin{aligned}
A_0 &= -4g_0g_1g_2g_3\Big[C_{00}^{(a)}+C_{00}^{(b)}-C_{00}^{(c)}+D_{00}(-{M_0}^2+{M_1}^2+{M_3}^2)-D_{00}(-4p_1\cdot p_3+{p_1}^2+{p_3}^2)\Big]\\
A_1 &= 2g_0g_1g_2g_3\Big[C_0^{(c)}-2C_{11}^{(a)}+2C_{11}^{(c)}+4C_{12}^{(c)}-C_1^{(a)}+3C_1^{(c)}+2C_{22}^{(c)}+3C_2^{(c)}+(D_1+2D_{11})\\
&\quad\times({M_0}^2-{M_1}^2-{M_3}^2)+(D_1+2D_{11})(-4p_1\cdot p_3+{p_1}^2+{p_3}^2)\Big]\\
A_2 &= -g_0g_1g_2g_3\Big[C_0^{(a)}+C_0^{(b)}+C_0^{(c)}+4C_{11}^{(c)}+4C_{12}^{(a)}+4C_{12}^{(c)}+2C_1^{(a)}+2C_1^{(b)}+4C_1^{(c)}+2C_2^{(a)}\\
&\quad+2C_2^{(c)}-({M_0}^2-{M_1}^2-{M_3}^2)(D_0+2(D_1+2D_{12}+D_2))-(-4p_1\cdot p_3+{p_1}^2+{p_3}^2)\\
&\quad\times(D_0+2(D_1+2D_{12}+D_2))\Big]\\
A_3 &= -2g_0g_1g_2g_3\Big[C_0^{(c)}+2C_{11}^{(c)}+2C_{12}^{(a)}+2C_{12}^{(c)}+C_1^{(a)}+3C_1^{(c)}+C_2^{(c)}-(D_1+2D_{12})\\
&\quad\times({M_0}^2-{M_1}^2-{M_3}^2)-(D_1+2D_{12})(-4p_1\cdot p_3+{p_1}^2+{p_3}^2)\Big]\\
A_4 &= -g_0g_1g_2g_3\Big[C_0^{(a)}+C_0^{(b)}+C_0^{(c)}+4C_{12}^{(c)}+2C_1^{(a)}+2C_1^{(c)}+4C_{22}^{(c)}+2C_2^{(b)}+4C_2^{(c)}\\
&\quad-({M_0}^2-{M_1}^2-{M_3}^2)(D_0+2(D_1+2D_{13}+D_3))-(-4p_1\cdot p_3+{p_1}^2+{p_3}^2)\\
&\quad\times(D_0+2(D_1+2D_{13}+D_3))\Big]\\
A_5 &= -4g_0g_1g_2g_3\Big[C_{12}^{(c)}+C_{22}^{(c)}+C_2^{(c)}+D_{13}(-{M_0}^2+{M_1}^2+{M_3}^2)-D_{13}(-4p_1\cdot p_3+{p_1}^2+{p_3}^2)\Big]\\
A_6 &= -g_0g_1g_2g_3\Big[C_0^{(a)}+C_0^{(b)}-C_0^{(c)}+4C_{11}^{(b)}-4C_{11}^{(c)}+4C_1^{(b)}-4C_1^{(c)}+4C_{22}^{(a)}+4C_2^{(a)}\\
&\quad-(D_0+4(D_2+D_{22}))({M_0}^2-{M_1}^2-{M_3}^2)-(D_0+4(D_2+D_{22}))(-4p_1\cdot p_3+{p_1}^2+{p_3}^2)\Big]\\
A_7 &= -g_0g_1g_2g_3\Big[C_0^{(a)}+C_0^{(b)}-C_0^{(c)}+4C_{12}^{(b)}-4C_{12}^{(c)}+2C_1^{(b)}-2C_1^{(c)}+2C_2^{(a)}+2C_2^{(b)}\\
&\quad-2C_2^{(c)}-({M_0}^2-{M_1}^2-{M_3}^2)(D_0+2(D_2+2D_{23}+D_3))-(-4p_1\cdot p_3+{p_1}^2+{p_3}^2)\\
&\quad\times(D_0+2(D_2+2D_{23}+D_3))\Big]\\
A_8 &= -2g_0g_1g_2g_3\Big[2C_{12}^{(b)}-2C_{12}^{(c)}+C_2^{(b)}-C_2^{(c)}-(2D_{23}+D_3)({M_0}^2-{M_1}^2-{M_3}^2)-(2D_{23}+D_3)\\
&\quad\times(-4p_1\cdot p_3+{p_1}^2+{p_3}^2)\Big]\\
A_9 &= -2g_0g_1g_2g_3\Big[2C_{22}^{(b)}-2C_{22}^{(c)}+C_2^{(b)}-C_2^{(c)}-(D_3+2D_{33})({M_0}^2-{M_1}^2-{M_3}^2)-(D_3+2D_{33})\\
&\quad\times(-4p_1\cdot p_3+{p_1}^2+{p_3}^2)\Big]
\end{aligned}
$$

B. Dipole Formulas

With regard to Ref. [204], further important formulas and definitions are presented here. The definitions of the quantities used in Eqs. (5.220) and (5.219) are:

$$\lambda(x,y,z) \;=\; x^2+y^2+z^2-2xy-2xz-2yz, \tag{B.1}$$

$$\tilde{z}_j \;=\; \frac{k_j k_k}{k_i k_k + k_j k_k}, \tag{B.2}$$

$$y_{ij,k} \;=\; \frac{k_j k_i}{k_i k_k + k_j k_k + k_i k_j}, \tag{B.3}$$

$$v_{ij,k} \;=\; \frac{\sqrt{[2\mu_k^2+(1-\mu_i^2-\mu_j^2-\mu_k^2)(1-y_{ij,k})]^2-4\mu_k^2}}{(1-\mu_i^2-\mu_j^2-\mu_k^2)(1-y_{ij,k})}, \tag{B.4}$$

$$\mu_i \;=\; \frac{m_i}{\sqrt{s}}, \tag{B.5}$$

$$\mu_{ij}^2 \;=\; \frac{m_i^2+m_j^2}{(k_i+k_j)^2-m_{ij}^2}, \tag{B.6}$$

$$\tilde{v}_{ij,k} \;=\; \frac{\lambda^{1/2}\big(1,\mu_{ij}^2,\mu_k^2\big)}{1-\mu_{ij}^2-\mu_k^2}. \tag{B.7}$$

The definitions used in Eq. (5.227) take the form

$$s_{jk} = 2k_j \cdot k_k, \tag{B.8}$$

$$\mathrm{K}_q \;=\; \left[\frac{7}{2}-\frac{\pi^2}{6}\right] C_F, \tag{B.9}$$

$$\gamma_q \;=\; \frac{3}{2} C_F \tag{B.10}$$

as well as

$$\Gamma_q(\mu, m_q; \epsilon) \;=\; C_F\left[\frac{1}{\epsilon}+\frac{1}{2}\ln\frac{m_q^2}{\mu^2}-2\right] \tag{B.11}$$

for massive quarks and

$$\Gamma_q(\epsilon) \;=\; \frac{1}{\epsilon}\gamma_q \tag{B.12}$$

for massless quarks. Finally, the singular part of Eq. (5.228) for all possible combinations of emitter-spectator masses are

$$\begin{aligned}\mathcal{V}^{(\mathrm{S})}(s_{jk}, m_j > 0, m_k > 0; \epsilon) &= \frac{1}{v_{jk}}\left[\frac{1}{\epsilon}\log\big(\rho\big) - \frac{1}{4}\log^2\big(\rho_j^2\big) - \frac{1}{4}\log^2\big(\rho_k^2\big) - \frac{\pi^2}{6}\right] \\ &\quad + \frac{1}{v_{jk}}\log\big(\rho\big)\log\left(\frac{Q_{jk}^2}{s_{jk}}\right), \end{aligned} \tag{B.13}$$

$$\begin{aligned}\mathcal{V}^{(\mathrm{S})}(s_{jk}, m_j > 0, 0; \epsilon) &= \frac{1}{2\epsilon^2} + \frac{1}{2\epsilon}\log\left(\frac{m_j^2}{s_{jk}}\right) - \frac{1}{4}\log^2\left(\frac{m_j^2}{s_{jk}}\right) - \frac{\pi^2}{12} \\ &\quad - \frac{1}{2}\log\left(\frac{m_j^2}{s_{jk}}\right)\log\left(\frac{s_{jk}}{Q_{jk}^2}\right) \\ &\quad - \frac{1}{2}\log\left(\frac{m_j^2}{Q_{jk}^2}\right)\log\left(\frac{s_{jk}}{Q_{jk}^2}\right), \end{aligned} \tag{B.14}$$

$$\mathcal{V}^{(\mathrm{S})}(s_{jk}, 0, 0; \epsilon) = \frac{1}{\epsilon^2}. \tag{B.15}$$

The non-singular part takes the form

$$\begin{aligned}\mathcal{V}_q^{(\mathrm{NS})}(s_{jk}, m_j > 0, m_k > 0) &= \frac{\gamma_q}{\mathbf{T}_q^2}\log\left(\frac{s_{jk}}{Q_{jk}^2}\right) - \frac{m_k}{Q_{jk} - m_k} + \frac{2m_k(2m_k - Q_{jk})}{s_{jk}} + \frac{\pi^2}{2} \\ &\quad + \frac{1}{v_{jk}}\Bigg[\log\big(\rho^2\big)\log\big(1+\rho^2\big) + 2\mathrm{Li}_2\big(\rho^2\big) - \mathrm{Li}_2\big(1-\rho_j^2\big) \\ &\quad - \mathrm{Li}_2\big(1-\rho_k^2\big) - \frac{\pi^2}{6}\Bigg] + \log\left(\frac{Q_{jk} - m_k}{Q_{jk}}\right) \\ &\quad - 2\log\left(\frac{(Q_{jk} - m_k)^2 - m_j^2}{Q_{jk}^2}\right) \\ &\quad - \frac{2m_j^2}{s_{jk}}\log\left(\frac{m_j}{Q_{jk} - m_k}\right), \end{aligned} \tag{B.16}$$

$$\begin{aligned}\mathcal{V}_q^{(\mathrm{NS})}(s_{jk}, m_j > 0, 0) &= \frac{\gamma_q}{\mathbf{T}_q^2}\log\left(\frac{s_{jk}}{Q_{jk}^2}\right) + \frac{\pi^2}{6} - \mathrm{Li}_2\left(\frac{s_{jk}}{Q_{jk}^2}\right) - 2\log\left(\frac{s_{jk}}{Q_{jk}^2}\right) \\ &\quad - \frac{m_j^2}{s_{jk}}\log\left(\frac{m_j^2}{Q_{jk}^2}\right), \end{aligned} \tag{B.17}$$

$$\begin{aligned}\mathcal{V}_q^{(\mathrm{NS})}(s_{jk}, 0, m_k > 0) &= \frac{\gamma_q}{\mathbf{T}_q^2}\left[\log\left(\frac{s_{jk}}{Q_{jk}^2}\right) - 2\log\left(\frac{Q_{jk} - m_k}{Q_{jk}}\right) - \frac{2m_k}{Q_{jk} + m_k}\right] \\ &\quad + \frac{\pi^2}{6} - \mathrm{Li}_2\left(\frac{s_{jk}}{Q_{jk}^2}\right), \end{aligned} \tag{B.18}$$

$$\mathcal{V}_q^{(\mathrm{NS})}(s_{jk}, 0, 0) = 0. \tag{B.19}$$

Here we have used

$$\rho_n(\omega_j, \omega_k) = \sqrt{\frac{1 - v_{j,k} + 2\omega_n/(1-\omega_j-\omega_k)}{1 + v_{j,k} + 2\omega_n/(1-\omega_j-\omega_k)}} \tag{B.20}$$

for $n = j, k$ and

$$\rho = \sqrt{\frac{1 - v_{j,k}}{1 + v_{j,k}}} \tag{B.21}$$

with

$$\omega_n = \frac{m_n^2}{Q_{jk}^2}, \tag{B.22}$$

$$Q_{jk} = \sqrt{Q_{jk}^2} = \sqrt{s_{jk} + m_j^2 + m_k^2}, \tag{B.23}$$

$$v_{j,k} = \frac{\sqrt{\lambda((k_j + k_k)^2, k_j^2, k_k^2)}}{(k_j + k_k)^2 - k_j^2 - k_k^2}. \tag{B.24}$$

C. The Coulomb Corrections

The function $\tilde{\Gamma}(p,q)$ serves as a starting point, which we require to fulfill the iterative equation

$$\tilde{\Gamma}(p,q) \;=\; 1+\int\frac{\mathrm{d}k^4}{(2\pi)^4}\frac{-\tilde{\Gamma}(k,q)}{\left[(\frac{q}{2}+k)^2-m_{\tilde{q}}^2+im_{\tilde{q}}\tilde{\Gamma}_{\tilde{q}}\right]\left[(\frac{q}{2}-k)^2-m_{\tilde{q}}^2+im_{\tilde{q}}\tilde{\Gamma}_{\tilde{q}}\right]} \times\left(\frac{-ig_s^2C_F(k+p+q)_\mu(k+p-q)^\mu}{(p-k)^2}\right) \tag{C.1}$$

as depicted in Fig. C.1. Eq. (C.1) is the so called Bethe-Salpeter equation [229], specified to our needs. We assume that the incoming scalar particles possess equal masses and

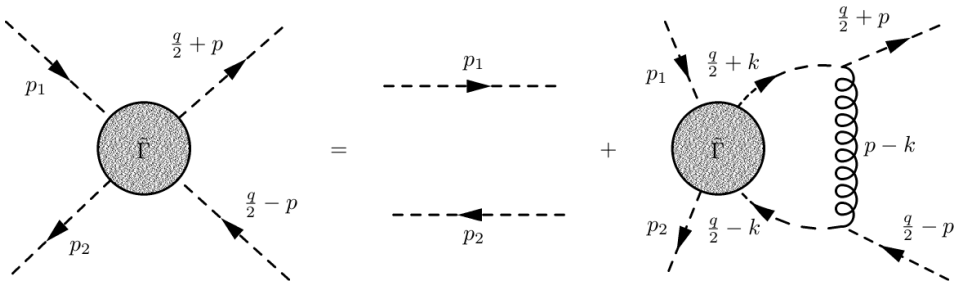

Figure C.1.: Iterative equation for $\tilde{\Gamma}$.

form a color singlet $1/N_c\sum_{ij}T^a_{ij}T^a_{ji}=C_F$ already averaged over incoming colors. If one can now explicitly construct a function $\tilde{\Gamma}(p,q)$ that fulfills Eq. (C.1), *it would sum up all ladder insertions to infinite order in perturbation theory* as depicted in Fig. 5.33. This can be seen by iteratively substituting the diagrammatic expression for Γ on the right hand side of Fig. C.1. We now set q to $q^\intercal=(2m_{\tilde{q}}+E,\vec{0})$, where E is the kinetic plus binding energy (in the CMS) of the incoming squark-antisquark (quasi-squarkonium) system.
Making use of the threshold expansion of Feynman integrals as described in Ref. [231], the non-relativistic limit of Eq. (C.1) is then reached by an expansion in the relative velocity v using the counting[1] $p_0,k_0\sim v^2$, $|\vec{p}|,|\vec{k}|\sim v$. Assuming $E\ll m_{\tilde{q}}$, Eq. (C.1) can then be brought to the form

$$\tilde{\Gamma}(p,q)\approx 1+\int\frac{\mathrm{d}k^4}{(2\pi)^4}\frac{-\tilde{\Gamma}(k,q)}{\left[2m_{\tilde{q}}(E/2+k_0-\frac{\vec{k}^2}{2m_{\tilde{q}}}+i\frac{\tilde{\Gamma}_{\tilde{q}}}{2})\right]\left[2m_{\tilde{q}}(E/2-k_0-\frac{\vec{k}^2}{2m_{\tilde{q}}}+i\frac{\tilde{\Gamma}_{\tilde{q}}}{2})\right]} \times\left(4m_{\tilde{q}}^2i\tilde{V}(|\vec{p}-\vec{k}|)\right). \tag{C.2}$$

Here, we have approximated

$$\frac{-ig_s^2C_F(k+p+q)_\mu(k+p-q)^\mu}{(p-k)^2}\approx\frac{-ig_s^2C_F4m_{\tilde{q}}^2}{|\vec{p}-\vec{k}|^2}\;=:\;4m_{\tilde{q}}^2i\tilde{V}(|\vec{p}-\vec{k}|) \tag{C.3}$$

[1]Note that we actually integrate over k after this expansion.

and, moreover, assumed that the squark width $\Gamma_{\tilde{q}}$ is momentum independent. $\tilde{V}(|\vec{p}-\vec{k}|)$ is the Fourier transformed of the leading order QCD-potential for a color-singlet

$$V(|\vec{r}|) \;=\; -\frac{C_F \alpha_s}{|\vec{r}|} \tag{C.4}$$

with $\alpha_s = g_s^2/4\pi$. This leading order potential can be supplemented by additional perturbative corrections (see Eq. (5.249)), e.g., a quark loop inserted into the gluon line. These contributions, approximated in the non-relativistic limit and calculated up to a certain order in α_s, are then repeatedly inserted between the incoming squark lines.
As it turns out that $\tilde{\Gamma}(p,q)$ in Eq. (C.2) is actually independent of p_0 ($\tilde{\Gamma}(p,q) \to \tilde{\Gamma}(\vec{p},q)$), we may assume the same for $\tilde{\Gamma}(k,q)$ in terms of k_0. This allows us to perform the k_0 integration of Eq. (C.2) using the residual theorem. Picking up the pole in the upper complex plane, we end up with the result

$$\tilde{\Gamma}(\vec{p},q) \;=\; 1 + \int \frac{\mathrm{d}k^3}{(2\pi)^3} \frac{\tilde{\Gamma}(\vec{k},q)\tilde{V}(|\vec{p}-\vec{k}|)}{\left[E - \frac{\vec{k}^2}{m_{\tilde{q}}} + i\Gamma_{\tilde{q}}\right]}. \tag{C.5}$$

We further define

$$\tilde{G}(\vec{k}, E + i\Gamma_{\tilde{q}}) \;:=\; -\frac{1}{\left[E - \frac{\vec{k}^2}{m_{\tilde{q}}} + i\tilde{\Gamma}_{\tilde{q}}\right]} \tilde{\Gamma}(\vec{k}, E + i\Gamma_{\tilde{q}}), \tag{C.6}$$

where we have used $\tilde{\Gamma}(\vec{k},q) = \tilde{\Gamma}(\vec{k}, E + i\Gamma_{\tilde{q}})$ since $\vec{q} = \vec{0}$ as introduced above. Plugging Eq. (C.6) into Eq. (C.5), we find

$$\left[\frac{\vec{p}^2}{m_{\tilde{q}}} - (E + i\tilde{\Gamma}_{\tilde{q}})\right] \tilde{G}(\vec{p}, E + i\Gamma_{\tilde{q}}) + \int \frac{\mathrm{d}^3 k}{(2\pi)^3} \tilde{V}(|\vec{p}-\vec{k}|)\tilde{G}(\vec{k}, \tilde{E} + i\Gamma_{\tilde{q}}) \;=\; 1, \tag{C.7}$$

where the one on the left hand side just symbolizes the lack of any interactions (see Fig. C.1 and Eq. (C.14) below). Eq. (C.7) can be expressed in position space via its Fourier transformed $G(\vec{r}, E + i\Gamma_{\tilde{q}})$ ($= G(\vec{r}, \vec{r}' = 0, E + i\Gamma_{\tilde{q}})$) as

$$\left[H - (E + i\Gamma_{\tilde{q}})\right] G(\vec{r}, E + i\Gamma_{\tilde{q}}) \;=\; \delta^{(3)}(\vec{r}) \tag{C.8}$$

with

$$H \;=\; -\frac{1}{m_{\tilde{q}}}\nabla^2 + V(|\vec{r}|). \tag{C.9}$$

Eq. (C.8) describes the propagation of the squarkonium with reduced mass $m_{\tilde{q}\tilde{q}^*} = m_{\tilde{q}}/2$ and total decay width $\Gamma_{\tilde{q}\tilde{q}^*} = 2\Gamma_{\tilde{q}}$. $\Pi(q^2)$ is the full (Coulomb-)loop corrected matrix element connected to the Fourier transformed of $\tilde{\Gamma}$. It can be related the fully corrected Coulomb cross section σ^{Coul} via the optical theorem Eq. (5.175). Together with Fig. C.2, this finally yields

$$\sigma^{\mathrm{Coul}}\big(\tilde{q}\tilde{q}^* \to \mathrm{EW}\big) \;=\; N\, \Im\{\Pi(q^2)\} \times \sigma^{\mathrm{LO}}\big(\tilde{q}\tilde{q}^* \to \mathrm{EW}\big) \tag{C.10}$$

with

$$
\begin{aligned}
i\Pi(q^2) &= \int \frac{\mathrm{d}p^4}{(2\pi)^4} \frac{-\tilde{\Gamma}(p,q)}{\left[(\frac{q}{2}+p)^2 - m_{\tilde{q}}^2 + i m_{\tilde{q}}\tilde{\Gamma}_{\tilde{q}}\right]\left[(\frac{q}{2}-p)^2 - m_{\tilde{q}}^2 + i m_{\tilde{q}}\tilde{\Gamma}_{\tilde{q}}\right]} \\
&\approx \frac{1}{4m_{\tilde{q}}^2} \int \frac{\mathrm{d}p^3}{(2\pi)^3} \frac{-i\tilde{\Gamma}(\vec{p},q)}{\left[E - \frac{\vec{p}^2}{m_{\tilde{q}}} + i\Gamma_{\tilde{q}}\right]} \\
&= \frac{i}{4m_{\tilde{q}}^2} \int \frac{\mathrm{d}p^3}{(2\pi)^3} \tilde{G}(\vec{p}, E + i\Gamma_{\tilde{q}}) \\
&= \frac{i}{4m_{\tilde{q}}^2} G(\vec{r}=\vec{0}, E + i\Gamma_{\tilde{q}}).
\end{aligned} \tag{C.11}
$$

In Eq. (C.10), N is a normalization factor, which is chosen in order that $\sigma^{\mathrm{Coul}} \to \sigma^{\mathrm{LO}}$ is

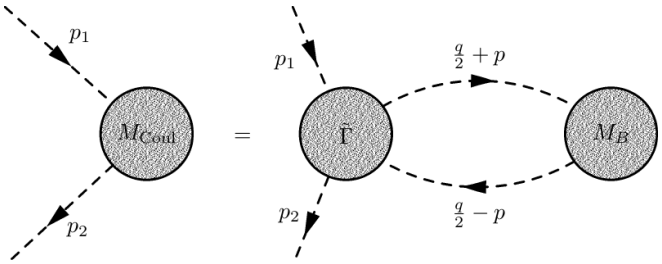

Figure C.2.: Connection between $\tilde{\Gamma}$ and the Born-level matrix element.

fulfilled in the limit $\alpha_s \to 0$ (see Eq. (5.246)). Note that in Eq. (C.11), we have implicitly assumed that the hard part σ^{LO} is independent of the momentum p. This assumption leads to the simple, factorized form of Eq. (C.10). However, this does not apply to the general case though it turns out to be a good approximation for the case of dominant s-wave annihilation (see Sec. 5.3). In this case the Coulomb corrected cross section σ^{Coul} can simply be related to the Born-level cross section σ^{LO} via [152]

$$
\frac{\sigma^{\mathrm{Coul}}}{\sigma^{\mathrm{LO}}} = |\psi(\vec{r}=\vec{0})|^2, \tag{C.12}
$$

where ψ is the solution to the stationary Schrödinger equation with the squarkonium Hamilton operator Eq. (C.9) and the energy eigenvalue $E + i\Gamma_{\tilde{q}}$. Its connection to the Green function takes the form

$$
\psi(\vec{r}) = \int \mathrm{d}^3 r' G(\vec{r}, \vec{r}', E + i\Gamma_{\tilde{q}}) V(|\vec{r'}|) \psi(\vec{r}'), \tag{C.13}
$$

which can be iteratively solved for $\psi(\vec{r})$ (see below).
To calculate $G(\vec{r}, \vec{r'}, E + i\Gamma_{\tilde{q}})$ we go back to Eq. (C.7), which we write in the more general form

$$
\left(\frac{\vec{p}^2}{m_{\tilde{q}}} - E\right) \tilde{G}(\vec{p}, \vec{p}', E + i\Gamma_{\tilde{q}}) + \int \frac{\mathrm{d}^3 k}{(2\pi)^3} \tilde{V}(\vec{k}) \tilde{G}(\vec{p} - \vec{k}, \vec{p}' \tilde{E}) = (2\pi)^3 \delta^{(3)}(\vec{p} - \vec{p}'). \tag{C.14}
$$

Here, we define $\tilde{E} = E + i\Gamma_{\tilde{q}}$. Eq. (C.14) can be brought to the form

$$
\tilde{G}(\vec{p}, \vec{p}', E + i\Gamma_{\tilde{q}}) = \frac{(2\pi)^3 \delta^{(3)}(\vec{p} - \vec{p}')}{\frac{\vec{p}^2}{m_{\tilde{q}}} - E} - \int \frac{\mathrm{d}^3 k}{(2\pi)^3} \tilde{V}(\vec{k}) \tilde{G}(\vec{p} - \vec{k}, \vec{p}' \tilde{E}), \tag{C.15}
$$

which allows us to iteratively determine $\tilde{G}(\vec{p},\vec{p}',E+i\Gamma_{\tilde{q}})$. Eq. (C.15) describes the propagation of a particle that undergoes repeated scattering at the potential $\tilde{V}(\vec{k})$. Starting with the propagator of a free particle

$$\tilde{G}^{(0)}(\vec{p},\vec{p}',E+i\Gamma_{\tilde{q}}) \;=\; \frac{(2\pi)^3\delta^{(3)}(\vec{p}-\vec{p}')}{\frac{\vec{p}^2}{m_{\tilde{q}}}-E} \tag{C.16}$$

on the right hand side of Eq. (C.15), we can calculate the Green function of the (re)scattered particle (C.15) iteratively to higher orders in the potential V (i.e, in higher orders of α_s). Here, Eq. (C.16) and Eq. (C.15) (iterated once) used together with the potential defined in Eq. (C.3) are already sufficient to resum all terms of $\mathcal{O}((\alpha_s/v)^n)$ to all orders in n. Hence, to end up with a Green function, calculated at the required accuracy as a solution of Eq. (C.14) (here, we use the NRQCD counting $\alpha_s \simeq v$ again) one has to do both, enough iterations (with a potential of appropriate accuracy in $\mathcal{O}(\alpha_s)$ which is repeatedly inserted into Eq. (C.14)) as well as using the potential $\tilde{V}(\vec{k})$ calculated up to the required order in perturbation theory (which is inserted only once)

$$G^{(n)} \;=\; \underbrace{G^{(0)}V|_{\mathcal{O}(\alpha_s)}G^{(0)}...G^{(0)}V|_{\mathcal{O}(\alpha_s)}G^{(0)}}_{\text{n times}} + ... + G^{(0)}V|_{\mathcal{O}(\alpha_s^n)}G^{(0)}. \tag{C.17}$$

The Green function $G(\vec{r},\vec{r'},E+i\Gamma_{\tilde{q}})$ can be finally obtained from the Fourier transformation of Eq. (C.15). In Eq. (C.11), it turns out that we actually need the Green function at the origin $G(\vec{r}=\vec{0},\vec{r'}=\vec{0},E+i\Gamma_{\tilde{q}})$, which features an ultraviolet divergence. We use dimensional regularization to render $G(\vec{r},\vec{r'},E+i\Gamma_{\tilde{q}})$ well defined at the origin

$$G(\vec{r},\vec{r'},E+i\Gamma_{\tilde{q}})\Big|_{\vec{r}=\vec{0},\vec{r'}=\vec{0}} \;=\; \left(\frac{\mu_G^2 e^{\gamma_E}}{4\pi}\right)^{\epsilon}\int\frac{d^d\vec{p}}{(2\pi)^d}\frac{d^d\vec{p}'}{(2\pi)^d}\tilde{G}(\vec{p},\vec{p}',E+i\Gamma_{\tilde{q}}) \tag{C.18}$$

with $d+1=4-2\epsilon$. The choice of the prefactor in Eq. (C.18) corresponds to the subtraction of the divergence in the $\overline{MS}$-scheme, i.e., subtracting the $1/\epsilon$-pole plus the additional terms $-\gamma_E+\ln(4\pi)$. The used potential $\tilde{V}(\vec{k})$ up to $\mathcal{O}(\alpha_s^2)$ as well as the corresponding result for $G(\vec{r}=\vec{0},\vec{r}'=\vec{0},E+i\Gamma_{\tilde{q}})$ are both given in Sec. 5.3.

D. The Hypergeometric Function

The hypergeometric function is defined as

$$ {}_pF_q(a_1, a_2, ..., a_p; b_1, b_2, ..., b_q; z) \; = \; \sum_{n=0}^{\infty} \frac{(a_1)_n (a_2)_n \dots (a_p)_n}{(b_1)_n (b_2)_n \dots (b_q)_n} \frac{z^n}{n!} \tag{D.1} $$

with the restriction $b_{\rm i} \neq 0, -1, ...$ for $i = 1, 2, ..., q$, where $(x)_n = \tilde{\Gamma}(x+n)/\tilde{\Gamma}(x)$ are the Pochhammer symbols. The series defined by Eq. (D.1) converges for ${}_4\mathrm{F}_3(1,1,1,1;2,2,1-\kappa;1)$, if

$$ \Re\left\{ \sum_{\rm n=1}^{\rm q} {\rm b_n} - \sum_{\rm n=1}^{\rm q+1} {\rm a_n} \right\} > 0. \tag{D.2} $$

To improve on the convergence of this series we have repeatedly employed

$$ \begin{aligned} {}_4\mathrm{F}_3(1,1,1,1;a,a,x;1) \; = \; & \frac{1}{a^2 x (x-2(2-a))(a-x)^2} \Big[a^2 (x-1)^4 \; {}_4\mathrm{F}_3(1,1,1,1;a,a,x+1;1) \\ & + a(a-1)^3 x (3a+1-4x) \; {}_4\mathrm{F}_3(1,1,1,1;a+1,a,x;1) \\ & + (a-1)^4 x (x-a) \; {}_4\mathrm{F}_3(1,1,1,1;a+1,a+1,x;1) \Big], \end{aligned} \tag{D.3} $$

$$ \begin{aligned} {}_4\mathrm{F}_3(1,1,1,1;a,b,x;1) = & \frac{1}{a+b+x-4} \Big[\frac{(a-1)^4}{a(a-b)(a-x)} \; {}_4\mathrm{F}_3(1,1,1,1;a+1,b,x;1) \\ & + \frac{(b-1)^4}{b(b-a)(b-x)} \; {}_4\mathrm{F}_3(1,1,1,1;a,b+1,x;1) \\ & + \frac{(x-1)^4}{x(x-a)(x-b)} {}_4\mathrm{F}_3(1,1,1,1;a,b,x+1;1) \Big], \end{aligned} \tag{D.4} $$

which is valid for $x \neq -1, -2, \dots$ and $a, b \in \mathbb{N}/\{0,1\}$, $a \neq b$ [220, 232].

Bibliography

[1] B. Herrmann, M. Klasen, K. Kovařík, M. Meinecke and P. Steppeler, Phys. Rev. D **89**, 114012 (2014) [arXiv:1404.2931 [hep-ph]].

[2] J. Harz, B. Herrmann, M. Klasen, K. Kovak and M. Meinecke, Phys. Rev. D **91**, 034012 (2015) [arXiv:1410.8063 [hep-ph]].

[3] M. Drees, R. M. Godbole and P. Roy, *Theory and Phenomoenology of Sparticles* (World Scientific, 2004)

[4] S. Weinberg, Phys. Rev. D**13**, 974 (1976)

G. 't Hooft, *Recent Developments in Gauge Theories* (Plenum, New York, 1980)

[5] G. Aad *et al.* [ATLAS Collaboration], Phys. Lett. B **716** (2012) 1 [arXiv:1207.7214 [hep-ex]].

[6] S. Chatrchyan *et al.* [CMS Collaboration], Phys. Lett. B **716** (2012) 30 [arXiv:1207.7235 [hep-ex]].

[7] H. Murayama, [arXiv:9410285v1 [hep-ph]].

[8] K. D. Lane, [arXiv:9401324v2 [hep-ph]].

[9] R. Foot, A. Kobakhidze and R. R. Volkas, Phys. Lett. B**655**, 156 (2007) [arXiv:0704.1165v3 [hep-ph]].

[10] S. R. Coleman and J. Mandula, Phys. Rev. D**159**, 1251 (1967).

[11] R. Haag, J. T. Łopuszański and M. Sohnius, Nucl. Phys. B**88**, 257 (1975).

[12] M. E. A. Peskin and D. V. A. Schroeder, Advanced book classics (Addison-Wesley Publishing Company 1995).

[13] L. O'Raifeartaigh, Nucl. Phys. B**96**, 331 (1975).

[14] P. Fayet and J. Iliopoulos, Phys. Lett. B**51**, 461 (1974).

[15] R. Barbier, C. Berat *et al.*, Phys. Rept. **420**, 1 (2005) [arXiv:0406039v2 [hep-ph]].

[16] K. S. Babu and Y. Mimura, [arXiv:0101046v1 [hep-ph]].

[17] J. Rosiek, hep-ph/9511250.

[18] A. Djouadi *et al.* [MSSM working group], [arXiv:9901246v1 [hep-ph]].

[19] K. Garett and G. Dūda, Adv. Astron. 968283 (2011) [arXiv:1006.2483v2 [astro-ph.CO]].

[20] J. H. Oort, Bulletin of the Astronomical Institutes of the Netherlands. **4**, 249. (1932)

[21] F. Zwicky, Helv. Phys. Acta **6**, 110-127 (1933).

F. Zwicky, Ap. J. **86**, 217-246 (1937).

[22] V. C. Rubin, N. Thonnard and W. K. Jr. Ford, Astrophys. J. **238**,471 (1980)

[23] G. F. Bertone et al., *Particle Dark Matter: Observations, Models and Searches* (Cambridge University Press, 2010)

[24] G. Bertone, D. Hooper and J. Silk Phys. Rept. **405**,279-390 (2005) [arXiv:0404175 [hep-ph]].

[25] P. Schneider, *Einführung in die extragalaktische Astronomie*, Springer (2007)

[26] D. Clowe *et al.* , Astrophys. J. **648**, L109 (2006) [arXiv:0608407v1 [astro-ph]].

[27] J. F. Navarro, S. C. Frenk and D. M. S. White, Astrophys. J. **462**, 563 (1996) [arXiv:9508025v1 [astro-ph]].

[28] J. R. Primack and M. A. K. Gross, [arXiv:0007165v1 [astro-ph]].

[29] F. Stoehr, S. D. M. White, V. Springel, G. Tormen and N. Yoshida, Mon. Not. Roy. Astron. Soc. Lett. **345**, 1313 (2003). [arXiv:0307026v2 [astro-ph]].

[30] D. D. Xu, S. Mao, J. Wang *et al.*, Mon. Not. Roy. Astron. Soc. Lett. **398**, 1235 (2009). [arXiv:0903.4559v2 [astro-ph]].

[31] A. A .Klypin, A. V. Kravtsov, V. Andrey, O. Velenzuela and F. Prada, Astrophys. J. **522**, 82 (1999). [arXiv:9901240v2 [astro-ph]].

[32] H. J. de Vega and N. G. Sanchez, [arXiv:1304.0759v3 [astro-ph.CO]].

[33] K. Choi, K.-Y. Choi and C. S. Shin, Phys. Rev. D**86**, 083529 (2012) [arXiv:1208.2496v1 [hep-ph]].

[34] M. Viel, G. D. Becker, S. J. Bolton *et al*, Phys. Rev. Lett. **100**, 041304 (2008) [arXiv:0709.0131v2 [astro-ph]].

[35] A. Schneider, D. Anderhalden, A. Maccio and J. Diemand, Mon. Not. Roy. Astron. Soc. Lett. **441**, 6 (2014). [arXiv:1309.5960v4 [astro-ph.CO]].

[36] T. M. Brown, J. Tumlinson, M. Geha *et al.*, [arXiv:1310.0824v1 [astro-ph.CO]].

[37] M. White and W. Hu, Astron. Astrophys. **321**, 8 (1997) [arXiv:0109522v1 [astro-ph]].

[38] G. F. Smoot *et al.* , Astrophys. J. **396**, L1 (1992) [arXiv:1303.5076v3 [astro-ph.CO]].

[39] http://lambda.gsfc.nasa.gov

[40] S. Clesse, [arXiv:1501.00460v1 [astro-ph.CO]].

[41] W. Hu, N. Sugiyama and J. Silk, Nature **386**, 37 (1997) [arXiv:9604166v1 [astro-ph]].

[42] http://lambda.gsfc.nasa.gov

[43] D. Samtleben, S. Staggs and B. Winstein, J. Phys. Stud. **5**, 177 (2001) [arXiv:0109522v1 [astro-ph]].

[44] R. Durrer, Ann. Rev. Nucl. Part. Si. **57**, 245 (2007) [arXiv:0803.08346v1 [astro-ph]].

[45] P. A. R. Ade *et al.* [Planck Collaboration], Astron. Astrophys. **571**, A16 (2014) [arXiv:1303.5076v3 [astro-ph.CO]].

[46] http://www.deepspace.ucsb.edu/wp-content/uploads/2013/03/Planck_Cosmic-recipe-pie-chart_v51-1024x723.jpg

[47] M. Meinecke, loc. bib Universität Bonn.

[48] P. A. R. Ade *et al.* [BICEP2 Collaboration], Phys. Rev. Lett. **112**, 241101 (2014) [arXiv:1403.3985v3 [astro-ph.CO]].

[49] P. A. R. Ade *et al.* [BICEP2 Collaboration,Planck Collaboration], [arXiv:1502.00612v1 [astro-ph.CO]].

[50] W. L. Freedman *et al.*, Astrophys. J. **553**, 47 (2001) [arXiv:0012376v1 [astro-ph]].

[51] T. K. Hemmick, D. Elmore, T. Gentile *et al.*, Phys. Rev. D**41**, 2074 (1990).

[52] M. Drees amd G. Gerbier *et al.*, [arXiv:1204.2373v1 [hep-ph]].

[53] M. Taoso, G. Bertone and A. Masiero, JCAP. **0803**, 022 (2008) [arXiv:0711.4996v2 [astro-ph]].

[54] P. Gondolo, NATO. Sci. Ser. II **187**, 279 (2005) [arXiv:0403064v1 [astro-ph]].

[55] J. Harz, PhD thesis (2013), p. 238.

[56] M. W. Goodman and E. Witten Phys. Rev. D**31** (1985) 3059

[57] T. Saab [arXiv:1203.2566v1 [physics.ins-det]].

[58] R. W. Schnee [arXiv:1101.5205v1 [astro-ph.CO]].

[59] A. Kurylov and M. Kamionkowski Phys. Rev. D**69** (2004) 063503 [arXiv:0307185v1 [hep-ph]].

[60] R. Mahapatra Pramana **79**,1045-1057 (2012).

[61] R. Agnese *et al.*, Phys. Rev. Lett. **112**, 241302 (2014)

[62] E. Aprile *et al.* Phys. Rev. Lett. **2**, 021301 (2013) [arXiv:1301.6620v2 [astro-ph.CO]].

[63] M. Felizardo *et al.* Phys. Rev. Lett. **108**, 201302 (2012) [arXiv:1106.3014v3 [astro-ph.CO]].

[64] E. Behnke *et al.* Phys. Rev. D **86**, 052001 (2012) [arXiv:1204.3094v2 [astro-ph.CO]].

[65] M. Felizardo *et al.* Phys. Rev. D **89**, 072013 (2014) [arXiv:1404.4309v1 [hep-ph]].

[66] D. S. Akerib *et al.*, Phys. Rev. Lett. **112**, 091303 (2014)

[67] E. Aprile *et al.*, Phys. Rev. Lett. **109**, 181301 (2012) [arXiv:1207.5988v2 [astro-ph.CO]].

[68] K. A. Olive. *et al.*, Chin. Phys. **C38**, 090001 (2014). [arXiv:1412.1408v3 [astro-ph.CO]].

[69] G. Angloher *et al.*, [arXiv:1407.3146v1 [astro-ph.CO]].

[70] *Resonaances-more mess withdark matter detection*, July 31, 2013

[71] K. Freese,M. Lisanti and C. Savage, Rev. Mod. Phys. **85**, 1561 (2013) [arXiv:1209.3339v3 [astro-ph]].

[72] R. Barnabei *et al.*, Eur. Phys. J. 12 **C73**, 2648 (2013) [arXiv:1308.5109v2 [astro-ph.GA]].

R. Barnabei *et al.*, Eur. Phys. J. **C67**, 39 (2010) [arXiv:1002.1028v1 [astro-ph.GA]].

[73] C. E. Aalseth *et al.*, Phys. Rev. Lett. **107**, 141301 (2011) [arXiv:1106.0650v3 [astro-ph.CO]].

[74] G. Angloher *et al.*, Eur. Phys. J. **C72**, 1971 (2012) [arXiv:1109.0702v1 [astro-ph.CO]].

[75] Z. Ahmed *et al.*, [arXiv:1203.1309v2 [astro-ph.CO]].

[76] R. Agnese *et al.*, Phys. Rev. Lett. **111**, 251301 (2013) [arXiv:1304.4279v3 [hep-ex]].

[77] J. Cherwinka *et al.*, Phys. Rev. 9 **D90**, 092005 (2014) [arXiv:1401.4804v3 [astro-ph.IM]].

[78] P. Ullio,M. Kamionkowski and P. Vogel, JHEP **0107**, 044 (2001) [arXiv:0010036 [hep-ph]].

[79] E. Aprile *et al.*, Springer Proc. Phys. **C12-02-22**, 93 (2013) [arXiv:1206.6288v1 [astro-ph.IM]].

[80] J. Maricic, talk given at ICHEP 2012, Melbourne http://darkside.lngs.infn.it/.

[81] H. Araújo, talk given at TIPP 2014, Amsterdam http://lz.lbl.gov/.

[82] J. Conrad, [arXiv:1411.1925v1 [hep-ph]].

[83] M. Cirelli, Pramana **79**, 1021 (2012) [arXiv:1202.1454v5 [hep-ph]].

[84] T. Bringmann *et al.*, JCAP **1207**, 054 (2012) [arXiv:1203.1312v4 [hep-ph]].

[85] W. B. Atwood *et al.*, Astrophys. J. **697**, 1071 (2009) [arXiv:0902.1089v1 [astro-ph.IM]].

[86] F. Aharonian *et al.*, Astron. Astrophys. **457**, 899 (2006) [arXiv:0607333v1 [astro-ph]].

[87] J. Aleksic *et al.*, Astropart. Phys. **35**, 435 (2012) [arXiv:1108.1477v2 [astro-ph.IM]].

[88] J. Holder *et al.*, AIP Conf. Proc. **1085**, 657 (2009) [arXiv:0810.0474v1 [astro-ph]].

[89] C. Weniger, JCAP **1208**, 007 (2012) [arXiv:1204.2797v2 [hep-ph]].

[90] T. Bringmann, X. Huang, A. Ibarra, S. Vogl and C. Weniger, JCAP **1207**, 054 (2012) [arXiv:1203.1312v4 [hep-ph]].

[91] A. Hektor, M. Raidal and E. Tempel, Astrophys. J. **762**, L22 (2013) [arXiv:1207.4466v3 [astro-ph.HE]].

[92] M. Ackermann *et al.*, Phys. Rev. D**88**, 082002 (2013) [arXiv:1305.5597v3 [astro-ph.HE]].

[93] A. A. Abdo et al., Astrophys. J. **712**, 147 (2010) [arXiv:1001.4531v1 [hep-ph]].

[94] L. Bergstrom, G. Bertone, J. Conrad, C. Farnier and C. Weniger, JCAP **1211**, 025 (2012) [arXiv:1207.6773v1 [hep-ph]].

[95] D. Hooper and L. Goodenough, Phys. Lett. B **697**, 412 (2011) [arXiv:1010.2752v3 [hep-ph]].

[96] F. Calore, I. Cholis and C. Weniger, [arXiv:1409.0042v1 [astro-ph.CO]].

[97] A. Boyarsky, D. Mayshev and O. Ruchayskiy, Phys. Lett. B **705**, 165 (2011) [arXiv:1012.5839v1 [hep-ph]].

[98] N. Mirabal, [arXiv:1411.7410v1 [astro-ph.HE]].

[99] M. G. Aartsen et al., [arXiv:1406.6868v2 [hep-ph.HE]].

M. G. Aartsen et al., Phys. Rev. D **88**, 122001 (2013) [arXiv:1307.3473v2 [astro-ph.HE]].

M. G. Aartsen et al., Phys. Rev. Lett. **110**, 131302 (2013) [arXiv:1212.4097v2 [astro-ph.HE]].

[100] S. Adrian-Martinez et al., JCAP **1311**, 032 (2013) [arXiv:1302.6516v2 [astro-ph.HE]].

[101] T. Tanaka et al., Astrophys. J. **742**, 78 (2011) [arXiv:1108.3384v2 [hep-ph]].

[102] O. Adriani et al., Nature **458**, 607 (2009) [arXiv:0810.4995v1 [astro-ph]].

[103] M. Aguilar et al., Phys. Rev. Lett. **110**, 141102 (2013).

L. Accardo et al., Phys. Rev. Lett. **113**, 121101 (2014).

[104] I. Cholis and D. Hooper, Phys. Rev. D**88**, 023013 (2013) [arXiv:1304.1840v2 [astro-ph.HE]].

[105] D. Hooper, T. Linden and P. Mertsch, [arXiv:1410.1527v1 [astro-ph.HE]].

[106] A. Ibarra, A. S. Lamperstorfer and J. Silk, Phys. Rev. D**89**, 063539 (2014) [arXiv:1309.2570v2 [hep-ph]].

[107] P. von Doetinchem et al., Astropart. Phys. **54**, 93 (2014) [arXiv:1307.3538v2 [astro-ph.IM]].

[108] S. Holmes, R. S. Moore, S. Ronald and V. Shiltsev, JINST **6**, T08001 (2011) [arXiv:1106.0909v1].

[109] Copies shelved as reports in LEP, PS and SPS libraries, Geneva: CERN, 2004.

[110] P. J. Fox, R. Harnik, J. Kopp and Y. Tsai, Phys. Rev. D**85**, 056011 (2012) [arXiv:1109.4398v2].

[111] J. Goodman, I. Masahiro, R. Arvind, W. Shepard, T. M. P. Tait and H.-B. Yu, Phys. Rev. D**82**, 116010 (2010) [arXiv:1008.1783v2 [hep-ph]].

[112] Copies shelved as reports in LEP, PS and SPS libraries, Geneva: CERN, 1984.

[113] H. Baer et al., [arXiv:1306.6352v1 [hep-ph]].

[114] P. J. Fox, R. Harnik, J. Kopp and Y. Tsai, Phys. Rev. D**84**, 014028 (2011) [arXiv:1103.0240v1 [hep-ph]].

[115] Y. Bai, P. J. Fox, and R. Harnik, JHEP. **1012**, 048 (2010) [arXiv:1005.3797v2 [hep-ph]].

[116] V. A. Mitsou, [arXiv:1402.3673v1 [hep-ex]].

[117] G. Aad et al., [arXiv:1410.4031v1 [hep-ex]].

[118] G. Aad et al., JHEP **1304**, 075 (2013) [arXiv:1210.4491v2 [hep-ex]].

[119] V. Khachatryan et al., [arXiv:1408.3583v1 [hep-ex]].

[120] N. Craig, [arXiv:1309.0528v2 [hep-ph]].

[121] H. Dreiner, M. Huck, M. Krämer, D. Schmeier and J. Tattersall, Phys. Rev. D**87**, 075015 (2013) [arXiv:1211.2254v1 [hep-ph]].

[122] A. Freitas and S. Westhoff, JHEP D**1410**, 116 (2014) [arXiv:1408.1959v1 [hep-ph]].

[123] J. Kopp, V. Niro, T. Schwetz and J. Zupan, Phys. Rev. D**80**, 083502 (2009) [arXiv:0907.3159v2 [hep-ph]].

[124] J. Edsjö and P. Gondolo, Phys. Rev. D **56**,1879-1894 (1997).

[125] P. Gondolo and G. Gelmini, Nucl. Phys. B **360**,145-179 (1991).

[126] E. Kolb and M. Turner, *The Early Universe* (Westview, 1994)

[127] K. Griest and D. Seckel, Phys. Rev. D **43**,3191 (1991).

[128] M. Srednicki, R. Watkins and K. A. Olive, Nucl. Phys. B **310**,693 (1988).

[129] J. Scherrer and M. S. Turner, Phys. Rev. D **33**,1585 (1986).

[130] P. Gondolo, J. Edsjö, P. Ullio and L. Bergstrom, JCAP **0407**,008 (2004) [arXiv:0406204 [astro-ph]]. P. Gondolo, J. Edsjö, P. Ullio, L. Bergström, M. Schelke, E.A. Baltz, T. Bringmann and G. Duda, http://www.darksusy.org.

[131] A. Arbey and F. Mahmoudi, Comput. Phys. Commun. **181**,1277-1292 (2010) [arXiv:0906.0369v1 [hep-ph]].

[132] F. E. Paige, S. D. Protopopescu, H. Baer and X. Tata [arXiv:0312045 [hep-ph]]. F. E. Paige, S. D. Protopopescu, H. Baer and X. Tata , http://www.nhn.ou.edu/ isajet/

[133] G. Bélanger, F. Boudjema, A. Pukhov and A. Semenov, Comput. Phys. Commun. **149**,103-120 (2002) [arXiv:0112278 [hep-ph]].

G. Bélanger, F. Boudjema, A. Pukhov and A. Semenov, Comput. Phys. Commun. **174**,577-604 (2006) [arXiv:0405253 [hep-ph]].

G. Bélanger, F. Boudjema, A. Pukhov and A. Semenov, Comput. Phys. Commun. **177** (2007) 894;

[134] C. E. Yaguna, JHEP **1108**,060 (2011) [arXiv:1105.1654v1 [hep-ph]].

[135] G. Mangano, G. Miele, S. Pastor and M. Peloso, Phys. Lett. B **534**,8-16 (2002) [arXiv:0111408v2 [astro-ph]].

[136] J. Haman, S. Hannestad and M. S. Martin, Phys. Rev. D **75**,023522 (2007) [arXiv:0611582v2 [astro-ph]].

[137] S. Profume and P. Ullio, JCAP **0311**,006 (2003) [arXiv:0309220v2[hep-ph]].

[138] C. Armendariz-Picon, V. Mukhanov and P. J. Steinhardt, Phys. Rev. D **63**,103510 (2001) [arXiv:0006373v1 [hep-ph]].

[139] A. Arbey, Phys. Rev. D **74**,043516 (2006) [arXiv:0601274v2 [astro-ph]].

[140] A. Arbey and F. Mahmoudi, Phys. Lett. D **669**,46-51 (2008) [arXiv:0803.0741 [hep-ph]].

[141] M. Hindmarsh and O. Philipsen, Phys. Rev. D **71**,087302 (2005) [arXiv:0501232 [hep-ph]].

[142] T. Wizansky, Phys. Rev. D **74**,065007 (2006) [arXiv:0605179v2 [hep-ph]].

[143] M. Beneke, F. Dighera and A. Hryczuk [arXiv:1409.3049 [astro-ph]].

[144] B. Herrmann and M. Klasen, Phys. Rev. D **76**,117704 (2007) [arXiv:0709.0043 [hep-ph]].

[145] B. Herrmann, M. Klasen and K. Kovařík, Phys. Rev. D **79**,061701 (2009) [arXiv:0901.0481 [hep-ph]].

[146] B. Herrmann, M. Klasen and K. Kovařík, Phys. Rev. D **80**,085025 (2009) [arXiv:0907.0030 [hep-ph]].

[147] J. Harz, B. Herrmann, M. Klasen, K. Kovařík and Q. Le Boulc'h, Phys. Rev. D **87**,054031 (2013) [arXiv:1212.5241 [hep-ph]].

[148] J. Harz, B. Herrmann, M. Klasen and K. Kovařík, [arXiv:1409.2898v1 [hep-ph]].

[149] F. Boudjema, G. Drieu La Rochelle and S. Kulkarni, Phys. Rev. D **84** (2011) 116001 [arXiv:1108.4291 [hep-ph]].

[150] A. Chatterjee, M. Drees and S. Kulkarni, [arXiv:1209.2328 [hep-ph]].

[151] N. Baro, F. Boudjema and A. Semenov, Phys. Lett. B **660** (2008) 550 [arXiv:0710.1821 [hep-ph]].

N. Baro, G. Chalons and S. Hao, AIP Conf. Proc. **1200** (2010) 1067 [arXiv:0909.3263 [hep-ph]].

N. Baro, F. Boudjema, G. Chalons and S. Hao, Phys. Rev. D **81** (2010) 015005 [arXiv:0910.3293 [hep-ph]].

[152] A. Freitas, Phys. Lett. B **652** (2007) 280 [arXiv:0705.4027 [hep-ph]].

[153] J. Ellis, K. A. Olive and J. Zheng, [arXiv:1404.5571v1 [hep-ph]].

[154] B. C. Allanch, S. Kraml and W. Porod JHEP **0303**,016 (2002) [arXiv:0302102v4 [hep-ph]].

[155] G. Belanger, S. Kraml and A. Pukhov Phys. Rev. D **72**,015003 (2005) [arXiv:0502079v4 [hep-ph]].

[156] W. Porod Comput. Phys. Commun. **153**,275-315 (2003) [arXiv:0301101 [hep-ph]].

W. Porod and F. Staub Comput. Phys. Commun. **183**,2458-2469 (2012) [arXiv:1104.1573 [hep-ph]].

[157] A. Djouadi, J.-L. Kneur and G. Moultaka Comput. Phys. Commun. **176**,426-455 (2007) [arXiv:0211331 [hep-ph]].

[158] B. C. Allanach Comput. Phys. Commun. **143**,305-331 (2002) [arXiv:0104145 [hep-ph]].

[159] C. Yaguna, Phys. Rev. D **81**,075024 (2010) [arXiv:1003.2730v1 [hep-ph]].

[160] U. Ellwanger, C. Hugonie and A. M. Teixeira, Phys. Rept. **496**,1-77 (2010) [arXiv:0910.1785v5 [hep-ph]].

[161] M. Schmaltz and D. Tucker-Smith, Ann. Rev. Nucl. Part. Sci. **55**,229-270 (2005) [arXiv:0502182v1 [hep-ph]].

[162] M. Drewes, Int. J. Mod. Phys **E22**,1330019 (2013) [arXiv:1303.6912v3 [hep-ph]].

[163] L. Lopez Honorez and C. E. Yaguna, JHEP. **1009**,046 (2010) [arXiv:1003.3125v3 [hep-ph]].

[164] A. Belyaev, N. D. Christensen and A. Pukhov, Comput. Phys. Commun. **184**,1729-1769 (2013) [arXiv:1207.6082v2 [hep-ph]].

[165] J. Guasch, P. Häfliger and M. Spira, Phys. Rev. D **68**, 115001 (2003) [arXiv:0305101v2 [hep-ph]].

[166] P. Z. Skands *et al.*, JHEP. **0407**,036 (2009) [arXiv:03111235v4 [hep-ph]].

B. C. Allanach *et al.*, Comput. Phys. Commun. **180**,8-25 (2009) [arXiv:0801.0045v3 [hep-ph]].

[167] J. A. Aguilar-Saavedra, A. Ali, B. C. Allanach, R. L. Arnowitt, H. A. Baer, J. A. Bagger, C. Balazs and V. D. Barger *et al.*, Eur. Phys. J. C **46** (2006) 43 [arXiv:hep-ph/0511344].

[168] G. Passarino and M. J. G. Veltman, Nucl. Phys. B **160**, 151 (1979).

[169] O. Buchmueller, M. J. Dolan, J. Ellis, T. Hahn, S. Heinemeyer, W. Hollik, J. Marrouche and K. A. Olive *et al.*, arXiv:1312.5233 [hep-ph].

[170] Y. Amhis *et al.* [Heavy Flavor Averaging Group Collaboration], arXiv:1207.1158 [hep-ex] and online update at `http://www.slac.stanford.edu/xorg/hfag`.

[171] J. Ellis, K. A. Olive and Y. Santoso, [arXiv:0112113v1 [hep-ph]].

[172] C. Kilic and B. Tweedie [arXiv:1211.6106v2 [hep-ph]].

[173] Z.-H. Yu, X.-J. Bi, Q.-S. Yan and P.-F. Yin [arXiv:1211.2997v1 [hep-ph]].

[174] G. Aad *et al.* [ATLAS Collaboration], ATLAS-CONF-2012-170, Dec. 2012.

[175] H. E. Haber,R. Hempfling and A. H. Hoang Z. Phys. C**75** (1997) 539 [arXiv:9609331 [hep-ph]].

[176] M. Badziak,E. Dudas,M. Olechowski and S. Pokorski JHEP **1207** 155 (2012) [arXiv:1205.1675 [hep-ph]].

[177] K.A. Olive *et al.* (Particle Data Group) Chin. Phys. C **38** (2014) 090001

[178] A. Pukhov, E. Boos, M. Dubinin *et al.* , [arXiv:9908288v2 [hep-ph]].

[179] A. Pukhov, A. Belyaev and N. Christensen, (19.7.2012)

[180] S. Catani and M. H. Seymour, Nucl. Phys. B **485**, 291 (1997).

[181] W. Kilian, "Übung zu Strahlungskorr. in Eichtheo.', Maria Laach (2001) ,"

[182] W. Siegel, Phys. Lett. B **84**, 193 (1979).

[183] W. Pauli and F. Villars, Rev. of Mod. Phys. **21**, 434 ((1949).

[184] I. Jack and D. R. T. Jones. Adv. Ser. Direct. High Energy Phys. **21**, 494 (2010) [arXiv:9707278v2 [hep-ph]].

[185] D. Stöckinger, JHEP. **0503**, 076 (2005) [arXiv:0503129v2 [hep-ph]].

[186] Z. F. Jegerlehner, Eur. Phys. J. C**18**, 673 (2001) [arXiv:0005255v1 [hep-th]].

[187] T. Hahn and M. Perez-Victoria, Comput. Phys. Commun. **118**, 153 (1999) [arXiv:9807565v1 [hep-ph]].

[188] S. Dittmaier, Nucl. Phys. B **675**, 447 (2003) [arXiv:0308246v1 [hep-ph]].

[189] A. Denner and S. Dittmaier, Nucl. Phys. B **844**, 199 (2011) [arXiv:1005.2076v1 [hep-ph]].

[190] R. K. Ellis and G. Zanderighi, JHEP **0802**, 002 (2008) [arXiv:0712.1851 [hep-ph]].

[191] S. Heinemeyer, H. Rzehak and C. Schappacher, Phys. Rev. D**82**, 075010 (2010) [arXiv:1007.0689v1 [hep-ph]].

[192] K. Melnikov and A. Yelkhovsky, Phys. Rev. D**59**, 114009 (1999) [arXiv:9805270v1 [hep-ph]].

A. Hoang, Phys. Rev. D**61**, 034005 (2000) [arXiv:9905550v2 [hep-ph]].

M. Beneke and A. Signer, Phys. Lett. B**471**, 233 (1999) [arXiv:9906475v2 [hep-ph]].

A. A. Penin and A.A. Pivovarov, Nucl. Phys. B**549**, 217 (1999) [arXiv:9807421v2 [hep-ph]].

[193] K. G. Chetyrkin, Phys. Lett. B **404**, 161 (1997) [arXiv:9703278v1 [hep-ph]].

[194] R. Harlander, P. Kant, L. Mihaila and M. Steinhauser, JHEP **0609**, 053 (2006) [arXiv:0607240v2 [hep-ph]].

[195] A. Bauer, L. Mihaila and J. Salomon, JHEP **0902**, 037 (2009) [arXiv:0810.5101v2 [hep-ph]].

[196] K. G. Chetyrkin, Phys. Lett. B **390**, 309 (1997) [arXiv:9608318v2 [hep-ph]].

P. A. Baikov, K. G. Chetyrkin and J. H. Kuhn, Phys. Rev. Lett. **96**, 012003 (2006) [arXiv:0511063v2 [hep-ph]].

K. G. Chetyrkin and A. Kwiatkowski, Nucl. Phys. B **461**, 3 (1996) [arXiv:9505358v1 [hep-ph]].

[197] M. S. Carena, D. Garcia, U. Nierste and C. E. M. Wagner, Nucl. Phys. B **577**, 88 (2000) [arXiv:9912516v3 [hep-ph]].

[198] D. Noth and M. Spira, JHEP **1106**, 084 (2011) [arXiv:1001.1935v2 [hep-ph]].

[199] A. Crivellin and C. Greub, Phys. Rev. D **87**, 015013 (2013) [arXiv:1210.7453v2 [hep-ph]].

[200] A. Crivellin, L. Hofer and J. Rosiek, JHEP **1107**, 017 (2011) [arXiv:1103.4272v4 [hep-ph]].

[201] H. Eberl, K. Hidaka, S. Kraml, W. Majerotto and Y. Yamada, Phys. Rev. D**62**, 055006 (2000) [arXiv:9912463v3 [hep-ph]].

[202] J. A. M. Vermaseren, S. A. Larin and T. van Ritbergen, Phys. Lett. B **405**, 327 (1997) [arXiv:9703284v1[hep-ph]].

[203] R. Harlander, L. Mihaila and M. Steinhauser, Phys. Rev. D **72**, 095009 (2005) [arXiv:0509048v1 [hep-ph]].

[204] S. Catani, S. Dittmaier, M. H. Seymour and Z. Trocsanyi, Nucl. Phys. B **627**, 189 (2002) [hep-ph/0201036].

[205] T. Bloch and A. Nordsieck, Phys. Rev. **52**, 54 (1937).

[206] T. Kinoshita, J. Math. Phys. **3**, 650 (1962).

T. D. Lee and M. Nauenberg, Phys. Rev. **133**, 1549 (1964).

[207] K. Kovařík *HitchHiker's Guide to Renormalization* (not yet published).

[208] G. 't Hooft and M. J. G. Veltman, Nucl. Phys. B**153**, 365 (1979) [arXiv:9807565v1 [hep-ph]].

[209] C. Weydert – *Recherche d'un boson de Higgs chargé avec le détecteur ATLAS: de la théorie à l'expérience*– PhD-thesis, University Grenoble

[210] G. Altarelli and G. Parisi, Nucl. Phys. B **126**, 298 (1977).

[211] V. Derya – *Color factors in QCD*– internship-report 2008, LPSC Grenoble

[212] H. E. Haber and G. L. Kane, Phys. Rept. **117**, 75 (198

[213] A. Denner, H. Eck, O. Hahn and J. Kublbeck, Phys. Lett. B **291**, 278 (1992).

[214] F. Feng and R. Mertig, arXiv:1212.3522.

[215] A. Sommerfeld, Annalen der Physik **403**, 257 (1931)

[216] M. Beneke, A. Signer and V. A. Smirnov, Phys. Lett. B **454** (1999) 137 [arXiv:9903260v1 [hep-ph]].

[217] A. Pineda and A. Signer, Nucl. Phys. B **762** (2007) 67 [arXiv:0607239v1[hep-ph]].

[218] G. T. Bodwin, E. Braaten and G. P. Lepage, Phys. Rev. D **51** (1995) 1125 [arXiv:9407339v2[hep-ph]].

[219] M. J. Strassler and M. E. Peskin, Phys. Rev. D **43** (1991) 1500

[220] M. R. Kauth, J. H. Kühn, P. Marquard and M. Steinhauser, Nucl. Phys. B **857** (2012) 28 [arXiv:1108.0361v2 [hep-ph]].

[221] Y. Kiyo, J. H. Kühn, S. Moch, M. Steinhauser and P. Uwer, Eur. Phys. J. C **60** (2009) 375 [arXiv:0812.0919v2 [hep-ph]].

[222] M. Beneke, [arXiv:9911490v1[hep-ph]].

[223] A. Hryczuk, Phys. Lett. B**699**, 271 (2011) [arXiv:1102.4295v2[hep-ph]].

[224] R. Harlander, L. Mihaila and M. Steinhauser, Phys. Rev. D**72**, 095009 (2005) [arXiv:0509048v1[hep-ph]].

[225] M. Beneke, P. Falgari and C. Schwinn Nucl. Phys. **B842** (2011) 414 [arXiv:1007.5414v2[hep-ph]].

[226] M. Beneke, Y. Kiyo and K. Schuller, Nucl. Phys. B **714** (2005) 67. [arXiv:0501289v2 [hep-ph]].

[227] M. R. Kauth, J. H. Kühn, P. Marquard and M. Steinhauser, Nucl. Phys. B **831** (2010) 285 [arXiv:0910.2612v1 [hep-ph]].

[228] R. Iengo, JHEP **0905** (2009) 024 [arXiv:0902.0688v3 [hep-ph]].

[229] S. Cassel, J. Phys. G **37** (2010) 105009 [arXiv:0903.5307v1 [hep-ph]].

[230] M. Drees and J. Gu, Phys. Rev. D **87**, no. 6, 063524 (2013) [arXiv:1301.1350v2 [hep-ph]].

M. Beneke, C. Hellmann and P. Ruiz-Femenia, JHEP **1303**, 148 (2013) [Erratum-ibid. **1310**, 224 (2013)] [arXiv:1210.7928v2 [hep-ph]].

C. Hellmann and P. Ruiz-Femena, JHEP **1308**, 084 (2013) [arXiv:1303.0200v2 [hep-ph]].

[231] M. Beneke and V. A. Smirnov, Nucl. Phys. B **522**, 321 (1998) [hep-ph/9711391].

[232] T. Huber and D. Maître, Comput. Phys. Commun. **175** (2006) 122 [arXiv:0507094v2 [hep-ph]].